Fault Tolerant Flight Control of a UAV with Asymmetric Damage to its Primary Lifting Surface

by

Wiaan Beeton

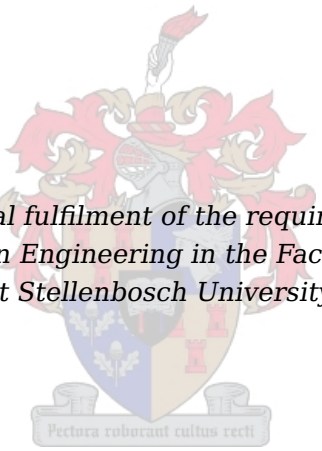

Thesis presented in partial fulfilment of the requirements for the degree of Master of Science in Engineering in the Faculty of Engineering at Stellenbosch University

Supervisor:

Mr J.A.A. Engelbrecht

Department of Electrical and Electronic Engineering

December 2013

Declaration

By submitting this thesis electronically, I declare that the entirety of the work contained therein is my own, original work, that I am the sole author thereof (save to the extent explicitly otherwise stated), that reproduction and publication thereof by Stellenbosch University will not infringe any third party rights and that I have not previously in its entirety or in part submitted it for obtaining any qualification.

December 2013

Abstract

In this thesis the design, analysis, implementation, and verification of a fault-tolerant unmanned aerial vehicle (UAV) flight control system which is robust to structural damage causing the natural flight dynamics of the vehicle to become asymmetric, is presented.

The main purpose of the robust control architecture is to maintain flight stability after damage has occurred. The control system must be able to handle an abrupt change from an undamaged to a damaged state, and must also not depend on explicit knowledge of the damage. A robust control approach is therefore preferred above an adaptive control approach. As a secondary objective, the system must provide robust flight performance to ensure adequate response times and acceptable transients' behaviour, both in normal flight, and after damage has occurred.

An asymmetric six degrees of freedom equations of motion model is derived. The model accounts for the changes in the aerodynamic model of the aircraft as well as changes in the centre of gravity location. Vortex lattice techniques are used to determine the aerodynamic coefficients of the aircraft for damage to the main wing resulting in 0% to 40% spanwise lifting surface loss. A sequential quadratic programming optimisation algorithm is applied to the force and moment equations to find the trim flight state and actuator deflections of the asymmetric aircraft for constant airspeed and altitude. The trim flight state can be further constrained to force zero bank angle, zero sideslip angle or a desired relative weighting of nonzero bank angle and nonzero sideslip angle. The calculated trim actuator deflections are compared to the physical deflection limits to determine the feasibility of maintaining trim flight for different percentages of wing loss. Assuming that a valid trim condition exists, the relative stability of the aircraft's natural modes is analysed as a function of percentage wing loss by tracing the locus of the open-loop poles.

An acceleration-based flight control architecture is designed and implemented, and the robustness of the flight control stability and performance is analysed as a function of percentage wing loss. The robustness and performance of the flight control system is verified with a nonlinear simulation for spanwise wing loss from 0 to 40%.

Practical flight tests are performed to verify the robustness and performance of the flight control systems to in-flight damage. A detachable wing with release mechanism is designed and manufactured to simulate 20% wing loss. The flight control system is implemented on a practical UAV and a successful flight test shows that it performs fully autonomous flight control, and is able to accommodate an in-flight partial wing loss.

Uittreksel

In hierdie tesis word die ontwerp, analise, implementasie en verifikasie van ’n fout-verdraende onbemande vliegtuig beheerstelsel wat robuust is tot strukturele skade wat die natuurlike vlug dinamika van die voertuig asimmetries maak, voorgestel.

Die hoofdoel van hierdie robuuste beheer argitektuur is om stabiliteit te verseker na die skade aangerig is. Die beheerstelsel moet die skielike verandering van normale na beskadigde vlug hanteer sonder enige eksplisiete kennis daarvan. Dus word ’n robuuste beheer aanslag verkies bo ’n aanpassende beheer struktuur. Tweedens moet die vlugbeheerstelsel robuust genoeg wees om steeds die gewenste reaksietyd en aanvaarbare oorgangsverskynsels te kan hanteer, tydens beide normale en beskadigde vlug.

’n Asimmetriese ses grade van vryheid beweginsvergelykings model word afgelei. Die model het die vermoë om veranderinge in die aerodinamiese model van die vliegtuig, sowel as massamiddelpunt verskuiwing, voor te stel. “Vortex Lattice” metodes is gebruik om die aerodinamiese koëffisiënte van die beskadigde vlerk voor te stel tussen 0% en 40% verlies. ’n Sekwensiële kwadratiese programmering optimiserings algorithme is aangewend op die krag en moment vergelykings om die ekwilibrium vlug toestand en aktueerder defleksies te vind vir ’n asimmetriese vliegtuig met konstante lugspoed en hoogte. Die ekwilibrium vlug toestand word verder beperk deur ’n nul rolhoek, ’n nul sygliphoek of ’n relatiewe weging van die twee. Die bepaalde ekwilibrium defleksies word dan vergelyk met die fisiese limiete om hulle geldigheid te bepaal vir ekwilibrium vlug. As ’n geldige ekwilibrium toestand bestaan, kan die relatiewe stabiliteit van die vliegtuig se natuurlike modusse ontleed word as ’n persentasie van vlerkverlies deur die wortellokusse van die ooplus pole na te gaan.

’n Versnellings-gebaseerde vlug beheerstelsel argitektuur is ontwerp en geïmplementeer. Daarna is die robuustheid ontleed as ’n funksie van die persentasie vlerkverlies. Die robuustheid en gedrag van hierdie vlugbeheerstelsel is geverifieer met ’n nie-linêre simulasie vir 0 tot 40% vlerkverlies.

Praktiese vlugtoetse is onderneem om die robuustheid en gedrag tydens/na skade gedurende ’n vlug, te verifeer. ’n Vlerkverlies meganisme is ontwerp en vervaardig om 20% vlerkverlies te simuleer. Die vlugbeheerstelsel is geïmplementeer op ’n onbemande vliegtuig en die daaropvolgende suksesvolle vlug lewer bewys dat die vlugbeheerstelsel wel skade, in die vorm van gedeeltelike vlerkverlies, tydens vlug kan hanteer.

Contents

List of Figures

List of Tables

Nomenclature

Abbreviations and Acronyms

AC Aerodynamic Centre

AEoM Asymmetric Equations of Motion

ASA Axial Specific Acceleration

AVL Athena Vortex Lattice

CAN-bus Controller Area Network bus

CG Centre of Gravity

CRC Climb-rate Controller

dB decibel

DCM Direction Cosine Matrix

DRD Dutch Roll Damper

EoM Equations of Motion

ESL Electronic Systems Laboratory

FDI Fault Detection and Isolation

GPS Global Positioning System

GS Ground Station

GSS Ground Station Software

GS_TXRX Ground Station Transmitter and Receiver

IMU Inertial Measurement Unit

LSA Lateral Specific Acceleration

NED North East Down reference frame

NSA Normal Specific Acceleration

OBC Onboard Computer

RAC Roll Angle Controller

RCR Radio Control Remote

RF-link Radio Frequency link

SAT Specific Acceleration Transformation

6DoF Six Degrees of Freedom

UAV Unmanned Aerial Vehicle

MMAE Multiple Model Adaptive Estimator

Greek Letters

α Angle of attack

β Side-slip angle

δ Control surface deflection

Δx, Δy, Δz x,y,z distance from main body's CG to specified piece's CG

Γ Circulation

γ Dihedral angle

ω Angular rates

ψ, θ, ϕ Heading, pitch and bank angles

ρ Distance between two points or Air density

τ Time constant

Lowercase Letters

a Acceleration / lift curve slope

b Span of the wing

c Chord length

$\bar{\bar{c}}$ Mean aerodynamic chord

e Oswald number

g Gravity

h Height or aerodynamic centre location when subscripted by 0

l Left side wing length or moment arm length

m Mass

v Velocity

q Dynamic air pressure

r Right side wing length

Uppercase Letters

A Aspect ration

C Side force

D Drag force

$C_{(\cdot)}$ Cosine of $(.)$

$C_{(\cdot)_{(\cdot)}}$ Non-dimensional coefficient

E Control surface chord fraction

G Gravitational force

I Moment of inertia matrix or identity matrix

F Force

$X_{(.)}$, $Y_{(.)}$, $Z_{(.)}$ Forces in the x-, y- and z-axis in reference frame $(.)$

L Lift force

$L_{(.)}$, $M_{(.)}$, $N_{(.)}$ Moments around the x-, y- and z-axis in reference frame $(.)$

M Moment in general or moment around the body referenced y-axis

H Angular moment

P, Q, R Roll, Pitch and Yaw rate

U, V, W Velocity in x-, y- and z-direction

$\dot{U}$, $\dot{V}$, $\dot{W}$ Linear acceleration in x-, y- and z-direction

$\dot{P}$, $\dot{Q}$, $\dot{R}$ Angular acceleration in x-, y- and z-direction

S Surface area

$S_{(.)}$ Sine of $(.)$

$\bar{V}$ Airspeed

Subscripts

B Body reference frame

D Drag

O Inertial reference frame

W Wind or stability reference frame

Ail, El, Rud Aileron, Elevator or Rudder actuator surface

dac Damaged aircraft

tip Damaged / Lost piece

L Lift

T Thrust or tail plane quantity

G Gravity

l, m, n Rolling-, pitching- and yawing moment

P, Q, R Roll-, pitch- and yaw rate

N, E, D North, East and Down in inertial reference frame

xx, yy, zz Principal inertial terms

xy, xz, yz Coupling inertial terms

Acknowledgements

Throughout the planning and writing of this thesis various people have played vital roles in enabling the completion thereof. The following acknowledgements go out to these people:

- First and foremost my family: Liana Beeton (mom), André Beeton (dad) and Suzaan Beeton (sister) for their loving support and understanding during the completion of this thesis
- My study leader, Japie Engelbrecht, for all his inputs, help and guidance during my work on this thesis, without whom successful completion would not have been possible
- Wessel Croukamp and Wynand van Eeden for their design and manufacturing input during the implementation of the wing loss mechanism
- Anton Runhaar and Lionel Basson as ESL Lab Engineers for their help in preparing for and conducting practical flight tests
- Everyone who studied in the ESL through 2011 to 2012 and spent many late nights working in the lab and keeping me company
- Michael Basson from Micton Hobbies for his help with manufacturing the new wing and also his service as safety pilot during flight tests
- My close friends at the residences of Berg en Dal 33 and 49, who were always there through the good and bad times during our M-thesis journeys
- Marilie and Marike for their late night coffee delivery initiative when I could not join them for one on the town
- Melanie Bailey for her language expertise and proofreading
- Lastly, the ESL's trustworthy coffee machine which kept me awake long enough to finish this thesis. This would also not have been possible without the help of Mastortons-, Switch-, Moka-, Strictly- and Häzz coffee roasters

Chapter 1

Introduction

In this chapter some background on the thesis topic will be provided, the problem statement will be defined, an overview of previous research done on the topic will be given and an overview of the project execution and the thesis outline will be explained.

1.1 Background

In today's world the unmanned aerial vehicle (UAV) plays an ever increasing role. Private, government, military and scientific organisations increase their reliance on UAVs as they provide a layer of abstraction from the human element. To clarify, having a thoroughly designed UAV out in the field decreases the chances of human error during a test or operation. It also reduces the risk of injury to the operator through removing him or her from the actual danger. The problem with a UAV is: we still rely strongly on a human operator to constantly supervise it and take control when something unexpected happens, like damage to its wing. If the UAV could continue after losing a part of its wing, the need for external intervention and supervision would be reduced. This would increase the UAV's reliability. It would also decrease the risk of injury to anyone in the vicinity of the UAV and not only its operator. In examining the possibilities of granting a UAV the capability to handle this type of event, a good place to start would be its underlying control system.

The problem with general control system design is that it is only as effective and reliable as the model it was built on. If this model becomes inaccurate due to some kind of damage, this will degrade the handling properties and performance and could cause the aircraft to become unstable. It is due to this fact that engineers started looking into various ways to accommodate these model uncertainties and changes. Their solutions led to fault tolerant control.

Fault tolerant control is a control architecture which is tolerant of some types of faults which occur in the system. These faults could be malfunctioning actuators, structural damage, etc. which change the characteristics of the aircraft. Solutions can be implemented in various ways, according to the desired outcomes. Two main methodologies in fault tolerant control systems are adaptive- and robust control theory. In the adaptive control approach, the controller adapts to changes in the aircraft dynamics. In the robust control approach, the controller does not adapt, but is designed to provide acceptable stability and performance over the range of possible aircraft dynamics models, which include the nominal case and all damaged cases. As is suggested by the topic of this thesis, the latter will be implemented with regard to a UAV experiencing partial wing loss.

1.2 Problem Statement

The objective during this project is to design and implement a UAV's control architecture which will be robust to partial wing loss. Achieving this will require an accurate model of the effects of partial wing loss on an aircraft. In order to design a control architecture, a valid equilibrium, accounting for the effects of partial wing loss, needs to be established. The robustness of an aircraft control architecture designed with classical control theory, as well as an alternative control architecture, should be analysed with regard to partial wing loss. A robust control architecture should then be implemented on a UAV and validated during a practical flight test.

1.3 Previous Research

This section is divided into two parts. In the first part research conducted within the fault tolerant control systems group in the Electronic Systems Laboratory (ESL) is described and the research gap for this project will be identified. In the second part the external research found and deemed applicable to solving the problem presented in this project will be described. The topics include modelling asymmetric aircraft dynamics, methods of determining the trim of an aircraft and robust control architectures.

1.3.1 ESL Conducted Research

The ESL was established in 2001 and since then, various projects required students to conduct research in the field of fault tolerant control on UAVs. A brief summary of some of the work done in this group will be provided.

In 2008 Dr. I.K. Peddle, [1], developed an acceleration based control system for his PhD. which used control of the UAV's axial, normal and lateral accelerations to perform guidance. As a result of this low level acceleration control architecture, model uncertainties were encapsulated by the innermost control loops and enabled decoupled mid-to-top level controller implementations. Due to this model's uncertainty encapsulation, it was stated that the control architecture should be robust to model parameter variation.

Wihan Pietersen, [2], performed system identification on a UAV. This included the development of the necessary equations for system identification, implementing them in regression methods and showing that they could accommodate changing parameters due to a fault event on the aircraft.

Bertus Basson, [3], worked on adaptive longitudinal fault tolerant control. This included the controller handling a shift in CG location in the longitudinal axis, but did not void the symmetric assumption made in the general aircraft modelling process. It did however require that a change in the aerodynamic coefficients be made to accurately model the behaviour of the UAV.

Lionel Basson, [4], developed a control allocation algorithm as part of a fault tolerant control system. This algorithm provided the control system with virtual actuators and reallocated them in an optimal way to the physical aircraft's actuators. A sequential quadratic programming (SQP) optimisation was used to solve the reallocation problem, taking into account various goals and constraints. It proved capable of reconfiguring control allocation for different aircraft and various fault scenarios.

Hendrik Odendaal, [5], investigated two fault detection and isolation (FDI) methods for actuator failures on a UAV. The first method involved a multiple model adaptive estimator (MMAE), consisting of a bank of Kalman filters conditioned with expected actuator faults. The second method used a parity space approach which uses the analytical redundancies available between sensors' outputs and actuator inputs. Both methods successfully detected actuator faults. The Kalman filter approach was less sensitive to actuator faults than the parity space approach but reported fewer false actuator failures.

To summarise, previous research on fault tolerant control in the ESL included fault detection and isolation, system identification, and adaptive control. An acceleration-based control system has also been developed that is robust to parameter variations. However, a flight control system that is robust to changes in the flight dynamics due to airframe damage has not been previously research within the ESL, and a research gap exists. The author therefore aims to address this gap by designing a control system that is robust to partial wing loss. In the process, the robustness of the acceleration-based control architecture to partial wing loss will also be investigated.

1.3.2 External Research

In this section, some of the relevant research on fault tolerant control and aircraft under the influence of damage, by researchers outside the ESL, will be described. Afterwards, a short summary will be provided linking this research to various aspects of this project.

B.J. Bacon and I.M. Gregory, [6], generalised the equations of motion to easily model asymmetric damage. This included deriving the mathematical equations without making any simplification assumptions. By further generalising this, they developed the equations around an arbitrary fixed point. This allowed

all external forces and moments to be defined on and around this arbitrary point, without the necessity of redefinition once damage has occurred. The only new moments created in this approach are those induced by the CG location shift. This provides an elegant way of representing both linear and angular accelerations in matrix notation for use in simulations.

G.H. Shah, [7], investigated the effect of wing- and tailplane-damage on the aerodynamic coefficients of an aircraft. This led to the conclusion that for accurate modelling, no symmetric assumptions may be made on any axes. Control surfaces should also be modelled individually instead of combined as usual. Due to asymmetric lift generation, the damping in roll dynamics will be different for positive and negative roll rates.

A. Marco, V. Claudio and E.L. Duke, [8], proposed a general trim solution to most desired trim conditions. They did this with a numerical method in order to find the control deflections which would deliver the desired trim. One of their trim conditions and solutions revolved around straight but not wings-level flight. This resulted in the aircraft flying with a non-zero bank angle, non-zero side-slip angle or a combination of both angles.

N. Nguyen, K. Krishnakumar, J. Kaneshige and P. Nespeca, [9], proposed asymmetric dynamics in such a way that the Δ change in coefficients and CG location between the nominal no damage case and off nominal damage cases are captured. These Δs are then used in the trim analysis to find a new trim point. At this stage an adaptive control architecture is used to negate these Δ changes.

M. Arruda, [10], also presented a control system resilient to asymmetric damages by implementing dynamic inversion. As described in [7], he also mentioned that lift imbalance will cause static rolling, pitching and yawing moments. He also took the shift in CG into account in the equations of motion, similar to the approach followed in [6].

S.I. AlSwailem, [11], used a pure robust design on a catapult launched UAV with a large flight envelope and high adverse flight conditions. These conditions included large shifts in UAV CG location. The v-gap metric was used to determine the nominal and worst-case off nominal models. This information was then used in the two degree of freedom controller designs based on H_∞. Although this might not be a design based on an asymmetric model, the use of robust techniques and shift in CG do make their research applicable to this thesis topic.

Examining this relevant external research provides a road-map of how this project should be conducted up to the point of the control architecture design. A UAV under the influence of partial wing loss is no longer a symmetric aircraft and will experience a shift in its CG. This requires the equations of motion to be derived without assuming symmetry, [6]. If a UAV experience partial wing loss, its aerodynamic properties will change and need to be taken into account, [7]. Once the model has been extended to take partial wing loss into account, a valid trim condition should be found, be it with a numerical or analytical method, [9]. This will allow for a proper model on which the robust control architecture can be designed and implemented.

1.4 Project Overview

Figure 1.1 shows Phoenix, the UAV that will be used in this project. It consists of a modified Trainer 60 model RC aircraft, fitted with a brush-less electric motor and custom ESL avionics pack. The left wing has also been modified to allow in-flight partial wing loss on demand.

Figure 1.2 provides a block diagram breakdown of the physical test system. It consists of three parts, the UAV, the test pilot and the ground station (GS). The ground station is able to communicate with the UAV through a RF-link. The safety pilot is equipped with RC remote control and can take control of the UAV at any time during a test. The UAV itself is equipped with a custom ESL avionics pack, which includes GPS, IMU and pressure sensors. It also has the capability to directly command the UAV's servos.

This project will start by deriving an asymmetric model, finding aerodynamic coefficients which describe partial wing loss, and modelling the shift in CG. Trim calculations will be conducted to find valid trim conditions for various partial wing loss percentages. A linear model will be presented, followed by a open-loop

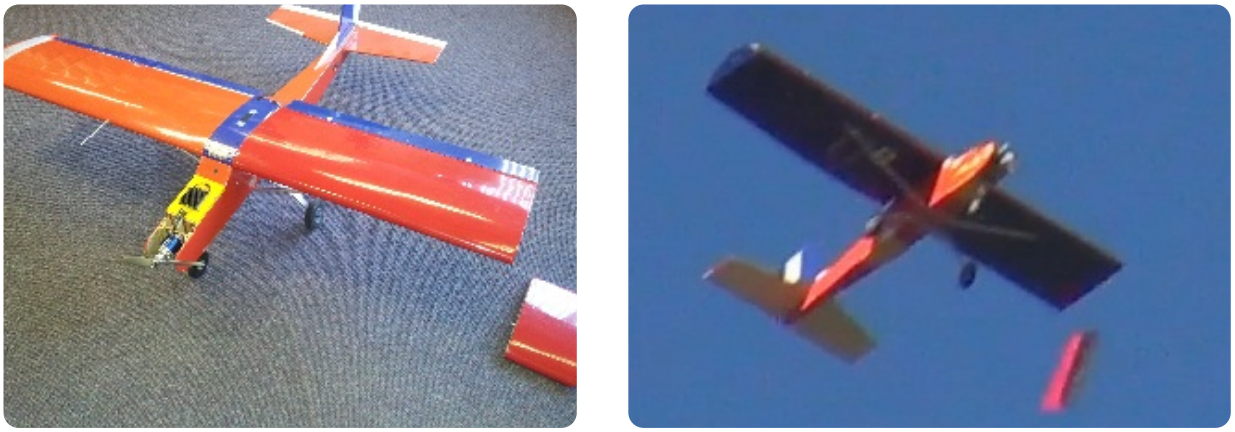

Figure 1.1 – Phoenix, the UAV used in this thesis

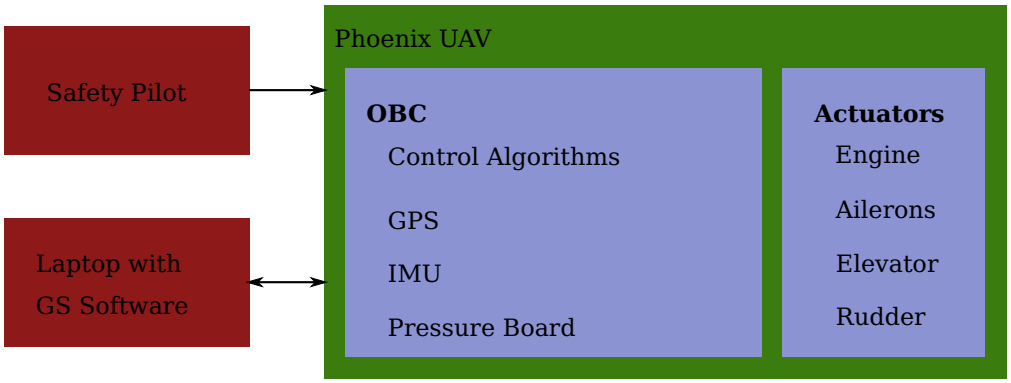

Figure 1.2 – Physical System overview

analysis of the dynamics. Classical control theory will be used to implement a control architecture, which will then be analysed for robustness. An acceleration based control architecture will be implemented and analysed for robustness. Non-linear simulations will be conducted, followed by mechanical modifications implemented on the UAV and then practical flight tests will be done.

1.5 Thesis Outline

In this section an outline of the thesis report will be provided.

In Chapter 2 the general model that will be used in this thesis is defined. As the UAV will no longer be symmetrical after partial wing loss has occurred, the general model cannot be used without voiding the main assumption behind its simplicity. The model for this thesis should be capable of handling partial wing loss accurately on both the physical and aerodynamic fronts which leave the UAV in an asymmetric configuration.

In Chapter 3 a trim study on the partially wing-damaged UAV is described. This will be done to determine the feasibility of applying control theory on a linearised version of the dynamics.

In Chapter 4 the full non-linear model, as described in Chapter 2, is linearised around the trim points calculated in Chapter 3. The chapter also investigates the validity of decoupling the model into longitudinal and lateral dynamics and analyses the stability of the aircraft dynamics about the trim points.

In Chapter 5 the implementation of various control architectures is described and their ability to handle partial wing loss is analysed. First a flight control system based on a classic aircraft control architecture is designed. Next, a flight control system based on an acceleration based control architecture proposed

by [1] is designed. The robustness of both control architectures to partial wing loss is compared and a decision is made regarding the necessity of designing explicitly for robustness. Finally, a hybrid control architecture is chosen for practical implementation and testing.

In Chapters 6, the preparations done to enable safe real-world flight testing of the practical control system are presented, including pre-flight simulations of the practical control architecture in both pure software simulations and hardware-in-the-loop simulations.

Chapter 7 describes the hardware modifications made to the UAV which were necessary to allow practical flight testing of partial wing loss.

Chapter 8 describes the practical flight tests conducted to perform real-world verification of the fault tolerant flight control system.

Chapter 9 summarises the conclusions of the research and makes recommendations for future work.

Chapter 2

Modelling

In this chapter, the mathematical model of the aircraft flight dynamics is extended to include the effects of partial wing loss. This extended aircraft model will serve as the basis for the analysis of the asymmetric flight dynamics, and for the design and simulation of a robust flight control system that is able to accommodate partial wing loss. The effect of partial wing loss on the aircraft will result in a change in aerodynamic coefficients, a shift in centre of gravity (CG) and a change in moment of inertia (MoI). All of the above will be included in the extended aircraft model.

A brief overview of the reference frames and conventions implemented will be discussed. The six degrees of freedom (6DoF) equations of motion (EoM) will be stated for a symmetric aircraft and extended to an asymmetric aircraft accounting for a shift in CG. The EoM will describe the motion of the aircraft through the various forces and moments acting in on it. The aerodynamic coefficients will be extended into a function of partial wing loss. This will be analysed by two methods: an analytic version for the well known coefficients and an Athena Vortex Lattice (AVL) numeric version. The analytic version will provide insight into the effects of physical aircraft changes on the aerodynamic coefficients, while the numeric version will provide a broader description on all affected coefficients. The physical effects of partial wing loss will be modelled in a CAD program to account for the change in aircraft mass, CG and MoI. All of these components will then be combined into a single non-linear model which will be able to represent the aircraft in its symmetric form or various stages of partial wing loss.

2.1 Reference Frames and Conventions

The aim in this section is to define the reference frames and conventions that will be used in this thesis. The reference frames that will be defined are the inertial, body axes, and wind reference frames. The conventions that will be described include conventions for defining the attitude, angular rates, position, velocity, forces and moments of the UAV and conventions for defining the actuator deflections.

2.1.1 Inertial, Body and Wind Reference Frames

Three reference frames are typically used when modelling the translational and rotational motion of an aircraft in three-dimensional space: the inertial reference frame, the body reference frame, and the wind reference frame.

2.1.1.1 Inertial Reference Frame

An inertial reference frame is required in which Newton's laws of motion can be applied. In this project the North, East, Down (NED) axis system will serve as the inertial reference frame. The NED axis system is a right hand axis system, fixed at some convenient origin in the environment. The environment in this case will be the earth and the origin a point on the runway. The x-axis will point in the northern direction, the y-axis in the eastern direction and the z-axis in the down direction as required to comply with a right handed orthogonal axis system. Figure 2.1 depicts the described NED axis. Any reference made with regard to the inertial reference frame can be identified by the subscripts N, E, or D depicting the represented axis or O depicting the origin of the vector.

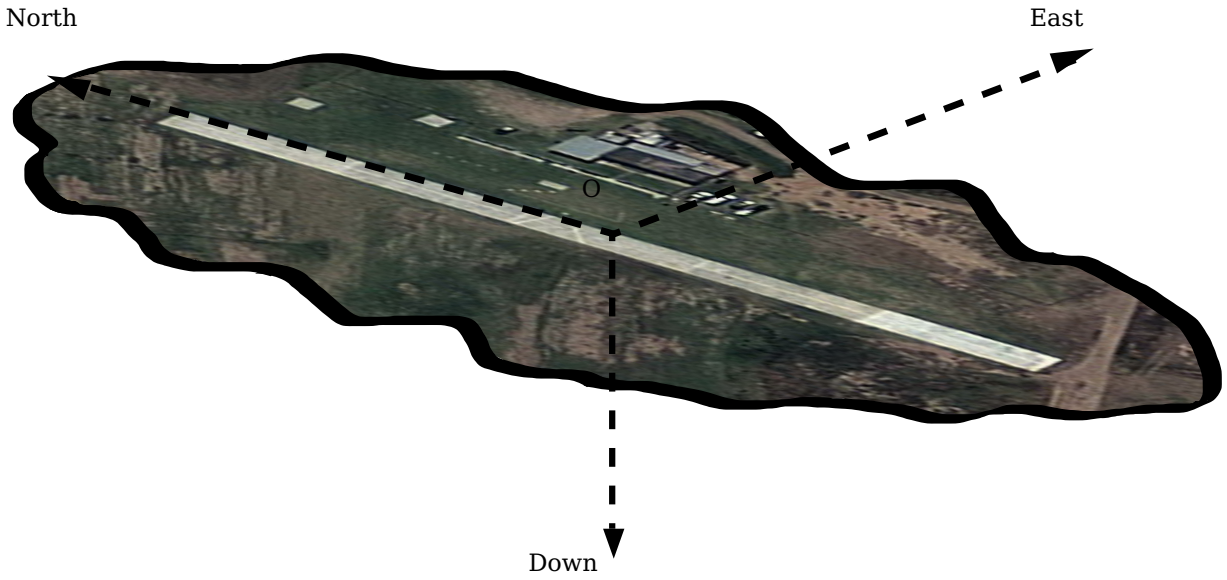

Figure 2.1 – Inertial Reference Frame

2.1.1.2 Body Reference Frame

The body reference frame represents the UAV itself and is fixed to its body. The point of fixture to the body is usually selected to simplify the mathematical equations describing any external forces and moments acting on the UAV. A commonly used location in the aerodynamic industry is either the UAV's centre of gravity or its aerodynamic reference centre. In this thesis, the original symmetric UAV's CG will be used as a fixed point. Although the CG may be in a different location after partial wing loss, the body axis system will not move to this new CG location. The reason behind this will be explained in Section 2.3. Any reference made with regard to the body axis can be identified by the subscript B. The alignment of this reference frame is defined in Figure 2.2. The positive x-axis is aligned with the nose of the UAV, the positive y-axis is aligned with the right wing and the positive z-axis is aligned to the bottom of the fuselage. These directions all adhere to the right hand rule and also ease the mathematical transforms necessary to convert any measurement from body to inertial and vice versa.

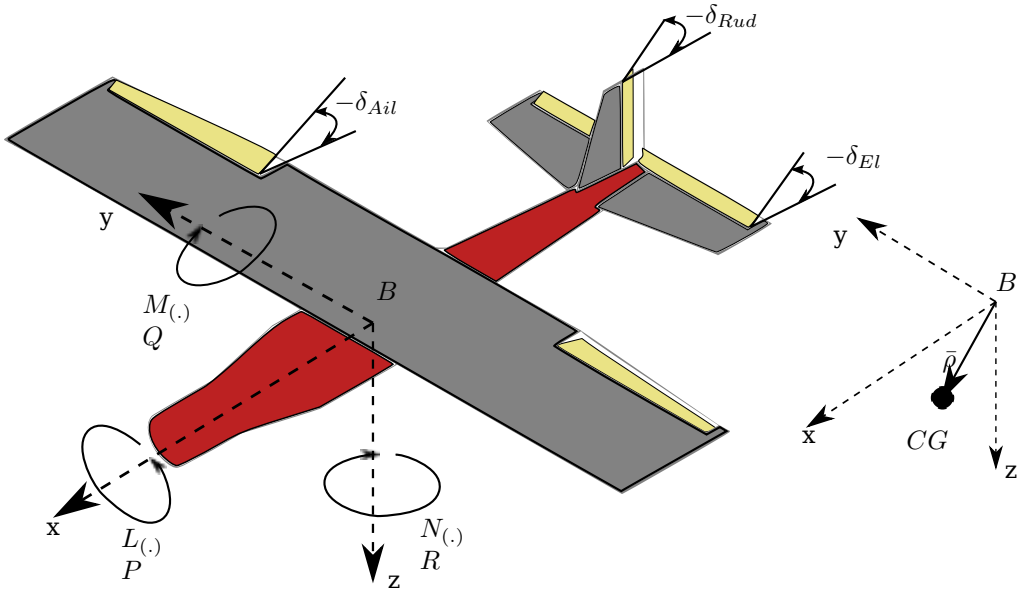

Figure 2.2 – Body Reference Frame

2.1.1.3 Wind Reference Frame

The wind reference frame represents the positive propagation frame of the UAV's movement. It is fixed at the same point on the UAV as the body frame but is rotated relative to the body frame. The rotations are usually around the body frame's y- and z- axes. Figure 2.3 depicts these rotations clearly. The first rotation around the y-axis is usually called the angle of attack of the UAV. The angle of attack, represented by α, defines the angle at which the UAV needs to "attack" the oncoming air column to generate enough lift at its current speed to stay airborne. The second rotation around the z-axis is called the side-slip angle, represented by β. The side-slip angle defines the angle at which the UAV must travel to counter any side-force while travelling forward. In more general terms, the wind reference frame is thus aligned with the UAV's forward velocity vector. Angle of attack and side-slip are thus used to describe the body relative to its forward velocity vector. Any reference made to a vector in the wind reference frame can be identified by the subscript W.

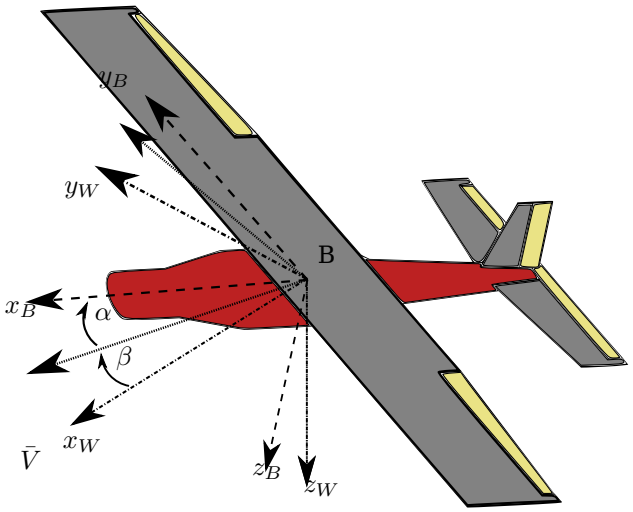

Figure 2.3 – Wind Reference Frame

2.1.2 Standard Notation and Conventions

General Conventions

Using the reference frames described in Section 2.1.1, the position, velocity, attitude and angular rates of the UAV, as well as the forces and moments acting on it, can now be defined.

There are three categories of forces and moments. These forces and moments have components in the x-, y-, and z- axes and will be denoted by an $X_{(.)}$, $Y_{(.)}$ or $Z_{(.)}$ according to their axis and the origin from which they originate. The first set originates from the aerodynamic properties of the UAV. These forces are usually described in the wind reference frame and will be introduced in the model as non-dimensional coefficients. Any force from this origin will be subscripted with an A. The second set originates from the engine of the UAV. This particular UAV has only one engine and it is aligned with the body reference frame's x-axis. Under the assumption that the engine generated force acts through the CG, no additional moments will be introduced by it. Any force from this origin will be subscripted by a T. The third and last force originates from gravity and exists in the inertial frame. Gravity will act through the UAV's CG and will thus also not create any additional moments at this stage. Any force from this origin will be subscripted with a G. All of the forces mentioned above will be defined according to their related reference frame's positive directions.

Every moment will be defined in the body reference axis. This is due to the UAV rotating around its centre of gravity. These moments will be represented by $L_{(.)}$, $M_{(.)}$ and $N_{(.)}$ respectively for the x-, y- and z-axis. Their subscripts will be the same as those mentioned for the forces. The rotational rates of the UAV will also be defined in the body reference axis. These rates will be represented by P, Q and R. The right hand rule will be used to define the positive direction of both moments and rotational rates around

the axis it is defined in.

The last few conventions include the UAV's attitude, velocities and position. The attitude of the UAV will be represented in Euler angles. $\begin{bmatrix}\psi & \theta & \phi\end{bmatrix}$ will be used to represent the aircraft's heading, pitch and bank angles. These angles will be used in an Euler 3-2-1 rotation to transform measurements back and forth between the inertial and body axes. The 3-2-1 convention consists of first rotating through the heading ψ, then through the pitch θ and lastly through the bank angle ϕ. The result of these rotations can be combined to form a direction cosine matrix or DCM in short. Equation (2.1.1) represents the inertial to body transformation, while the transpose of this transform represents the body to inertial transformation.

$$DCM_{I\to B} = \begin{bmatrix} C_\psi C_\theta & S_\psi C_\theta & -S_\theta \\ C_\psi S_\theta S_\phi - S_\psi C_\phi & S_\psi S_\theta S_\phi + C_\psi C_\phi & C_\theta S_\phi \\ C_\psi S_\theta C_\phi + S_\psi S_\phi & S_\psi S_\theta C_\phi - C_\psi S_\phi & C_\theta C_\phi \end{bmatrix} ...C_{(.)} = cos(.), S_{(.)} = sin(.) \tag{2.1.1}$$

The position of the UAV will primarily be described in the inertial reference frame. The curvature of the earth can be taken into account but for this particular project a flat earth model will be used. This is due to short distances on which these tests will be conducted. Lastly the velocities of the UAV are described in various ways. The current airspeed of the UAV is represented in the x-axis of the wind reference frame. This is the basic forward movements of the UAV and can be represented by the norm of the body velocities as described in equation (2.1.2), where U_B, V_B and W_B are the x, y and z velocities respectively.

$$\bar{V} = \sqrt{U_B^2 + V_B^2 + W_B^2} \tag{2.1.2}$$

$$\alpha = atan(\frac{W_B}{U_B}) \tag{2.1.3}$$

$$\beta = asin(\frac{V_B}{\bar{V}}) \tag{2.1.4}$$

Referring back to Figure 2.3, The α and β values can also be used to transform measurements and quantities between wind and body axis and vice versa. Equation (2.1.5) transforms quantities from wind to body and the transpose from body to wind. It should be noted that the β rotation direction is typically the opposite of the yaw rotation direction.

$$DCM_{W\to B} = \begin{bmatrix} C_\alpha C_\beta & -C_\alpha S_\beta & -S_\alpha \\ S_\beta & C_\beta & \\ S_\alpha C_\beta & -S_\alpha S_\beta & C_\alpha \end{bmatrix} ...C_{(.)} = cos(.), S_{(.)} = sin(.) \tag{2.1.5}$$

The inertial velocities will be represented by V_N, V_E and V_D respectively. These velocities will also take on the positive directions as described in the inertial frame.

Actuator Conventions

The convention for the actuators on the UAV is that a positive actuator deflection is defined as one that produces a negative moment.

The ailerons, represented by δ_{Ail}, are deflected in a differential manner to produce a moment around the x-axis. This moment is called the rolling moment. Positive differential deflections will be defined as depicted in Figure 2.2. A positive deflection will thus roll the UAV in the positive y-axis direction, while a negative deflection will roll the UAV in the negative y-axis direction

The elevator, represented by δ_{El}, deflects to cause a moment around the y-axis, called the pitching moment. A positive deflection is depicted in Figure 2.2 and causes a nose up movement, in the negative z-axis direction.

The rudder, represented by δ_{Rud}, deflects to cause a moment around the z-axis, called the yawing moment. A positive deflection of the rudder, as depicted in Figure 2.2 will cause a positive yawing moment around the z-axis.

To conclude this section, a short list of all the variables defined above, will be provided to summarise all of the important variables and references defined:

- P, Q, R : x-, y- and z- body referenced angular rates
- U, V, W : x-, y- and z- body referenced velocities
- V_N, V_E, V_D : x-, y- and z- inertial referenced velocities
- $(.)_N$, $(.)_E$, $(.)_D$: North East or Down inertial frame identifiers
- $(.)_O$, $(.)_B$, $(.)_W$: Inertial, Body or Wind reference frame identifier
- δ_{Ail}, δ_{El}, δ_{Rud} : Actuator surface deflections
- $\bar{V}$, α, β : Airspeed, Angle of attack and Angle of Side-slip

The UAV's motion under the influence of external forces and moments can now be described using the reference frames and conventions covered in the previous section. Figure 2.4 depicts the various components needed to describe aircraft flight mechanics due to partial wing loss. They are divided into five different parts.

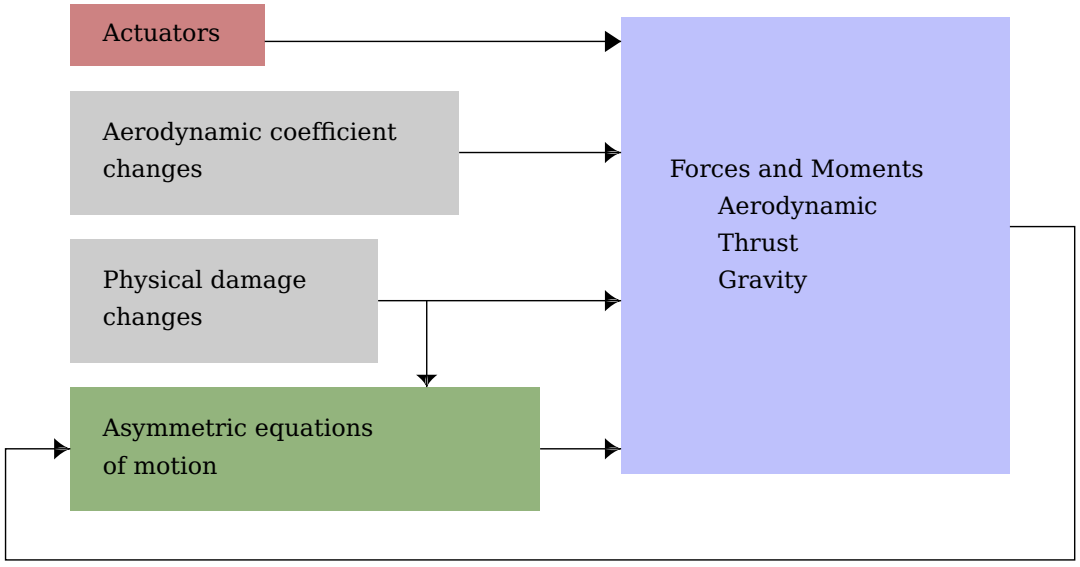

Figure 2.4 – System Overview

- Actuators: The actuators are what the control system uses to influence the system. Sections 2.1.2 and 2.2.2.3 describe the aircraft's aileron, elevator, rudder and thrust actuations that are used
- Aerodynamic coefficient changes: These coefficients will be described in Section 2.4. They will change due to partial wing loss and be implemented as a discrete data set to represent partial wing loss. Interpolation will be used for points between those recorded in the data set. They are fed into the forces and moments
- Physical damage changes: The physical damage changes include the changes in mass, CG and moment of inertia of the UAV. This will be described in Section 2.3.3 and represented by a discrete data set. They are fed into both the asymmetric equations of motion and the forces and moments
- Asymmetric equations of motion: The equations of motion form the core of this system as they have the capability to describe the changes with regard to CG shift and loss of symmetry. They can be found in Section 2.3. The EoM is fed by the forces and moments and also feeds the forces and moments
- Forces and moments: These include all of the forces and moments acting on the aircraft's body. Due to the implementation of the EoM, only gravity will result in additional moments that need to be taken into account. The various forces and moments combined here can be found in Sections 2.2.2.3, 2.3.2 and 2.4. This part is fed from the EoM and also feeds the EoM

The above-mentioned points focus on the effects of partial wing loss. As the common UAV will usually not be produced in an asymmetric configuration, a short description of a UAV's motion under symmetric assumptions will be discussed. This discussion will then be extended into an extensive derivation of the asymmetric model, accounting for partial wing loss. This derivation will include changes made to the six degrees of freedom (6DoF) model to account for a shift in CG, the effect of partial wing loss on the aerodynamic coefficients and how the mass moment of inertia and CG change due to partial wing loss.

2.2 Standard Symmetric Aircraft Flight Mechanics

In this section an overview of the commonly used model to describe a UAV in flight will be provided. As can be seen in Figure 2.4, the symmetric aircraft flight mechanics can be described by removing physical damage and aerodynamic coefficient changes. Use is also made of the asymmetric equations of motion (AEoM) under the assumption of symmetry.

2.2.1 Standard Six Degrees of Freedom

Developing the model which describes a UAV in flight in a three-dimensional space requires six degrees of freedom. The six degrees are defined by the linear movements in the x, y and z axis and the rotational movement around each of these axes. A six degrees of freedom model usually consists of two branches: the kinetics branch, which represents all the forces and moments working on the object, and the kinematics branch, which describes the relative motion variables.

2.2.1.1 Kinetics

The kinematic equations given in equations 2.2.1 to 2.2.6 represent the forces and moments acting in on the UAV due to its position, velocity and acceleration [12]. They are referenced in the body axis as most of the measurements are done on the UAV and the forces and moments act in and around the UAV's CG location.

$$\Sigma \mathbf{F}_{x_B} = m\left(\dot{U}_B + QW_B - RV_B\right) \tag{2.2.1}$$

$$\Sigma \mathbf{F}_{y_B} = m\left(\dot{V}_B + RU_B + PW_B\right) \tag{2.2.2}$$

$$\Sigma \mathbf{F}_{z_B} = m\left(\dot{W}_B + PV_B - QU_B\right) \tag{2.2.3}$$

$$\Sigma L = I_{xx}\dot{P} + (I_{zz} - I_{yy})\,QR \tag{2.2.4}$$

$$\Sigma M = I_{yy}\dot{Q} + (I_{xx} - I_{zz})\,PR \tag{2.2.5}$$

$$\Sigma N = I_{zz}\dot{R} + (I_{yy} - I_{xx})\,PQ \tag{2.2.6}$$

The above equations rely on two simplifying assumptions. Firstly, that the aircraft is symmetric around the xz-plane which implies that the cross product of inertia terms I_{xy} and I_{yz} are zero. Secondly, that the cross product of inertia I_{xz} is negligibly small.

2.2.1.2 Kinematics

As stated previously, kinematics relate the various motion variables to each other over time. This is commonly done by describing the aircraft with Euler 3-2-1 attitude parameters relating the body axis system to inertial space and its position vector in the inertial axes.

As defined in Section 2.1.2 the attitude of the UAV can be described by the Euler angles $\begin{bmatrix}\psi & \theta & \phi\end{bmatrix}$. These angles can be propagated by considering their time rate of change as described in equation (2.2.7), the full derivation can be found in [13].

$$\begin{bmatrix}\dot{\phi}\\ \dot{\theta}\\ \dot{\psi}\end{bmatrix} = \begin{bmatrix}1 & sin(\phi)\,tan(\theta) & cos(\phi)\,tan(\theta)\\ 0 & cos(\phi) & -sin(\phi)\\ 0 & sin(\phi)\,sec(\theta) & cos(\phi)\,sec(\theta)\end{bmatrix}\begin{bmatrix}P\\ Q\\ R\end{bmatrix} \tag{2.2.7}$$

The DCM stated in equation (2.1.1) relates the inertial to body axis ($DCM_{I\rightarrow B}$). Taking the inverse of this DCM, the body axis can be related to the inertial axis ($DCM_{B\rightarrow I}$). As this DCM is orthogonal, the inverse is only the transpose of the DCM. Multiplying this inverted DCM with the aircraft's velocity vector in the body axis delivers the aircraft's velocity in the inertial axis. As velocity is the rate of change of position, equation 2.2.8 depicts the aircraft's position dynamics.

$$\begin{bmatrix}\dot{N}\\ \dot{E}\\ \dot{D}\end{bmatrix} = DCM_{B\rightarrow I}\begin{bmatrix}U\\ V\\ W\end{bmatrix} = \begin{bmatrix}C_\psi C_\theta & C_\psi S_\theta S_\phi - S_\psi C_\phi & C_\psi S_\theta C_\phi + S_\psi S_\phi\\ S_\psi C_\theta & S_\psi S_\theta S_\phi + C_\psi C_\phi & S_\psi S_\theta C_\phi - C_\psi S_\phi\\ -S_\theta & C_\theta S_\phi & C_\theta C_\phi\end{bmatrix}\begin{bmatrix}U\\ V\\ W\end{bmatrix} \tag{2.2.8}$$

2.2.2 Forces and Moments

The forces and moments acting on the UAV can be divided into three groups: aerodynamic, gravitational and thrust. The aerodynamic group represents the forces and moments due to the specific aerodynamic properties of the airframe used. The gravitational group represents the earth's gravitational pull acting on the airframe. The thrust group represents the aircraft's own propulsion.

2.2.2.1 Aerodynamic

The aerodynamic forces and moments are a rather complex set to model and thus produce a lot of uncertainty into the aircraft model. Using Bernoulli's equation and the Continuity principle for incompressible fluids [14] gives the relationship of aerodynamic forces and moments to aerodynamic coefficients as shown in equations (2.2.17) to (2.2.22).

$$X_{Aero} = qSC_X \tag{2.2.9}$$
$$Y_{Aero} = qSC_Y \tag{2.2.10}$$
$$Z_{Aero} = qSC_Z \tag{2.2.11}$$
$$L_{Aero} = qSbC_l \tag{2.2.12}$$
$$M_{Aero} = qS\bar{c}C_m \tag{2.2.13}$$
$$N_{Aero} = qSbC_n \tag{2.2.14}$$

where $q = \frac{1}{2}\rho\bar{V}^2$ is the dynamic pressure, S the wing surface area, b the wing span, $\bar{c}$ the aerodynamic chord and $C_{(.)}$ the aerodynamic coefficient set. It should be noted that all of these coefficients are non-dimensional and if dimensionalised by the qS, qSb or $qS\bar{c}$ terms before they represent the forces and moments.

Equations (2.2.17) to (2.2.22) depict the relationship between a set of coefficients to allow them to be added together, describing their cumulative effect.

$$C_L = C_{L_\alpha}\alpha + \frac{\bar{c}}{2\bar{V}}C_{L_Q}Q + C_{L_{\delta_{El}}}\delta_{El} \tag{2.2.15}$$
$$C_D = \frac{C_L^2}{\pi Ae} \tag{2.2.16}$$
$$C_X = -C_D cos(\alpha) + C_L sin(\alpha) \tag{2.2.17}$$
$$C_Z = -C_L cos(\alpha) - C_D sin(\alpha) \tag{2.2.18}$$
$$C_y = C_{y_\beta}\beta + \frac{b}{2\bar{V}}C_{y_P}P + \frac{b}{2\bar{V}}C_{y_R}R + C_{y_{\delta_{Ail}}}\delta_{Ail} + C_{y_{\delta_{Rud}}}\delta_{Rud} \tag{2.2.19}$$
$$C_l = C_{l_\beta}\beta + \frac{b}{2\bar{V}}C_{l_P}P + \frac{b}{2\bar{V}}C_{l_R}R + C_{l_{\delta_{Ail}}}\delta_{Ail} + C_{l_{\delta_{Rud}}}\delta_{Rud} \tag{2.2.20}$$
$$C_m = C_{m_\alpha}\alpha + \frac{\bar{c}}{2\bar{V}}C_{m_Q}Q + C_{m_{\delta_{El}}}\delta_{El} \tag{2.2.21}$$
$$C_n = C_{n_\beta}\beta + \frac{b}{2\bar{V}}C_{n_P}P + \frac{b}{2\bar{V}}C_{n_R}R + C_{n_{\delta_{Ail}}}\delta_{Ail} + C_{n_{\delta_{Rud}}}\delta_{Rud} \tag{2.2.22}$$

A is the aspect ratio of the wing and e the Oswald number.

As stated earlier, the aerodynamic coefficients are implemented in their non-dimensional form and referenced in the wind axis reference frame. This allows easy scaling with model size. Various analytic,

empiric and numeric methods exist to calculate these coefficients. The analytic methods are usually not very accurate but provide a decent understanding of how the physical structure affects the coefficients. The empiric methods make use of experimental results to determine coefficient values and can be very accurate but are very specific to the airframe used in the experiment. The numeric methods are usually much more accurate but provide a poor understanding of how coefficients are affected by the physical structure.

In practice most designers and developers use experimental methods or programs to calculate the coefficients based on a description of the physical structure. As experimental methods usually require wind tunnels and flight tests to determine these coefficients, they are not very attractive methods due to cost and time. Some programs are available as open source packages and implement numeric methods to solve coefficients. These numerical methods include vortex lattice codes, computational fluid dynamics, etc. One such a program is Athena Vortex Lattice (AVL) and will be used to calculate these coefficients. Although these programs can provide a wide set of coefficients, only a few of these coefficients are necessary to model a UAV. A detailed description will be provided at a later stage. The coefficient notation consists of a double subscript. The first subscript describes the force or moment this coefficient represents and the second subscript depicts the cause of this force. The list below provides only a short description of some of these coefficients as acquired from [13] and [12]:

Side Force Coefficients

- C_{y_β} : The coefficient associated with the side force caused by the lateral lift originating from the fuselage
- C_{y_P} : The coefficient associated with the side force caused by roll rate perturbations. It is usually negligible
- C_{y_R} : The coefficient associated with the side force caused by a yaw rate perturbation. It is usually negligible
- $C_{y_{\delta_{Ail}}}$: The coefficient associated with the side force caused by aileron perturbation. It is usually negligible
- $C_{y_{\delta_{Rud}}}$: The coefficient associated with the side force caused by rudder deflection. It is usually negligible

Lift Coefficients

- C_{L_α} : The coefficient associated with lift as a function of angle of attack. This coefficient is usually associated with the UAV's lift curve slope and can have a maximum value of 2π
- C_{L_Q} : The coefficient associated with lift caused by a pitching motion. It is usually negligible
- $C_{L_{\delta_{El}}}$: The coefficient associated with lift caused by elevator perturbation. It is usually negligible

Rollint Moment Coefficients

- C_{l_β} : The coefficient associated with rolling moment due to side slip motions. This coefficient usually plays a dominant roll
- C_{l_P} : The coefficient associated with rolling moment due to roll rate. This coefficient usually plays a dominant roll
- C_{l_R} : The coefficient associated with rolling moment due to yaw rate
- $C_{l_{\delta_{Ail}}}$: The coefficient associated with rolling moment due to aileron perturbation
- $C_{l_{\delta_{Rud}}}$: The coefficient associated with rolling moment due to rudder perturbation

Pitching Moment Coefficients

- C_{m_α} : The coefficient associated with pitching moment due to angle of attack. This coefficient usually plays a dominant roll in the UAV's dynamics
- C_{m_Q} : The coefficient associated with pitching moment due to pitch rate
- $C_{m_{\delta_{El}}}$: The coefficient associated with pitching moment due to elevator perturbation

Yawing Moment Coefficients

- C_{n_β} : The coefficient associated with yawing moment due to side slip
- C_{n_P} : The coefficient associated with yawing moment due to roll rate
- C_{n_R} : The coefficient associated with yawing moment due to yaw rate
- $C_{n_{\delta_{Ail}}}$: The coefficient associated with yawing moment due to aileron perturbation
- $C_{n_{\delta_{Rud}}}$: The coefficient associated with yawing moment due to rudder perturbation

2.2.2.2 Gravitational

In general, the CG location will be situated at the centre of the body reference frame. Gravity can be approximated by an acceleration of $g = 9.81 m.s^{-2}$ in the z-axis of the inertial reference frame. Equation (2.2.23) shows the resulting force when transforming the gravity vector from the inertial to the body reference frame.

$$F_{G_B} = \begin{bmatrix} X_G \\ Y_G \\ Z_G \end{bmatrix} = DCM_{I \to B} \begin{bmatrix} 0 \\ 0 \\ mg \end{bmatrix} = \begin{bmatrix} -S_\theta mg \\ C_\theta S_\phi mg \\ C_\theta C_\phi mg \end{bmatrix} \tag{2.2.23}$$

2.2.2.3 Thrust

As stated in [12], a lot of different and complex methods are available to model the propulsion response of a UAV. In most cases these methods and models only provide a little more accuracy for a lot more complexity in the mathematical representation. Due to this, the model will be kept simple by using a first-order lag approximation for the response. This model is quite easy to implement and delivers a fairly accurate response. The first-order lag model is provided below,

$$\dot{T} = -\frac{1}{\tau} T + \frac{1}{\tau} T_c \tag{2.2.24}$$

with T the thrust magnitude, T_c the command issued and τ the engine time constant. For this UAV, the assumption will be made that the force which the engine exerts on the UAV acts directly on the CG in the x-axis body reference frame. Even though this may not be the precise position in practice, it is usually fairly close for a single propellor aircraft.

2.2.3 Summary

In this section some of the standard definitions and models to describe a UAV was provided. The 6DoF model consists of both symmetric kinetic and kinematic equations. These equations are fed by aerodynamic, gravitational and thrust forces and moments as shown in Figure 2.5.

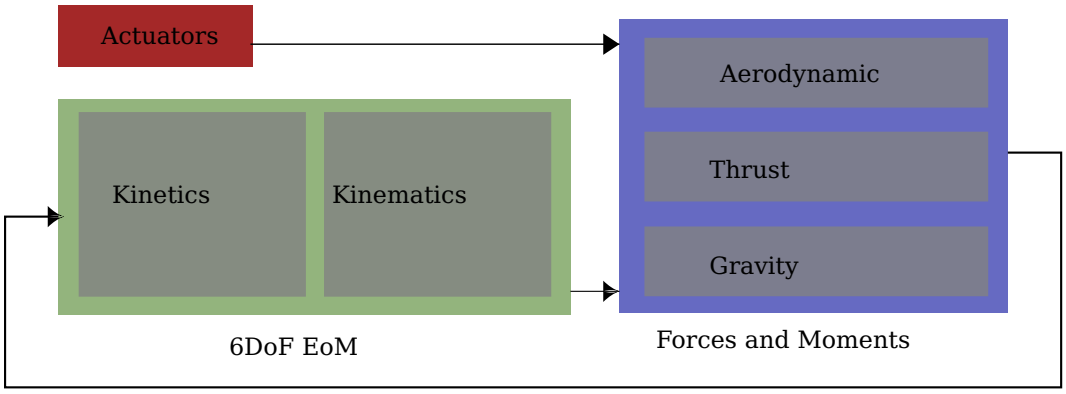

Figure 2.5 – Standard Aircraft Model

2.3 Extended Aircraft Flight Mechanics Model to Include Effects of Partial Wing Loss

Up to this point, the flight mechanics have been modelled based on the standard symmetric aircraft assumption. In the case of a UAV with partial wing loss, the symmetric assumption is invalidated and thus requires the standard flight mechanics model to be extended to include the effects of partial wing loss.

This section will derive the 6DoF model from basic principles, without assuming a symmetric aircraft. It will also be extended to accommodate an instantaneous CG shift. The effects of partial wing loss will be examined on the aerodynamic coefficients, mass, moment of inertia and CG location. The changes in the overall forces and moments will then conclude this section.

2.3.1 Asymmetric Six Degrees of Freedom Model

As stated in Section 2.2.1, a six degrees of freedom model consists of kinetics and kinematics. The kinetics branch can be described by using Newton's second law. Both linear and rotational movement will be discussed in the subsections to follow. Their original derivation can be found in [6]. The two parts will then be combined to form the kinetics part of the six degrees of freedom model. As the kinematics part does not change from the one discussed in Section 2.2.1, it will not be restated.

2.3.1.1 Force Equations

Referring to Figure 2.2, the derivation done below will be around the symmetric aircraft's CG location, designated as B. Figure 2.6 shows some of the extra variables and vectors needed for these derivations. Note that the new CG location may now be a distance ρ away from the original CG location at B.

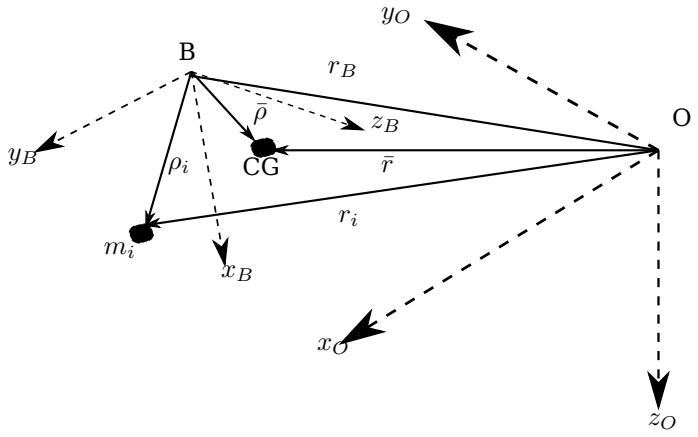

Figure 2.6 – Inertial to body reference frame

As depicted in Figure 2.6, it is clear that the mass m_i is a distance r_i away from the inertial axis and r_i can be described by the equation (2.3.1).

$$r_i = r_B + \Delta p \tag{2.3.1}$$

When referring to the forces, one uses Newton's second law, as stated in equation (2.3.2),

$$F_i = \Sigma m a_i \tag{2.3.2}$$

where a_i can also be described by $a_i = \ddot{r}_i = (\ddot{r})_O$. At this stage we want the components as measured in the body-fixed reference frame. This can be done by taking the time derivative of the inertial axis frame. This leads to a time derivative term in the body axis, accompanied by the cross product of the angular rate with the offset distance from B to the point.

$$\left(\frac{d[]}{dt}\right)_O = \left(\frac{d[]}{dt}\right)_B + \omega \times [] \tag{2.3.3}$$

Implementing equation (2.3.3) with respect to r results in

$$\begin{aligned} (\dot{r}_i)_O &= (\dot{r}_B)_O + (\dot{\rho}_i)_O \\ (\dot{r}_i)_O &= v_B + \dot{\rho}_i + \omega \times \rho_i \end{aligned} \tag{2.3.4}$$

Taking equation (2.3.2) into account, it's clear that $\dot{r}_O$ needs to be differentiated again to acquire the acceleration of this particular point. This results in

$$\begin{aligned} (\ddot{r}_i)_O = & \left(\tfrac{d}{dt}\left(v_B + \dot{\rho}_i + \omega \times \rho_i\right)\right)_B + \omega \times (v_B + \dot{\rho}_i + \omega \times \rho_i) \\ = & \dot{v}_B + \omega \times v_B + \ddot{\rho}_i + \dot{\omega} \times \rho_i + 2 \cdot (\omega \times \dot{\rho}_i) + \omega \times (\omega \times \rho_i) \end{aligned} \tag{2.3.5}$$

At this stage, the acceleration term as calculated above in equation (2.3.5) can be inserted into Newton's second law, equation (2.3.2). This leads to the following result,

$$\begin{aligned} \Sigma \mathbf{F} = & \Sigma m_i \left(\dot{\mathbf{v}}_B + \omega \times \mathbf{v}_B + \ddot{\rho}_i + \dot{\omega} \times \rho_i + 2 \cdot (\omega \times \dot{\rho}_i) + \omega \times (\omega \times \rho_i)\right) \\ = & \; m\left(\dot{\mathbf{v}}_B + \omega \times \mathbf{v}_B\right) + \Sigma m_i \ddot{\rho}_i + 2 \cdot (\omega \times \Sigma m_i \dot{\rho}_i) + \dot{\omega} \times \Sigma m_i \rho_i + \omega \times (\omega \times \Sigma m_i \rho_i) \\ = & \; m\left(\dot{\mathbf{v}}_B + \omega \times \mathbf{v}_B\right) + m\ddot{\overline{\rho}} + 2 \cdot \left(\omega \times m\dot{\overline{\rho}}\right) + \dot{\omega} \times m\overline{\rho} + \omega \times (\omega \times m\overline{\rho}) \end{aligned} \tag{2.3.6}$$

Taking into account that the body is assumed to be rigid, ρ is a constant. Even though the CG may shift when the UAV enters a partial wing loss state, this is regarded as an instantaneous shift and not a time varying occurrence and thus ρ equalling a constant still stays a valid assumption. This leads to $\ddot{\overline{\rho}} = \dot{\overline{\rho}} = 0$, which results in equation (2.3.7) when inserted into equation (2.3.6).

$$\Sigma \mathbf{F} = m\left(\dot{\mathbf{v}}_B + \omega \times \mathbf{v}_B\right) + \dot{\omega} \times m\overline{\rho} + \omega \times \left(\omega \times m\overline{\rho}\right) \tag{2.3.7}$$

Using equation (2.3.7) with the following vector representations for the angular rates, CG position and body velocity,

$$\begin{aligned} \omega &= P\mathbf{i} + Q\mathbf{j} + R\mathbf{k} \\ \overline{\rho} &= \Delta x\mathbf{i} + \Delta y\mathbf{j} + \Delta z\mathbf{k} \\ \mathbf{v}_B &= U_B\mathbf{i} + V_B\mathbf{j} + W_B\mathbf{k} \end{aligned}$$

$\Sigma\mathbf{F}$ can be divided into its x, y and z components respectively and be represented by equations (2.3.8) to (2.3.10)

$$\Sigma \mathbf{F}_x = m\left(\dot{U}_B + QW_B - RV_B - \left(Q^2 + R^2\right)\Delta x + \left(QP - \dot{R}\right)\Delta y + \left(RP + \dot{Q}\right)\Delta z\right) \tag{2.3.8}$$

$$\Sigma \mathbf{F}_y = m\left(\dot{V}_B + RU_B + PW_B + \left(PQ + \dot{R}\right)\Delta x - \left(P^2 + R^2\right)\Delta y + \left(QR - \dot{P}\right)\Delta z\right) \tag{2.3.9}$$

$$\Sigma \mathbf{F}_z = m\left(\dot{W}_B + PV_B - QU_B + \left(PR - \dot{Q}\right)\Delta x + \left(QR + \dot{P}\right)\Delta y + \left(P^2 + Q^2\right)\Delta z\right) \tag{2.3.10}$$

At this stage equations (2.3.8) to (2.3.10) allow the CG location to move away from its original location. If we apply the assumption that the CG is situated at point B ($\bar{\rho} = \mathbf{0}$), equations (2.3.8) to (2.3.10) reduce to equations (2.2.1) to (2.2.3) as stated in the standard symmetric aircraft case. Thus the resulting force equations allow the simulation of an aircraft in its original symmetric state and an asymmetric state due to partial wing loss.

2.3.1.2 Moment Equations

In the previous subsection, the equations for translational motion of the UAV were derived. In this subsection, the equations for the rotational motion will be derived.

The absolute angular moment around B can be described by

$$\mathbf{H}_B = \Sigma\left(\rho_i \times m_i\mathbf{v}_i\right) \tag{2.3.11}$$

In equation (2.3.11), $\mathbf{v}_i = \left(\dot{\mathbf{r}}_i\right)_O$ and represents the velocity of the incremental mass point, m_i, as observed from the inertial reference frame. Using equation (2.3.3) on (2.3.11), the derivative of $\mathbf{H}_B$ with respect to the inertial reference frame can be written as

$$\left(\dot{\mathbf{H}}_B\right)_O = \Sigma\left(\left(\dot{\rho}_i\right)_O \times m_i\mathbf{v}_i\right) + \Sigma\left(\rho_i \times \left(\dot{\mathbf{v}}_i\right)_O\right) \tag{2.3.12}$$

Figure 2.6 represents, $\left(\dot{\rho}_i\right)_O = \left(\dot{\mathbf{r}}_i - \dot{\mathbf{r}}_B\right)_O$ and $\left(\dot{\mathbf{v}}_i\right)_O = \left(\ddot{\mathbf{r}}_i\right)_O$. Since the cross-product of $\left(\dot{\mathbf{r}}_i\right)_O \times \mathbf{v}_i = 0$ and the sum of external moments around B is defined by $\Sigma\mathbf{M}_B = \Sigma\left(\rho_i \times m_i\left(\ddot{\mathbf{r}}_i\right)_O\right)$ equation (2.3.12) reduces to

$$\Sigma\mathbf{M}_B = \left(\dot{\mathbf{H}}_B\right)_O + \left(\dot{\mathbf{r}}_B\right)_O \times \Sigma m_i\mathbf{v}_i \tag{2.3.13}$$

Using the centre of mass and its velocity in the inertial reference frame, $m\overline{\mathbf{v}} = \Sigma m_i\mathbf{v}_i$. Furthermore $\overline{\mathbf{v}}$ can be defined as $\mathbf{v}_B + \left(\dot{\bar{\rho}}\right)_O$ with regard to Figure 2.6 and simplifies equation (2.3.13) to

$$\Sigma\mathbf{M}_B = \left(\dot{\mathbf{H}}_B\right)_O + \mathbf{v}_B \times m_i\left(\dot{\bar{\rho}}\right)_O \tag{2.3.14}$$

If the centre of mass / gravity is also situated at B, then equation (2.3.14) turns out in its usual form as $\Sigma\mathbf{M}_B = \left(\dot{\mathbf{H}}_B\right)_O$. Expressing equation (2.3.14) in its body measured components requires equation (2.3.11) to be expressed in its body measured components.

$$\mathbf{H}_B = \Sigma\left(\rho_i \times m_i\left(\mathbf{v}_B + \dot{\rho}_i + \omega \times \rho_i\right)\right) \tag{2.3.15}$$

Under the assumption that the body is rigid, $\dot{\rho}_i = 0$ and thus

$$\begin{aligned} \mathbf{H}_B &= \Sigma m_i\rho_i \times \mathbf{v}_B + \Sigma\rho_i \times m_i\left(\omega \times \rho_i\right) \\ \mathbf{H}_B &= m\rho \times \mathbf{v}_B + \mathbf{I}\omega \end{aligned} \tag{2.3.16}$$

At this stage the derivatives, as measured in the inertial reference frame, can be derived with the help of equation (2.3.3)

$$\left(\dot{\mathbf{H}}_B\right)_O = \left(\dot{\mathbf{H}}_B\right)_b + \omega \times \mathbf{H}_B \tag{2.3.17}$$

$$\left(\dot{\overline{\rho}}\right)_O = \left(\dot{\overline{\rho}}\right)_b + \omega \times \overline{\rho} \tag{2.3.18}$$

Substituting the above into equation (2.3.16) yields

$$\begin{aligned}\left(\dot{\mathbf{H}}_B\right)_O &= \left(\tfrac{d}{dt}\left(m\overline{\rho} \times \mathbf{v}_B + \mathbf{I}\omega\right)\right)_B + \omega \times \left(m\overline{\rho} \times \mathbf{v}_B + \mathbf{I}\omega\right) \\ &= m\dot{\overline{\rho}} \times \mathbf{v}_B + m\overline{\rho} \times \dot{\mathbf{v}}_B + \mathbf{I}\dot{\omega} + \omega \times \left(m\overline{\rho} \times \mathbf{v}_B\right) + \omega \times \mathbf{I}\omega \\ &= \mathbf{I}\dot{\omega} + \omega \times \mathbf{I}\omega + m\overline{\rho} \times \dot{\mathbf{v}}_B + \omega \times \left(m\overline{\rho} \times \mathbf{v}_B\right)\end{aligned} \tag{2.3.19}$$

Substituting equation (2.3.19) into equation (2.3.14), with the knowledge that $\dot{\overline{\rho}} = 0$ and $\left(\dot{\overline{\rho}}\right)_O = \omega \times \overline{\rho}$ yields

$$\Sigma\mathbf{M}_B = \mathbf{I}\dot{\omega} + \omega \times \mathbf{I}\omega + m\overline{\rho} \times \dot{\mathbf{v}}_B + m\omega \times \left(\overline{\rho} \times \mathbf{v}_a\right) + m\mathbf{v}_B \times \left(\omega \times \overline{\rho}\right) \tag{2.3.20}$$

Thus taking into account that

$$\mathbf{I}\omega = \left(I_{xx}P - I_{xy}Q - I_{xz}R\right)\mathbf{i} + \left(-I_{xy}P + I_{yy}Q - I_{yz}R\right)\mathbf{j} + \left(-I_{xz}P - I_{yz}Q + I_{zz}R\right)\mathbf{k} \tag{2.3.21}$$

the sum of the individual moments around their axis can be defined as follows

$$\begin{aligned}\Sigma L = \; & I_{xx}\dot{P} - I_{xy}\dot{Q} - I_{xz}\dot{R} + I_{xy}PR - I_{xz}PQ + \left(I_{zz} - I_{yy}\right)QR + \left(R^2 - Q^2\right)Iyz \\ & + m\left(\left(PV_B - QU_B + \dot{W}_B\right)\Delta y + \left(PW_B - RU_B - \dot{V}_B\right)\Delta z\right)\end{aligned} \tag{2.3.22}$$

$$\begin{aligned}\Sigma M = \; & -I_{xy}\dot{P} + I_{yy}\dot{Q} - I_{yz}\dot{R} + I_{yz}PQ - I_{xy}QR + \left(I_{xx} - I_{zz}\right)PR + \left(P^2 - R^2\right)Ixz \\ & + m\left(\left(QU_B - PW_B - \dot{W}_B\right)\Delta x + \left(QW_B - RV_B + \dot{U}_B\right)\Delta z\right)\end{aligned} \tag{2.3.23}$$

$$\begin{aligned}\Sigma N = \; & -I_{xz}\dot{P} - I_{yz}\dot{Q} + I_{zz}\dot{R} + I_{xz}QR - I_{yz}PR + \left(I_{yy} - I_{xx}\right)PQ + \left(Q^2 - P^2\right)Ixy \\ & + m\left(\left(RU_B - PW_B + \dot{V}_B\right)\Delta x + \left(RV_B - QW_B - \dot{U}_B\right)\Delta y\right)\end{aligned} \tag{2.3.24}$$

At this stage equations (2.3.22) to (2.3.24) allow the CG location to move away from its original location. If we apply the assumption that the CG is situated at point B, terms Δ_x, Δ_y and Δ_z also equal zero. Furthermore, if the CG has not shifted and is symmetric in the xy plane of the body reference frame, the off-diagonal inertial terms I_{xy}, I_{xz} and I_{yz} equal zero and can be removed. This reduces equations (2.3.22) to (2.3.24) to equations (2.2.4) to (2.2.6). Thus the resulting moment equations allow the simulation of an aircraft in its original symmetric state and an asymmetric state due to partial wing loss.

2.3.1.3 Implementation

After the forces and moments have been described, a method of implementing them as changes in aircraft states has to be constructed. There are various ways to do this but due to the choice of fixing the body axis to the symmetric aircraft's CG location an easy method named the non centre of mass configuration can be used, as found in [6]. The complete set of linear and rotational equations, as specified in equations (2.3.8)-(2.3.10) and (2.3.22)-(2.3.24) can be rewritten in matrix notation, representing the states of the aircraft $\mathbf{v}_B$ and ω as rates of change $\dot{\mathbf{v}}_B$ and $\dot{\omega}$. This leads to the following format,

$$\begin{bmatrix} \dot{\mathbf{v}}_B \\ \dot{\omega} \end{bmatrix} = \begin{bmatrix} m\mathbf{I}_3 & -\mathbf{D}_x \\ \mathbf{D}_x & \mathbf{I} \end{bmatrix}^{-1} \left[\begin{bmatrix} \Sigma\mathbf{F} \\ \Sigma\mathbf{M}_B \end{bmatrix} - \begin{bmatrix} m\boldsymbol{\Omega}_x & -\boldsymbol{\Omega}_x\mathbf{D}_x \\ \boldsymbol{\Omega}_x\mathbf{D}_x & \boldsymbol{\Omega}_x\mathbf{I} - \mathbf{V}_x\mathbf{D}_x \end{bmatrix} \begin{bmatrix} \mathbf{v}_B \\ \omega \end{bmatrix} \right] \tag{2.3.25}$$

with

$$\mathbf{D}_x = \begin{bmatrix} 0 & -m\Delta z & m\Delta y \\ m\Delta z & 0 & -m\Delta x \\ -m\Delta y & m\Delta x & 0 \end{bmatrix} \quad \boldsymbol{\Omega}_x = \begin{bmatrix} 0 & -R & Q \\ R & 0 & -P \\ -Q & P & 0 \end{bmatrix} \quad \mathbf{V}_x = \begin{bmatrix} 0 & -W_B & V_B \\ W_B & 0 & -U_B \\ -V_B & U_B & 0 \end{bmatrix}$$

$$I = \begin{bmatrix} I_{xx} & -I_{xy} & -I_{xz} \\ -I_{xy} & I_{yy} & -I_{yz} \\ -I_{xz} & -I_{yz} & I_{zz} \end{bmatrix}$$

where the inertia matrix is expressed around the reference point B and the distance between the reference point B and the new CG is represented by $\overline{\rho} = (\Delta x, \Delta y, \Delta z)$.

Implementing the above matrix representation of the forces and moments concludes the kinetics branch of the six degrees of freedom model. Although this model is highly over-complicated for a symmetric UAV, it allows the simulation of an asymmetric aircraft without invalidating any assumptions. An important aspect of the implementation discussed above is that all the forces and moments are still calculated around the original symmetric aircraft's CG. The only extra moment one needs to calculate is that of the shifted CG around point B. The mass displacement matrix D_x and inertia matrix I account for the change in CG location, mass and inertia. They transform the forces and moments around B to the new CG location. The moment created by the new CG location around point B will be discussed next.

2.3.2 Gravity

In Section 2.2.1 the force due to gravity was discussed. This force's equation stays the same for the partial wing loss case but an additional moment equation is added. If the CG location is at a distance $\begin{bmatrix}\Delta_x & \Delta_y & \Delta_z\end{bmatrix}^T$ away from the origin of the body reference frame at point B, the cross product of the Δ vector with the body's gravitational force will produce the moment generated by gravity on the UAV. The result of this cross product can be found in equation (2.3.26).

$$M_{G_B} = \begin{bmatrix} L_G \\ M_G \\ N_G \end{bmatrix} = \begin{bmatrix} \Delta_x \\ \Delta_y \\ \Delta_z \end{bmatrix} \times \begin{bmatrix} -S_\theta mg \\ C_\theta S_\phi mg \\ C_\theta C_\phi mg \end{bmatrix} = \begin{bmatrix} \Delta_y C_\theta C_\phi mg - \Delta_z C_\theta S_\phi mg \\ -\Delta_x C_\theta C_\phi mg - \Delta_z S_\theta mg \\ \Delta_x C_\theta S_\phi mg + \Delta_y S_\theta mg \end{bmatrix} \tag{2.3.26}$$

The augmentation of CG, mass and moment of inertia due to partial wing loss will be discussed in the next section.

2.3.3 The Effect of Partial Wing Loss on Centre of Gravity, Mass and Moment of Inertia

As described in the force and moment equations in Section 2.3.1, it is possible to take an instantaneous CG shift into account. We know that if a part of the wing is lost, a part of the mass of the UAV is lost with it. If a loss of mass occurs, the CG of the UAV will change along with its moment of inertia. In this section the focus will be on how to represent this change. Before the loss of mass, change in CG and inertia can be described, the mathematics of how this change will be implemented needs to be discussed.

When examining the matrices in equation (2.3.25), it becomes apparent that $\mathbf{D}_x$ and $\mathbf{I}$ hold the key to adapting the CG and inertia of the UAV. By applying a basic understanding of the parallel theorem, the inertia matrix can be adapted while knowing only the mass of the broken-off wing, its CG and inertia. Equations (2.3.27) to (2.3.31) can be used to adapt the UAV's mass, CG and inertia.

$$m \rightarrow m_{dac} = m - m_{tip} \tag{2.3.27}$$

$$\overline{\rho} \rightarrow \overline{\rho}_{dac} = m\overline{\rho} = m_{tip}\overline{\rho}_{tip}/m_{dac} \tag{2.3.28}$$

$$\mathbf{I}_{ij} \rightarrow \mathbf{I}_{ij,dac} = \mathbf{I}_{ij} - \mathbf{I}_{ij,tip} \quad \ldots i,j = x,y,z \tag{2.3.29}$$

$$\mathbf{I}_{ii,tip} = \mathbf{I}_{ii,tip,cm} + m_{tip\left(\Delta j_{tip}^2 + \Delta k_{tip}^2\right)} \quad \ldots i,j,k = x,y,z | x \neq j \& i \neq k \tag{2.3.30}$$

$$\mathbf{I}_{ij,tip} = \mathbf{I}_{ij,tip,cm} + m_{tip}\Delta i_{tip}\Delta j_{tip} \quad \ldots i,j = x,y,z | i \neq j \tag{2.3.31}$$

Using the above, it is now possible to only calculate the mass, CG and inertia of the wing loss section to adapt the equations of motions. This can be done by calculating the applicable applied mathematics equations for an object's inertia and CG or just by using a CAD program which calculates these values based on the structure and material density.

The second method will be used to find these values, as it allows for rapid changes in the model, which automatically translate into inertial and CG values. The method for finding the mass, CG and inertial properties was implemented as follow:

- Construct a full wing according to the manufacturer's specifications and cross reference these specifications with the wing's physical measurements
- Place this wing the exact distance away from the UAV's CG location in the reference frame
- Start to section off increments of the wing from the fuselage to the tip, starting with 90% which will represent only 10% wing loss

- Calculate the remaining tip's relative CG location to the reference axis
- Calculate the tip's inertial properties around its principal axis
- Calculate the tip's mass

Using the technique described above, a full wing's mass, CG and inertial properties can be calculated for the implementation of an instantaneous CG shift. The figures below show how this method was implemented to acquire 20% and 40% wing loss values. The values necessary to calculate equations 2.3.27 to 2.3.31 can be found in Appendix F.

Figure 2.7 – Inventor: Full Wing

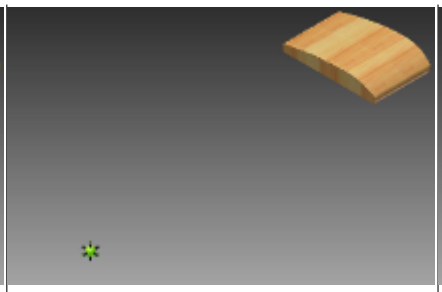

Figure 2.8 – Inventor: 20% Tip

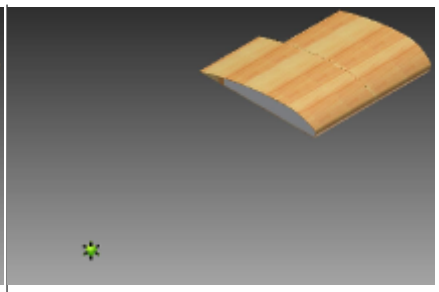

Figure 2.9 – Inventor: 40% Tip

2.4 The Effects of Partial Wing Loss on Aerodynamic Coefficients

In this section, the effects of partial wing loss on the aerodynamic forces and moments acting on the UAV are modelled. This examination will include redefinition of the available mathematics describing coefficients to include partial wing loss (analytical calculation), how AVL will be used to calculate the coefficients (numerical calculation) and a discussion of the results.

As the partial loss of a wing reduces its contact area with the air it moves in, it is possible to predict the following:

- The amount of lift generated should reduce as the loss increases
- The amount of drag generated should reduce as less of the wing is in contact with the air
- Little effect should be observed on side force
- A bias in rolling moment should arise due to the lift imbalance over the total wing. This bias should induce a rolling moment in the direction of the wing loss
- The pitching moment should decrease
- A bias in yawing moment should arise due to the decreased drag on the partial loss side. The bias should tend to cause a yawing moment in the direction of the undamaged wing
- The effectiveness of the ailerons to roll the aircraft should decrease
- The effectiveness of the elevator should not be influenced
- The effectiveness of the rudder should not be influenced

2.4.1 Analytical Calculation

In this section available mathematical equations will be adapted to represent aerodynamic coefficients under the influence of partial wing loss.

2.4.1.1 Lift Force

First, the lift produced by the wing will be determined. For the most part the derivations acquired from [15] will be used. In the general case it can be shown that the lift produced by the wing will be dependent on the circulation distribution of the particular wing. This circulation is represented with a Fourier series of which only the first term carries any real value but all the terms need to be calculated in order to accurately acquire the first one. This results in the circulation taking on the form of the elliptical wings circulation distribution. Due to this fact and the statements in both [15] and [16] that a rectangular wing's circulation can be reasonably approximated by that of an elliptical wing's circulation, the lift calculation will be based on the elliptical case. This calculation is only done to improve the general understanding of lift change to wing loss and thus it's not necessary to over-complicate these equations.

The circulation distribution of an elliptical wing is given by equation (2.4.1),

$$\Gamma(y) = \Gamma_0 \sqrt{1 - \left(\frac{2y}{b}\right)^2} \tag{2.4.1}$$

with Γ_0 the circulation at the origin, y the distance along the wing and b the full span on the wing. Furthermore the lift at a specific point on the wing can be described by $L'(y) = \rho_0 V_0 \Gamma(y)$, which results in

$$L'(y) = \rho_0 V_0 \Gamma_0 \sqrt{1 - \left(\frac{2y}{b}\right)^2} \tag{2.4.2}$$

Finding the total lift, equation (2.4.2) will be integrated over the entire wing. At this stage it becomes necessary to separate the equation into two parts, representing the left and right side of the wing. This also requires that b be redefined to accommodate left and right side length changes, thus $b = r + l$. Because the circulation is only over half the wing, $y/\frac{b}{2}$, with the new definition of b, equation (2.4.1) will be split into a left and right side. This results in equation (2.4.2) being modified as follows:

$$L = \rho_0 V_0 \Gamma_0 \left(\int_{-l}^{0} \sqrt{1 - \left(\frac{y}{l}\right)^2} dy + \int_{0}^{r} \sqrt{1 - \left(\frac{y}{r}\right)^2} dy \right) \tag{2.4.3}$$

Using the transform $y = aCos\theta$ with $dy = -aSin\theta d\theta$, results in

$$L = \rho_0 V_0 \Gamma_0 \frac{\pi(l + r)}{4} \tag{2.4.4}$$

Knowing that the total lift $L = \frac{1}{2}\rho_0 V_0^2 S C_L$, equation (2.4.4) can be redefined into

$$\Gamma_0 = \frac{2 V_0 S C_l}{\pi(l + r)} \tag{2.4.5}$$

At this stage we need to look into the aerodynamic properties of the wing in more detail. Considering the downwash generated by the wing, we first need to obtain a change in circulation. Equation (2.4.6) represents the derivative of (2.4.1) with respect to only one side of the wing.

$$\frac{d\Gamma}{dy} = -\frac{2\Gamma_0}{a^2} \frac{y}{\sqrt{1 - \left(\frac{y}{a}\right)^2}} \tag{2.4.6}$$

Using the downwash equation provided by [15], with additional modification to allow separate wing side length,

$$\begin{aligned} w(\theta_0) &= -\frac{1}{4\pi} \int_{-\frac{b}{2}}^{\frac{b}{2}} \frac{\frac{d\Gamma}{dy} dy}{y_0 - y} \\ &= -\frac{1}{4\pi} \int_{-l}^{0} \frac{\frac{d\Gamma}{dy} dy}{y_0 - y} - \frac{1}{4\pi} \int_{0}^{r} \frac{\frac{d\Gamma}{dy} dy}{y_0 - y} \end{aligned} \tag{2.4.7}$$

and inserting (2.4.6) into it with the substitution used in (2.4.4) results in

$$\begin{aligned} w(\theta_0) &= -\frac{\Gamma_0}{4\pi} \int_{\pi}^{\frac{\pi}{2}} -1 d\theta - \frac{\Gamma_0}{4\pi} \int_{\frac{\pi}{2}}^{0} -1 d\theta \\ &= -\frac{\Gamma_0}{4} \frac{l + r}{2lr} \end{aligned} \tag{2.4.8}$$

Referring back to [15], the angle of incidence $\alpha_i = -\frac{w}{V_0}$ which results in

$$\alpha_i = \frac{\Gamma_0(l + r)}{8 l r V_0} \tag{2.4.9}$$

Using thin aerofoil theory, $C_L = 2\pi(\alpha - \alpha_i)$ and substituting equation (2.4.4) for Γ_0, the lift coefficient can be defined as

$$C_L = \frac{4\pi lr}{2lr + S}\alpha \tag{2.4.10}$$

Due to the assumption of thin aerofoil theory, the drag induced by the aerofoil cannot be analytically calculated and will be approximated by the equation (2.4.11).

$$C_D = \frac{C_L^2}{\pi A} \tag{2.4.11}$$

with $A = \frac{b^2}{S}$ the aspect ratio of the wing.

In the following sections, only the asymmetric reduced equations will be provided. The derivation of the symmetric equations can be found in [13]. When these equations take into account that both wings will not be the same length, the results are as stated in the following section. All equations are also provided in non-dimensional form.

2.4.1.2 Side force

$\mathbf{C_{y_\beta}}$ - Side force due to side-slip

According to [13], the main contributions to this coefficient are made by the fuselage and fin. Due to the wing not equating to the main contributions of this coefficient, the equation can be used in the exact form as provided from within [13] and can thus be represented by

$$C_{y_\beta} = \frac{S_B}{S} y_B - \frac{S_F}{S} a_{1_F} \tag{2.4.12}$$

where S_B is the side surface of the fuselage, S_F is the surface of the fin, y_B is the side force on the fuselage and a_{1_F} is the fin lift slope curve. Observing equation (2.4.12), the only term affected by wing loss is the surface area, represented by S. This term is only due to non-dimensionalising and will thus disappear when redimensionalising the term again. Thus wing loss should not exhibit any real effect on this coefficient.

$\mathbf{C_{y_P}}$ - Side force due to roll rate

This coefficient represents the side force generated by the roll rate. This is mainly due to the vertical tail plane (fin) as described in [13] and can be described by

$$C_{y_P} = -\frac{1}{Sb}\int_0^{H_F} a_h c_h h dh \tag{2.4.13}$$

In equation (2.4.13), H_F is fin height, a_h is fin lift curve slope and c_h is fin chord length. As with the previous coefficient, the only two terms representing the effect of wing loss are due to non-dimensionalising and thus should not affect the dimensionalised coefficient in any way.

$\mathbf{C_{y_R}}$ - Side force due to yaw rate

The side force due to yaw rate coefficient is mainly influenced by the fin. In its equational, non-dimensional form it can be described by

$$C_{y_R} = \frac{S_F l_F a_{1_F}}{Sb} \tag{2.4.14}$$

with l_F representing the fin moment arm. As with the previous two coefficients, this one should not be affected much by wing loss.

2.4.1.3 Rolling Moments

$\mathbf{C_{l_\beta}}$ - Rolling moment due to side-slip

The effect of sideslip on rolling moment can mainly be described by the contributions of wing and fin combined.

$$C_{l_\beta} = C_{l_{\beta_{wing}}} + C_{l_{\beta_{fin}}} \tag{2.4.15}$$

The effect of the wing on the coefficient can be described by equation (2.4.16)

$$C_{l_{\beta_{wing}}} = -\frac{1}{Sb}\left[\int_0^l c_y a_y \gamma y dy + \int_0^r c_y a_y \gamma y dy\right] \tag{2.4.16}$$

with c_y the chord length at position y, a_y the sectional lift at position y and γ the dihedral of the wing. Because both the chord length and sectional lift will change according to the percentage wing loss, this part of the coefficient should change.

The contribution of the fin is expressed in equation (2.4.17)

$$C_{l_{\beta_{fin}}} = -\frac{S_F h_F}{Sb} a_{1_F} \tag{2.4.17}$$

with h_F the distance between the fin's aerodynamic centre and the stability axis. This coefficient will undergo little change due to wing loss because the only parameters affected by wing loss are those used to non-dimensionalise the coefficient.

$\mathbf{C_{l_P}}$ - Rolling moment due to roll rate

The effect of roll rate on the rolling moment is mainly described by the wing's contribution. The full non-dimensional coefficient can be found in equation (2.4.18)

$$C_{l_P} = \frac{V_0}{Sb^2 P}\left[\int_0^l \left(a_y \alpha_e - \left(a_y + C_{D_y}\right)\left(\frac{Py}{V_0}\right)\right) c_y y dy - \int_0^r \left(a_y \alpha_e + \left(a_y + C_{D_y}\right)\left(\frac{Py}{V_0}\right)\right) c_y y dy\right] \tag{2.4.18}$$

with V_0 the current stability axis forward velocity, P the roll rate of the aircraft, α_e the steady equilibrium incidence angle of the wing (also known as the trim angle of attack) and C_{D_y} the sectional drag at position y. Observing equation (2.4.18) in its non-dimensional form, it is clear that due to asymmetry the coefficient possesses a lot more terms than its symmetric counterpart. These extra terms lead to static effects observed when the aircraft is affected by partial wing loss. It is believed that these effects could be trimmed out until the control deflection, used to null the effect, saturates. Due to the effect explained and the strong dependency on the wing's defining parameters, this coefficient will undergo great change due to wing loss.

$\mathbf{C_{l_R}}$ - Rolling moment due to yaw rate

The effect on the rolling moment due to yaw rate, is also mainly influenced by the wing and can be described with equation (2.4.19)

$$C_{l_R} = \frac{1}{Sb^2 R}\left[\int_0^l \left(V_0 + 2Ry\right) c_y y^2 C_{L_y} - \int_0^r \left(V_0 - 2Ry\right) c_y y^2 C_{L_y}\right] \tag{2.4.19}$$

with R the yaw rate of the aircraft and C_{L_y} the sectional lift at position y on the wing. As in the C_{l_P} coefficient case, static terms are again visible due to wing loss. These terms are the effect of the imbalance created by the different wing lengths which do not cancel each other out as in the symmetric case. This coefficient will also be greatly affect by wing loss as the pre-integrated equations stand in a cubic relationship to wing length.

2.4.1.4 Pitching Moment

$\mathbf{C_{m_\alpha}}$ - Pitching moment due to angle of attack

This coefficient represents the pitching moment experienced due to angle of attack. In both the symmetric and asymmetric aircraft it is described by the following equation.

$$C_{m_\alpha} = -ah_0 - \overline{V}_T a_1\left(1 - \frac{d\epsilon}{d\alpha}\right) + aCG \tag{2.4.20}$$

In equation (2.4.20), a represents the lift curve slope (C_{L_α}), h_0 the aerodynamic centre location of the mean aerodynamic chord, $\frac{d\epsilon}{dz}$ the rate of change of down wash angle, a_1 the tail plane lift curve slope, $\overline{V}_T = \frac{S_T l_T}{S\overline{c}}$ the tail plane volume ratio and the CG location. Due to a, h_0 and h being dependent on the wing's describing parameters, this coefficient should change with wing loss.

C_{m_Q} - Pitching moment due to pitch rate

The pitching moment due to the pitch rate is mainly due to the tailplane's contribution.

$$C_{m_Q} = -\overline{V}_T \frac{l_T}{\overline{\overline{c}}} a_1 \tag{2.4.21}$$

Parameters not defined by earlier equations are: l_T, the tail arm measured from CG to tail plane $\frac{1}{4}$ chord and $\overline{\overline{c}}$, the mean aerodynamic chord. Due to the main influence being the tailplane, wing loss should have little effect on this coefficient. There will however be signs of the loss effect due to the change in the mean aerodynamic chord.

2.4.1.5 Yawing Moments

C_{n_β} - Yawing moment due to side-slip

The yawing moment due to sideslip is mainly affected by the fin's contribution and is displayed in equation (2.4.22)

$$C_{n_\beta} = \overline{V}_T a_{1_F} \tag{2.4.22}$$

This coefficient will not be affected greatly by wing loss as the only affected terms are those used in the non-dimensionalisation.

C_{n_P} - Yawing moment due to roll rate

Regarding the roll rate's effect on the yawing moment, the wing plays a vital role. Equation (2.4.23) describes this coefficient in full.

$$C_{n_P} = \frac{V_0}{Sb^2P}\left[\int_0^l \left(a_y\alpha_e\left(\frac{Py}{V_0}\right) - a_y\left(\frac{Py}{V_0}\right)^2 + \alpha C_{D_y} - \left(\frac{Py}{V_0}\right)C_{D_y}\right)c_y y dy + \int_0^r \left(a_y\alpha_e\left(\frac{Py}{V_0}\right) + a_y\left(\frac{Py}{V_0}\right)^2 - \alpha C_{D_y} - \left(\frac{Py}{V_0}\right)C_{D_y}\right)c_y y dy\right] \tag{2.4.23}$$

When observing this equation, static, dynamic and extended dynamic terms are visible. The static terms αC_{D_y} and extended dynamic terms $a_y\left(\frac{Py}{V_0}\right)^2$ would have cancelled each other out in the symmetric case. The static effect can be passively trimmed out until the control deflection saturates but the extended dynamic effect will require active trimming due to its squared relationship to P. If the roll rate is relatively small it should have little effect, due to the left / right side imbalance being small. If the rate begins to increase, this term's imbalance will also increase and become significant. Thus this coefficient will be influenced by partial wing loss.

C_{n_R} - Yawing moment due to yaw rate

The yawing moment due to yaw rate is mainly described by the wing and fin.

$$C_{n_R} = C_{n_{R_{wing}}} + C_{n_{R_{fin}}} \tag{2.4.24}$$

Regarding the wing, equation (2.4.24) explains its influence on the coefficient.

$$C_{n_{R_{wing}}} = \frac{1}{Sb^2R}\left[-\int_0^l (V_0 + 2Ry)\, c_y y C_{D_y} dy + \int_0^r (V_0 - 2Ry)\, c_y y C_{D_y} dy\right] \tag{2.4.25}$$

In the symmetric case, the V_0 term would have cancelled out but in the asymmetric case this term creates an imbalance. The effect can be viewed as static due to no influence from the yaw rate and thus should allow for a trim condition that can null the effect, if sufficient control deflection is available. The remaining term is the usual symmetric contributor to this coefficient and due to its squared wing length nature will definitely be influenced by wing loss. The fin's contribution to this coefficient can be explained by the following equation

$$C_{n_{R_{fin}}} = \overline{V}_T a_{1_F} \frac{l_F}{b} = -C_{n_\beta} \frac{l_F}{b} \tag{2.4.26}$$

Again, due to the only terms influenced by wing loss being those used to non-dimensionalise the coefficient, it should not change much due to wing loss. Thus, as a whole, this coefficient will be influenced by wing loss.

2.4.1.6 Control Moments

In order to acquire the change in lift curve slope induced by a control surface, hinge moments will be used. The description for a hinge moment found in [17] and described here by equation (2.4.27)

$$C_{L_{\delta(.)}} = 2\left[\pi - aCos\left(2E_a - 1\right) + sin\left(aCos\left(2E_a - 1\right)\right)\right] \tag{2.4.27}$$

will be used to define the change in lift due to a control surface deflection with E_a the length of the control surface as a fraction of the chord on which it is situated.

It is quite clear what effect each control surface should produce but to be thorough a short explanation will be provided for each derivative.

$C_{y_{\delta Rud}}$ - Side force due to rudder deflection

The side force influence due to the rudder is mainly because of the lift change caused by its deflection and can be found in equation (2.4.28). It is clear from the coefficient's non-dimensional form that the only dependent terms are due to the non-dimensionalisation and thus it should not be affected by wing loss.

$$C_{y_{\delta Rud}} = \frac{S_F}{S} C_{L_{\delta Rud}} \tag{2.4.28}$$

$C_{l_{\delta Ail}}$ - Rolling moment due to Aileron deflection

The effect on the rolling moment due to aileron deflection can be seen in equation (2.4.29). The dominant effect of the ailerons in this case is to create a differential change in lift, which then induces a rolling moment. This coefficient is thus described by its placement on the wing and its surface area. Due to these facts it will be greatly influenced by wing loss.

$$C_{l_{\delta Ail}} = -\frac{1}{Sb}\left[\int_{y_{l_1}}^{y_{l_2}} C_{L_{\delta Ail}} c_y y dy + \int_{y_{r_1}}^{y_{r_2}} C_{L_{\delta Ail}} c_y y dy\right] \tag{2.4.29}$$

$C_{l_{\delta Rud}}$ - Rolling moment due to Rudder deflection

The rolling moment effect due to rudder deflection can be found in equation (2.4.30). It is clear that as in the case of the rolling moment due to roll rate due to the fin, the rudder only changes the lift created by the fin. None of the terms defining the coefficient, except the terms used to non-dimensionalise it, are dependent on wing loss and thus the coefficient should not change.

$$C_{l_{\delta Rud}} = \frac{S_F h_F}{Sb} C_{L_{\delta Rud}} \tag{2.4.30}$$

$C_{m_{\delta El}}$ - Pitching moment due to Elevator deflection

The pitching moment due to elevator deflection can be found in equation (2.4.31). Due to the elevator positioned on the tailplane, the coefficient describing it should not be affected by wing loss.

$$C_{m_{\delta El}} = -\overline{V}_T C_{L_{\delta El}} \tag{2.4.31}$$

$C_{n_{\delta Ail}}$ - Yawing moment due to Aileron deflection

The yawing moment due to aileron deflection can mainly be described by the induced drag generated by the deflection and can be found in equation (2.4.32). As in Section (2.4.1.6), the position and surface of an aileron will be affected by wing loss. Thus the coefficient will also change due to wing loss.

$$C_{n_{\delta Ail}} = \frac{1}{Sb}\left[\int_{y_{l_1}}^{y_{l_2}} C_{D_{\delta Ail}} c_y y dy + \int_{y_{r_1}}^{y_{r_2}} C_{D_{\delta Ail}} c_y y dy\right] \tag{2.4.32}$$

$C_{n_{\delta Rud}}$ - Yawing moment due to Rudder deflection

The yawing moment due to rudder deflection can be found in equation (2.4.33). This moment is created by the lift change due to deflection multiplied by the fin moment arm length. This coefficient will thus not be greatly affected by wing loss as the only terms influenced are those used to non-dimensionalise the

coefficient.

$$C_{n_{\delta Rud}} = -\frac{S_F l_F}{Sb} C_{L_{\delta Rud}} \tag{2.4.33}$$

The analytical derivation of the equations above provide a better understanding of which aerodynamic coefficients are affected by partial wing loss and which are not. As the analytical mathematics can not model all of the coefficients accurately, a numerical approach will be followed in the next section. This will provide more insight on how these coefficients are affected.

2.4.2 Numerical Calculation

In this section a software package is used to numerically calculate the effect of partial wing loss on the aerodynamic coefficients.

AVL provides a structured method of defining aerofoils and computing flow over them with vortex sheets [18]. It can compute the effects on coefficients due to the wing, tail and vertical fin aerodynamic surfaces but provides less accuracy with fuselage effects. It requires various inputs such as angle of attack, side-slip, etc. around which it solves the coefficients numerically.

AVL allows simulation of the fuselage as a slender body but warns the user to use this feature with caution. As it can only simulate a fuselage (body) with a circular circumference, any other shape should be estimated with a circular area. As the fuselage shape of the UAV did not produce any real difference in calculated coefficients, it was deemed acceptable to rather leave out the body entirely from the simulation. The reasoning behind this is that neglecting the body will introduce fewer inaccuracies than including an inaccurate body simulated with an inaccurate method.

The wing, tail and vertical fin are modelled in the software package using measurements taken of the physical dimensions of the UAV. As this UAV has been previously used in the laboratory, the coefficients calculated by the software package were compared with previous calculations before continuing. The wing surface is now incrementally sectioned off to observe the change in coefficients. As the number of vortex sheets on a surface is a pre-defined fixed number, they will be scaled according to the incremental loss of the wing. This is done to ensure the same accuracy on both sides of the model and the effect can be observed in Figure 2.10.

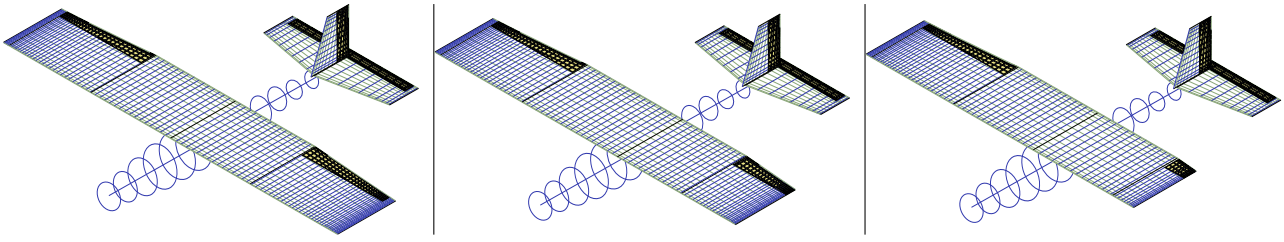

Figure 2.10 – AVL modelled wing with 0, 20 and 40% loss to one side

It should be noted that due to the inaccuracies introduced by neglecting the fuselage, some of the coefficients, especially those associated with yawing motions, will not be particularly accurate.

2.4.3 Discussion

In this section, the plots of the aerodynamic coefficients with respect to percentage partial wing loss, calculated both analytically and numerically, are presented. The results of the analytical calculation and the numerical calculation are compared, and are checked against the expected behaviour when considering the underlying physics. This will help point out any discrepancies and improve the general understanding of each coefficient. Though both techniques represent the coefficients in their non-dimensional form, it is difficult for the human mind to conceptualise the meaning of the response. When comparing the behaviour of the two techniques, the non-dimensional form can be used, but to interpret the physical behaviour of every coefficient, they will have to be in the dimensionalised form. The lift generated is represented in

Figure 2.11.

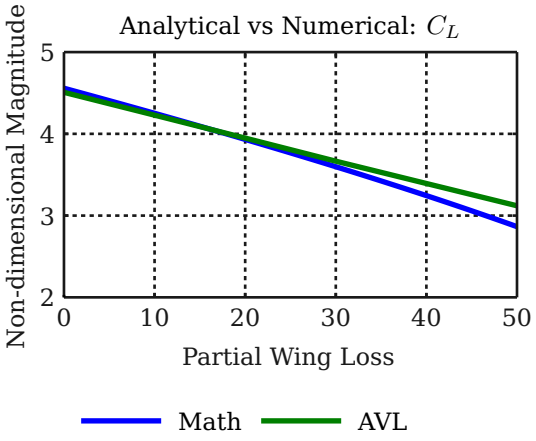

Figure 2.11 – Analytic vs AVL: Lift Coefficient Plot

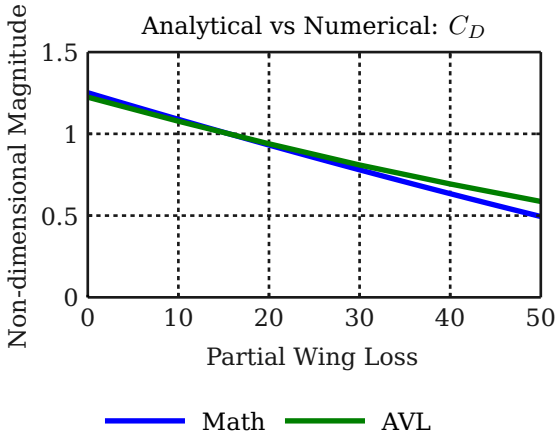

Figure 2.12 – Analytic vs AVL: Drag Coefficient Plot

It is clear that the assumptions around the lift calculation are fairly accurate in most of the wing loss case. The drag is approximated from the lift and also holds fairly well. The results acquired also confirm the intuitively expected results as described at the beginning of this section. Regarding the rest of the coefficients, the following matches between techniques are listed below and are displayed in Figures A.1 to A.16 in Appendix A:

Good matches (Small magnitude difference)
C_L, C_D, C_{y_P}, $C_{y_{\delta Rud}}$, C_{l_P}, $C_{l_{\delta Ail}}$,C_{m_α}, C_{n_β}, $C_{n_{\delta Rud}}$
Good matches (Big magnitude difference)
C_{y_R}, C_{m_Q}, C_{n_R}, $C_{m_{\delta El}}$
Negative behaviour match (Sign difference)
C_{l_β}, C_{n_P}, $C_{l_{\delta Rud}}$
Bad Matches
C_{l_R}, $C_{n_{\delta_A il}}$

When we examine these matches, it is clear that most of the results match. Some differences are observed between the analytical and numerical results but they usually agree with what is expected. The side force, elevator and rudder coefficients are hardly affected and the roll, pitch and aileron coefficients decrease in effectiveness. The expected biases are not seen on these plots due to being removed by the analytical calculations and the numerical package combining these effects into coefficients instead of showing them separately. However, if the equations in Section 2.4.1 are examined, the bias on the rolling moment due to the lift imbalance caused by partial wing loss is clearly visible.

A full review of the analytic and numeric method was made to try to find the discrepancies as depicted in Appendix A. No faults could be found. At this stage a decision was made to trust the coefficients acquired from AVL. The reasoning behind this is that the analytical ones only provide the capability to model some of the coefficients. The UAV has also been flown before with a set of similar AVL coefficients, which proved to work quite well.

When examining the physical behaviour of the coefficients, they first need to be dimensionalised appropriately. There are two options for dimensionalising the coefficients, the first being dimensionalisation using the instantaneous span, chord, and wing area and the second being dimensionalisation using the nominal undamaged span, chord and wing area. The first case, the dimensionalisation has a variable “gain”, due to the change in reference wing span and surface area. The second case, the dimensionalisation has a fixed “gain”. Using AVL with the second method will provide us with a more accurate coefficient for the robust control system to use. Instead of the change in aerodynamical behaviour being captured in the dimensionalisation and non-dimensionalisation terms, the coefficients themselves hold the behaviour. Figures 2.13 to 2.17 show the dimensional coefficient response to partial wing loss. These figures show all eight coefficients in a group to illustrate the dominant behaviour. Individual plots of every coefficient are

available in Appendix A.3

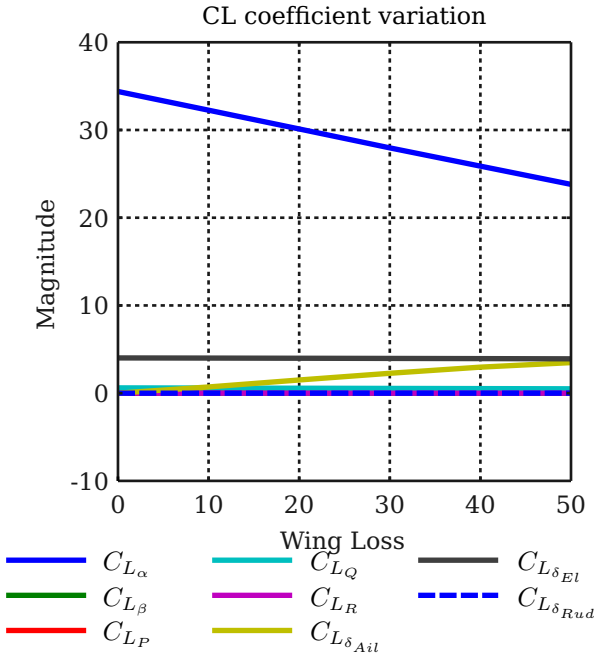

Figure 2.13 – AVL Dimensional Coefficients Plot - C_L

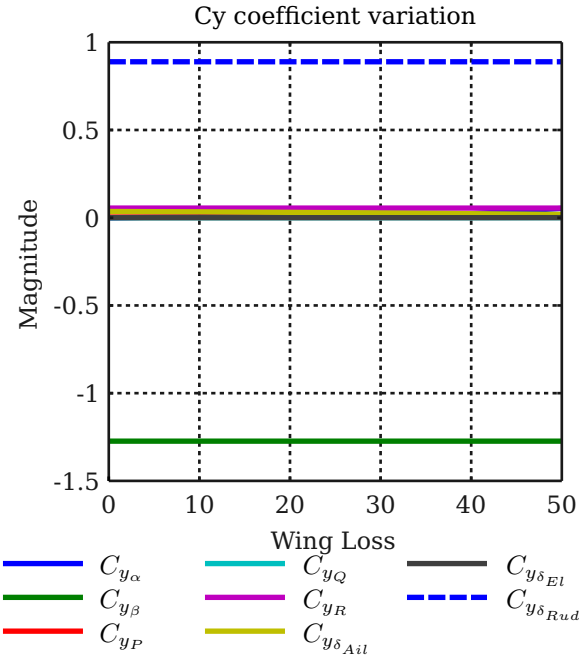

Figure 2.14 – AVL Dimensional Coefficients Plot - C_y

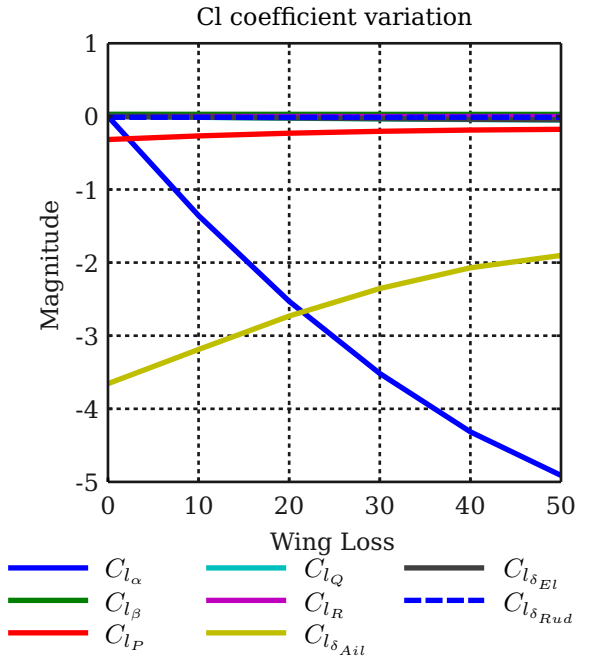

Figure 2.15 – AVL Dimensional Coefficients Plot - C_l

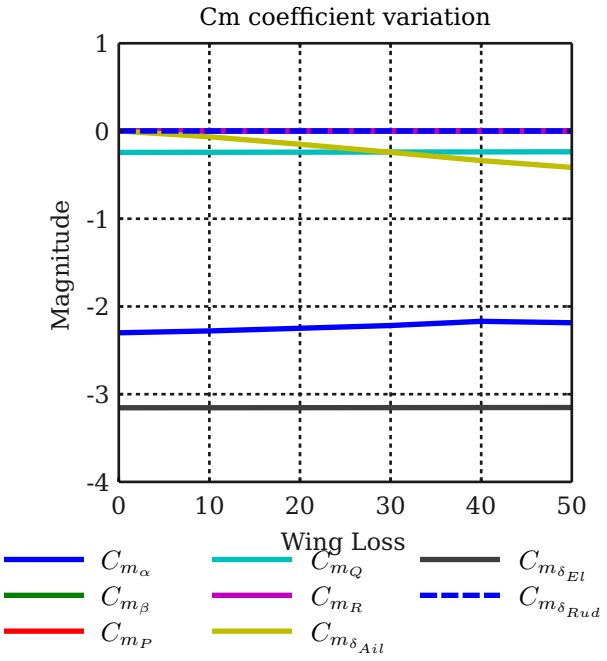

Figure 2.16 – AVL Dimensional Coefficients Plot - C_m

It is clear from Figures 2.13 to 2.17 that certain coefficients are not affected by partial wing loss, while others range from varying slightly to greatly. Any change relating to less than 5% will be regarded as no effect. A change between 5% and 20% will be regarded as a slight change and lastly any change above 20% will be regarded as a significant change. The summary below depicts the variations in coefficients.

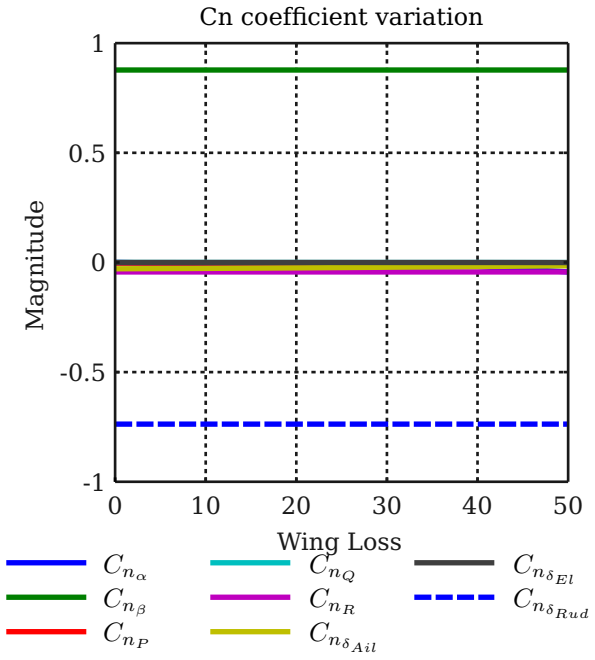

Figure 2.17 – AVL Dimensional Coefficients Plot - C_n

Indifferent to partial wing loss
$C_{y_\beta}, C_{y_R}, C_{y_{\delta_{Rud}}}, C_{m_{\delta_{El}}}, C_{n_\beta}, C_{n_{\beta_{Rud}}}$
Slight variation
$C_{L_{\delta_{El}}}, C_{l_R}, C_{l_{\delta_{Rud}}}, C_{m_Q}$
Great variation
$C_{L_\alpha}, C_{L_\beta}, C_{L_P}, C_{L_Q}, C_{L_R}, C_{L_{\delta_{Ail}}}, C_{L_{\delta_{Rud}}}, C_{y_\alpha}, C_{y_P}, C_{y_Q}, C_{y_{\delta_{Ail}}}$,
$C_{y_{\delta_{El}}}, C_{l_\beta}, C_{l_P}, C_{l_Q}, C_{l_{\delta_{Ail}}}, C_{l_{\delta_{El}}}, C_{m_\alpha}, C_{m_\beta}, C_{m_P}, C_{m_R}, C_{m_{\delta_{Ail}}}$,
$C_{m_{\delta_{Rud}}}, C_{n_\alpha}, C_{n_P}, C_{n_Q}, C_{n_{\delta_{Ail}}}, C_{n_{\delta_{El}}}$

It should however be noted that even if a coefficient depicts a significant change, if its original value is very small in comparison to the others of its group, it will still have an insignificant effect on the system. If all coefficients with a value in the of $< 10^{-3}$ and those starting from 0 and not reaching a maximum value of within a factor 10 of the closest variable in the group, are removed, the above summary is reduced to the following:

Indifferent to wing loss
$C_{y_\beta}, C_{y_R}, C_{y_{\delta_{Rud}}}, C_{m_{\delta_{El}}}, C_{n_\beta}, C_{n_{\beta_{Rud}}}$
Slight variation
$C_{L_{\delta_{El}}}, C_{l_{\delta_{Rud}}}, C_{m_Q}$
Great variation
$C_{L_\alpha}, C_{L_P}, C_{L_Q}, C_{L_{\delta_{Ail}}}, C_{y_\alpha}, C_{y_P}, C_{y_{\delta_{Ail}}}, C_{l_\beta}, C_{l_P}$,
$C_{l_Q}, C_{l_{\delta_{Ail}}}, C_{l_{\delta_{El}}}, C_{m_\alpha}, C_{m_{\delta_{Ail}}}, C_{n_\alpha}, C_{n_{\delta_{Ail}}}$

When examining the list above and comparing it to the list in Section 2.2.2.1, it becomes apparent that $C_{L_P}, C_{L_{\delta_{Ail}}}, C_{y_\alpha}, C_{l_\beta}, C_{l_Q}, C_{l_{\delta_{El}}}, C_{m_P}, C_{m_{\delta_{Ail}}}$ and C_{n_α} should be included in the equations expressing the forces and moments. Some of these coefficients may still be small in comparison to their defining group but start to become significant when loss increases.

2.5 Summary

In this chapter the reference frames and conventions used in this thesis, were explained. The standard aircraft flight mechanics used when describing a symmetric undamaged UAV were given and then adapted

for the purpose of this project. This included extending the symmetric six degrees of freedom equations of motion to an asymmetric six degrees of freedom equations of motion which can represent a shift in CG location. The origin for the body axis system of the asymmetric six degrees of motion equations was chosen as the CG of the symmetric UAV, and the same force and moment equations as for the symmetric UAV was used, except that a gravity moment was added to represent the shifted CG. Next, equations to change the CG location, mass and inertia matrix were derived and numeric values were calculated with a CAD program. Lastly the aerodynamic coefficients were calculated for the partial wing loss cases, both analytically and numerically and compared with what was intuitively expected. All of the equations were combined to create a non-linear model of a UAV in various stages of partial wing loss.

Chapter 3

Asymmetric Trim

To enable analysis of the stability and dynamic behaviour of the aircraft, the full non-linear equations of motion must first be linearised about an equilibrium condition, or trim condition. A trim condition requires that all the forces, moments, velocities and accelerations adhere to a predefined set of values, meaning that their time derivatives are zero. This behaviour can be straight and level flight, straight flight, coordinated turning, etc. The trim condition is a critical part of system analysis because it provides a working point within the UAV's dynamics, around which the non-linear system can be linearised. Linearising the dynamics about a trim condition allows us the use of the many analysis and design tools available in the field of linear systems theory. It can be reasoned that if this working point is an equilibrium, a control system should be able to stabilise the UAV's dynamics around this point, even though it might be an unstable equilibrium. This will however require that enough control authority is available.

In the general symmetric situation, only forces and moments in the longitudinal direction are trimmed to produce straight and level flight. This is due to the assumption that the lateral forces and moments acting on the UAV are in equilibrium because of its symmetry in the xy-plane. In the case of the asymmetric damaged UAV, the UAV is asymmetric in the xy-plane and thus both forces and moments in the lateral and longitudinal directions need to be trimmed. Specifying straight flight as the required trim for the asymmetric aircraft can be achieved in one of three ways. Either the aircraft can be trimmed with a non-zero side-slip and zero bank angle, a non-zero bank angle and zero side-slip or a combination of both with non-zero values. Furthermore, for straight flight, $p = q = r = 0$ with a constant altitude and airspeed. This also implies that their derivatives will equal zero. The three contributors to the forces and moments experienced by the UAV are those created by gravity, thrust and the UAV's aerodynamic characteristics.

Usually a trim condition is specified for the forces and moments acting through the CG of a UAV. This causes a problem when partial wing loss occurs to the aircraft and as a result the CG shifts. If this location is still used for trim, it will cause both the aerodynamic forces and thrust to induce moments. If however the point B, as specified in Section 2.3.1, is used, only gravity will cause an extra moment. Figure 3.1 shows the free body diagram of the aircraft. Note that only $\mathbf{G_I}$ does not act in on point B and will generate a moment around B.

In this chapter there is a description of how a few trim methods are implemented. First the analytic symmetric trim will be explained as background. Two asymmetric analytic trims, one adhering to zero side-slip and one adhering to zero bank angle will be calculated. Finally a numerical method will be implemented to try and solve the trim problem in an optimal way.

3.1 Symmetric Trim: Analytic Solution

When considering the nominal case trim, straight and level flight is usually used. This implies that the UAV will stay at a constant altitude and travel wings level to the horizon. As explained in the introduction, the UAV is considered symmetric in the xy-plane. This implies that no lateral forces will act in on it and thus do not need to be included in the calculations. Airspeed is usually specified, which also defines the trim air pressure at the given altitude and trim α will be equal to trim ω. With reference to Figure 3.1, the forces in the xz-plane and moments around the y-axis need to be zero. This leaves the problem of determining values for α, δ_{El} and T.

Using the equations for x- and y-forces and pitching moment as specified in Section 2.2 under the con-

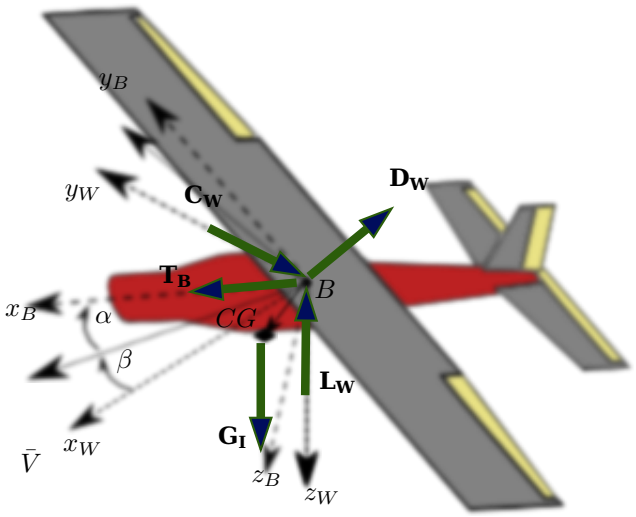

Figure 3.1 – Forces and Moments diagram

ditions described above result in equations (3.1.1) to (3.1.3).

$$(-q_T S C_{D_T} cos\alpha_T + q_T S C_{L_T} sin\alpha_T) + T_T - mgSin\Theta_T = 0 \tag{3.1.1}$$

$$(-q_T S C_{L_T} cos\alpha_T - q_T S C_{D_T} sin\alpha_T) + mgCos\Theta_T = 0 \tag{3.1.2}$$

$$q_T S \bar{c} C_{m_T} = 0 \tag{3.1.3}$$

To solve the above simultaneous non-linear equations without making any simplifying assumptions would require the use of iterative numerical methods. However, by making two assumptions that hold well, a closed form solution for the trim states can be found. One, the angle of attack is relatively small and two, the lift is an order of magnitude greater than the drag. If these two assumptions hold, and generally speaking they do, the equations can be simplified to an analytical solution as stated in equations (3.1.4) and (3.1.5).

$$-q_T S C_{L_T} + mg = 0 \tag{3.1.4}$$

$$q_T S \bar{c} C_{m_T} = 0 \tag{3.1.5}$$

If we substitute C_{L_T} and C_{m_T} with equations (2.2.15) and (2.2.21), the result can be represented in a matrix as specified by equation (3.1.6). Rearranging this matrix, α_T and δ_{El_T} can be solved as displayed in equation (3.1.7)

$$\begin{bmatrix} C_{L_0} \\ C_{m_0} \end{bmatrix} + \begin{bmatrix} C_{L_\alpha} & C_{L_{\delta_{El}}} \\ C_{m_\alpha} & C_{m_{\delta_{El}}} \end{bmatrix} \begin{bmatrix} \alpha_T \\ \delta_{El_T} \end{bmatrix} = \begin{bmatrix} \frac{mg}{q_T S} \\ 0 \end{bmatrix} \tag{3.1.6}$$

$$\begin{bmatrix} \alpha_T \\ \delta_{El_T} \end{bmatrix} = \begin{bmatrix} C_{L_\alpha} & C_{L_{\delta_{El}}} \\ C_{m_\alpha} & C_{m_{\delta_{El}}} \end{bmatrix}^{-1} \begin{bmatrix} \frac{mg}{q_T S} - C_{L_0} \\ -C_{m_0} \end{bmatrix} \tag{3.1.7}$$

By rearranging equation (3.1.1) in the form of equation (3.1.8) and substituting the values acquired for α_T and δ_{El_T}, T_T can be solved. For more information on this method, refer to [12] and [13].

$$T_T = q_T S C_{D_T} cos\alpha_T - q_T S C_{L_T} sin\alpha_T + mgSin\alpha_T \tag{3.1.8}$$

Using the above equations, Table 3.1 represents the calculated trim values along with the resultant forces and moments presented in Table 3.2. It should be noted that the trim actuations as depicted in Table 3.1 were acquired with the reduced model, while the resultant forces and moments in Table 3.2 were acquired using the full asymmetric non-linear model. Figure 3.2 depicts the results of the nominal trim, with regard to wing loss. It is clear that in the partial wing loss cases the symmetric assumption is invalidated and the trim does not produce a valid equilibrium.

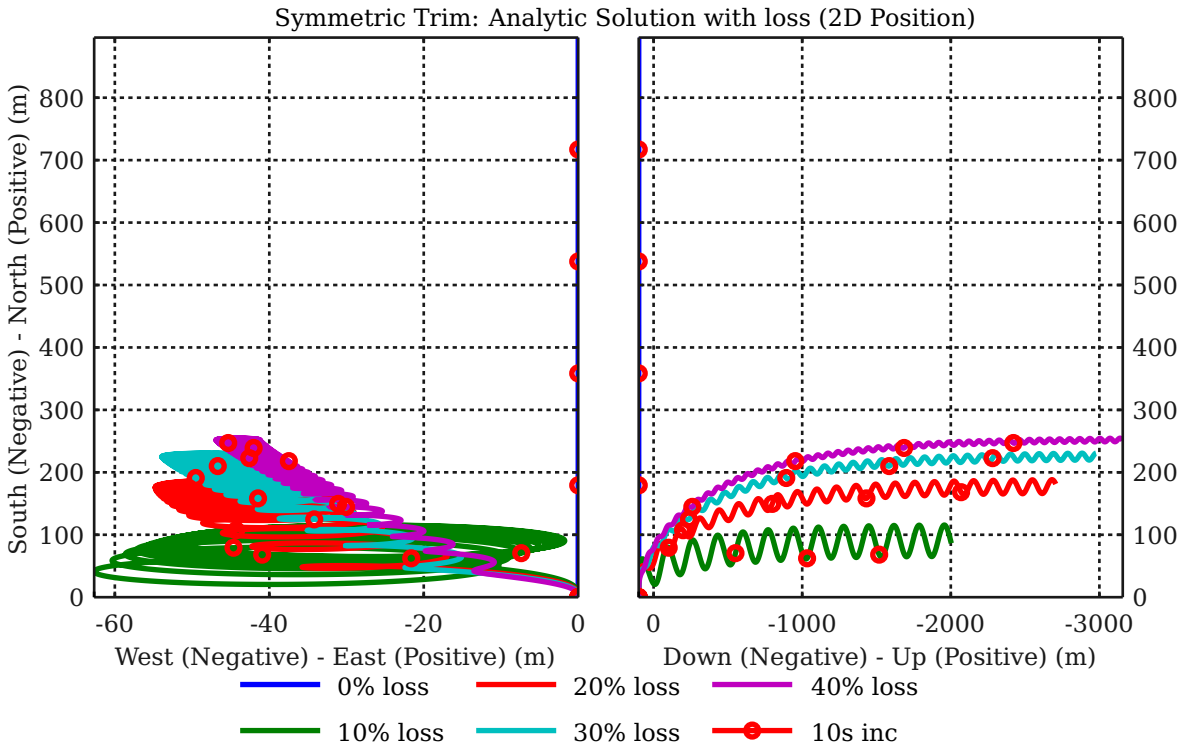

Figure 3.2 – Symmetric Trim: Analytic Solution with Wing loss

	Thrust	α	β	ϕ	δ_{Ail}	δ_{El}	δ_{Rud}
0%	4.71235	6.10401	0.00000	0.00000	0.00000	-4.45049	0.00000
10%	4.70839	6.53875	0.00000	0.00000	0.00000	-4.72384	0.00000
20%	4.70350	7.03913	0.00000	0.00000	0.00000	-5.01830	0.00000
30%	4.69729	7.62684	0.00000	0.00000	0.00000	-5.36291	0.00000
40%	4.68972	8.28809	0.00000	0.00000	0.00000	-5.70369	0.00000

Table 3.1 – Symmetric Trim: Analytic Solution values at $18m.s^{-1}$ for partial wing loss cases

	F_X	F_Y	F_Z	L	M	N
0%	0.00000	0.00000	-0.50394	0.00000	0.00000	0.00000
10%	0.05474	0.00000	-1.01724	-2.36370	-0.02778	-0.27093
20%	0.26568	0.00000	-2.73245	-3.78231	-0.08223	-0.46703
30%	0.50517	0.00000	-4.40160	-5.36971	-0.18529	-0.71903
40%	0.64484	0.00000	-5.10980	-7.74762	-0.25618	-1.12861

Table 3.2 – Symmetric Trim: Analytic Solution cases

3.2 Asymmetric Trim: Analytic Solution with Zero Bank Angle

In this section a trim based on zero bank angle, with side-slip angle will be calculated. As can be seen in Figure 3.1, forces **C**, **D** and **L** act on the body, referenced in the wind axis, force **G** acts on the body, referenced in the inertial axis and force **T** acts on the body and is referenced in the body axis. Translating the above forces from wind to body axis can be done with equation (2.1.5) and translating from the inertial to body axis can be accomplished with equation (2.1.1). Using equation (2.1.5) on **C**, **D** and **L** and equation (2.1.1) on **G** results in

$$\begin{bmatrix} X_{BW} \\ Y_{BW} \\ Z_{BW} \end{bmatrix} = DCM_{W\to B} \begin{bmatrix} -D \\ -C \\ -L \end{bmatrix} = \begin{bmatrix} -C_\alpha C_\beta D + C_\alpha S_\beta C + S_\alpha L \\ -S_\beta D - C_\beta C \\ -S_\alpha S_\beta D + S_\alpha S_\beta - C_\alpha L \end{bmatrix} \tag{3.2.1}$$

$$\begin{bmatrix} X_{BI} \\ Y_{BI} \\ Z_{BI} \end{bmatrix} = DCM_{I\to B} \begin{bmatrix} 0 \\ 0 \\ G \end{bmatrix} = \begin{bmatrix} -S_\theta G \\ C_\theta S_\phi G \\ C_\theta C_\phi G \end{bmatrix} \tag{3.2.2}$$

Summing the above equations along with **T** results in the total force acting on the body.

$$\begin{bmatrix} X_B \\ Y_B \\ Z_B \end{bmatrix} = \begin{bmatrix} X_{BW} \\ Y_{BW} \\ Z_{BW} \end{bmatrix} + \begin{bmatrix} X_{BI} \\ Y_{BI} \\ Z_{BI} \end{bmatrix} + \begin{bmatrix} T \\ 0 \\ 0 \end{bmatrix} = \begin{bmatrix} -C_\alpha C_\beta D + C_\alpha S_\beta C + S_\alpha L - S_\theta G + T \\ -S_\beta D - C_\beta C + C_\theta S_\phi G \\ -S_\alpha S_\beta D + S_\alpha S_\beta - C_\alpha L + C_\theta C_\phi G \end{bmatrix} \tag{3.2.3}$$

With regard to the moments, the normal pitch, roll and yaw moments apply as described by the aerodynamic equations and additional moments are generated due to the CG shift. As stated earlier, only gravity itself is defined through the CG. Translating gravity from the inertial to body reference frame and finding the moments generated by it leads to

$$\begin{bmatrix} L_G \\ M_G \\ N_G \end{bmatrix} = \begin{bmatrix} 0 & -\Delta_z & \Delta_y \\ \Delta_z & 0 & -\Delta_x \\ -\Delta_y & \Delta_x & 0 \end{bmatrix} \begin{bmatrix} -S_\theta G \\ C_\theta S_\phi G \\ C_\theta C_\phi G \end{bmatrix} = \begin{bmatrix} \Delta_y C_\theta C_\phi G - \Delta_z C_\theta S_\phi G \\ -\Delta_x C_\theta C_\phi G - \Delta_z S_\theta G \\ \Delta_x C_\theta S_\phi G + \Delta_y S_\theta G \end{bmatrix} \tag{3.2.4}$$

Thus $L = L_A + L_G, M = M_A + M_G$ and $N = N_A + N_G$. Due to the fact that in straight trim the UAV's attitude should represent the orientation of the wind axis, it is safe to state that $\theta = \alpha$, $\psi = -\beta$ and $\phi = 0$ because the relation between attitude and wind axis angles is known. Using the small angle assumption on equations (3.2.3) and (3.2.4),

$$\begin{bmatrix} X_B \\ Y_B \\ Z_B \end{bmatrix}_{sa} = \begin{bmatrix} -D + \beta C + \alpha L - \alpha G + T \\ -\beta D - C \\ -\alpha D + \alpha\beta C - L + G \end{bmatrix} \tag{3.2.5}$$

$$\begin{bmatrix} L_G \\ M_G \\ N_G \end{bmatrix}_{sa} = \begin{bmatrix} \Delta_y G \\ -\Delta_x G - \Delta_z \alpha G \\ \Delta_y \alpha G \end{bmatrix} \tag{3.2.6}$$

Furthermore, with the assumption that the lift is an order of magnitude larger than the drag, its effect is negligible. Due to small angle assumption, one small angle multiplied by another is a magnitude smaller and also negligible. If the above mentioned is taken into account the forces and moments can be defined in matrix format by,

$$\begin{bmatrix} 0 & C_{Y_\beta} & C_{Y_{\delta_{Ail}}} & 0 & C_{Y_{\delta_{Rud}}} \\ C_{L_\alpha} & 0 & C_{L_{\delta_{Ail}}} & C_{L_{\delta_{El}}} & 0 \\ C_{l_\alpha} & C_{l_\beta} & C_{l_{\delta_{Ail}}} & C_{l_{\delta_{El}}} & C_{l_{\delta_{Rud}}} \\ -\frac{\Delta_z G}{(qSc)} + C_{m_\alpha} & 0 & C_{m_{\delta_{Ail}}} & C_{m_{\delta_{El}}} & 0 \\ \frac{\Delta_y G}{(qSb)} & C_{n_\beta} & C_{n_{\delta_{Ail}}} & 0 & C_{n_{\delta_{Rud}}} \end{bmatrix} \begin{bmatrix} \alpha \\ \beta \\ \delta_{Ail} \\ \delta_{El} \\ \delta_{Rud} \end{bmatrix} = \begin{bmatrix} 0 \\ \frac{G}{(qS)} \\ -\frac{\Delta_y G}{(qSb)} \\ \frac{\Delta_x G}{(qSc)} \\ 0 \end{bmatrix} \tag{3.2.7}$$

Solving equation (3.2.7) for $\begin{bmatrix} \alpha & \beta & \delta_{Ail} & \delta_{El} & \delta_{Rud} \end{bmatrix}$ enables the thrust to be calculated from equation (3.2.8).

$$T = C_\alpha C_\beta D - C_\alpha S_\beta C - S_\alpha L + S_\theta G \tag{3.2.8}$$

The trim values solved analytically can be found in Table 3.3 and the resultant forces and moments can be found in Table 3.4. As stated in Section 3.1, the trim values were acquired using the reduced equations as explained above, but the resultant forces' and moments' values were acquired using the full asymmetric non-linear equations. Examining the results, it is clear that almost maximum deflection on both the ailerons and rudder is necessary to fly the UAV at wings-level trim. When these trim values are used as initial conditions in the full asymmetric non-linear simulation, the effect of the unbalanced forces and moments as presented in Figure 3.3 can be observed. It is clear that the UAV starts to diverge due to an unstable equilibrium and the small initial force moment imbalances.

3.3 Asymmetric Trim: Analytic Solution with Zero Side-Slip Angle

When calculating a trim based on zero side-slip with a bank angle, the same approach will be followed as in Section 3.2. The main difference here is the fact that $\beta = 0$ while the trim will calculate a ϕ angle to fly

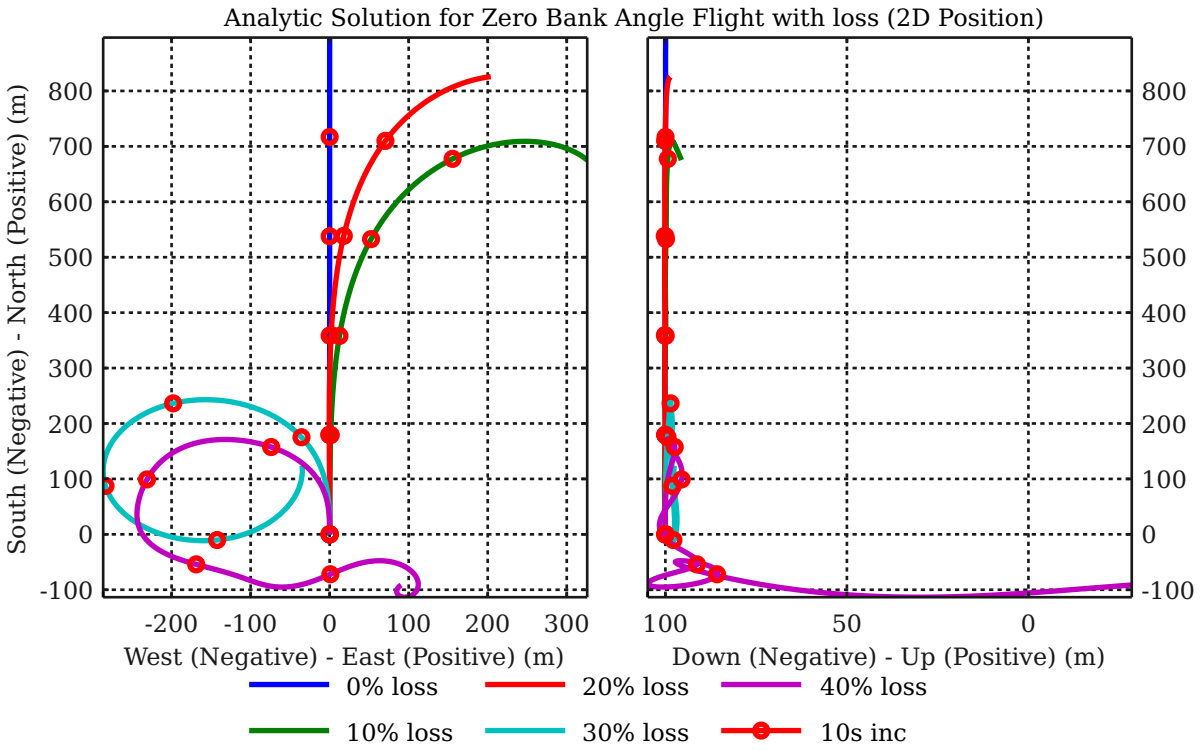

Figure 3.3 – Analytic solution for zero bank angle with partial wing loss

	Thrust	α	β	ϕ	δ_{Ail}	δ_{El}	δ_{Rud}
0%	4.71103	6.10401	0.00000	0.00000	0.00000	-4.45049	0.00000
10%	4.67801	6.54095	0.90360	0.00000	-2.31681	-4.70465	1.38209
20%	4.58175	7.01053	3.99920	0.00000	-4.29506	-4.87374	5.87784
30%	4.50296	7.75582	7.42437	0.00000	-7.31127	-5.07485	10.85902
40%	4.47553	9.23513	10.08664	0.00000	-13.67969	-5.15142	14.80460

Table 3.3 – Analytic solution for zero bank angle with values at $18m.s^{-1}$ for partial wing loss cases

	F_X	F_Y	F_Z	L	M	N
0%	-0.00132	0.00000	-0.50394	0.00000	0.00000	0.00000
10%	-0.00013	-0.07427	-0.53639	0.00372	-0.00114	-0.05236
20%	0.02084	-0.32127	-0.56086	0.00247	-0.02440	-0.23216
30%	0.07236	-0.58268	-0.60344	-0.04262	-0.07710	-0.43781
40%	0.13115	-0.78295	-0.70637	-0.09144	-0.12031	-0.60432

Table 3.4 – Analytic solution for zero bank angle cases

at. The initial wind to body ($DCM_{W\to B}$) will be changed to the DCM displayed in equation (3.3.1).

$$DCM_{W\to B} = \begin{bmatrix} C_\alpha & 0 & -S_\alpha \\ S_\alpha S_\phi & C_\phi & C_\alpha S_\phi \\ S_\alpha C_\phi & -S_\phi & C_\alpha C_\phi \end{bmatrix} ...C_{(.)} = cos(.), S_{(.)} = sin(.) \tag{3.3.1}$$

Using equations (3.3.1) to transform **C**,**D** and **L** results in

$$\begin{bmatrix} X_{BW} \\ Y_{BW} \\ Z_{BW} \end{bmatrix} = DCM_{W\to B} \begin{bmatrix} -D \\ -C \\ -L \end{bmatrix} = \begin{bmatrix} -C_\alpha D + S_\alpha L \\ -S_\alpha S_\phi D - C_\phi C - C_\alpha S_\phi L \\ -S_\alpha C_\phi D + S_\phi C - C_\alpha C_\phi L \end{bmatrix} \tag{3.3.2}$$

Equation (3.2.4) can be used as is. Applying the small angle assumption on equations (3.2.4) and (3.3.2) results in,

$$\begin{bmatrix} X_B \\ Y_B \\ Z_B \end{bmatrix} = \begin{bmatrix} -D + \alpha L - \alpha G \\ -\alpha\phi D - C - \phi L + \phi G \\ -\alpha D + \phi C - L + G \end{bmatrix} \quad (3.3.3) \qquad \begin{bmatrix} L_G \\ M_G \\ N_G \end{bmatrix}_{sa} = \begin{bmatrix} \Delta_y G - \Delta_z \phi G \\ -\Delta_x G - \Delta_z \alpha G \\ \Delta_x \phi G + \Delta_y \alpha G \end{bmatrix} \quad (3.3.4)$$

When this pre-defined choice is substituted, equation (3.3.5) arises.

$$\begin{bmatrix} 0 & \frac{mg}{(qS)} & -C_{y_{\delta_{Ail}}} & 0 & -C_{y_{\delta_{Rud}}} \\ C_{L_\alpha} & 0 & C_{L_{\delta_{Ail}}} & C_{L_{\delta_{El}}} & 0 \\ C_{l_\alpha} & -\frac{\Delta_z mg}{qSb} & C_{l_{\delta_{Ail}}} & C_{l_{\delta_{El}}} & C_{l_{\delta_{Rud}}} \\ C_{m_\alpha} & -\frac{\Delta_z mg}{qSc} & C_{m_{\delta_{Ail}}} & C_{m_{\delta_{El}}} & 0 \\ \frac{\Delta_y mg}{qSb} & \frac{\Delta_x mg}{qSb} & C_{n_{\delta_{Ail}}} & 0 & -C_{n_{\delta_{Rud}}} \end{bmatrix} \begin{bmatrix} \alpha \\ \phi \\ \delta_{Ail} \\ \delta_{El} \\ \delta_{Rud} \end{bmatrix} = \begin{bmatrix} 0 \\ \frac{mg}{qS} \\ -\frac{\Delta_y mg}{qSb} \\ \frac{\Delta_x mg}{qSc} \\ 0 \end{bmatrix} \quad (3.3.5)$$

Solving equation (3.3.5) for $\begin{bmatrix} \alpha & \phi & \delta_{Ail} & \delta_{El} & \delta_{Rud} \end{bmatrix}$ enables the thrust to be calculated with the help of equation (3.3.6).

$$T = C_\alpha D - S_\alpha (L - mg) \quad (3.3.6)$$

Implementing this trim on the UAV for the different loss cases, results in trim values as described in Table 3.5, with the resultant forces and moments displayed in Table 3.6. As stated previously, the trim values originate from the reduced equations above, while the resultant forces and moments originate from implementing the trim values in the full asymmetric non-linear model. The results of implementing these trim values while flying with partial wing loss is depicted in Figure 3.4. The UAV diverges more quickly than the one with a zero bank angle trim. These results are also supported when comparing Tables 3.4 and 3.6. Almost all the forces and moments are larger for the zero side-slip case. The side force however is almost twice as large as the one displayed in Table 3.4. Any side force experienced by the UAV will cause it to start side-slipping, even in this banked configuration. Due to this fact the trajectory will start to diverge rapidly from straight and level flight because of the initial forces not being cancelled out properly and this will lead to the observed behaviour.

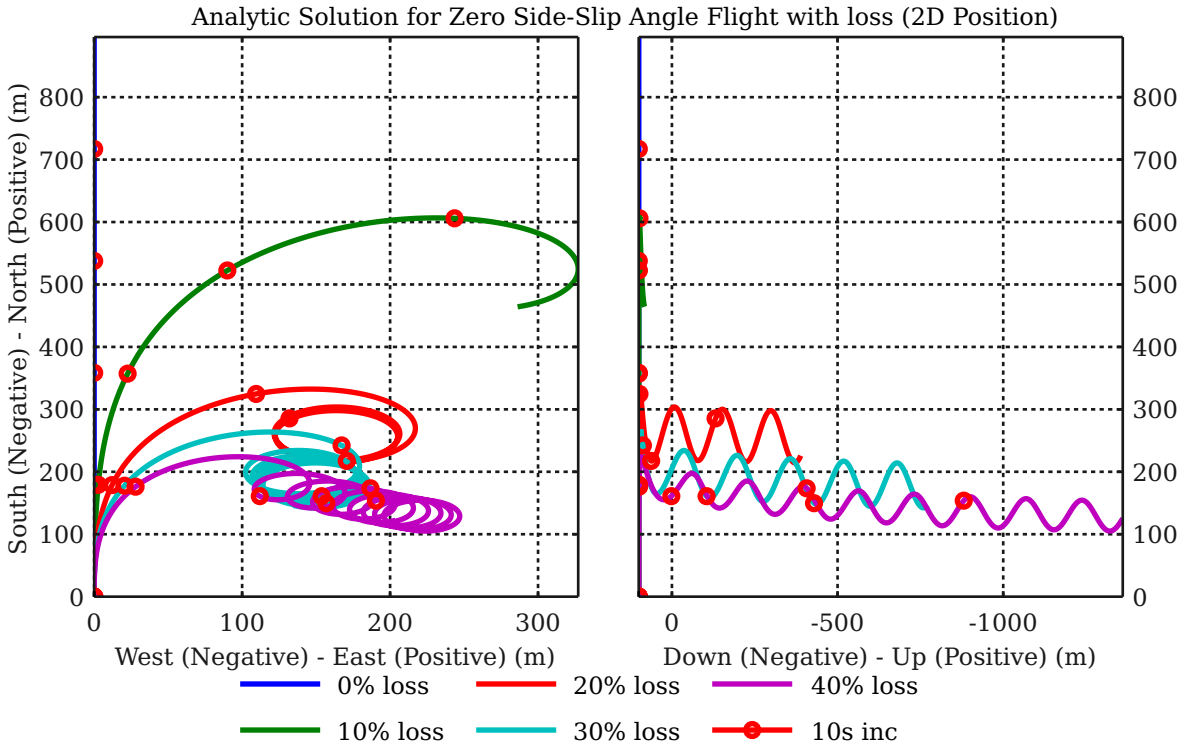

Figure 3.4 – Analytic solution with zero side-slip flight

It is clear at this stage that neither of the analytic solutions are able to provide a satisfactory trim over the whole range of wing loss. The zero bank angle trim does fare better but still uses a significant amount of aileron. Also, the analytical solution of the trim does not produce a force and moment balance that is exactly zero, due to the approximations made. In the following section, a numerical method is used to find a trim for the UAV. The numerical method allows the trim to be determined using the full non-linear differential equations, and produces a force and moment balance that is practically zero. It also provides

	Thrust	α	β	ϕ	δ_{Ail}	δ_{El}	δ_{Rud}
0%	4.71103	6.10401	0.00000	0.00000	0.00000	-4.45049	0.00000
10%	4.67743	6.54104	0.00000	0.05854	-2.32079	-4.70463	0.30664
20%	4.57080	7.01157	0.00000	0.26670	-4.31683	-4.87345	1.11916
30%	4.46686	7.75985	0.00000	0.51032	-7.36301	-5.07371	2.02921
40%	4.41132	9.24528	0.00000	0.70270	-13.77209	-5.14857	2.81343

Table 3.5 – Analytic solution with zero side-slip values at $18m.s^{-1}$ for partial wing loss cases

	F_X	F_Y	F_Z	L	M	N
0%	-0.00132	0.00000	-0.50394	0.00000	0.00000	0.00000
10%	-0.00129	0.12490	-0.53650	0.00598	0.00024	-0.05210
20%	-0.00122	0.55309	-0.56295	0.02819	0.00075	-0.22896
30%	-0.00115	1.02838	-0.61113	0.05789	0.00202	-0.42410
40%	-0.00112	1.39709	-0.72250	0.09375	0.00374	-0.57441

Table 3.6 – Analytic solution with zero side-slip cases

the capability to specify a cost function, which will enable the exploration of possible control surface deflections that are optimal in some way.

3.4 SQP Trim Solver

When examining the above derivations of Section 3.1 to 3.3, it is clear that only six different variables can be solved at one time. This restricts the application of this method to choosing some variables beforehand and then using them to find a solution, which may not be an optimal one.

In this section the trim condition will be calculated using the numerical method of SQP. It is believed using a numeric solver with the right constraints, will lead to a more optimal solution being found. A brief overview on SQP will be provided, followed by the implementation used in this thesis. A thorough description of SQP can be found in [19], with the implementation used in this thesis acquired from the work done in [4] and [17].

3.4.1 Sequential Quadratic Programming Overview

SQP is an iterative numerical method used to find the optimal solution to a predefined problem. The problem to solve is described by a design vector and a cost function, with certain equality and inequality constraints. These constraints provide the bounding region in which solutions are feasible. The iterations are done by calculating a step size and direction for the search.

The design vector consists of the variables to solve in the problem specified. At each iterative step the design variables are updated with the step size and direction calculated,

$$x_{(k+1)} = x_k + \Delta x_k \tag{3.4.1}$$

where Δx_k equals the step size multiplied by the direction.

Calculating the direction of the next step requires the algorithm to solve the non-linear optimisation problem through linearisation around the design point. This is done using an approximated standard quadratic form of the linear approximated constraints. Due to the approximation and linearisation, the problem is only solved for a small region around the current design point. This leads to the exclusion of solving for global minima as the solution will only iterate until it finds the first local minima. Another aspect of the approximation is that the quadratic sub-problem should remain valid and thus the search step size should be limited. The quadratic sub-problem can be defined as follows:

$$min\ q(x) = c^T x + \frac{1}{2} x^T H x \tag{3.4.2}$$

with the equality and inequality constraints represented by

$$N^T x = e \tag{3.4.3}$$

$$A^T x \leq b \tag{3.4.4}$$

with $x \geq 0$. The variables used in this quadratic sub-problem are as follows: c represents the derivative of the defined problem cost function, H represents the hessian matrix of the problem cost function, N represents the derivatives of the equality constraints, A represents the derivatives of the inequality constraints, e represents the equality constraints and b the inequality constraints. At this stage the quadratic sub-problem can now be solved for the variables provided. In this implementation, the simplex method will be used to solve the quadratic sub-problem. A full description of the simplex method can be found in [17], which was acquired from [19].

After the completion of a search direction, the actual step size needs to be determined. This is an easier task due to the fact that the search direction now only needs a valid magnitude for the current iteration. Regarding the previous statement, finding the step size reduces to a one dimensional problem and thus a line search method can be used [17]. Due to the constraints of the problem, a combination of a decent function with an inaccurate line search will be used as proposed by [19]. The step size will be represented by

$$\alpha_j = \left(\frac{1}{2}\right)^j : j = 0, 1, 2, 3, ... \tag{3.4.5}$$

The descent function used is represented in equation (3.4.6)

$$\Phi_k = f_k + RV_k \tag{3.4.6}$$

with R the penalty parameter and V_k the constraint violation. The iteration in step size will thus continue until a smaller function value than the previous one is reached or the step size decreases below its minimum threshold.

$$\Phi_{(k+1),j} + \alpha_j \beta_k \leq \Phi_k \tag{3.4.7}$$

3.4.2 Problem Setup for Optimisation

In using SQP to find a trim point for the damaged UAV, the following are needed: a design vector to be solved, a cost function to minimise and a structured weight system allowing the specification of variable importance, equality constraints, inequality constraints and a starting location. Due to the implementation of the current SQP code available, the derivatives of the cost function, equality constraints and inequality constraints are needed with respect to the design variables. These are necessary for validation during the iteration process.

In normal trim calculations, control surface deflection and engine thrust are used to find a point where the forces and moments are at an equilibrium. This usually goes hand in hand with the calculation of constant values for α, β and ϕ as a result of the deflections and thrust. The design vector used will thus encapsulate all the uncertain variables to find an optimal solution for the problem.

$$x = \begin{bmatrix} \delta_A & \delta_E & \delta_R & T & \alpha & \beta & \phi \end{bmatrix}' \tag{3.4.8}$$

When implementing the cost function it was decided to use the control deflections and α, β and ϕ angles. By including the control deflections, an optimal configuration can be found which will need the least amount of control. Including the angles allows for their optimisation, which will result in the smallest possible angles. If α, β and ϕ are small values, the wind and body axes will be very close to one another. This allows easier linearisation at a later stage as the transform of the wind to body axis will be greatly reduced under the small angle assumption. The cost function is represented below in mathematical form.

$$J_O = w_\alpha \alpha^2 + (1 - w_\alpha)(w_{\beta\phi}\beta^2 + (1 - w_{\beta\phi})\phi^2) \tag{3.4.9}$$

$$J_\delta = (w_{\delta a}\delta a^2 + w_{\delta e}\delta e^2 + w_{\delta r}\delta r^2)/w_{\delta T} \tag{3.4.10}$$

$$J_T = (w_O J_O + w_\Delta J_\delta) / (w_O + w_\Delta) \tag{3.4.11}$$

The equality constraints in this case will be represented by the full equations of motion, as specified

in equation (2.3.25). This equation can be simplified by assuming P, Q and R equal to zero and also to imply that the body velocities exerted should be equal to the current airspeed transformed between wind and body axis. In equations (2.3.25), both the linear and angular accelerations should also be zero for the applicable straight flight trim.

$$\dot{v}_B = \mathbf{0} \tag{3.4.12}$$

$$\dot{\omega} = \mathbf{0} \tag{3.4.13}$$

The inequility constraints used will represent the maximum and minimum limits of the control deflections and engine thrust.

$$\delta_{min} \leq \delta \leq \delta_{max} \tag{3.4.14}$$

Due to minimum and maximum limit nature of an actuator, the inequality needs to be rearranged into two $\leq$ inequalities for implementation in the SQP algorithm. This results in the following representation,

$$\delta_{min} - \delta \leq 0 \tag{3.4.15}$$

$$\delta - \delta_{max} \leq 0 \tag{3.4.16}$$

Lastly, the starting location needs to be specified. Because it is known that the UAV will be in a symmetric, undamaged state just prior to wing loss, the symmetric trim results will be used to determine a suitable starting location for the design vector. The implemented control system will also "start" at this location once the UAV enters an asymmetric state. It was thus hypothesised that if a valid trim location can be found, the possibility exists that the control system should be able to do the same.

3.5 Effect of Different Weightings in Cost Function

When using the cost function as described in the previous section with different weights, a variety of trim options come into play. In the previous section, it was explained that the SQP algorithm can only find the first local minima or maxima and will not progress to find the global ones. The cost function and weight system has thus been chosen to allow quick exploration of a few critical points or combinations thereof. In the process of finding a suitable trim, some of these options were analysed. The list below shows these various weight choices with a short description of each result. Tables and plots of every trim can be found in Appendix B.

- Equal weighting: $w_O = w_\Delta = 1$, $w_{\delta_a} = w_{\delta_e} = w_{\delta_r} = 1$, $w_\alpha = 0.\dot{3}$ and $w_{\beta\phi} = 0.5$
  - This weight set was chosen to find the best possible trim, minimising all the applicable variables. This set delivered a trim with forces and moments in the range of 10^{-3} and used more relative control surface deflection to achieve this.
- Stability Angle weighting: $w_O = 1, w_\Delta = 0$
  - This weight set was chosen to find the best possible trim, minimising the stability angles of the UAV. This method delivered a variety of trims with forces and moments sets in the ranges of 10^{-3} to 10^{-10}.
    - The minimised β trim delivered the best result with forces and moments in the range of 10^{-10}. This is in contrast to the analytic banked angle trim, which fared worse than the analytic side-slip trim.
    - The minimised ϕ trim deliver fairly good trim with forces and moments in the range of 10^{-4}. It did however require almost full rudder deflection and also demanded quite a large side-slip angle.
    - The minimised α trim delivered a good trim with respect to forces and moments at 10^{-5} but did not really minimise the AoA as much and demands quite a bit of side-slip and rudder deflection. The UAV also diverges from this trim quite quickly.
- Actuator weighting: $w_\Delta = 1, w_O = 0$
  - This weight set was chosen to find the best possible trim, minimising over the stability angles of the UAV. This method delivered a trim with forces and moments in the range 10^{-3} to 10^{-5}.

* The minimised δ_{Ail} provides quite a good trim at forces and moments cancelled out to 10^{-4} but did not really minimise the aileron actuation needed. It also requires quite a bit side-slip angle and rudder deflection. The UAV also diverges from this trim quite quickly.
* The minimised δ_{El} provided the same time of response as observed with the ailerons.
* The minimised δ_{Rud} delivered a fairly good trim with forces and moments arranged in values of 10^{-4}. It required almost half the amount of rudder necessary for the previous trims. The same can be said for the side-slip angle. The UAV also flew fairly straight with regard to the previous trims and only really diverged at 30 seconds of flight.

All of the above have been conducted from 0 to 40% wing loss at $18m.s^{-1}$. The minimum airspeed for the UAV to not stall in flight, without damage, is $12m.s^{-1}$ and the maximum airspeed the engine can produce is roughly $30m.s^{-1}$. Using this information the trim airspeed of $18m.s^{-1}$ was justified as a reasonable airspeed for analysis and testing. The reason for stopping at 40% wing loss is due to the lack of sufficient lift to keep the UAV in the air at $18m.s^{-1}$. At this stage the aileron control surfaces are almost maxed out and also impair the controllability of the UAV.

It should be noted that as the UAV travels faster through the air, it generates more lift. As it generates more lift, the amount of wing it can lose also increases. Testing this hypothesis with SQP found that if the UAV travelled at $35m.s^{-1}$, it could easily lose up to 60% of its wing and still have a bit of aileron control surface deflection left. At this point it should also be taken into account that the whole aileron on the wing with loss has been removed. It would however require that any form of control be very quick in response. This could however pose a problem for any safety pilot during testing and for this reason a maximum wing loss of 40% will be assumed.

After examining the list above, the decision was made to implement side-slip optimised weighting. It is clear from the SQP trim results that a UAV with the closest to nominal orientation will diverge slowest from its trim. It also became apparent that the ailerons are the most effective surface to counteract the induced rolling moment and lift imbalance caused by wing loss. Referring back to Section 2.4.1.3 also supports this notion as the ailerons have the greatest effect on rolling moment. It is also depicted in Figure 2.15 by the coefficients acquired from AVL. The results acquired with this trim can be found in Table 3.7 and 3.8.

	Thrust	α	β	ϕ	δ_{Ail}	δ_{El}	δ_{Rud}
0%	4.73463	6.05468	0.00000	0.00000	0.00000	-4.41453	0.00000
10%	4.70676	6.48423	-0.00000	0.00057	-2.29587	-4.66386	0.08458
20%	4.60693	6.94481	-0.00000	0.00100	-4.25040	-4.82817	0.14297
30%	4.51467	7.67429	-0.00000	0.00154	-7.22435	-5.02199	0.21400
40%	4.48637	9.11827	-0.00000	0.00250	-13.49015	-5.08720	0.33983

Table 3.7 – SQP Trim values at $18m.s^{-1}$ for partial wing loss cases

	F_X	F_Y	F_Z	L	M	N
0%	-3.92e-012	0.00e+000	-4.19e-013	0.00e+000	7.08e-016	0.00e+000
10%	-1.89e-013	1.73e-018	-1.42e-014	1.11e-016	1.73e-017	1.46e-015
20%	-2.97e-010	-6.51e-019	-3.62e-011	-1.14e-012	-5.55e-013	9.39e-012
30%	6.18e-012	1.08e-018	8.24e-013	4.53e-014	1.93e-014	-3.37e-013
40%	-1.75e-012	-1.60e-017	-2.84e-013	-1.69e-014	-6.05e-015	1.10e-013

Table 3.8 – SQP Trim cases

When examining Table 3.7, it can be seen that the trim uses basically no side-slip angle, a small amount of bank angle and very little rudder. The ailerons have been used to cancel out the rolling moment generated by the decreased lift on the one wing. The elevator has been used to increase the AoA, which increases the lift generated. As the AoA increases, the thrust will need to decrease to keep the current airspeed. Taking into consideration that this is a minimisation of β, the other angles and deflections obtained are

well within the limits even though some are a bit high. In comparison to the other weighted trims obtained these are not unreasonable and, as stated earlier, conceptually they do agree with what is expected to occur. The trimmed flight of these results can be found in Figure 3.5.

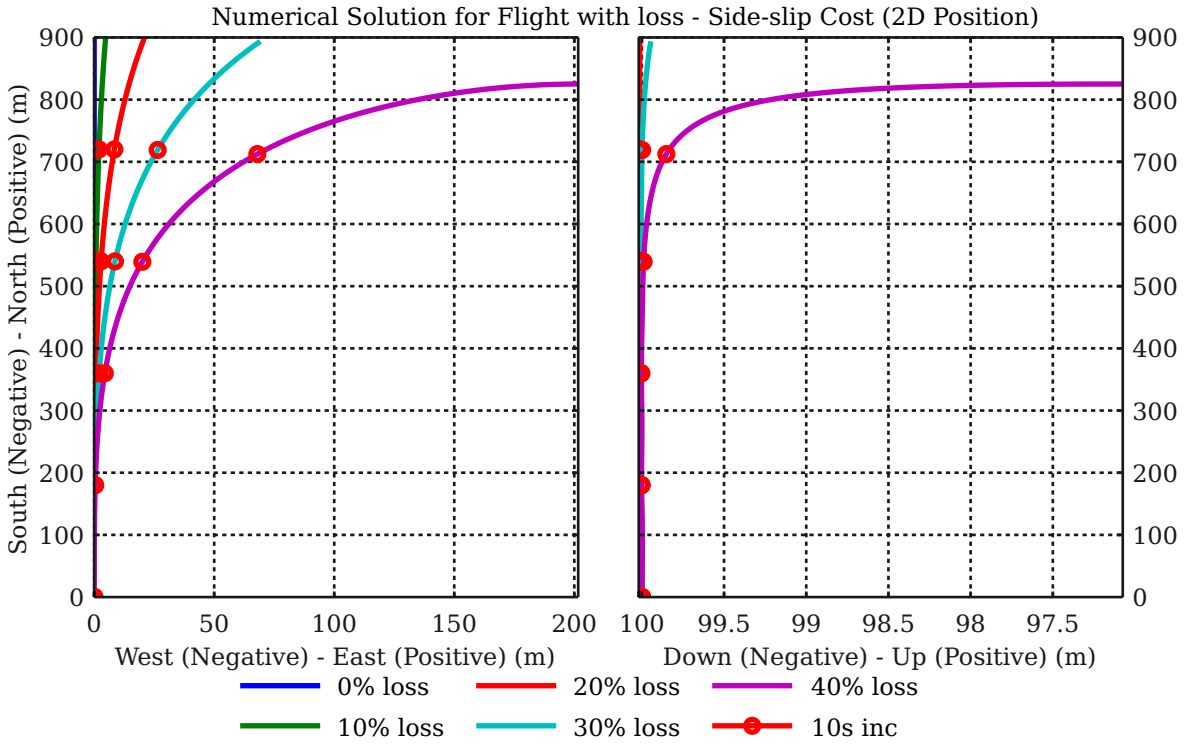

Figure 3.5 – SQP Trim Flight with Wing loss

It is clear from Figure 3.5 that the trim is valid, even though it is situated at an unstable equilibrium. Due to the small forces acting on the UAV, it slowly diverges from this equilibrium.

3.6 Summary

Different trim calculations, both analytic and numeric were implemented. As a baseline, the symmetric analytic trim was calculated based on assumptions to transform the standard non-linear equations into a closed set of linear equations. The trim calculations were done over the whole range of applicable partial wing loss. When these calculated values were substituted into the full asymmetric non-linear equations, the forces and moments did not balance out as they should for a valid equilibrium point.

The trim calculations were adapted to enable an asymmetric analytic solution through explicitly constraining either side-slip of bank angle to zero. This solution also required the full asymmetric non-linear equations to be simplified through a few assumptions. The zero bank angle constraint fared better than the zero side-slip constraint but still produced significant force and moment imbalances.

A numerical trim was calculated using Sequential Quadratic Programming to solve the full non-linear differential equations. This relied on a cost function which optimised the trim calculation in some way. When these trim values were substituted into the full asymmetric non-linear equations, the force and moment balance was practically zero. The small non-zero force and moment results are due to exit conditions reached by the SQP algorithm, such as the maximum number of iterations or reaching the step accuracy limit of the algorithm.

The following cost functions were explored:

- Minimising over α, β, ϕ, δ_{Ail} ,δ_{El} and δ_{Rud} with equal penalties
- Minimising over α, β, and ϕ separately with no penalties on δ_{Ail} ,δ_{El} and δ_{Rud}

- Minimising over δ_{Ail} ,δ_{El} and δ_{Rud} separately with no penalties on α, β and ϕ

After exploring the cost functions, it was found that minimising the side-slip angle with no penalties on the other variables, resulted in the best force and moment balance. This also delivered the best combination of control surface deflections and attitude parameters. It was decided that the equilibrium point produced by this cost function will be used when linearising the aircraft's dynamics and serve as the basis for control system design.

Chapter 4

Stability Analysis of Open-Loop Dynamics

Thus far in this thesis the ability to describe the behaviour of a damaged UAV, in an environment as close to the real world as possible, has been developed. This has laid the groundwork to find an equilibrium point, also known as a trim point, for the UAV in its unhealthy state. Finding an equilibrium point opens up the possibility to represent the system in a linear manner.

At the start of this chapter the non-linear AEoM will be linearised around the trim location and the open-loop dynamics will be described. The effect of wing loss on the open-loop dynamics will be examined, followed by a description of the natural modes of the UAV. The lateral and longitudinal stability of the open-loop dynamics will be examined, followed by the implications on control system design, and at the end of this chapter a conclusion will be drawn on the effect of wing loss on the open-loop dynamics.

4.1 Open-Loop Dynamics

Acquiring the trim conditions for the UAV provides a working point around which linearisation can be performed. This enables the creation of a linear model on which classic and modern control theory can be implemented. According to [12] the dynamics of the UAV can be described by the EoM, in this case the AEoM represented in equation (2.3.25) and two auxiliary equations found in equation (2.2.7),

$$\dot{\phi} = P + Qsin(\phi)tan(\theta) + Rcos(\phi)tan(\theta) \tag{4.1.1}$$

$$\dot{\theta} = Qcos(\phi) - Esin(\phi) \tag{4.1.2}$$

The equations above can be displayed in a nonlinear state space form as described by

$$\dot{x} = f(x, u)$$

with

$$x = \begin{bmatrix} U & V & W & P & Q & R & \phi & \theta \end{bmatrix}^T$$

$$u = \begin{bmatrix} \delta_{Ail} & \delta_{El} & \delta_{Rud} & T \end{bmatrix}^T$$

Knowing that trim provides an equilibrium point in the UAV's dynamics, small disturbance theory can be implemented if the UAV is only subjected to small perturbations and external disturbances. It should be noted that for a large amount of wing loss an equilibrium point will not exist. This is due to the primary lifting surface not being able to generate enough lift and thus not being able to overcome gravity. However, if it is taken into account that for all the cases of wing loss examined in Chapter 3 a valid trim point could be found, the assumption still holds on each of these points and only invalidates during the transition between them.

Implementing small disturbance theory on a variable it can be divided into two parts, the first being a constant and the second being a disturbance. The trim equilibrium point can be substituted as the constant value part of every variable and the deviations from this point as the small disturbances. When expanding the nonlinear system with a Taylor series, the constant part due to trim and the deviations from this trim can be separated as follows:

$$\dot{x}_{Trim} + \Delta x = f(x_{Trim} + \Delta x, u_{Trim} + \Delta u) = f(x_{Trim}, u_{Trim}) + \frac{df}{dx}|_{Trim}\Delta x + \frac{df}{du}|_{Trim}\Delta u + h.o.t. \tag{4.1.3}$$

Due to the small disturbance assumption, all the higher order terms (h.o.t.) will result in very small values due to the power of the nth term and can be assumed negligible. As stated earlier, the trim condition is a point of equilibrium and implies that no changes will happen at this point and thus renders

$$\dot{x}_{Trim} = f(x_{Trim}, u_{Trim}) = 0 \tag{4.1.4}$$

This leads to the change in model response only depending on the small disturbances it is subjected to.

$$\Delta\dot{x} \approx \frac{df}{dx}|_{Trim}\Delta x + \frac{df}{du}|_{Trim}\Delta u \tag{4.1.5}$$

At this point one would usually start decoupling the system into lateral and longitudinal systems. This would simplify the control needed and provide increased insight in the linearised model. Due to the general assumption of symmetry being invalidated in this thesis, the full model will first have to be accounted for in the linearised model. This is due to cross-coupling between the lateral and longitudinal motions of the UAV which come into play because of its asymmetric nature.

The full linearised model thus results in the following state space representation being found in equation (4.1.6)

$$\begin{bmatrix} \dot{U} \\ \dot{V}v \\ \dot{W} \\ \dot{P} \\ \dot{Q} \\ \dot{R} \\ \dot{\theta} \\ \dot{\phi} \end{bmatrix} = \begin{bmatrix} \frac{d\dot{U}}{dU} & \frac{d\dot{U}}{dV} & \frac{d\dot{U}}{dW} & \frac{d\dot{U}}{dP} & \frac{d\dot{U}}{dQ} & \frac{d\dot{U}}{dR} & \frac{d\dot{U}}{d\theta} & \frac{d\dot{U}}{d\phi} \\ \frac{d\dot{V}}{dU} & \frac{d\dot{V}}{dV} & \frac{d\dot{V}}{dW} & \frac{d\dot{V}}{dP} & \frac{d\dot{V}}{dQ} & \frac{d\dot{V}}{dR} & \frac{d\dot{V}}{d\theta} & \frac{d\dot{V}}{d\phi} \\ \frac{d\dot{W}}{dU} & \frac{d\dot{W}}{dV} & \frac{d\dot{W}}{dW} & \frac{d\dot{W}}{dP} & \frac{d\dot{W}}{dQ} & \frac{d\dot{W}}{dR} & \frac{d\dot{W}}{d\theta} & \frac{d\dot{W}}{d\phi} \\ \frac{d\dot{P}}{dU} & \frac{d\dot{P}}{dV} & \frac{d\dot{P}}{dW} & \frac{d\dot{P}}{dP} & \frac{d\dot{P}}{dQ} & \frac{d\dot{P}}{dR} & \frac{d\dot{P}}{d\theta} & \frac{d\dot{P}}{d\phi} \\ \frac{d\dot{Q}}{dU} & \frac{d\dot{Q}}{dV} & \frac{d\dot{Q}}{dW} & \frac{d\dot{Q}}{dP} & \frac{d\dot{Q}}{dQ} & \frac{d\dot{Q}}{dR} & \frac{d\dot{Q}}{d\theta} & \frac{d\dot{Q}}{d\phi} \\ \frac{d\dot{R}}{dU} & \frac{d\dot{R}}{dV} & \frac{d\dot{R}}{dW} & \frac{d\dot{R}}{dP} & \frac{d\dot{R}}{dQ} & \frac{d\dot{R}}{dR} & \frac{d\dot{R}}{d\theta} & \frac{d\dot{R}}{d\phi} \\ \frac{d\dot{\theta}}{dU} & \frac{d\dot{\theta}}{dV} & \frac{d\dot{\theta}}{dW} & \frac{d\dot{\theta}}{dP} & \frac{d\dot{\theta}}{dQ} & \frac{d\dot{\theta}}{dR} & \frac{d\dot{\theta}}{d\theta} & \frac{d\dot{\theta}}{d\phi} \\ \frac{d\dot{\phi}}{dU} & \frac{d\dot{\phi}}{dV} & \frac{d\dot{\phi}}{dW} & \frac{d\dot{\phi}}{dP} & \frac{d\dot{\phi}}{dQ} & \frac{d\dot{\phi}}{dR} & \frac{d\dot{\phi}}{d\theta} & \frac{d\dot{\phi}}{d\phi} \end{bmatrix} \begin{bmatrix} U \\ V \\ Q \\ P \\ Q \\ R \\ \theta \\ \phi \end{bmatrix} + \begin{bmatrix} \frac{d\dot{U}}{d\delta_A} & \frac{d\dot{U}}{d\delta_E} & \frac{d\dot{U}}{d\delta_R} & \frac{d\dot{U}}{d\delta T} \\ \frac{d\dot{V}}{d\delta_A} & \frac{d\dot{V}}{d\delta_E} & \frac{d\dot{V}}{d\delta_R} & \frac{d\dot{V}}{d\delta T} \\ \frac{d\dot{W}}{d\delta_A} & \frac{d\dot{W}}{d\delta_E} & \frac{d\dot{W}}{d\delta_R} & \frac{d\dot{W}}{d\delta T} \\ \frac{d\dot{P}}{d\delta_A} & \frac{d\dot{P}}{d\delta_E} & \frac{d\dot{P}}{d\delta_R} & \frac{d\dot{P}}{d\delta T} \\ \frac{d\dot{Q}}{d\delta_A} & \frac{d\dot{Q}}{d\delta_E} & \frac{d\dot{Q}}{d\delta_R} & \frac{d\dot{Q}}{d\delta T} \\ \frac{d\dot{R}}{d\delta_A} & \frac{d\dot{R}}{d\delta_E} & \frac{d\dot{R}}{d\delta_R} & \frac{d\dot{R}}{d\delta T} \\ \frac{d\dot{\theta}}{d\delta_A} & \frac{d\dot{\theta}}{d\delta_E} & \frac{d\dot{\theta}}{d\delta_R} & \frac{d\dot{\theta}}{d\delta T} \\ \frac{d\dot{\phi}}{d\delta_A} & \frac{d\dot{\phi}}{d\delta_E} & \frac{d\dot{\phi}}{d\delta_R} & \frac{d\dot{\phi}}{d\delta T} \end{bmatrix} \begin{bmatrix} \delta_{Ail} \\ \delta_{El} \\ \delta_{Rud} \\ \Delta T \end{bmatrix} \tag{4.1.6}$$

It should be noted at this stage that the derivation to acquire a linear model consisting of the partial differentiation of equation (4.1.6) will be calculated by a Matlab script and requires some manual oversight afterwards. Referring back to equation (2.3.25), the 6x6 inverse matrix poses a hindrance to calculate without the aid of a computer. It also implies that every term in the second matrix, the matrix after the 6x6 inverse matrix of the AEoM, will be presented multiple times in each derivation. The chances of an error are just too high when doing these equations on paper and thus Matlab's Symbolic Toolbox will be used. The script sets up the EoM in matrix form, implements the necessary substitutions, partially differentiates the equations and simplifies the results. After the script has simplified the results, it is necessary to go back and manually remove all the α and β terms not associated with the trim lift generation term. This process can also be automated but requires a logical structure to be implemented. It was deemed faster to just remove these terms by hand. The script used, along with the revised results acquired, can be found in Appendix C.

Regarding the differentiating script mentioned above, the full script enables calculating of any UAV configuration. This would however require alteration of some of the substitutions. If some UAV specific data is taken into consideration, the script can be simplified to produce a more digestible result. Considering the effect of losing a part of the wing, the mass and inertia changes should be rather small, with regard to this specific UAV. In calculating the 6x6 inverse matrix, as defined in equation (2.3.25) for 0 to 40% wing loss, it can be noted that the diagonal terms are mostly the dominant ones. The off-diagonal terms are usually a factor 10 to 100 smaller than the diagonal terms, with the exception of terms $(1,6)$ and $(3,4)$. This is expected as terms $(1,6)$ and $(3,4)$ represent the CG shift in the y-direction, which is the dominant factor in the CG shift. Referring back to the kinetics part in Section 2.2.1, two assumptions reduced the inertial matrix of a symmetric aircraft to only a diagonal term by stating that I_{xy}, I_{yz} and I_{xz} are negligibly small. Although the first assumption of symmetry does not apply here, the values of I_{xy} and I_{yz} are negligibly small in comparison to their diagonal counterparts. Taking this into account, the 6x6 inverse matrix can safely be reduced to only the diagonal terms, along with terms $(1,6)$ and $(3,4)$. As this matrix was symmetrical before the reduction, terms $(6,1)$ and $(4,3)$ will also be included.

It is common practice to transform $\begin{bmatrix} U & V & W \end{bmatrix}$ to $\begin{bmatrix} \bar{V} & \alpha & \beta \end{bmatrix}$. This can easily be achieved due to the

small disturbance assumption and the trim condition for straight flight.

$$\begin{aligned}
\bar{V} = \sqrt{U^2 + V^2 + W^2} \approx \sqrt{U^2} = U \\
W = \bar{V} sin(\alpha) \approx (U_{Trim} + U)\alpha \approx U_{Trim}\alpha = \bar{V}_{Trim}\alpha \\
V = \bar{V} sin(\beta) \approx (U_{Trim} + U)\beta \approx U_{Trim}\beta = \bar{V}_{Trim}\beta
\end{aligned}$$

$$\begin{aligned}
\dot{U} \approx \dot{\bar{V}}_{Trim} \\
\dot{V} \approx \bar{V}_{Trim}\dot{\alpha} \\
\dot{W} \approx \bar{V}_{Trim}\dot{\beta}
\end{aligned}$$

Substituting these relations into equation (4.1.6) and rearranging the terms to $\begin{bmatrix}\bar{V} & \alpha & Q & \theta & \beta & P & R & \phi\end{bmatrix}^T$ to fit into the their longitudinal / lateral nature, results in

$$\begin{bmatrix} \dot{\bar{V}} \\ \bar{V}_T\dot{\beta} \\ \bar{V}_T\dot{\alpha} \\ \dot{P} \\ \dot{Q} \\ \dot{R} \\ \dot{\theta} \\ \dot{\phi} \end{bmatrix} = \begin{bmatrix} \frac{d\dot{U}}{dU} & \frac{d\dot{U}}{dV} & \frac{d\dot{U}}{dW} & \frac{d\dot{U}}{dP} & \frac{d\dot{U}}{dQ} & \frac{d\dot{U}}{dR} & \frac{d\dot{U}}{d\theta} & \frac{d\dot{U}}{d\phi} \\ \frac{d\dot{V}}{dU} & \frac{d\dot{V}}{dV} & \frac{d\dot{V}}{dW} & \frac{d\dot{V}}{dP} & \frac{d\dot{V}}{dQ} & \frac{d\dot{V}}{dR} & \frac{d\dot{V}}{d\theta} & \frac{d\dot{V}}{d\phi} \\ \frac{d\dot{W}}{dU} & \frac{d\dot{W}}{dV} & \frac{d\dot{W}}{dW} & \frac{d\dot{W}}{dP} & \frac{d\dot{W}}{dQ} & \frac{d\dot{W}}{dR} & \frac{d\dot{W}}{d\theta} & \frac{d\dot{W}}{d\phi} \\ \frac{d\dot{P}}{dU} & \frac{d\dot{P}}{dV} & \frac{d\dot{P}}{dW} & \frac{d\dot{P}}{dP} & \frac{d\dot{P}}{dQ} & \frac{d\dot{P}}{dR} & \frac{d\dot{P}}{d\theta} & \frac{d\dot{P}}{d\phi} \\ \frac{d\dot{Q}}{dU} & \frac{d\dot{Q}}{dV} & \frac{d\dot{Q}}{dW} & \frac{d\dot{Q}}{dP} & \frac{d\dot{Q}}{dQ} & \frac{d\dot{Q}}{dR} & \frac{d\dot{Q}}{d\theta} & \frac{d\dot{Q}}{d\phi} \\ \frac{d\dot{R}}{dU} & \frac{d\dot{R}}{dV} & \frac{d\dot{R}}{dW} & \frac{d\dot{R}}{dP} & \frac{d\dot{R}}{dQ} & \frac{d\dot{R}}{dR} & \frac{d\dot{R}}{d\theta} & \frac{d\dot{R}}{d\phi} \\ \frac{d\dot{\theta}}{dU} & \frac{d\dot{\theta}}{dV} & \frac{d\dot{\theta}}{dW} & \frac{d\dot{\theta}}{dP} & \frac{d\dot{\theta}}{dQ} & \frac{d\dot{\theta}}{dR} & \frac{d\dot{\theta}}{d\theta} & \frac{d\dot{\theta}}{d\phi} \\ \frac{d\dot{\phi}}{dU} & \frac{d\dot{\phi}}{dV} & \frac{d\dot{\phi}}{dW} & \frac{d\dot{\phi}}{dP} & \frac{d\dot{\phi}}{dQ} & \frac{d\dot{\phi}}{dR} & \frac{d\dot{\phi}}{d\theta} & \frac{d\dot{\phi}}{d\phi} \end{bmatrix} \begin{bmatrix} \bar{V} \\ \bar{V}_T\beta \\ \bar{V}_T\alpha \\ P \\ Q \\ R \\ \theta \\ \phi \end{bmatrix} + \begin{bmatrix} \frac{d\dot{U}}{d\delta_A} & \frac{d\dot{U}}{d\delta_E} & \frac{d\dot{U}}{d\delta_R} & \frac{d\dot{U}}{d\delta T} \\ \frac{d\dot{V}}{d\delta_A} & \frac{d\dot{V}}{d\delta_E} & \frac{d\dot{V}}{d\delta_R} & \frac{d\dot{V}}{d\delta T} \\ \frac{d\dot{W}}{d\delta_A} & \frac{d\dot{W}}{d\delta_E} & \frac{d\dot{W}}{d\delta_R} & \frac{d\dot{W}}{d\delta T} \\ \frac{d\dot{P}}{d\delta_A} & \frac{d\dot{P}}{d\delta_E} & \frac{d\dot{P}}{d\delta_R} & \frac{d\dot{P}}{d\delta T} \\ \frac{d\dot{Q}}{d\delta_A} & \frac{d\dot{Q}}{d\delta_E} & \frac{d\dot{Q}}{d\delta_R} & \frac{d\dot{Q}}{d\delta T} \\ \frac{d\dot{R}}{d\delta_A} & \frac{d\dot{R}}{d\delta_E} & \frac{d\dot{R}}{d\delta_R} & \frac{d\dot{R}}{d\delta T} \\ \frac{d\dot{\theta}}{d\delta_A} & \frac{d\dot{\theta}}{d\delta_E} & \frac{d\dot{\theta}}{d\delta_R} & \frac{d\dot{\theta}}{d\delta T} \\ \frac{d\dot{\phi}}{d\delta_A} & \frac{d\dot{\phi}}{d\delta_E} & \frac{d\dot{\phi}}{d\delta_R} & \frac{d\dot{\phi}}{d\delta T} \end{bmatrix} \begin{bmatrix} \delta_A \\ \delta_E \\ \delta_R \\ \Delta T \end{bmatrix}$$

$$\begin{bmatrix} \dot{\bar{V}} \\ \dot{\alpha} \\ \dot{Q} \\ \dot{\theta} \\ \dot{\beta} \\ \dot{P} \\ \dot{R} \\ \dot{\phi} \end{bmatrix} = \begin{bmatrix} \frac{d\dot{U}}{dU} & \frac{d\dot{U}}{dW}\bar{V} & \frac{d\dot{U}}{dQ} & \frac{d\dot{U}}{d\theta} & \frac{d\dot{U}}{dV}\bar{V} & \frac{d\dot{U}}{dP} & \frac{d\dot{U}}{dR} & \frac{d\dot{U}}{d\phi} \\ \frac{d\dot{W}}{dU}\frac{1}{\bar{V}} & \frac{d\dot{W}}{dW} & \frac{d\dot{W}}{dQ}\frac{1}{\bar{V}} & \frac{d\dot{W}}{d\theta}\frac{1}{\bar{V}} & \frac{d\dot{W}}{dV} & \frac{d\dot{W}}{dP}\frac{1}{\bar{V}} & \frac{d\dot{W}}{dR}\frac{1}{\bar{V}} & \frac{d\dot{W}}{d\phi}\frac{1}{\bar{V}} \\ \frac{d\dot{Q}}{dU} & \frac{d\dot{Q}}{dW}\bar{V} & \frac{d\dot{Q}}{dQ} & \frac{d\dot{Q}}{d\theta} & \frac{d\dot{Q}}{dV}\bar{V} & \frac{d\dot{Q}}{dP} & \frac{d\dot{Q}}{dR} & \frac{d\dot{Q}}{d\phi} \\ \frac{d\dot{\theta}}{dU} & \frac{d\dot{\theta}}{dW}\bar{V} & \frac{d\dot{\theta}}{dQ} & \frac{d\dot{\theta}}{d\theta} & \frac{d\dot{\theta}}{dV} & \frac{d\dot{\theta}}{dP} & \frac{d\dot{\theta}}{dR} & \frac{d\dot{\theta}}{d\phi} \\ \frac{d\dot{V}}{dU}\frac{1}{\bar{V}} & \frac{d\dot{V}}{dW} & \frac{d\dot{V}}{dQ}\frac{1}{\bar{V}} & \frac{d\dot{V}}{d\theta}\frac{1}{\bar{V}} & \frac{d\dot{V}}{dV} & \frac{d\dot{V}}{dP}\frac{1}{\bar{V}} & \frac{d\dot{V}}{dR}\frac{1}{\bar{V}} & \frac{d\dot{V}}{d\phi}\frac{1}{\bar{V}} \\ \frac{d\dot{P}}{dU} & \frac{d\dot{P}}{dW}\bar{V} & \frac{d\dot{P}}{dQ} & \frac{d\dot{P}}{d\theta} & \frac{d\dot{P}}{dV}\bar{V} & \frac{d\dot{P}}{dP} & \frac{d\dot{P}}{dR} & \frac{d\dot{P}}{d\phi} \\ \frac{d\dot{R}}{dU} & \frac{d\dot{R}}{dW}\bar{V} & \frac{d\dot{R}}{dQ} & \frac{d\dot{R}}{d\theta} & \frac{d\dot{R}}{dV}\bar{V} & \frac{d\dot{R}}{dP} & \frac{d\dot{R}}{dR} & \frac{d\dot{R}}{d\phi} \\ \frac{d\dot{\phi}}{dU} & \frac{d\dot{\phi}}{dW}\bar{V} & \frac{d\dot{\phi}}{dQ} & \frac{d\dot{\phi}}{d\theta} & \frac{d\dot{\phi}}{dV}\bar{V} & \frac{d\dot{\phi}}{dP} & \frac{d\dot{\phi}}{dR} & \frac{d\dot{\phi}}{d\phi} \end{bmatrix} \begin{bmatrix} \bar{V} \\ \alpha \\ Q \\ \theta \\ \beta \\ P \\ R \\ \phi \end{bmatrix} + \begin{bmatrix} \frac{d\dot{U}}{d\delta_A} & \frac{d\dot{U}}{d\delta_E} & \frac{d\dot{U}}{d\delta_R} & \frac{d\dot{U}}{d\delta T} \\ \frac{d\dot{W}}{d\delta_A}\frac{1}{\bar{V}} & \frac{d\dot{W}}{d\delta_E}\frac{1}{\bar{V}} & \frac{d\dot{W}}{d\delta_R}\frac{1}{\bar{V}} & \frac{d\dot{W}}{d\delta T}\frac{1}{\bar{V}} \\ \frac{d\dot{\theta}}{d\delta_A} & \frac{d\dot{\theta}}{d\delta_E} & \frac{d\dot{\theta}}{d\delta_R} & \frac{d\dot{\theta}}{d\delta T} \\ \frac{d\dot{Q}}{d\delta_A} & \frac{d\dot{Q}}{d\delta_E} & \frac{d\dot{Q}}{d\delta_R} & \frac{d\dot{Q}}{d\delta T} \\ \frac{d\dot{V}}{d\delta_A}\frac{1}{\bar{V}} & \frac{d\dot{V}}{d\delta_E}\frac{1}{\bar{V}} & \frac{d\dot{V}}{d\delta_R}\frac{1}{\bar{V}} & \frac{d\dot{V}}{d\delta T}\frac{1}{\bar{V}} \\ \frac{d\dot{P}}{d\delta_A} & \frac{d\dot{P}}{d\delta_E} & \frac{d\dot{P}}{d\delta_R} & \frac{d\dot{P}}{d\delta T} \\ \frac{d\dot{R}}{d\delta_A} & \frac{d\dot{R}}{d\delta_E} & \frac{d\dot{R}}{d\delta_R} & \frac{d\dot{R}}{d\delta T} \\ \frac{d\dot{\phi}}{d\delta_A} & \frac{d\dot{\phi}}{d\delta_E} & \frac{d\dot{\phi}}{d\delta_R} & \frac{d\dot{\phi}}{d\delta T} \end{bmatrix} \begin{bmatrix} \delta_A \\ \delta_E \\ \delta_R \\ \Delta T \end{bmatrix} \tag{4.1.7}$$

Equation (4.1.7) can now be used to analyse the stability of the UAV. It contains all modifications done in Chapter 2 but represents it in a linear form.

4.2 Validity of Decoupling the Full Linear Model

As stated in the previous section, except for the diagonal reduction, most of the AEoM have been taken into account. After the linear system has been transformed into the form as described by equation (4.1.7), it is usually decoupled by some valid assumptions. These assumption may prove invalid due to the AEoM's ability to take into account a shift in CG , a change in inertia and the change in aerodynamic coefficients.

When implementing the relevant UAV data into the derivations done in Section 4.1, the effect on the A-matrix can be observed. Figure 4.1 shows the A-matrix for the 20% wing loss case. The rest of these matrices are available in Appendix D.

$$\begin{bmatrix} \dot{\bar{V}} \\ \dot{\alpha} \\ \dot{Q} \\ \dot{\theta} \\ \dot{\beta} \\ \dot{P} \\ \dot{R} \\ \dot{\phi} \end{bmatrix} = \begin{bmatrix} -0.03266 & 15.62679 & -0.21270 & -9.81035 & 0.65295 & -0.05653 & -0.03724 & 0.00275 \\ -0.06143 & -5.00303 & 1.09847 & -0.06606 & -0.00181 & 0.03981 & -0.00068 & 0.00041 \\ 0.00000 & -80.97873 & -8.93449 & -0.21742 & 0.00000 & -0.03738 & 0.00000 & 0.00000 \\ 0.00000 & 0.00000 & 1.00000 & 0.00000 & 0.00000 & 0.00000 & -0.00002 & 0.00000 \\ 0.00000 & 0.00213 & 0.00000 & -0.00000 & -0.23258 & 0.00061 & -0.99072 & 0.54503 \\ 1.65169 & -57.14095 & -1.53730 & -0.00020 & 1.02187 & -8.52884 & 0.38469 & -0.23565 \\ 0.02101 & 0.81990 & -0.12005 & 0.00374 & 20.51552 & -0.08199 & -1.17013 & 0.08632 \\ 0.00000 & 0.00000 & 0.00000 & 0.00000 & 0.00000 & 1.00000 & 0.12121 & 0.00000 \end{bmatrix} \begin{bmatrix} \bar{V} \\ \alpha \\ Q \\ \theta \\ \beta \\ P \\ R \\ \phi \end{bmatrix} +$$

$$\begin{bmatrix} 0.02071 & 0.75489 & -0.54849 & 0.16713 \\ -0.08441 & -0.68816 & 0.00078 & 0.00000 \\ -5.43897 & -113.58812 & 0.00000 & 0.00000 \\ 0.00000 & 0.00000 & 0.00000 & 0.00000 \\ 0.00521 & 0.00000 & 0.15103 & 0.00000 \\ -97.49427 & 3.86984 & -0.43832 & 0.00000 \\ -0.64618 & 0.12241 & -17.23328 & 0.04035 \\ 0.00000 & 0.00000 & 0.00000 & 0.00000 \end{bmatrix} \begin{bmatrix} \delta_{Ail} \\ \delta_{El} \\ \delta_{Rud} \\ T \end{bmatrix}$$

Figure 4.1 – Open-loop dynamics: 20% loss A-matrix

Over the range of 0 to 40% wing loss, it is apparent that some terms grow in value, while others shrink. This is expected as wing loss will have a greater effect in some directions and a smaller effect in others. What is concerning, is the sign change on the partial derivative of the change in yaw rate with regard to yaw rate ($\frac{d\dot{R}}{dR}$). Luckily this value is small relative to the others affecting yaw and should not be able to cause instability by itself.

It also becomes apparent that cross coupling starts to play a role from the initial loss point. It can however be noted that the longitudinal couples a lot more strongly into the lateral than vice versa. This observation can lead to the statement that the lateral coupling into the longitudinal is negligible but the longitudinal coupling into the lateral should be taken into account for the case of wing loss with this particular UAV.

The conclusion drawn from this is that the normal longitudinal dynamics can be decoupled from the lateral dynamics. This should allow the usual methods of design to provide fairly stable results, if the gains are kept in check. The lateral however will experience cross couple from the longitudinal dynamics and should be investigated more extensively.

4.3 Natural Modes and the Effect of Wing Loss

As the dynamics of the system can't be fully decoupled over the whole range of loss, the full dynamics pole plot is displayed in Figure 4.2. Figures 4.3 and 4.4 provide a view of what the poles would look like if decoupling could be done. This is done to provide a better understanding of the natural modes depicted in Figure 4.2.

When examining Figure 4.2 it is clear that none of the poles, which are originally stable, turn unstable as a result of partial wing loss. It is clear that one pole starts off unstable and stays unstable throughout partial wing loss. When observing all of the poles, only a slight increase or decrease in rate is observed, while a much larger increase or decrease in damping ratio is observed. In addition to this fact it is also observed that the poles near the $j\omega$ axis propagate away from it. The only group of poles moving towards the $j\omega$ axis are those at roughly $-11.8 rad.s^{-1}$. The fact that only one pair of poles moves towards the $j\omega$, while the rest move away is considered a very positive reaction to what was expected. Taking into account only the natural modes, it can be stated that this particular UAV should be fairly robust against partial wing loss, if it can handle the transition whilst acquiring the new trim.

After examining Figures 4.3 and 4.4 a better understanding of the effect on the natural modes can be obtained. The longitudinal modes can be identified as the groups of poles at roughly $-11.8 rad.s^{-1}$ and $-0.615 rad.s^{-1}$. The lateral modes can be identified as the groups of poles at roughly $-8.09 rad.s^{-1}$, $-4.19 rad.s^{-1}$ and $0.0576 rad.s^{-1}$. Tables 4.1 & 4.2 show the pole groups variation in both $rad.s^{-1}$ and damping ratio.

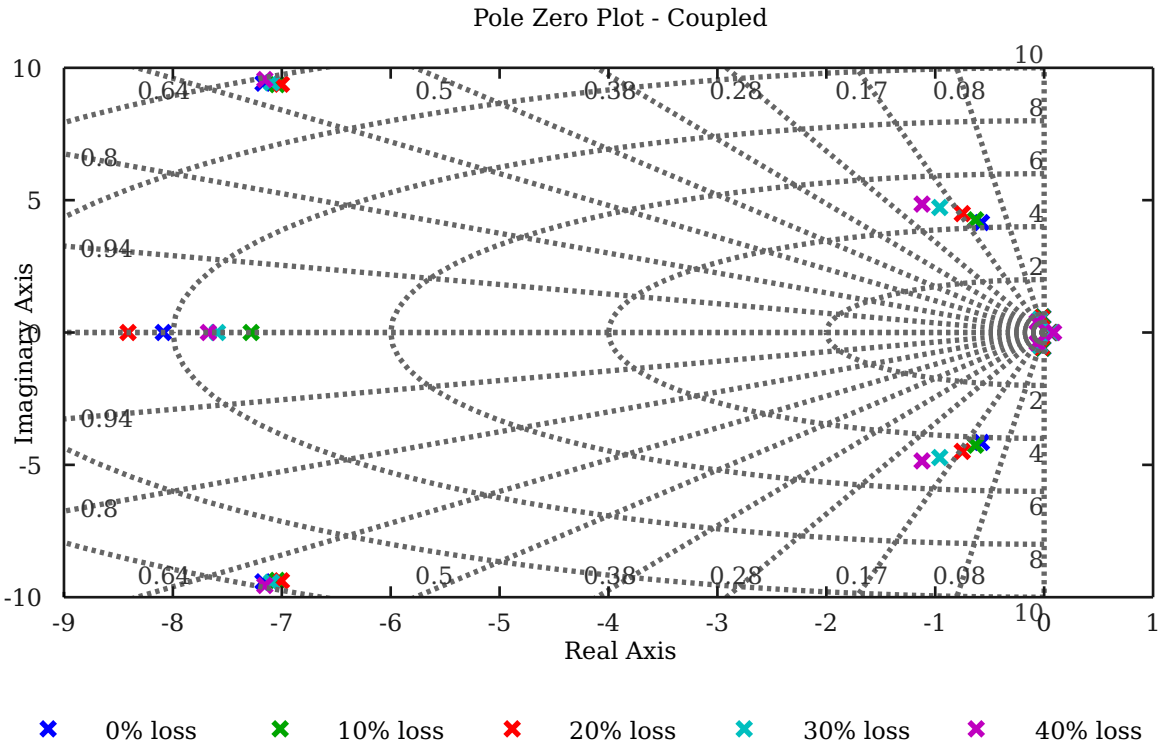

Figure 4.2 – Full Coupled Natural Modes

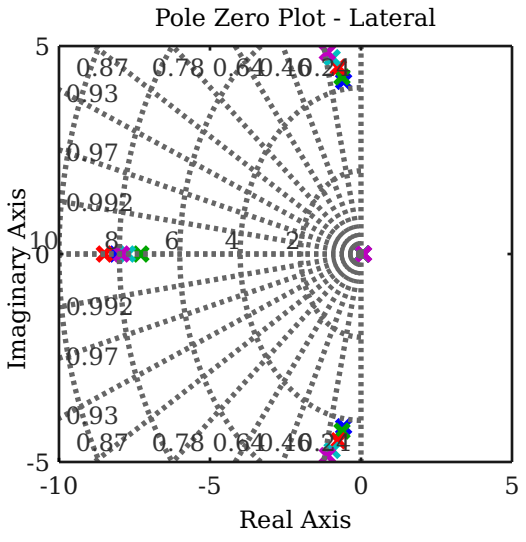

Figure 4.3 – Lateral Modes

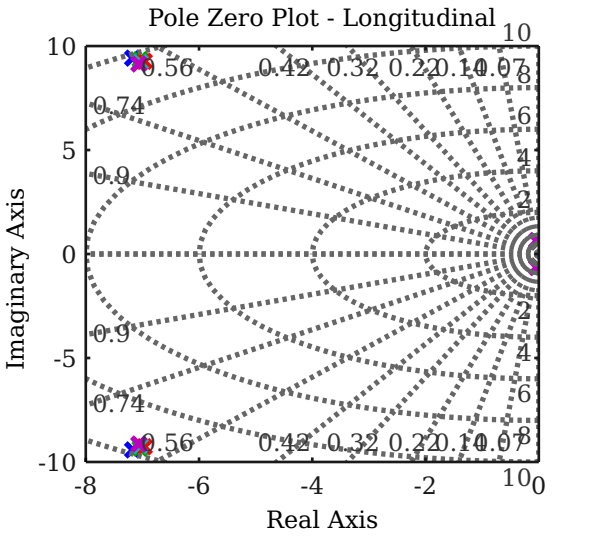

Figure 4.4 – Longitudinal Modes

When examining the values displayed in these tables, it almost seems that the UAV becomes more stable as wing loss progresses. The slow modes increase their speed and damping ratio, whereas the faster modes manifest an oscillatory nature around the nominal case. If we express these variations as percentages, the spiral mode results in the most drastic change with almost 50% increase in frequency. The Dutch Roll and Phugoid are second at roughly 20% increase. Lastly the Roll mode and Short period are at only 1% overall change. The spiral mode behavioural change makes perfect sense. As wing loss progresses,

loss	Pole ($rad.s^{-1}$)	ω_w	ζ
Dutch Roll Mode			
0%	-0.575 ± 4.15j	4.19	0.137
10%	-0.63 ± 4.26j	4.3	0.146
20%	-0.752 ± 4.49j	4.55	0.165
30%	-0.959 ± 4.72j	4.82	0.199
40%	-1.12 ± 4.85j	4.98	0.225
Roll Mode			
0%	-8.09	N/A	
10%	-7.28	N/A	
20%	-8.41	N/A	
30%	-7.59	N/A	
40%	-7.67	N/A	
Spiral Mode			
0%	0.0575	N/A	
10%	0.0616	N/A	
20%	0.0659	N/A	
30%	0.0728	N/A	
40%	0.0868	N/A	

Table 4.1 – Lateral Modes

loss	Pole ($rad.s^{-1}$)	ω_w	ζ
Phugoid			
0%	-0.0119 ± 0.589j	0.589	0.0202
10%	-0.0142 ± 0.587j	0.587	0.0243
20%	-0.023 ± 0.557j	0.557	0.0413
30%	-0.0398 ± 0.496j	0.498	0.0799
40%	0.0653 ± 0.394j	0.399	0.164
Short Period			
0%	-7.17 ± 9.42j	11.8	0.606
10%	-7.04 ± 9.37j	11.7	0.601
20%	-7 ± 9.38j	11.7	0.598
30%	7.09 ± 9.44j	11.8	0.601
40%	7.16 ± 9.56j	11.9	0.599

Table 4.2 – Longitudinal Modes

any disturbance will cause a lift imbalance on the UAV, which in turn will cause a rolling moment. As it is now not in equilibrium anymore, it will start to roll to one side and cause the UAV to enter a banked turn.

The Dutch Roll and Phugoid experiencing a frequency increase also makes sense. In the Dutch Roll mode, the one wingtip is now shorter. This implies that it is lighter and thus its inertia is less. On the other side, the longer wing has more drag at this stage and more lift. This will also cause it to respond faster, as lift usually has a bigger influence than drag at the airspeed the UAV is operating at. Regarding the Phugoid, as the UAV is a little bit lighter; it will manoeuvre a bit faster at the same airspeed.

The Roll mode's behaviour is a little unexpected. As one of the main coefficients affected by wing loss, it was suspected that this mode would show a relatively big change. It should be noted that the absolute change is still bigger than that experienced by any of the previous modes. This highlights the problem of just looking at percentage values. The modes which underwent the largest relative change are an order of magnitude smaller than the absolute change experienced by this mode. The same can be said for the Short period's behaviour.

As observing how the poles move as a function of partial wing loss is a very qualitative way of analysing robustness to parameter variation, a look will be taken in the next section at the Bode plots of the various transfer functions from the inputs to the outputs to determine how much open-loop gain and phase variation can be expected due to partial wing loss.

4.4 Stability Analysis

Gain margin and phase margin provide quantitative measures of robustness of a feedback loop to variations in gain and phase. The gain margin and phase margin are obtained by inspecting the Bode plot of the open-loop transfer function. Bode plots comprise of representing stability with magnitude and phase plots over frequency. One would usually describe the stability by the magnitude and phase margins acquired from values from the zero-crossing and $-180°$ boundaries. Due to this being an open-loop system with no control loops closed, the normal gain and phase margins cannot be used to determine the stability of the system. The variation in gain and phase, over all the cases of partial wing loss can however provide a feasible measure of how much gain and phase a controller should add to stay stable. The Bode plots of the open-loop transfer functions will be plotted for different percentages of partial wing loss, and the maximum variation in plant gain and plant phase will be determined. As this system has four inputs and eight states this amounts to an excessive number of figures and only some will be displayed here.

In this section the input to state output behaviour as listed below will be discussed with some plots displayed.

- Longitudinal inputs to Longitudinal states
  - Thrust to Airspeed
  - Elevator to Pitch
- Lateral inputs to Lateral states
  - Ailerons to Roll
  - Rudder to Yaw
- Longitudinal inputs to Lateral states
- Lateral inputs to Longitudinal states

4.4.1 Longitudinal Inputs to Longitudinal States

In this section various longitudinal inputs to longitudinal state outputs will be discussed. It should be noted beforehand that in general the magnitude increases with wing loss and the phase delay increases.

4.4.1.1 Thrust to Airspeed

The thrust to airspeed bode plot behaviour can be found in Figure 4.5. Due to the engine being situated in the x-axis of the body reference frame, is should not be adversely affected by wing loss. The magnitudes differ with 10dB at low frequencies over the 0 to 40% wing loss plants and only by 4.5dB for the higher range. The phases hardly differ from each other, except at the point where they suddenly change $180°$. As no real difference in behaviour is observed, it is believed that this controller should stay stable if it is provided with enough gain and phase.

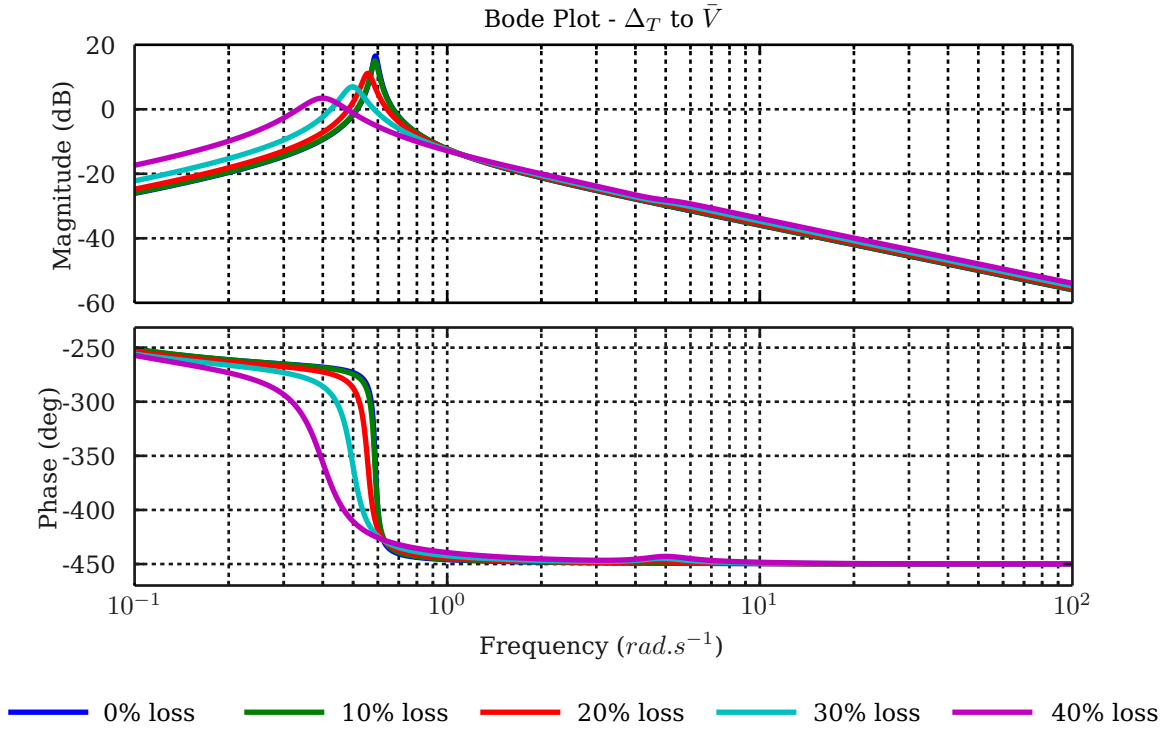

Figure 4.5 – Bode plot: Thrust to Airspeed Behaviour

4.4.1.2 Elevator to Pitch Rate

The elevator to pitch rate behaviour can be observed in Figure 4.6. It is clear that this behaviour is not really affected by wing loss. The low frequencies differ with 10dB in magnitude, while the higher frequencies differ only 1dB in magnitude. The phase ranges about $5°$ over most of the frequency range. It does however lead to a $180°$ drop at about the same frequencies as the thrust to airspeed. Taking this behaviour into account, it should also stay stable for most nominal case controller designs.

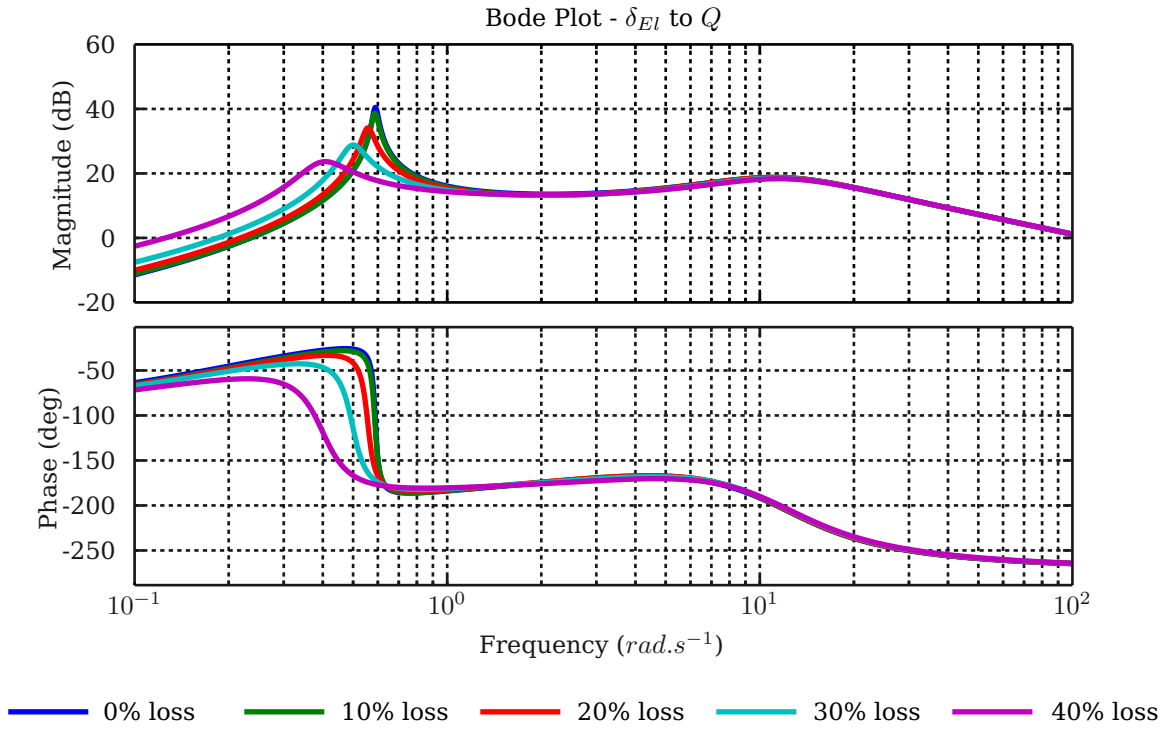

Figure 4.6 – Bode plot: Elevator to Pitch Behaviour

4.4.2 Lateral Input to Lateral State

In this subsection the various lateral inputs to lateral states will be discussed. It should be noted beforehand that rudder input bode magnitude increases with wing loss and the phase gets delayed and lowers. In the case of the ailerons, the bode magnitude decreases and the phase also lowers.

4.4.2.1 Ailerons to Roll Rate

The ailerons to roll rate behaviour is depicted in Figure . As pointed out earlier in this section, the effect of the ailerons on roll rate should show a noticeable difference as part of the actuating surface is lost along with the wing. As can be seen in Figure 4.7, the magnitudes differ with roughly 4dB over most of the frequency range. The phases however differ with $15°$ and show a dip of roughly $70°$ at the same frequencies as the above presented bodes. As an acceptable phase margin is usually $30°$ of phase, this should not pose too much of a problem in design but should be taken into account. The dip of $70°$ in response is a reason for concern at this stage but does not cross a zero or $180°$ phase line.

4.4.2.2 Rudder to Yaw Rate

The rudder to yaw rate behaviour is shown in Figure 4.8. The physical rudder surface is not primarily affected by wing loss and thus the behaviour should also stay unaffected. This does seem to be the case as the magnitude only differs between 6 and 3dB from low to high frequencies. The phases start off with a $30°$ difference and decreases to only $5°$ towards the higher frequencies. A $180°$ drop in phase response is observed at frequencies 10 times faster than the previous bodes. As the differences in values are fairly small, except for the phase at lower frequencies, it is believed that a controller or compensator affecting this plant should stay stable.

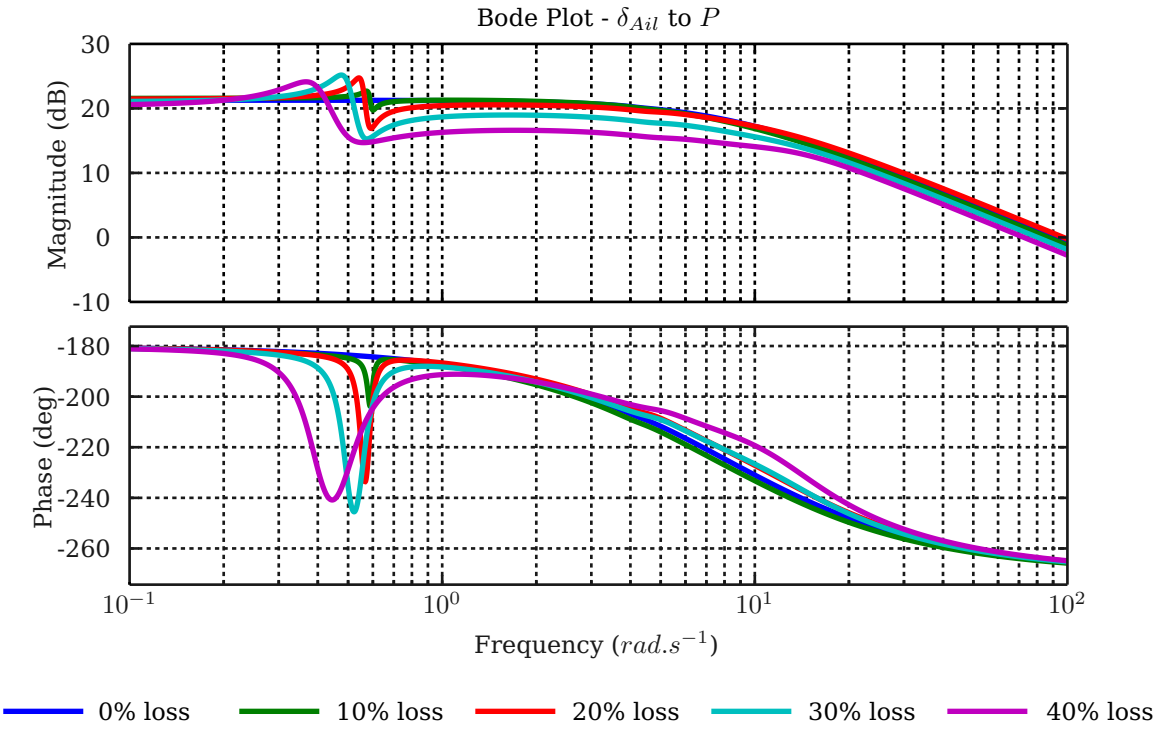

Figure 4.7 – Bode plot: Ailerons to Roll Behaviour

4.4.3 Longitudinal Inputs to Lateral State Outputs

The longitudinal inputs to lateral states are usually assumed to have very little effect on a symmetric system and are removed. As this system is asymmetric after the incident of partial wing loss, some of these inputs will in fact affect the behaviour of the UAV. The longitudinal inputs to lateral state outputs are listed below. Negligible gain refers to an input to output response below 0dB. This response is naturally suppressed by the plant and can be viewed as a decoupled input-output pair. Small gain variation refers to a response where the gain itself does not vary with more than 20dB over all the partial wing loss cases. Large gain variation refers to a response with more than 20dB change in gain and could possibly cause unwanted cross-coupling effects.

Negligible gain	**Small gain variation**	**Large gain variation**
• Thrust to Roll Rate	• Thrust to Yaw Rate	• Elevator to Roll Rate
	• Thrust to Bank Angle	• Elevator to Yaw Rate

When looking at the list above, it is already clear that the elevator will couple into the lateral dynamics, with very little effect from the thrust. Initially the behaviour is quite low and ranges around the same magnitude levels as the aileron input to specific lateral state. This however changes as partial wing loss increases. At low frequencies the magnitude differs by roughly 20dB, while at higher frequencies this difference is reduced to about 10dB. The behaviour of the elevator input to roll state output can be observed in Figure 4.9. As the rest of the elevator inputs resemble this response, they will be left out and are available for viewing in Appendix E.1. The effect of the elevator coupling into the lateral states should thus be examined during or after controller design. As the thrust couples only slightly into the lateral states, it is hypothesised that its effect can be left out during control design on these lateral states.

4.4.4 Lateral Inputs to Longitudinal States

The lateral input to longitudinal states are usually assumed to be very small and left out. As stated in the previous section this may not be the case in an asymmetric setup and they should be examined. As done in the previous section, these input to output pairs will again be categorised in negligible gain, small gain variation and large gain variations groups and displayed in the following list.

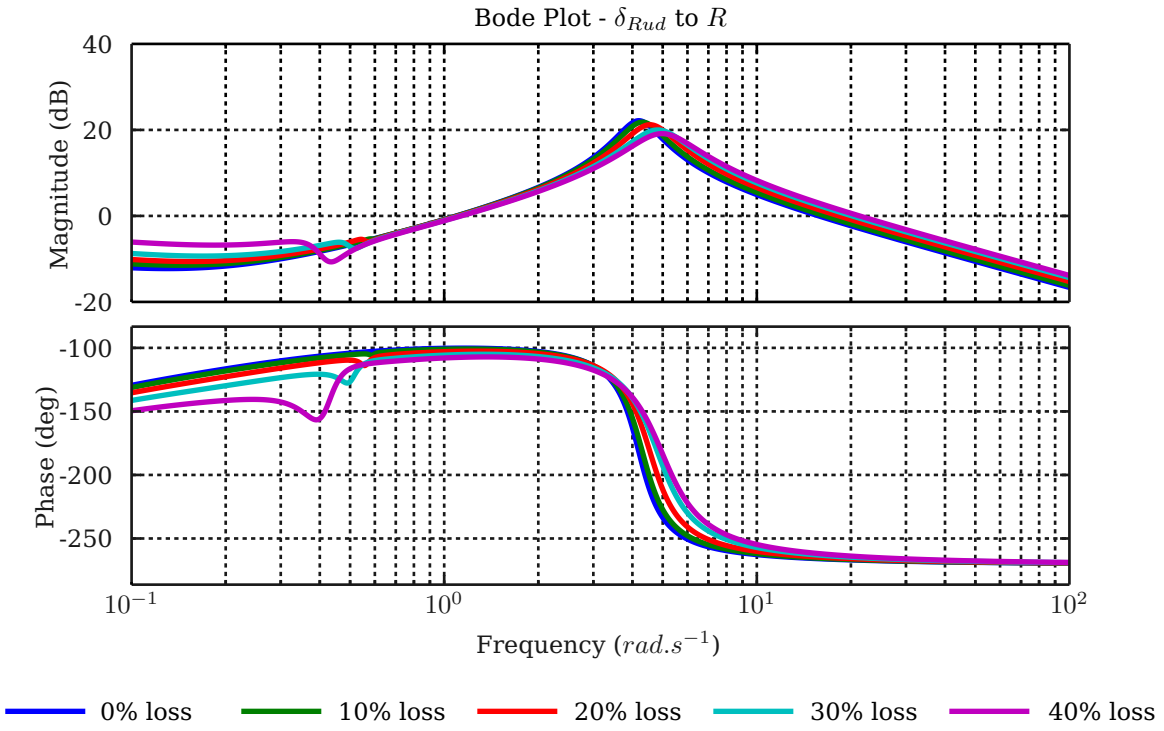

Figure 4.8 – Bode plot: Rudder to Yaw Behaviour

Negligible gain	**Small gain variation**	**Large gain variation**
• Rudder to Airspeed	• Ailerons to Pitch Rate	• Ailerons to Airspeed
• Rudder to Pitch Rate		

With regard to the list above, it is clear that the lateral inputs do not really couple into the longitudinal states. The negligible gain group is well below 0dB in most cases and can be assumed decoupled due to the input to state output relation being naturally suppressed in the plant. The only really important input to output pair here is the ailerons to airspeed. This input to output pair starts with a 10dB difference and ends with roughly a 20dB difference. This input to output pair could cause come unwanted cross-coupling and should be checked after the addition of control architectures. The behaviour described above can be observed in Figure 4.10.

4.5 Chapter Summary and Conclusion

In this chapter the linearisation of the full non-linear dynamics was described, scripted and implemented. In the linearisation process it was noted that most of the off-diagonal terms of the inverse matrix described in equation (2.3.25), are at least a factor 10 smaller than the diagonal terms. This was true for all the cases from 0 to 40% wing loss and enables the reduction of this matrix to a diagonal one with only four off-diagonal terms.

Next the validity of decoupling the system was discussed. At this stage it became clear that decoupling holds for the longitudinal dynamics but not the other way around. This led to the effect of wing loss on the poles and natural modes of the UAV which clarified that if the mode was stable to begin with, it stays stable. The Dutch roll mode increased both its frequency and damping, while the Phugoid decreased both. The short period increases its frequency, while decreasing its damping and lastly the Roll mode oscillated around its nominal frequency, while the Spiral mode increases its frequency.

Lastly the variation in plant gain and phase was analysed by looking at the Bode plots of the open loop dynamics. The maximum variation will be used as a guideline for the required gain and phase margins to be designed for in order to ensure robustness. It was concluded that the behaviour of the general longit-

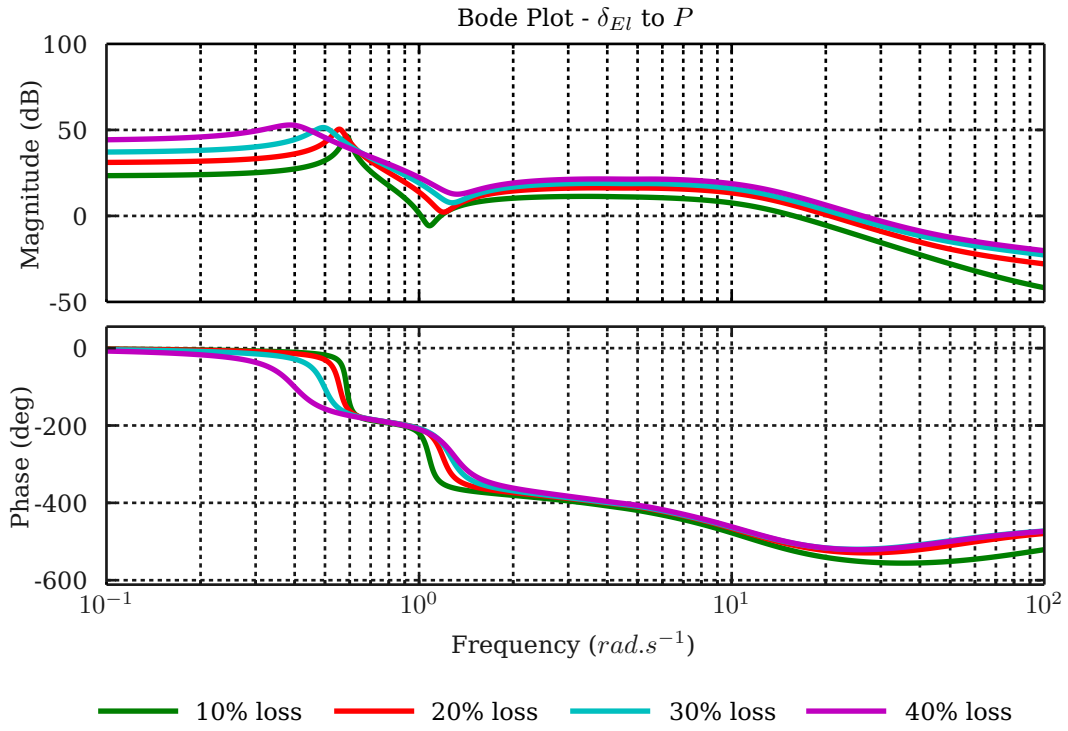

Figure 4.9 – Elevator to Roll

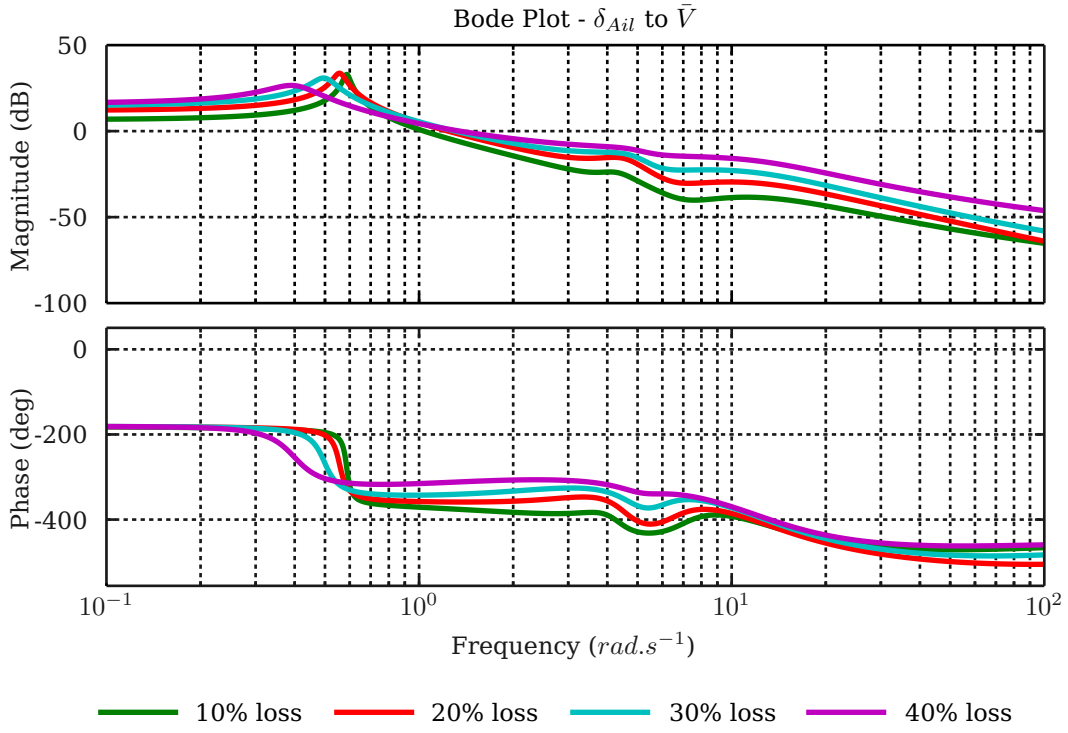

Figure 4.10 – Ailerons to Airspeed

udinal to longitudinal and lateral to lateral input to state output transfers do no change dramatically. The coupling terms however do depict significant differences in magnitude response and in some cases phase response. Except for the ailerons to airspeed, the longitudinal states' behaviours are not influenced much by the lateral inputs. The lateral states' behaviour are however significantly affected by the longitudinal elevator input but not the thrust.

Chapter 5

Controller Design

In this chapter, the design and implementation of two different flight control architectures are described. Both control system designs are analysed and tested in simulation to evaluate their performance and robustness to partial wing loss. Neither of the controllers adapt to the changes caused by the aircraft damage, but are rather designed to be robust, non-adaptive controllers. The first set of controllers will be constructed with classic control theory, built on the basic theory of root locus design found in [20]. The second set will be constructed using acceleration based control, as formulated in [1]. The analyses of the classical controllers and the acceleration-based controllers show that both architectures already exhibit sufficient robustness to the partial wing loss. The final controller that will be implemented, simulated and flight-tested is then constructed as a hybrid of the classical and acceleration-based architectures.

5.1 Classical Aircraft Control

In this section a classic approach to aircraft controller design will be implemented on the UAV. Taking into account that the controllers will not be aware of the damage that has occurred, the design will assume the classical decoupled longitudinal and lateral plants. The longitudinal controllers usually consist of a pitch rate damper (PRD), an airspeed and climb rate controller (ASCRC) and an attitude controller (AtC). The lateral controllers usually consist of a Dutch roll damper (DRD), a roll angle controller (RAC) and a heading controller (HC). The basic concept for this implementation can be found in [12] and [13].

A slight alteration has been made to the longitudinal control set. The MIMO ASCRC has been separated into two controllers. The reason behind this decision is the practical aspects of properly tuning a MIMO controller. In this case, the classic control will not be flight tested but will still adhere to the general specifications of the designs. This should allow a clearer measure of robustness and performance when comparing the different control sets.

The root locus design method is used for most of the controllers. This method alters the root locus with pole and zero placements to acquire the desired response. Two equations are of importance when implementing this method: the angle and magnitude criteria.

$$\sum_{i=1}^{n} \angle (s - z_i) - \sum_{i=1}^{m} \angle (s - p_i) = \pm 180^\circ (2q + 1) \tag{5.1.1}$$

$$\frac{\prod_{i=1}^{m} (s - p_i)}{\prod_{i=1}^{n} (s - z_i)} = K \tag{5.1.2}$$

By using equations (5.1.1) and (5.1.2), the controller transfer function can be designed to obtain the desired dominant closed-loop poles. In most cases it will be necessary to reshape the root locus with a controller so that is passes through the desired closed-loop poles. In these designs, PI control will be implemented to improve the steady state errors. This leaves two uncertainties within these criteria, the position of the integrator zero and the total loop gain, which can easily be determined.

5.1.1 Decoupling

As mentioned in Section 4.2, the assumptions on which decoupling of the lateral and longitudinal dynamics are based do not hold for the lateral case once loss has occurred. This may cause stability issues with the designed controllers. As stated at the beginning of this section, the controller will not be explicitly

aware of the damage that has occurred and because of this the initial designs will be done on the nominal decoupled system. This will provide a basis for the analysis of the stability of the classically designed aircraft control system.

Decoupling the system under the nominal assumptions of symmetry and small cross-coupling terms results in equations (5.1.3) & (5.1.4). If, at any stage in this section mention is made of the decoupled plants this will refer back to these two equations.

$$\begin{bmatrix} \dot{\bar{V}} \\ \dot{\alpha} \\ \dot{q} \\ \dot{\theta} \end{bmatrix} = \begin{bmatrix} \frac{d\dot{U}}{d\bar{U}} & \frac{d\dot{U}}{dW}\bar{V} & \frac{d\dot{U}}{dQ} & \frac{d\dot{U}}{d\Theta} \\ \frac{d\dot{W}}{d\bar{U}}\frac{1}{\bar{V}} & \frac{d\dot{W}}{dW} & \frac{d\dot{W}}{dQ}\frac{1}{\bar{V}} & \frac{d\dot{W}}{d\Theta}\frac{1}{\bar{V}} \\ \frac{d\dot{Q}}{d\bar{U}} & \frac{d\dot{Q}}{dW}\bar{V} & \frac{d\dot{Q}}{dQ} & \frac{d\dot{Q}}{d\Theta} \\ \frac{d\dot{\Theta}}{d\bar{U}} & \frac{d\dot{\Theta}}{dW}\bar{V} & \frac{d\dot{\Theta}}{dQ} & \frac{d\dot{\Theta}}{d\Theta} \end{bmatrix} \begin{bmatrix} \bar{V} \\ \alpha \\ q \\ \theta \end{bmatrix} + \begin{bmatrix} \frac{d\dot{U}}{d\delta_E} & \frac{d\dot{U}}{d\delta T} \\ \frac{d\dot{W}}{d\delta_E}\frac{1}{\bar{V}} & \frac{d\dot{W}}{d\delta T}\frac{1}{\bar{V}} \\ \frac{d\dot{Q}}{d\delta_E} & \frac{d\dot{Q}}{d\delta T} \\ \frac{d\dot{\Theta}}{d\delta_E} & \frac{d\dot{\Theta}}{d\delta T} \end{bmatrix} \begin{bmatrix} \delta_E \\ \Delta T \end{bmatrix} \tag{5.1.3}$$

$$\begin{bmatrix} \dot{\beta} \\ \dot{p} \\ \dot{r} \\ \dot{\phi} \end{bmatrix} = \begin{bmatrix} \frac{d\dot{V}}{dV} & \frac{d\dot{V}}{dP}\frac{1}{\bar{V}} & \frac{d\dot{V}}{dR}\frac{1}{\bar{V}} & \frac{d\dot{V}}{d\Phi}\frac{1}{\bar{V}} \\ \frac{d\dot{P}}{dV}\bar{V} & \frac{d\dot{P}}{dP} & \frac{d\dot{P}}{dR} & \frac{d\dot{P}}{d\Phi} \\ \frac{d\dot{Q}}{dV}\bar{V} & \frac{d\dot{Q}}{dP} & \frac{d\dot{Q}}{dR} & \frac{d\dot{Q}}{d\Phi} \\ \frac{d\dot{\Phi}}{dV}\bar{V} & \frac{d\dot{\Phi}}{dP} & \frac{d\dot{\Phi}}{dR} & \frac{d\dot{\Phi}}{d\Phi} \end{bmatrix} \begin{bmatrix} \beta \\ p \\ r \\ \phi \end{bmatrix} + \begin{bmatrix} \frac{d\dot{V}}{d\delta_A}\frac{1}{\bar{V}} & \frac{d\dot{V}}{d\delta_R}\frac{1}{\bar{V}} \\ \frac{d\dot{P}}{d\delta_A} & \frac{d\dot{P}}{d\delta_R} \\ \frac{d\dot{R}}{d\delta_A} & \frac{d\dot{R}}{d\delta_R} \\ \frac{d\dot{\Phi}}{d\delta_A} & \frac{d\dot{\Phi}}{d\delta_R} \end{bmatrix} \begin{bmatrix} \delta_A \\ \delta_R \end{bmatrix} \tag{5.1.4}$$

The modes of the longitudinal and lateral decoupled systems with reference to aircraft specific data are represented in Figures 5.1 and 5.2.

Longitudinal Mode Poles:

- -7.1972 + 9.4314i
- -7.1972 - 9.4314i
- -0.0086 + 0.5875i
- -0.0086 + 0.5875i

Lateral Mode Poles:

- -8.0880
- -0.5755 + 4.1527i
- -0.5755 - 4.1527i
- 0.0575

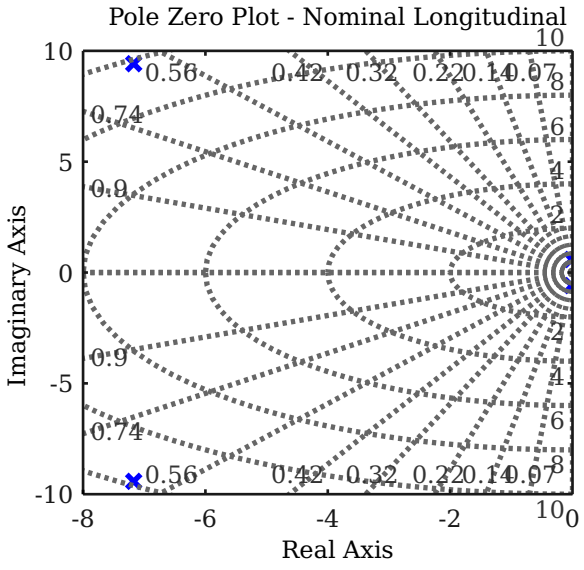

Figure 5.1 – Longitudinal Mode Poles

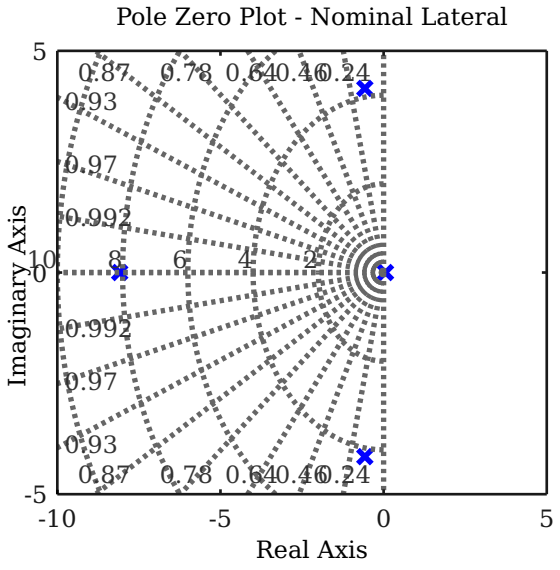

Figure 5.2 – Lateral Mode Poles

5.1.2 Longitudinal Control

5.1.2.1 Pitch Rate Damper

The function of the PRD is to add artificial damping to the aircraft's pitch rate and a diagram can be found in Figure 5.3. This artificial damping is usually done by increasing the short period mode's damping with

a gain in the feedback loop from pitch rate (q) to elevator deflection (δ_{El}). With regard to the longitudinal plant, found in the transfer function specified by equation (5.1.5), the unmodified plant's short period damping equals 0.6, which is fairly close to optimal.

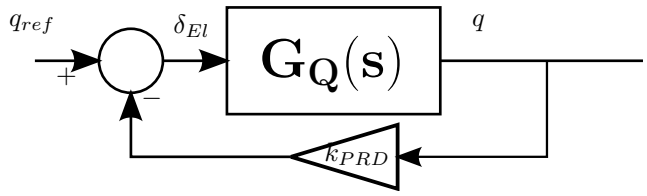

Figure 5.3 – Classic Controller: PRD

$$G_{PR}(s) = -113.6167\frac{s(s+4.969)(s+0.2156)}{(s^2+0.01854s+0.3443)(s^2+14.44s+142.6)} \tag{5.1.5}$$

When improving equation (5.1.5)'s damping, the system will be augmented with an in-loop feedback gain from q to δ_{El}. The gain can now be determined with specifications of $\zeta = 0.707$ and the same natural frequency by applying the magnitude criterion. This results in a controller gain of

$$k_{PRD} = -0.0278 \tag{5.1.6}$$

As this gain is so small, it may be regarded as negligible and rather left out to avoid unnecessary computation.

5.1.2.2 Airspeed and Climb Rate Controller

As explained at the beginning of Section 5.1, the airspeed and climb rate controller will be implemented as two separate controllers. An augmented PI control will be implemented as the airspeed controller based on the one found in Ruan De Hart's Thesis [21]. The control structure is based on the forces acting in on the aircraft in the x-axis. The effect of gravity is removed through feedback linearisation. The controller is then implemented as depicted in Figure 5.4 with direct feedback of the aircraft's velocity and also the integral of the error between the commanded and actual velocity.

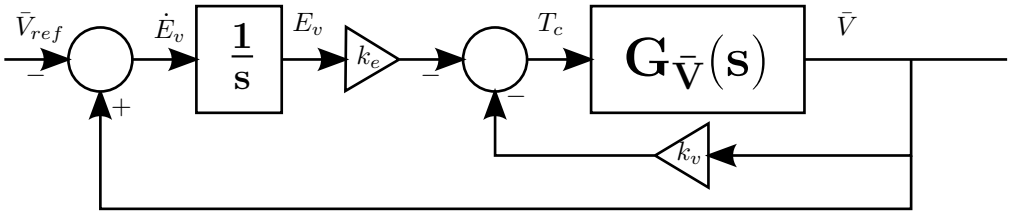

Figure 5.4 – Classic Controller Augmentation: Airspeed

Equations (5.1.7) and (5.1.8) are used to calculate the gains with which both the velocity and error will be fed back.

$$k_v = m\tau_T\left[\left(1-4\zeta_v^2\right)\omega_v^2 + \frac{2\zeta_v\omega_v}{\tau_t}\right] \tag{5.1.7}$$

$$k_e = m\tau_T\left(\frac{1}{\tau_T} - 2\zeta_v\omega_v\right)\omega_v^2 2\zeta_v\omega_v^2 \tag{5.1.8}$$

$\omega_v = \frac{1}{2\tau_T}$ which ensures that the complex poles will be slower than the real ones and the damping ζ_v is

chosen as optimal. Using the engine constant of $\tau = 0.25$ with optimal damping resulted in the following values for k_v and k_e

$$k_v = 11.52 \tag{5.1.9}$$

$$k_e = 7.384 \tag{5.1.10}$$

At this stage the climb rate controller can be implemented on the augmented airspeed controlled system. Climb rate can be estimated from the longitudinal dynamics as $\dot{h} = -\bar{V}_T\alpha + \bar{V}_T\theta$. Thus, the δ_{El} input to climb rate output transfer function can be represented by equation (5.1.11).

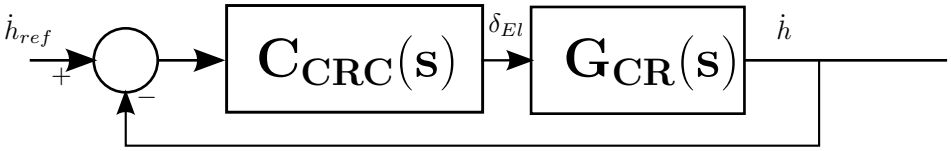

Figure 5.5 – Classic Controller: Climb Rate

$$G_{CR}(s) = -11.9022\frac{(s+46.38)(s-19.34)(s+1.932)}{(s+1.729)(s+0.1484)(s^2+17.66s+159.1)} \tag{5.1.11}$$

A climb rate controller with zero steady state error can be implemented with an integrator and a gain. Using the criteria specified in equations (5.1.1) and (5.1.2) with optimal damping and a settling time of 2 seconds, resulted in the controller described in equation (5.1.12).

$$C_{CR} = -0.030989\frac{(s+0.6777)}{s} \tag{5.1.12}$$

It should be noted that these two controllers are closely coupled. A rise in airspeed will automatically induce a climb rate and vice versa. Due to this fact, the designed decoupled responses will differ from the actual coupled implementation. Implementing this separate design leads to an airspeed response of less than 2% overshoot and settles in 4.2 seconds, while the climb rate response has 15% overshoot and settles in 4 second.

5.1.2.3 Altitude Controller

In designing the altitude controller, proportional control will be used on the system, as specified by equation (5.1.13).

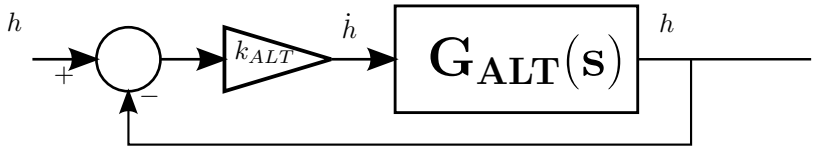

Figure 5.6 – Classic Controller: Altitude

$$G_{ALT}(s) = -0.38199\frac{(s+46.38)(s-19.34)(s+0.5522)(s^2+1.932s+1.179)}{s(s^2+1.202s+0.4972)(s^2+3.616s+4.307)(s^2+14.33s+104.2)} \tag{5.1.13}$$

The natural integration from climb rate to altitude makes the system type 1, which means it should be able to follow a constant altitude reference with zero error at steady state. This is supported by the airspeed and climb rate controllers which are equipped with integrators and thus ensure zero steady state error. The reasoning behind this is that if airspeed and climb rate are followed with zero error, an altitude reference change will also be followed with zero steady state error. Using the criteria specified in equations (5.1.1) and (5.1.2), with optimal damping and a settling time of 10 seconds, resulted in a gain of $k_{ALT} = 0.4$.

5.1.3 Lateral Control

5.1.3.1 Dutch Roll Damper (DRD)

A Dutch roll damper is usually implemented due to the lightly damped nature of the Dutch roll mode on most aircraft [12]. The DRD will be implemented with a washout filter (high pass filter) in the loop between yaw rate output and the rudder input as depicted in Figure 5.7. This loop's transfer function can be represented by equation (5.1.14).

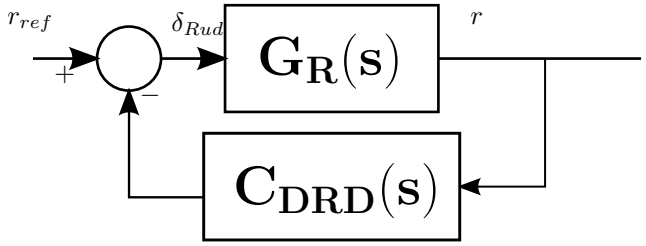

Figure 5.7 – Classic Controller: DRD

$$G_{DR}(s) = -14.7133\frac{(s+8.089)(s+0.1843)(s-0.1296)}{(s+8.088)(s-0.05755)(s^2+1.151s+17.58)} \tag{5.1.14}$$

This is done to reject high frequency perturbations, which are usually disturbances, and allow low frequency perturbations, which are usually commands issued by either the pilot or control system. A general approach uses a scaled version of the DRD natural frequency for the filter's cut-off point. Using a scaling for the cut-off as $\tau_{DR} = 0.5\frac{2\pi}{\omega_{DR}} = 0.7494$ resulted in a gain of $K_{DR} = 0.6824$. This leads to rather excessive rudder usage and the gain was deceased to $K_{DR} = 0.2730$. Although the decrease in gain caused a slower response, the reason behind the DRD is not speed improvement but damping and thus the response was found to be sufficient without using too much control. The controller can thus be defined by,

$$C_{DRD}(s) = -0.2730\frac{s}{s+1.334} \tag{5.1.15}$$

5.1.3.2 Roll Angle Controller (RAC)

This controller will be implemented on the aileron input, with feedback from the current roll angle. Its transfer function is represented by equation (5.1.16).

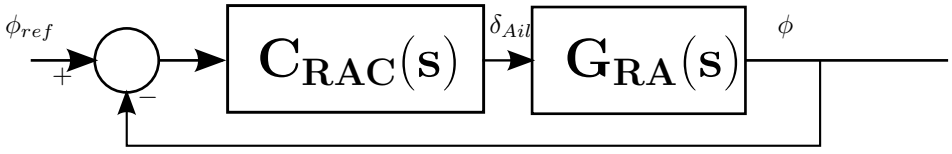

Figure 5.8 – Classic Controller: RAC

$$G_{RA}(s) = -93.5431\frac{(s+2.5)(s^2+3.932s+9.361)}{(s+8.087)(s+2.412)(s-0.05771)(s^2+4.091s+9.699)} \tag{5.1.16}$$

It is desired that the roll angle be followed without any steady state error and it will thus be implemented with PI control. Using the criteria specified in equations (5.1.1) and (5.1.2), with optimal damping and a settling time of 1.5 seconds, results in,

$$C_{RAC}(s) = -0.26401\frac{(s+0.9211)}{s} \tag{5.1.17}$$

5.1.3.3 Heading Controller

The heading controller controls the heading of the UAV by closing a loop from the heading output to the roll angle input. The transfer function can be represented by equation (5.1.18).

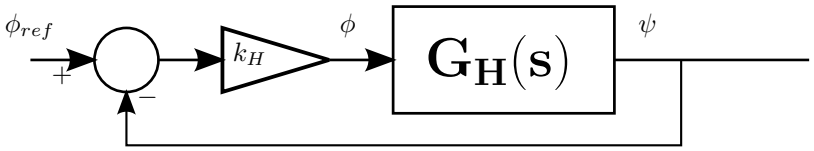

Figure 5.9 – Classic Controller: Heading

$$G_H(s) = 24.6964\frac{(s+2.5)(s+0.9211)(s^2+3.932s+9.361)}{s(s+3.173)(s+1.498)(s^2+3.627s+7.353)(s^2+6.234s+15.23)} \tag{5.1.18}$$

Due to the PI controller used in the RAC to ensure zero steady state error and the natural integrator from heading rate to heading, the heading controller can be implemented using a proportional controller. The heading controller should follow a desired heading within 7.5 seconds and without any overshoot. Using the magnitude criterion, equation (5.1.2), with these specifications, the gain needed is,

$$k_H = 0.6196 \tag{5.1.19}$$

This results in a settling time of 6.9 seconds with zero overshoot.

5.1.4 Control Analysis with Partial Wing Loss

In this section the controllers designed in both Sections 5.1.2 and 5.1.3 will be analysed according to their responses in different wing loss scenarios. This will include pole, bode and step response plots up unto the maximum trimmable point at which the wings can't generate enough lift to keep the UAV in the air. All pole and response plots are done at a trim speed of $18m.s^{-1}$. Responses are induced with a step input of either 1° or $1m.s^{-1}$. All plots include data from 0 to 40% wing loss, displayed in increments of 10% loss increase.

5.1.4.1 Longitudinal Controller Poles and Responses

PRD

From Figures 5.10 to 5.11, it can be seen that the compensated plants closely resemble each other. The poles mostly stay on the same frequency band, with just a slight change in damping ratio. This is also clear from the step responses, where the behaviours of the controller do not vary by much. In general, this is a good sign as the necessary commanded pitch rate will be accomplished in every case of wing loss. Figure 5.12 shows the bode plot of the implemented PRD. It suppresses the response by roughly 30dB. As this compensator should only add a little damping, it is expected that it will suppress unwanted disturbances. This suppression on eigenvalue state initialisation is clearly visible in Figure 5.11.

Airspeed

When examining the airspeed compensated plant (Figure 5.14 and 5.15), it can be seen that the poles hardly change in both damping and natural frequency. A little less thrust is however needed to achieve the same effect. This might seem odd at first but referring back to Section 3.5, it is the result we expect. All trim solutions pointed to less thrust being used. As the thrust to airspeed variables are not primarily affected by wing loss, the miniscule change in response is also as expected. The Bode plot of this plant is available in Figure 5.13. It provides roughly 47.5° of phase margin and a gain margin of 5.6dB. The overall change in magnitude and phase is small compared to the gain and phase margins, with only a 2dB change in magnitude and 7° change in phase.

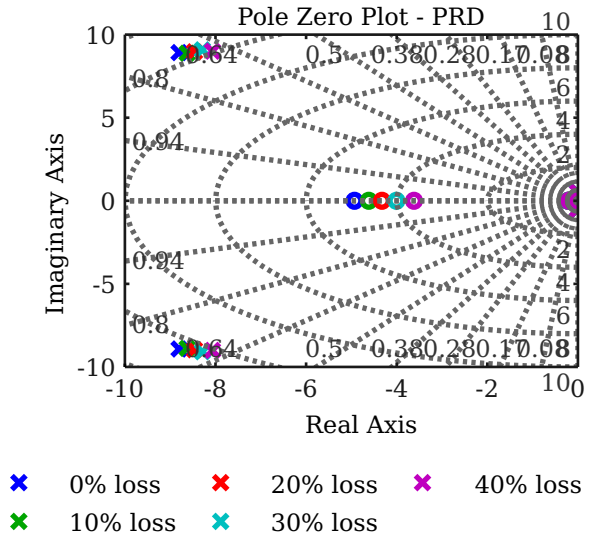

Figure 5.10 – Classic Control - Longitudinal - Poles - PRD

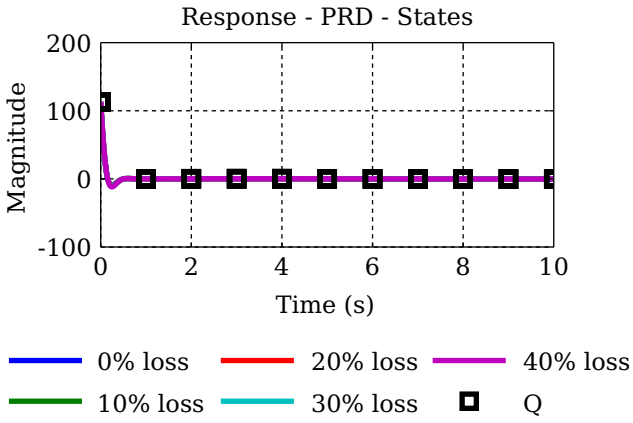

Figure 5.11 – Classic Control - Longitudinal - Response - PRD

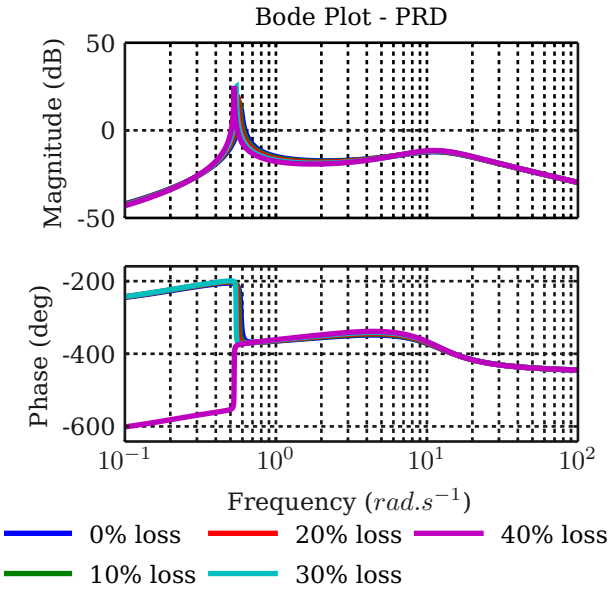

Figure 5.12 – Classic Control - Bode - PRD

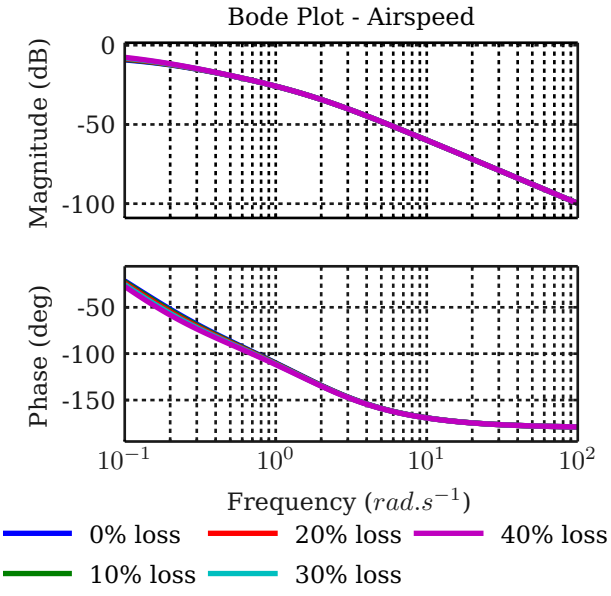

Figure 5.13 – Classic Control - Bode - Airspeed

Climb Rate

When examining the climb rate compensated system (Figures 5.18 and 5.19), the same effects as described for the airspeed compensator are observed. The climb rate poles do experience a larger change in natural frequency than that of the airspeed poles but overall they have roughly the same damping. This is also supported by the response plotted in Figure 5.20. When analysing the controller's Bode plot as displayed in Figure 5.22, a worrisome feature presents itself, namely multiple $-180°$ crossings. The usual Bode analysis assumes one crossing and thus conventionally will lead to the conclusion that the plant is unstable.

According to [22] the above statement actually does not mean that the plant is unstable but only points to the lack of ability of the Bode analysis to determine if it is indeed stable. At this stage it becomes necessary to use the Nyquist stability criterion to determine stability as the Bode analysis can easily provide the wrong conclusion on stability. Nyquist states that critical point $0j - 1$ should not be clockwise encircled by

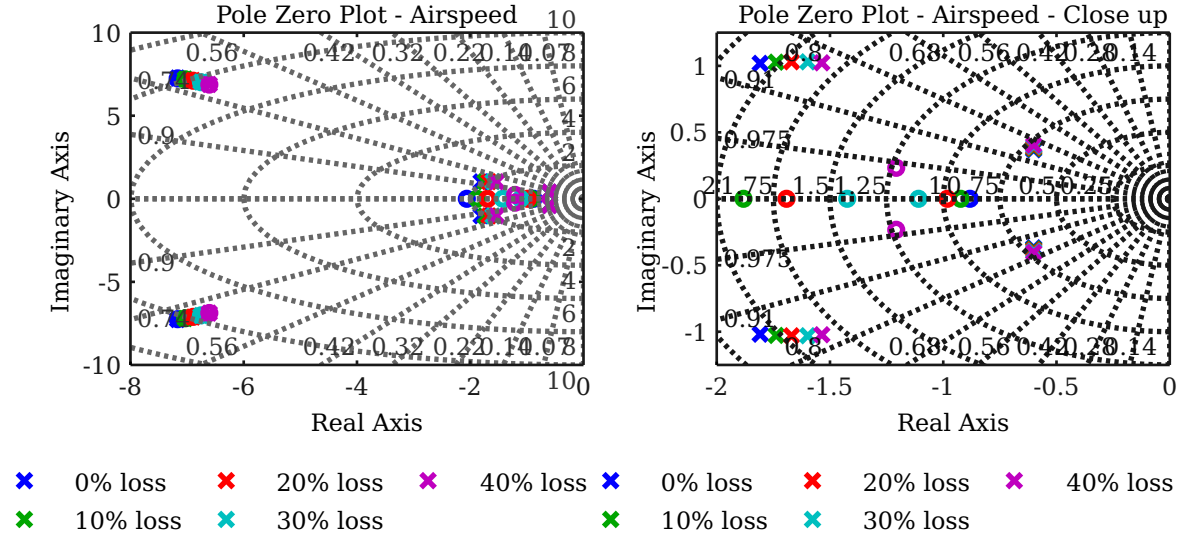

Figure 5.14 – Classic Control - Longitudinal - Poles - Airspeed Control

Figure 5.15 – Classic Control - Longitudinal - Poles - Airspeed Control - Close up Version

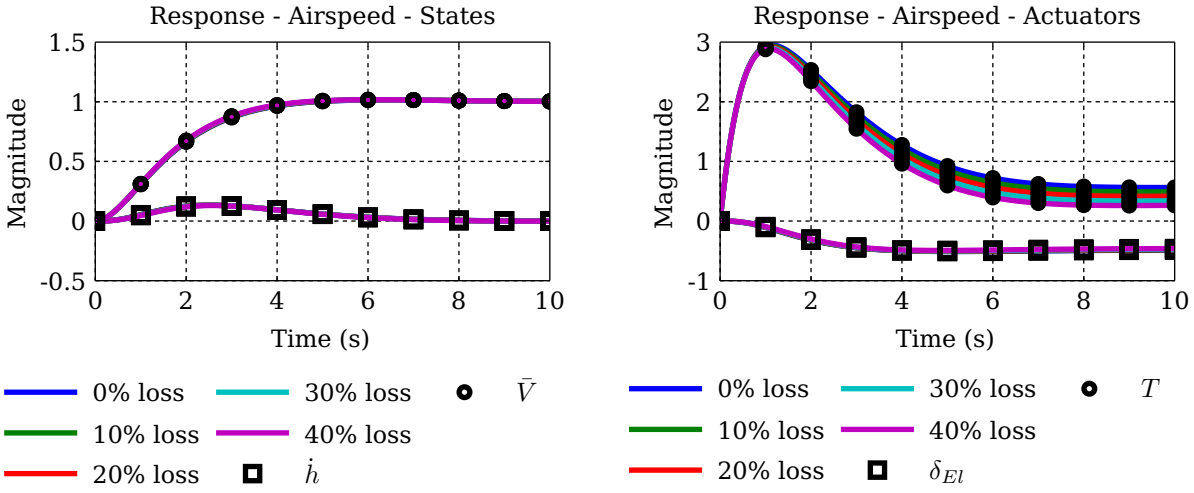

Figure 5.16 – Classic Control - Longitudinal - Response - Airspeed

Figure 5.17 – Classic Control - Longitudinal - Actuators - Airspeed

the plant's open-loop Nyquist contour in the s-plane. In addition to no clockwise encirclements, the critical point should be counter-clockwise encircled as many times as there are poles in the right half plane (RHP) of the open-loop system. Figure 5.23 shows the Nyquist plot of the plant encircling the critical point counter-clockwise. Although it has not been stated earlier, the climb-rate augmented output places an open-pole in the RHP, which warrants the counter-clockwise encirclement. As this encirclement passes to the left side of the critical point, it is concluded that this plant will be closed-loop stable for all cases of wing loss. When using Figure 5.22, the magnitude margin is 13.8dB with 1.5dB variation, while the phase margin is $58.3°$ with $9.2°$ variation.

Altitude

When examining the altitude compensated plant represented in Figure 5.24 is a bit harder than the rest. The dominant effects are produced by a combination of complex pole pairs, a real pole and zero. The major problem with this plant is the zero which restricts the plant's response. It causes a fast rise time but

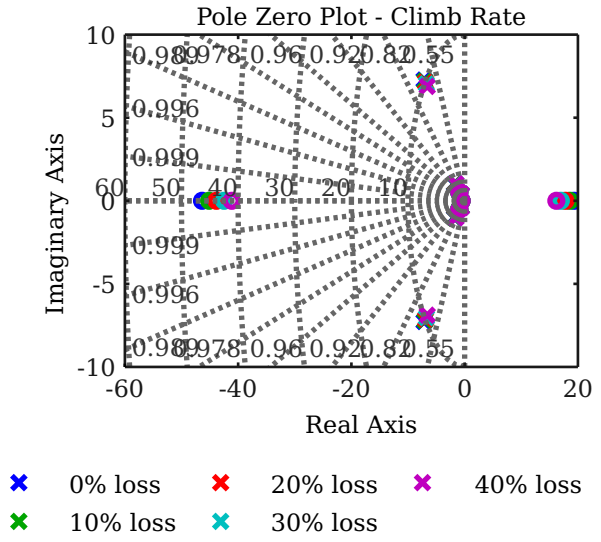

Figure 5.18 – Classic Control - Longitudinal - Poles - Climb rate Control

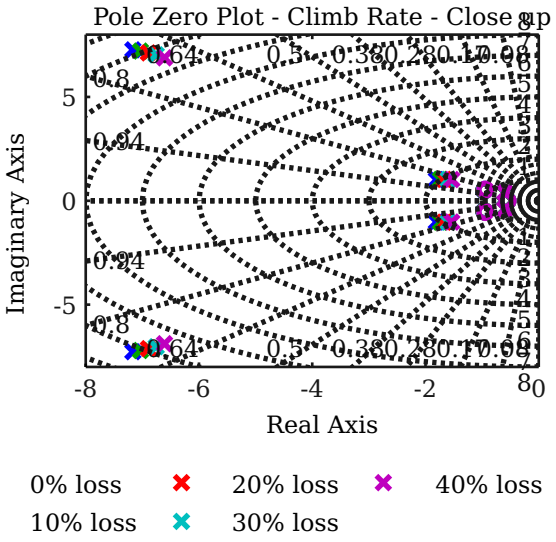

Figure 5.19 – Classic Control - Longitudinal - Poles - Climb rate - Close up Version

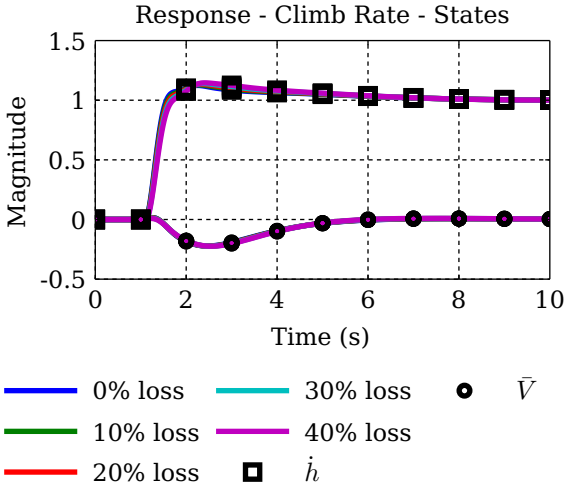

Figure 5.20 – Classic Control - Longitudinal - Response - Climb rate

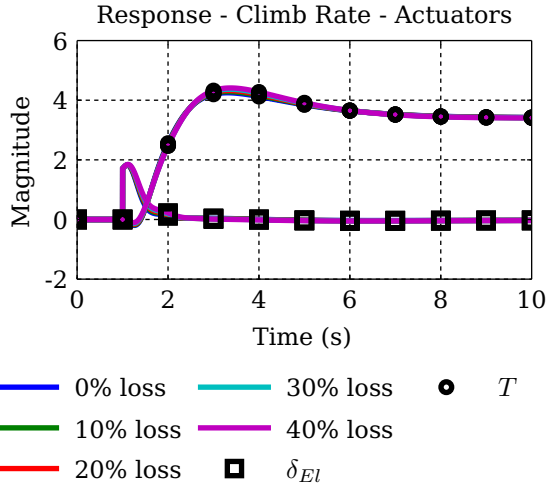

Figure 5.21 – Classic Control - Longitudinal - Actuators - Climb rate

slow settling time as depicted in Figure 5.20. In trying to improve this response the plant either becomes very slow or underdamped. The Bode diagram depicting the compensated system's stability can be found in Figure 5.28. A rather large phase margin of $65.5°$ and a magnitude margin of 14.5dB are observed. The largest change in phase is $15°$ between plants but falls in a well-suppressed frequency region. The magnitude on the other hand, changes by hardly 1dB over the entire frequency range. It is thus believed that this compensated plant should be fairly robust against wing loss.

It is clear from the set of figures provided in this section that if the controllers are designed conservatively, there will be no problem with their ability to handle the effects produced by wing loss on longitudinal dynamics. If, however, the controllers are optimised for performance, the control effort needed can become rather large with the varying plant, and cause undesirable commanded rates to stabilise the aircraft.

5.1.4.2 Lateral Controller Poles and Responses

As stated in Chapter 4, the longitudinal dynamics are hardly affected by the lateral dynamics and can be decoupled. The reverse of this statement is not true and thus the analysis of the lateral dynamics needs to

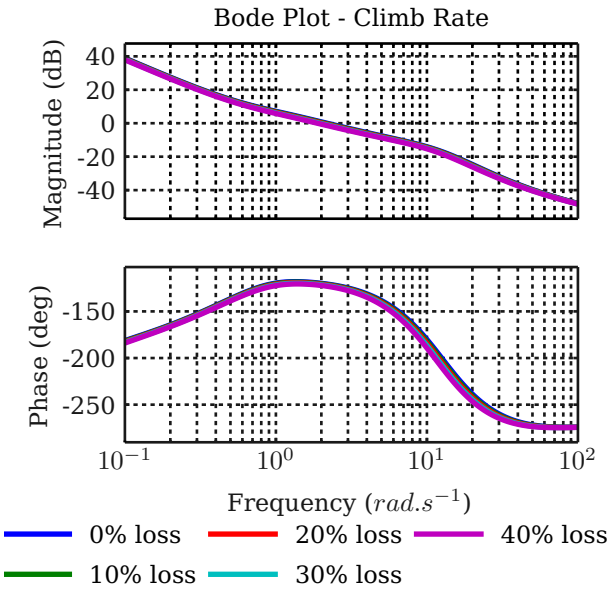

Figure 5.22 – Classic Control - Bode - Climb rate

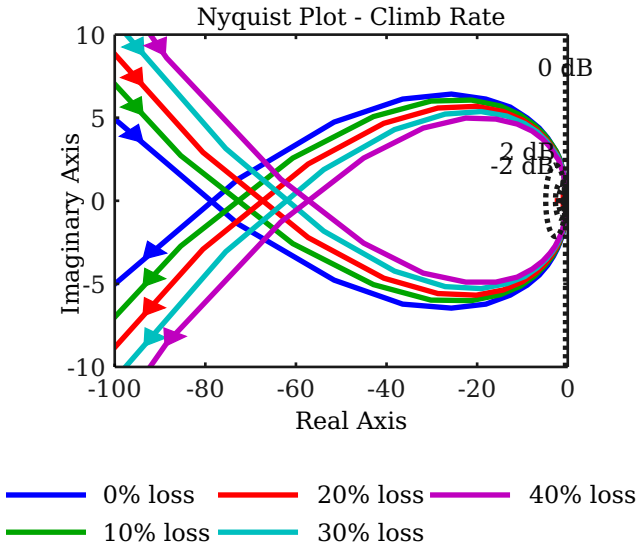

Figure 5.23 – Classic Control - Nyquist - Climb rate

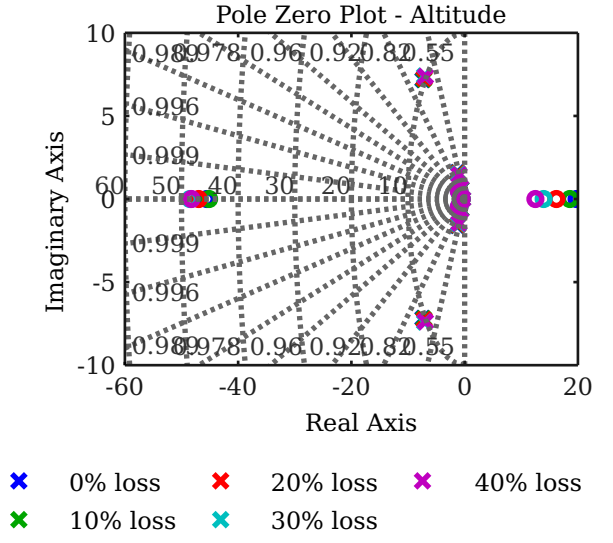

Figure 5.24 – Classic Control - Longitudinal - Poles - Altitude Control

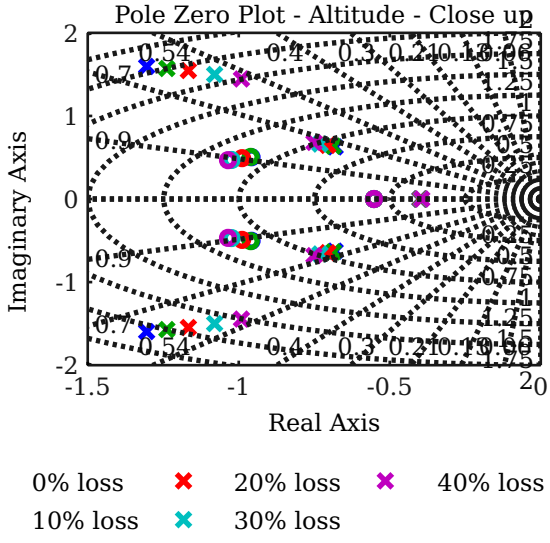

Figure 5.25 – Classic Control - Longitudinal - Poles - Altitude Control - Close up

be conducted on the full coupled plant. As the longitudinal controllers have already been designed, they will be augmented into the plant, before analysis. This should provide a “stable” environment in which to conduct lateral response analysis.

DRD

When examining Figure 5.29, it can be seen that the Dutch roll poles are fairly constant. Their damping and natural frequency increase as percentage wing loss increases but the amount of change is fairly small and should not influence the response greatly. This is supported by the simulated responses plotted in Figure 5.30. The response is obtained with scaled eigenvalues. Analysing the Bode plot of the DRD as depicted in Figure 5.31 the compensator, should only help to increase the damping of the system and not improve its response time. What is important about this controller is the fact that for all cases of loss the frequency response stays basically the same, which supports the response observed in Figure 5.30.

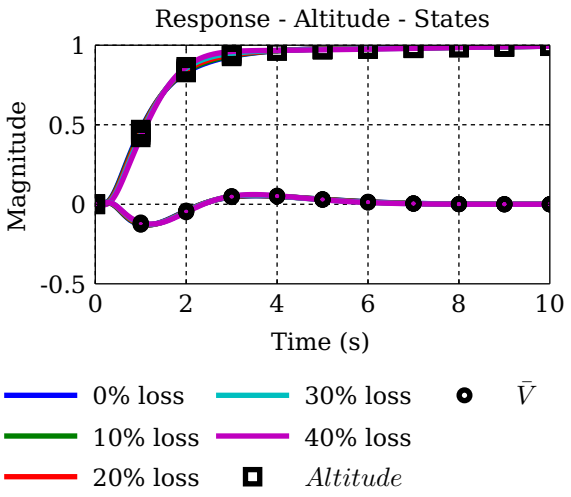

Figure 5.26 – Classic Control - Longitudinal - Response - Altitude

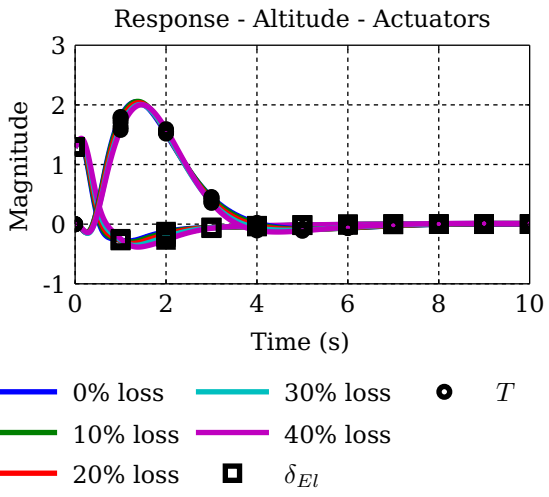

Figure 5.27 – Classic Control - Longitudinal - Actuators - Altitude

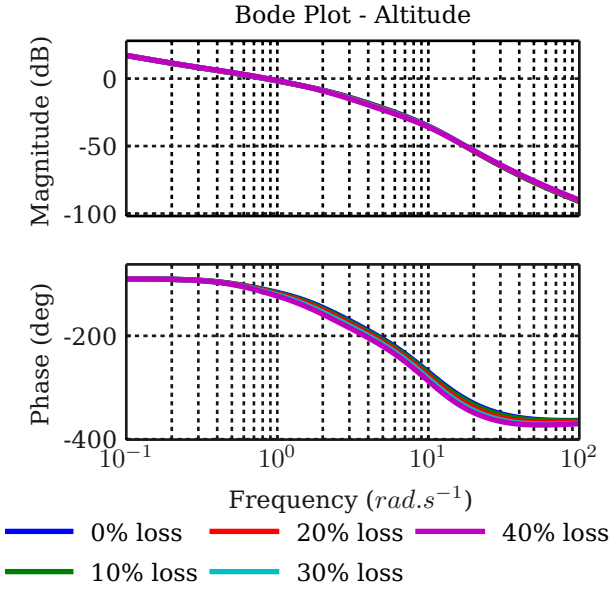

Figure 5.28 – Classic Control - Bode - Altitude Control

Roll Angle

When examining the roll angle controller, it can be seen that its response is quite excessive to the amount of control input commanded to the actuators. Only $0.2°$ deflection is needed to cause one degree of roll angle with a rise time of under 1 second. It also settles quite slowly. Designed for 2 seconds settling time, it reaches the 2% mark at only 5.4 seconds. Decreasing this settling time through gain adjustment causes the overshoot experienced to exceed 20%, which is already quite high, with only a minimal decrease in settling time. When adjusting the zeros position, it results in a similar change in response. This leads to the following conclusion: for this specific plant, a PI controller will not be enough to induce the desired response. When examining the pole plot in Figure 5.32, it can be seen that only the two fastest real poles change significantly with regard to the other "stationary" poles and zeros. This will thus cause the response to slow down, while only slightly decreasing the damping. Figure 5.34 supports this conclusion. Figure 5.33 shows that there is still a large amount of control authority left but that a more complex con-

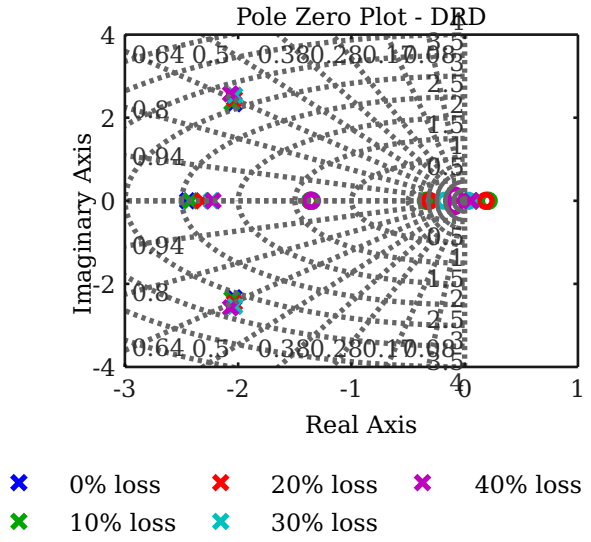

Figure 5.29 – Classic Control - Lateral - Poles - Dutch Roll Damper

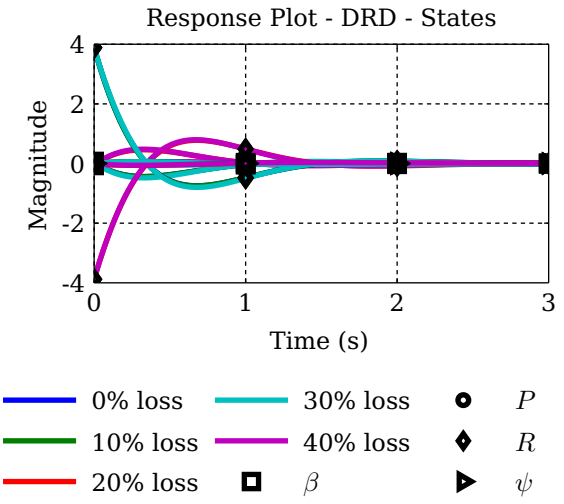

Figure 5.30 – Classic Control - Lateral - States - Dutch Roll Damper

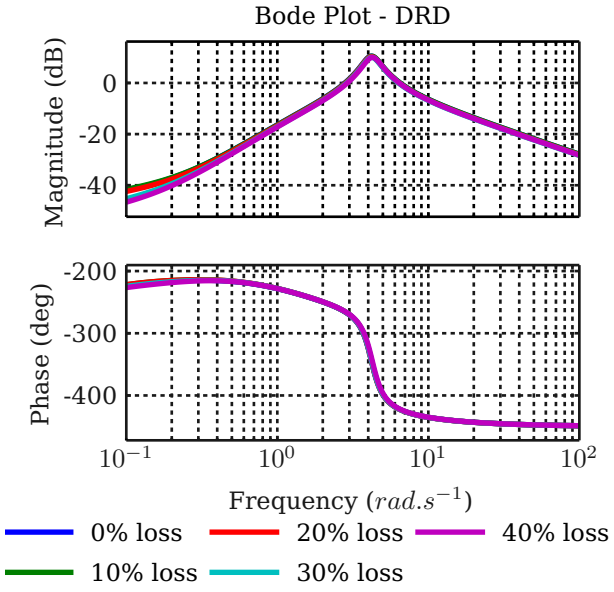

Figure 5.31 – Classic Control - Lateral - Bode - Dutch Roll Damper

troller will be required to harness it. When analysing the Bode plot in Figure 5.36, it can be seen that the frequency response over all wing loss cases presents a worrisome feature. It crosses the $-180°$ line twice. Again, use of the Nyquist criterion will be used to determine if the system is stable.

Figure 5.35 shows the Nyquist contour of this plant. As the plant into which the roll angle controller is augmented had a RHP pole, one counter-clockwise encirclement is expected. The contour itself also passes on the left side of the critical point and in a counter-clockwise manner. The Nyquist criterion thus proves that the plant is closed-loop stable. It can be seen in Figure 5.35 that the magnitude margin is 24.9dB with 4.5dB variation and the phase margin is $54.4°$ with $7.2°$ variation.

Heading

Lastly the heading controller is represented in Figures 5.38 to 5.40. All the poles tend to move towards the imaginary axis. They lose damping, with the largest change being 0.1, and become slightly slower in

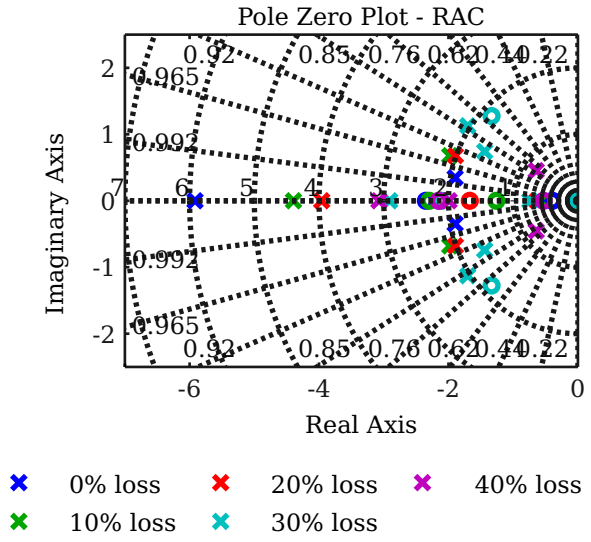

Figure 5.32 – Classic Control - Lateral - Poles - Roll Angle Controller

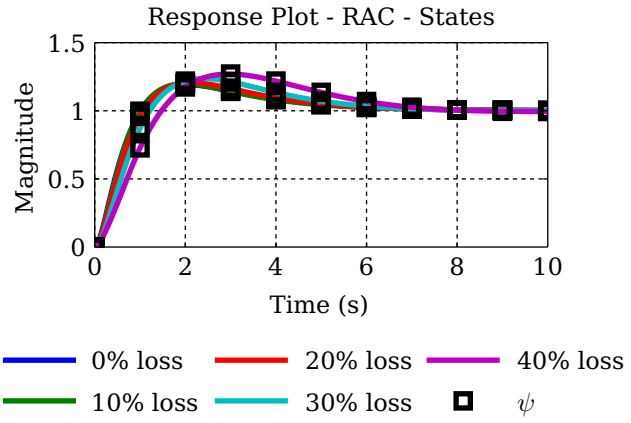

Figure 5.33 – Classic Control - Lateral - State - Roll Angle

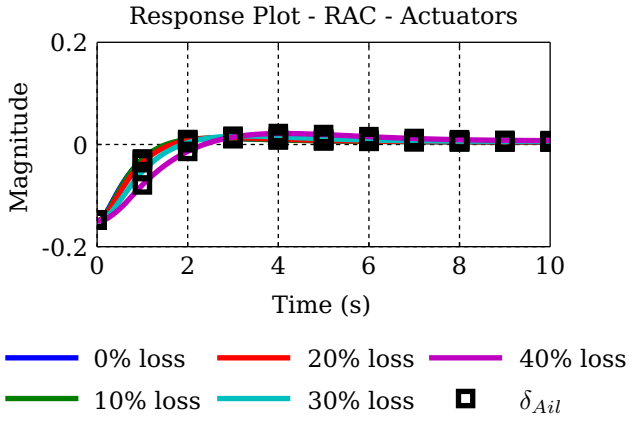

Figure 5.34 – Classic Control - Lateral - Actuators - Roll Angle

frequency. This can be explained by looking at the root locus of roll angle input to heading output. An increase in gain is needed to provide a faster heading response but causes all of the other poles to move towards the imaginary axis. This in turn also reduces most of their damping. Thus trying to improve the heading response alone, results in degrading the rest of the plant, which in turn degrades the heading response. It is also noted that when trying to speed up the response, excessive actuator deflection is needed. It can be seen from the Bode plot in Figure 5.41, that the plant has a 12.3dB magnitude margin with 0.2dB variation and a $81.5°$ phase margin with $24°$ variation. If the response is speeded up, these margins drop quickly. At this stage it becomes apparent that a proportional heading compensator results in a trade-off situation. If a faster response is required, a decrease in stability margins and damping will occur. If more damping is required, the response itself will be slower but more stable. As this thesis is about stability, the slower response, with more damping and larger stability margins is the preferred choice. This may be in contradiction with the design specifications but after examining these responses, root loci and Bode plots, it is apparent that the plant itself does not allow these specifications with only a proportional controller.

Overall the lateral controllers fare well with the imposed wing damage. It should be noted that all of these linear plants assume zero pitch roll and yaw rates, thus as long as there exists a trim configuration, the controllers should be able to find a stable equilibrium point and be able to maintain the aircraft's attitude.

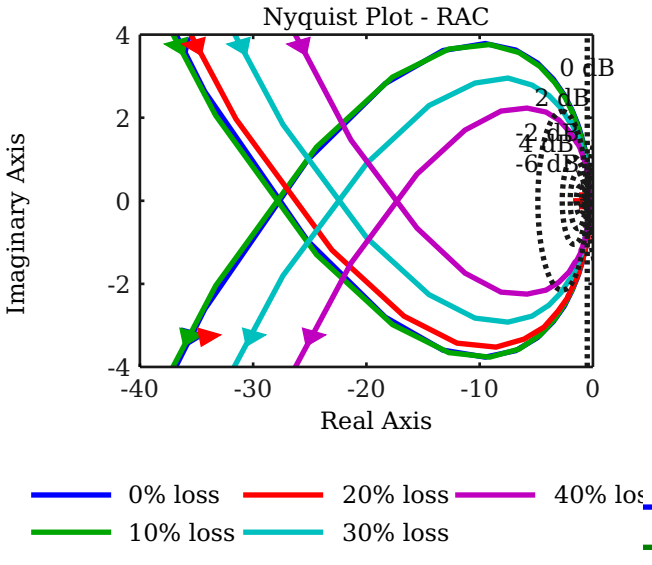

Figure 5.35 – Classic Control - Nyquist - Roll Angle

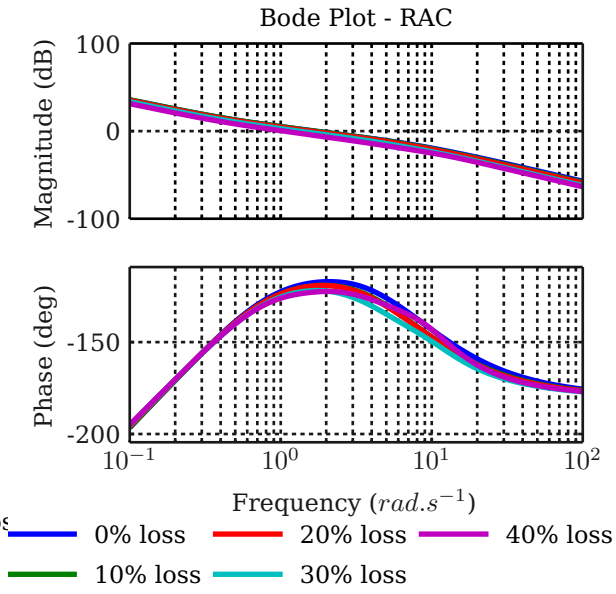

Figure 5.36 – Classic Control - Bode - Roll Angle

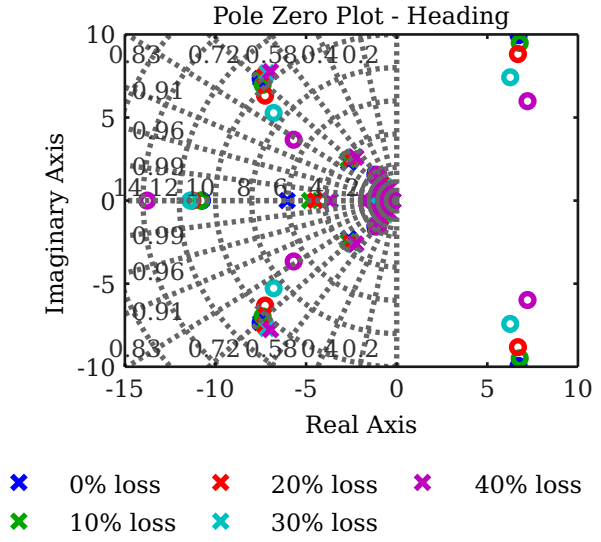

Figure 5.37 – Classic Control - Lateral - Poles - Heading Control

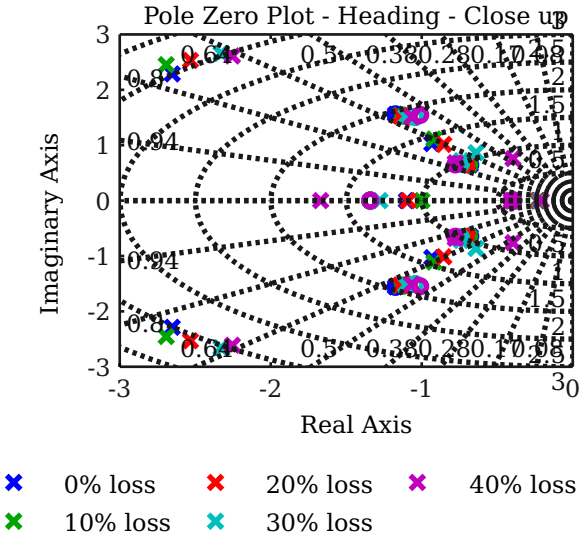

Figure 5.38 – Classic Control - Lateral - Poles - Heading - Close up Control

5.1.5 Possible Cross-Coupling Issues

As observed in Chapter 4, Sections 4.4.3 & 4.4.4 the following input to output pairs were identified as possible cross-coupling areas which could influence the system negatively.

- Ailerons to Airspeed
- Elevator to Roll Rate
- Elevator to Yaw rate

Figure 5.42 shows the influence of the ailerons on airspeed. The low range frequency response has been thoroughly suppressed and only peaks at -22.7dB. The gain variation is roughly 15dB. This is a 56.4dB suppression from the uncompensated open-loop dynamics. The gain variation however did not change. Due to the high suppression of 22.7dB below 0, it can be stated that this input to output pair is uncoupled and should not cause any notable disturbances.

Figure 5.43 shows the elevator's influence on roll rate. It is clear from this figure that the initial high

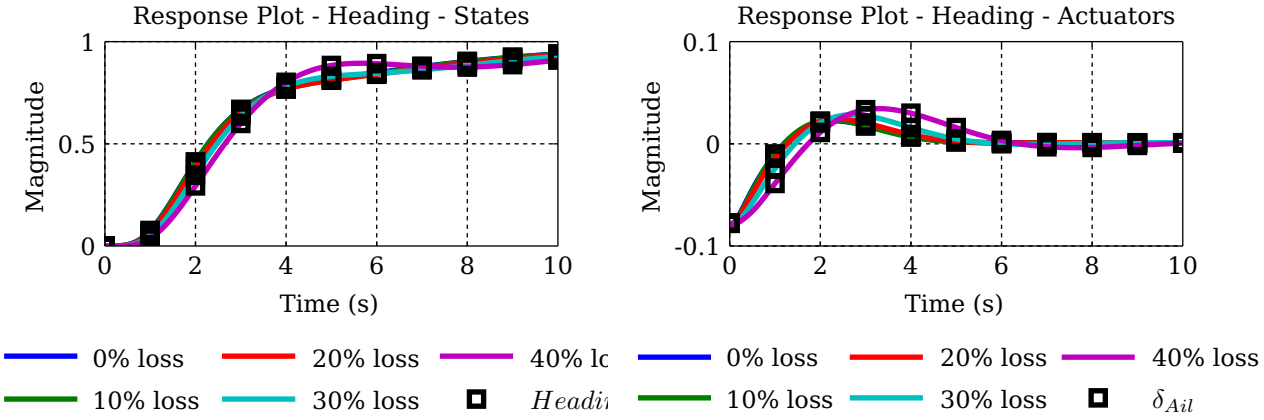

Figure 5.39 – Classic Control - Lateral - Response - Heading Control

Figure 5.40 – Classic Control - Lateral - Actautors - Heading Control

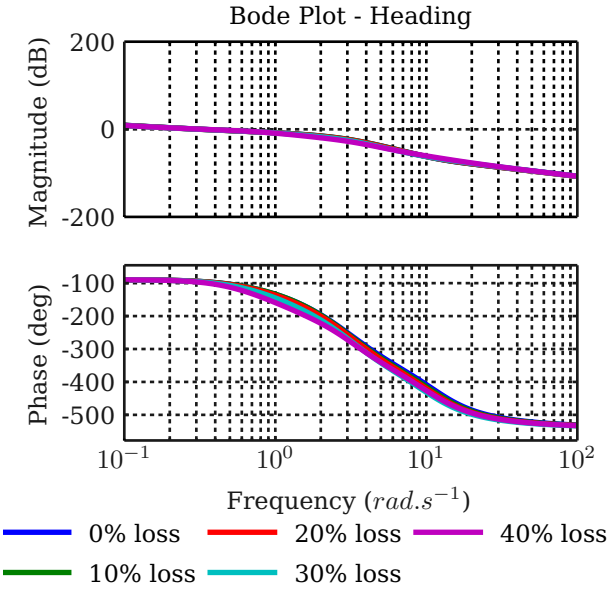

Figure 5.41 – Classic Control - Bode - Heading Control

gain low range frequency response has been suppressed quite well with regard to the uncompensated open-loop dynamics shown in Figure 4.9. The response peaks at -5.49dB but has an overall gain variation of 12.15dB. This response has been suppressed from 38.6dB in the uncompensated dynamics case and the gain variation reduced from 21.1dB. Although -5.49dB is not a great suppression, it is still an improvement end should not couple strongly into the output. The airspeed controller should be able to handle this disturbance.

Figure 5.44 shows the elevator to yaw rate. As with the previous two input to output pairs, this response is suppressed strongly at low frequencies. It peaks at -15.1dB, with a maximum gain variation of 13.7dB. This is a 72.2dB suppression from the uncompensated open-loop dynamics in overall response and the gain variation has been reduced from 25.5dB by 11.8dB. This input to output pair can thus been described as decoupled and should not cause any notable disturbances in the aircraft.

5.1.6 Conclusion

In this section classic aircraft flight control theory was applied to the UAV to test its robustness to partial wing loss. This discussion in Chapter 3 showed that it seemed possible that by only applying classic theory, in the form of proportional and proportional integral control, the UAV could be stabilised. The initial design

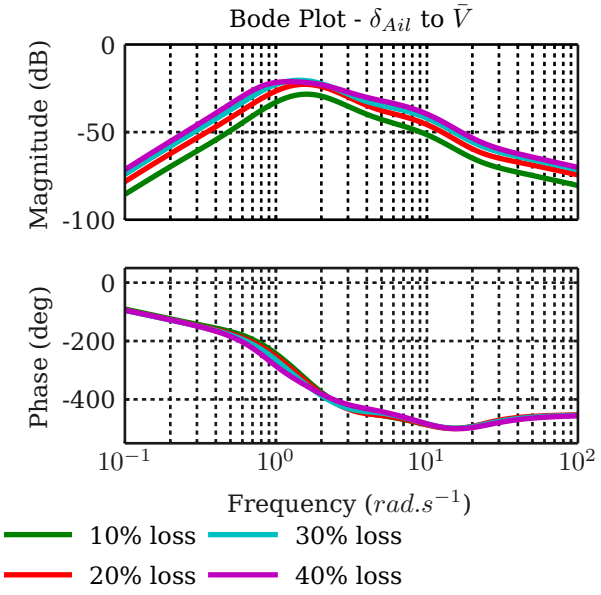

Figure 5.42 – Classic Control - Bode - δ_{Ail} to $\bar{V}$

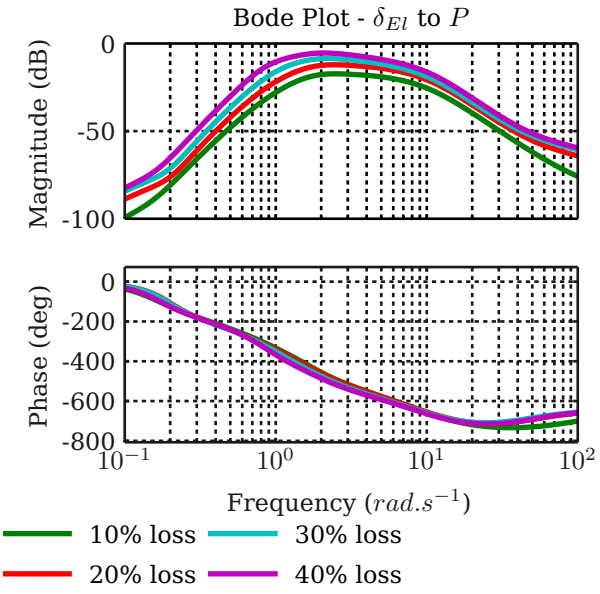

Figure 5.43 – Classic Control - Bode - δ_{El} to P

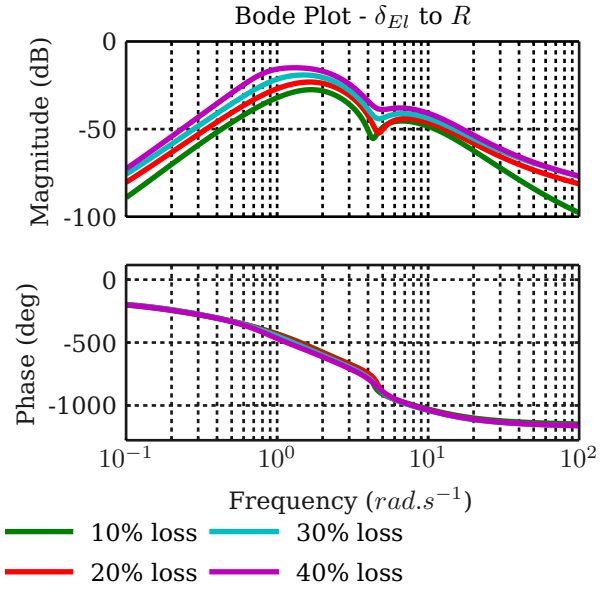

Figure 5.44 – Classic Control - Bode - δ_{El} to R

was done on the nominal decoupled longitudinal and lateral plants, without knowledge of the effects of wing loss on them. Even though these plants are coupled after wing loss, their decoupled versions still provided enough information to design a stable control system. It should be noted that even though the decoupled system proved adequate, the coupled system should be used to do the analyses of the lateral controllers. In this case the controller proved sufficient to suppress the cross-coupling. The suppression may not be far below the 0dB line in some cases and frequency ranges, but is still properly suppressed with regard to the uncompensated system.

5.2 Acceleration-Based Control (ABC) Architecture

In this section a theoretical version of ABC design will be implemented and tested according to Dr. I.K. Peddle's design methodology [1]. The design methodology also specifies criteria which determine valid pole placement for the specific aircraft. The final part of this design will conclude the possible stability of these controllers with a Bode and / or Nyquist stability analysis. The results will then be compared to those in the previous section, which will help in concluding how these dynamical changes, due to wing loss, affect the total stability of these controllers. This will then be used in the decision whether to redesign the control structure with robust methods, or only to adapt the current version.

The ABC design process makes use of specific acceleration feedback in the inner-loops to stabilise the given plant. This requires first designing a regulator for each feedback and then adding an integrator to the input output error to ensure that a response with zero steady state error can be achieved. By ensuring zero steady state error in the inner-loops, simple proportional controllers can be implemented on velocity and position feedback loops. This control architecture design can be simplified further if time scale separation (TSS) conditions hold. By assuming that TSS holds, the inner-loop dynamics can either be ignored or replaced by lag dynamics.

Lastly, all of the acceleration regulation is done in wind axis. This will not cause a problem as the trim condition chosen in Chapter 3 aligns the wind and body axes. In the subsections to follow a brief overview on how to implement these controllers is provided. A full implementation, analysis and simulation can be found in [1].

5.2.1 Inner-loop Controllers

The inner-loop controllers exist to ensure two outcomes:

- Regulation of the response to adhere to a certain damping and settling time, as specified by upper and lower bounds
- Zero steady state errors on the commanded accelerations

This requires four controllers to encapsulate the fast dynamics of the UAV: axial, normal and lateral specific acceleration controllers and a roll rate controller. The design and implementation of these controllers will be discussed in the following sections.

5.2.1.1 Axial Specific Acceleration

The axial controller is used to regulate and control all accelerations in the x-axis direction. The main actuator used for this purpose is the engine to generate the thrust necessary to accomplish this. In performing this controller implementation, the only real restriction is the engine time constant, τ_T. The dynamics of the axial decoupled system is defined by.

$$\dot{T} = \left[-\tfrac{1}{\tau_T}\right] T + \left[-\tfrac{1}{\tau_T}\right] T_c \tag{5.2.1}$$

$$A_W = \left[\tfrac{1}{m}\right] T + \left[-\tfrac{1}{m}\right] D \tag{5.2.2}$$

In the above equations, T_c is the commanded thrust, A_W is the axial acceleration in the wind reference frame and D is the drag of the UAV. The control law, as designed in [1], can now be described by

$$T_S = -K_A A_W - K_E E_A \tag{5.2.3}$$

$$\dot{E}_A = A_W - A_{W_C} \tag{5.2.4}$$

K_A is the axial acceleration feedback gain, K_E is the integrator gain and $\dot{E}_A$ is the time rate of change in error. Implementing this law on the above dynamics result in the control configuration as depicted by Figure 5.45.

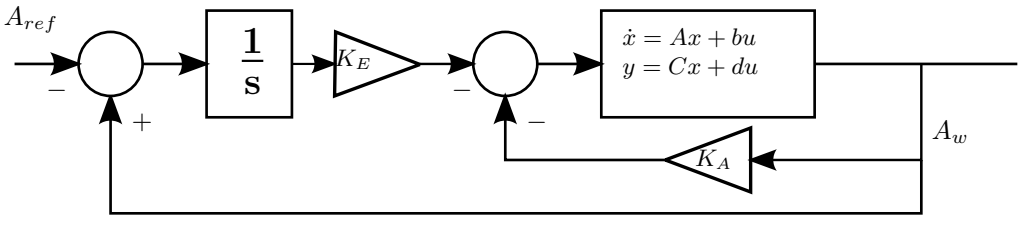

Figure 5.45 – ABC - ASA Control Block Diagram

If the control law is added, this becomes a second order system. At this stage the simplified dynamics allow the use of a second order characteristic equation to define the controller poles and behaviour. The control gains can thus be determined as follows,

$$K_A = m\left(\tau_T \alpha_1 - 1\right) \tag{5.2.5}$$

$$K_E = m\tau_T \alpha_0 \tag{5.2.6}$$

After implementing $\tau_T = 0.25ms$, the control gains can be calculated, given that an appropriate characteristic equation is chosen. Using $\zeta = 0.8$ and a natural frequency $\omega_T = \frac{1}{0.9\tau}$, a frequency just slower than the engine bandwidth to ensure that no excessive control authority is required, results in the following gain values.

$$K_A = 2.7720 \tag{5.2.7}$$

$$K_E = 20.4120 \tag{5.2.8}$$

5.2.1.2 Normal Specific Acceleration (NSA)

Implementation of the NSA controller is done to regulate and control the UAV's normal acceleration. This is mainly done by deflecting the elevator control surface. Some restrictions come into play when considering the validity of use of a NSA controller on a given UAV. The first arises from the analysis of the dynamics, which is done by [1] and will not be restated here. In short this analysis concludes that a zero will lei in the right half plane (RHP) and cause the system to have non-minimum phase. This can however be ignored if an upper bound on the system's poles is placed at $\frac{|\omega_{NMP}|}{3}$. The second restriction comes from the slow thrust response of the system. As every elevator deflection will cause an increase or decrease in thrust response, this deflection needs to be taken into account. If, however TSS can be enforced on the system, it can be ignored. Thus this creates a lower bound on the system with a frequency 5 times that of τ_T. Thus the two bounds to consider are,

$$\omega_n = \left| \frac{1}{3} \sqrt{\frac{L_{\delta_{El}}}{I_{yy}} \left(l_T - l_N\right)} \right| \tag{5.2.9}$$

$$\omega_v = 5\frac{1}{\tau_T} \tag{5.2.10}$$

In the above equations $L_{\delta_{El}}$ is the partial derivative of the lift force with respect to elevator deflection, I_{yy} is the UAV's inertia around the y-axis, l_T is the effective length to the tail-plane and l_N is the length to the neutral point. If the above bounds are met, the dynamics of the normal specific acceleration system can be represented in the following simple decoupled form,

$$\begin{bmatrix} \alpha \\ Q \end{bmatrix} = \begin{bmatrix} -\frac{L_\alpha}{mV} & 1 \\ \frac{M_\alpha}{I_{yy}} & \frac{M_Q}{I_{yy}} \end{bmatrix} \begin{bmatrix} \alpha \\ Q \end{bmatrix} + \begin{bmatrix} 0 \\ \frac{M_{\delta_{El}}}{I_{yy}} \end{bmatrix} \tag{5.2.11}$$

$$C_w = \begin{bmatrix} -\frac{L_\alpha}{m} & 0 \end{bmatrix} \begin{bmatrix} \alpha \\ Q \end{bmatrix} + \begin{bmatrix} 0 \end{bmatrix} \delta_{El} + \begin{bmatrix} -\frac{L_\alpha}{m} \end{bmatrix} \tag{5.2.12}$$

As stated previously, this approach uses a regulator to achieve the desired response and implements an integrator on top of that to ensure zero steady state error tracking of the desired input. This can be implemented with the following control law:

$$\delta_E = -K_Q Q - K_C C_w - K_E E_C + \delta_{E_{cg}} \tag{5.2.13}$$

If this control law is implemented on the normal dynamics, the block diagram in Figure 5.46 depicts the clear implementation of the current setup.

In the case of the NSA, the addition of the controller creates a third order system. Thus the characteristic

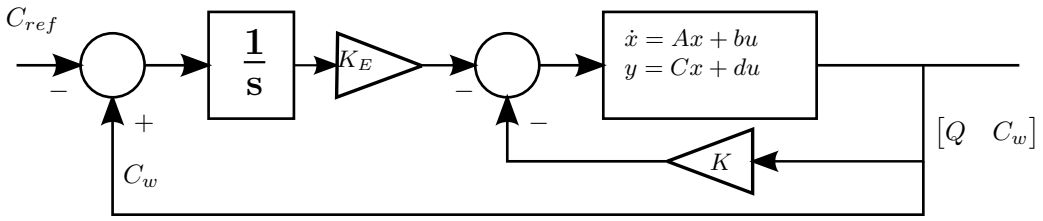

Figure 5.46 – ABC - NSA Control Block Diagram

equation, with which to describe the desired response, will also be of the third order. Taking this into consideration with the dynamics described in this section, the controller gains can be determined as follows,

$$K_Q = \frac{I_{yy}}{M_{\delta_{El}}}\left(\alpha_2 + \frac{M_Q}{I_{yy}} - \frac{L_\alpha}{m\bar{V}}\right) \tag{5.2.14}$$

$$K_C = \frac{mI_{yy}}{L_\alpha M_{\delta_{El}}}\left(\alpha_1 + \frac{M_\alpha}{I_{yy}} - \frac{L_\alpha}{m\bar{V}}\left(\alpha_2 - \frac{L_\alpha}{m\bar{V}}\right)\right) \tag{5.2.15}$$

$$K_E = -\frac{mI_{yy}}{L_\alpha M_{\delta_{El}}}\alpha_0 \tag{5.2.16}$$

with $M_{\delta_{El}}$ the pitching moment relative to elevator deflection, M_Q the pitching moment relative to pitch rate, L_α the lift force due to α and M_α the pitching moment relative to α. Using equations (5.2.14) to (5.2.16), with $\zeta = 0.8$, $\omega_n = 15rad$ and $\omega_I = 15rad$ results in the following calculated control gains,

(5.2.17)

$$K_Q = -0.2169 \tag{5.2.18}$$

$$K_C = 0.0276 \tag{5.2.19}$$

$$K_E = 0.2954 \tag{5.2.20}$$

5.2.1.3 Lateral Specific Acceleration

The LSA controller is implemented to regulate and control all lateral accelerations. As there is no lateral lifting surface, the only surface to directly achieve this is the rudder. It is thus expected that stability compensation will be a large part of this controller but that it will be ineffective with regard to physically enforcing acceleration in the lateral direction. The lateral dynamics will first be regulated to achieve the desired behaviour in term of damping ratio, before an attempt will be made to control the lateral acceleration. The lateral dynamics can be defined as follow:

$$\begin{bmatrix}\dot{\beta}\\ \dot{R}\end{bmatrix} = \begin{bmatrix}\frac{Y_\beta}{m\bar{V}} & -1\\ \frac{\bar{N}_\beta}{I_{zz}} & \frac{\bar{N}_R}{I_{zz}}\end{bmatrix}\begin{bmatrix}\beta\\ R\end{bmatrix} + \begin{bmatrix}\frac{Y_{\delta_{Rud}}}{m\bar{V}}\\ \frac{\bar{N}_{\delta_{Rud}}}{I_{zz}}\end{bmatrix} + \begin{bmatrix}-\frac{Y_{\delta_R}}{m\bar{V}}\frac{\bar{N}_{\delta_{Ail}}}{\bar{N}_{\delta_{Rud}}}\\ 0\end{bmatrix}\delta_{Ail} \tag{5.2.21}$$

$$B_W = \begin{bmatrix}\frac{Y_\beta}{m} & \frac{Y_R}{m}\end{bmatrix}\begin{bmatrix}\beta\\ R\end{bmatrix} + \begin{bmatrix}\frac{Y_{\delta_{Rud}}}{m}\end{bmatrix}\delta_{Rud} + \begin{bmatrix}-\frac{Y_{\delta_{El}}}{m}\frac{N_{\delta_{Ail}}}{N_{\delta_{Rud}}}\end{bmatrix}\delta_{Ail} \tag{5.2.22}$$

In the above equations Y_β is the side-force due to β, $Y_{\delta_{Rud}}$ is the side-force due to rudder deflection, $\bar{N}_R$ is the yaw moment due to yaw rate, $\bar{N}_\beta$ is the yaw moment due to β, $\bar{N}_{\delta_{Rud}}$ is the yaw moment due to rudder deflection $\bar{N}_{\delta_{Ail}}$ is the yaw moment due to aileron deflection and I_{zz} the UAV's inertia around the z-axis. Implementing only the regulation part of the control law results in

$$\delta_{Rud} = -K_R R - K_B B + \delta_{Rud_R} \tag{5.2.23}$$

This is necessary to ensure that none of the restrictions are voided when implementing the designed controller. The restrictions that must be met to ensure validity of the assumptions made for the dynamics are

stated below,

$$\left|\frac{K-\beta}{K_R}\right| << \left|\frac{ml_f}{Yr(l_d-l_f)}\right| \tag{5.2.24}$$

$$|K_R| << \left|\frac{m\bar{V}_T l_w}{Y_{\delta_{Rud}}(l_w-l_f)}\right| \tag{5.2.25}$$

with l_d the damping arm length, l_f the effective length to the fin and l_w the weathercock arm length. According to [1] these equations are in most cases easily met but still need to be checked to ensure compliance. Assuming that the conditions have been met, the gains can be calculated with the following equations,

(5.2.26)

$$K_B = \frac{Y_\beta N_r}{m\bar{V}_T I_{zz}} + \frac{N_\beta}{I_{zz}-\alpha_0}\frac{1}{(Y_{\delta_{Rud}}/m(\alpha_0 - Y_\beta/I_{zz}(N_\beta/Y_\beta - N_{\delta_{Rud}}/Y_{\delta_{Rud}})))} \tag{5.2.27}$$

$$K_R = \frac{I_{zz}}{N_{\delta_{Rud}}}\left(\frac{Y_\beta}{m\bar{V}_T} + \frac{N_r}{Izz} + \alpha_1\left(1 + K_B\frac{Y_{\delta_{Rud}}}{m}\right)\right) \tag{5.2.28}$$

Implementing the above equations with $\zeta = 0.707$, $\omega_n = 4.8$ and $\omega_I = 0.6$ led to an acceptable response for the stability augmentation. The values acquired when substituted into equations (5.2.27) and (5.2.28) are

$$K_B = -0.0772 \tag{5.2.29}$$

$$K_R = -0.2958 \tag{5.2.30}$$

Once the above have been designed, δ_{R_R} can be implemented.

$$\delta_{R_R} = -K_E\dot{E}_B \tag{5.2.31}$$

where

$$E_B = B_W - B_{W_C} \tag{5.2.32}$$

This regulation is used to remove any lateral accelerations, thus $\dot{E}_B = \left[-K_{SS}K_E\right]E_B + \left[-1\right]B_{W_C}$, which leads to

$$K_E = \frac{\alpha_0}{K_{SS}} = -1.1911 \tag{5.2.33}$$

Implementing the acceleration regulation proved to be a problem for the controller. The integrator dynamics interfered with the stabilisation and resulted in an unsatisfactory response when used to regulate lateral acceleration. This is due to the integrator augmenting the root-locus and decreasing the stability when active. [1] cites a special case where the LSA is only used for stabilisation and roll to turn is used to enforce lateral accelerations. This removes the integrator and results in the designed damped response. It was thus decided to implement this special case, rather than the full LSA, as the fully implemented design only requires compensation and not regulation. The results of both these cases can be observed in Section 5.2.4.

5.2.1.4 Roll Rate Controller

According to [1], there are two ways to implement this controller. One can either ignore the dynamics of the roll rate if they are fast enough or take them into account during the design process. In this approach to design, the dynamics will be taken into account due to the necessary requirements placed later on in the specific acceleration translation (SAT) and the normal specific acceleration vector direction changing

(NSAVDC) algorithm. The roll rate dynamics can be described as follows:

$$\begin{bmatrix} \dot{P} \\ \dot{E}_P \\ \dot{\phi} \end{bmatrix} = \begin{bmatrix} \frac{\bar{L}_P}{I_{xx}} & 0 & 0 \\ 1 & 0 & 0 \\ -1 & 0 & 0 \end{bmatrix} \begin{bmatrix} P \\ E_P \\ \phi \end{bmatrix} + \begin{bmatrix} 0 \\ -1 \\ 0 \end{bmatrix} P_R + \begin{bmatrix} 0 \\ 0 \\ 1 \end{bmatrix} P_{W_C} + \begin{bmatrix} \frac{\bar{L}_{\delta_{Ail}}}{I_{xx}} \\ 0 \\ 0 \end{bmatrix} \delta_{Ail} \tag{5.2.34}$$

In the above equation $\bar{L}_P$ is the rolling moment relative to roll rate, $\bar{L}_{\delta_{Ail}}$ the rolling moment relative to aileron deflection and I_{xx} the UAV's inertia around the x-axis. Using the control law stated below, the roll rate controller can be implemented by taking the slower dynamics into account.

$$\delta_{Ail} = -K_P P - K_E E_P + N_P P_R \tag{5.2.35}$$

$$\dot{E}_P = P - P_R \tag{5.2.36}$$

$$\dot{\phi} = P_{W_C} - P_W \tag{5.2.37}$$

$$P_R = P_{W_C} + K_\phi \phi \tag{5.2.38}$$

Figure 5.47 decipts the configuration of this controller.

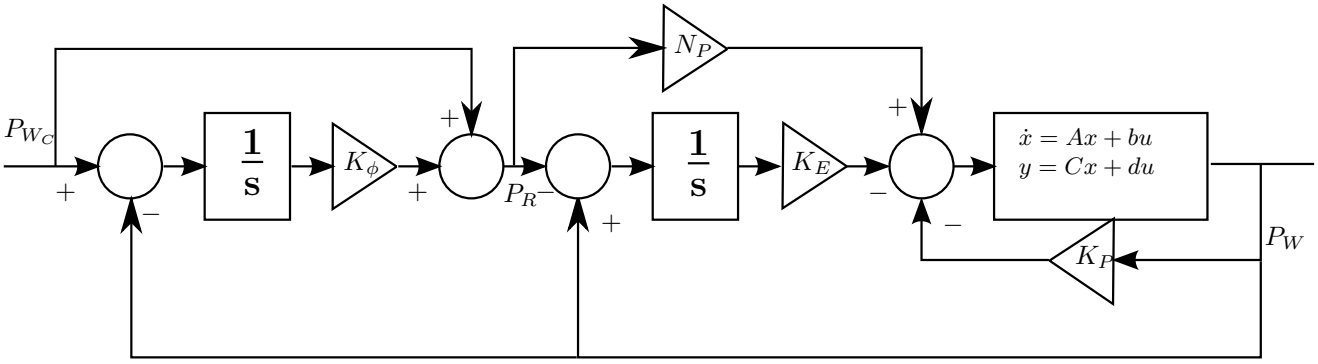

Figure 5.47 – ABC - Roll Rate Control Block Diagram

After implementing the above control law on the roll rate dynamics, the following equations are obtained to calculate the gains needed to obtain the desired characteristic equation.

$$K_P = \frac{1}{\bar{L}_{\delta_A}} \left(\alpha_2 + \bar{L}_P + I_{xx} \alpha_1 \right) \tag{5.2.39}$$

$$K_E = \frac{I_{xx}}{L_{\delta_A}} \left(\alpha_1 + \frac{\alpha_0}{z_{int}} \right) \tag{5.2.40}$$

$$K_\phi = \frac{0}{\alpha_0} \alpha_1 + \frac{\alpha_0}{z_{int}} \tag{5.2.41}$$

$$N_P = -\frac{K_E}{z_{int}} \tag{5.2.42}$$

Using the dynamics of this specific UAV, the following values were calculated for these gains.

$$K_P = -0.8227 \tag{5.2.43}$$

$$K_E = -8.0229 \tag{5.2.44}$$

$$K_\phi = 7.5000 \tag{5.2.45}$$

$$N_P = -0.6418 \tag{5.2.46}$$

5.2.2 Specific Acceleration Transformation Algorithm (SAT) and Normal Specific Acceleration Vector Direction Controller

These controllers can be seen as intermediate controllers. They accept the reference acceleration vector commanded by the velocity and position controllers and transform it into axial and normal specific acceleration commands and a roll rate command. In this implementation roll to turn is thus used instead of skid to turn. In short, the DCM vectors are used to extract the axial, normal and lateral accelerations from the commanded acceleration vector. The axial acceleration is sent through directly, while the normal and lateral accelerations are combined into a normal acceleration accompanied by a roll angle calculated from the angle between the normal and lateral DCM vectors. A thorough description of these two controllers can be found in [1].

5.2.3 Outer-loop Controllers: Velocity and Position

After the inner-loops, SAT and NSAVDC have been designed; the velocity and position controller can be implemented. As stated in [1], once the inner-loops have been designed, the dynamics can be abstracted to lag dynamics, described in equation 5.2.47, through enforcing TSS between them. This simplifies the design process and thus only proportional controllers are needed to ensure correct trajectory track following.

$$\dot{()} = -\frac{1}{\tau_{()}}() + \frac{1}{\tau_{()}}()_c \tag{5.2.47}$$

Taking all of the specifications used to design the controllers in Sections 5.2.1.1 through 5.2.1.4 into consideration, the outer-loop controllers can be designed with $\zeta = 0.8$ and settling times of,

$$t_{s2}P = 0.2 \tag{5.2.48}$$
$$t_{s2}A = 2.2 \tag{5.2.49}$$
$$t_{s2}B = 6 \tag{5.2.50}$$
$$t_{s2}C = 1 \tag{5.2.51}$$

5.2.4 Robustness of Controllers to Partial Wing Loss

In this section the relative stability of the controllers will be evaluated over 0% to 40% wing loss. In Chapter 4, only the states of the UAV were examined and not the additional outputs. As this control architecture relies on acceleration feedback, the actuator input to acceleration output will first be displayed for comparison purposes.

When examining the above figures, it's clear that the variation in both gain and phase over all the controllers are small. Thrust to axial accelerations experiences less than 1dB in gain and 1° phase over all the partial wing loss cases. Elevator to normal accelerations experiences a 5dB gain and 11° phase change. Rudder to lateral acceleration experiences less than 1dB in gain and 1° phase. These changes are rather small in comparison to the thrust, elevator and rudder input to state outputs depicted in Chapter 4. Taking this into consideration, it is clear that controllers augmenting these input-output pairs should be robust.

In the following sections the responses and stability of the acceleration compensated plants will be analysed. It should be noted that the controllers will be augmented onto the full linear plant and that each subsequent controller will be augmented onto the previous section's compensated plant. In simplifying the pole plots, Matlab's minreal function has been used to remove and pole-zero pair with a tolerance smaller than 0.05.

5.2.4.1 Axial Specific Acceleration Controller (ASA)

The robustness of the ASA is presented in Figures 5.51 to 5.54. The closed-loop step response of the ASA controller for different wing loss percentages is shown in Figures 5.51 and 5.52. The closed-loop pole plot of the ASA controller as a function of percentage wing loss is shown in Figure 5.53. The Bode plot

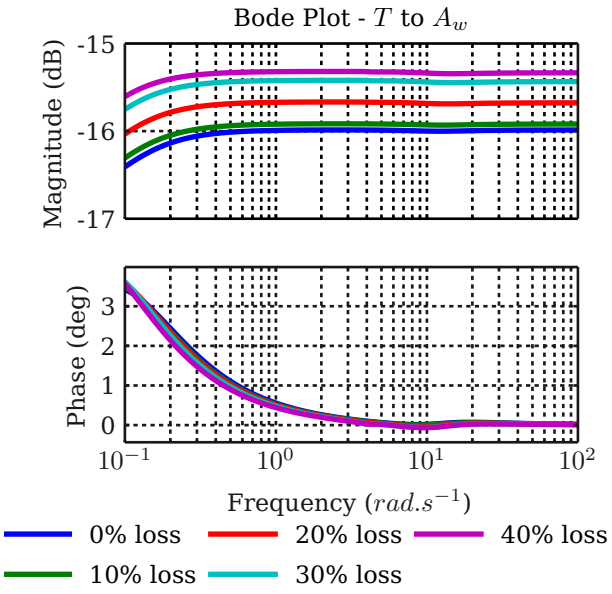

Figure 5.48 – ABC - Bode - Thrust to Axial Acceleration

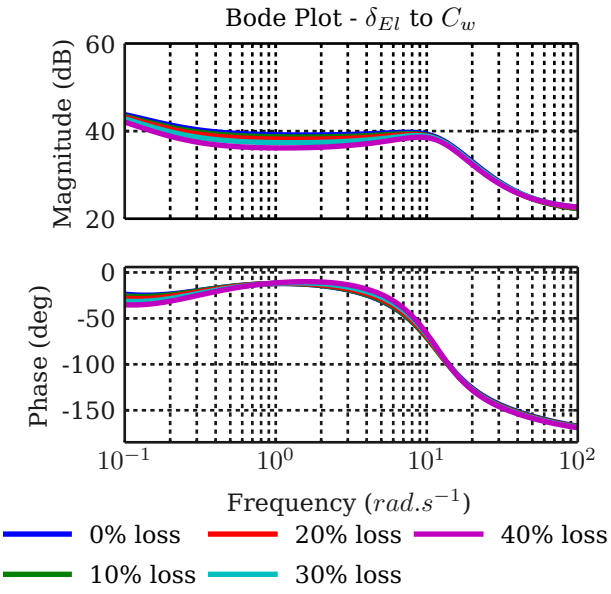

Figure 5.49 – ABC - Bode - Elevator to Normal Acceleration

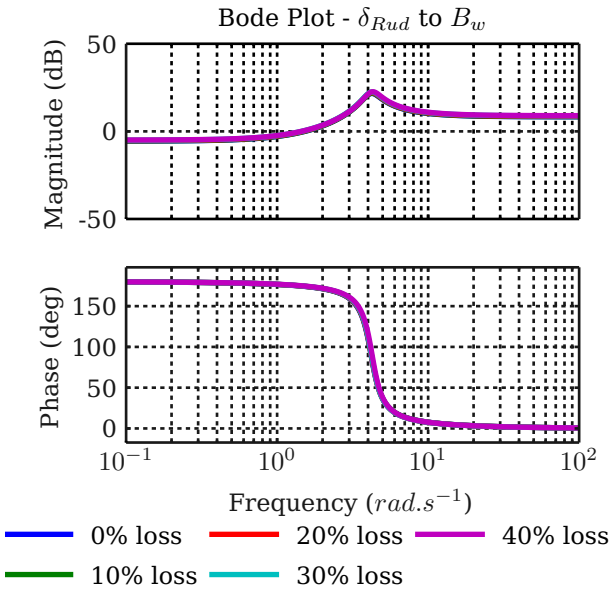

Figure 5.50 – ABC - Bode - Rudder to Lateral Acceleration

of the open-loop transfer function of the ASA controller for different wing loss percentages is shown in Figure 5.54.

The acceleration step response looks particularly robust with hardly any deviation in response over the range of percentage wing loss but requires less thrust with increased wing loss. The pole plot shows that the closed-loop poles remain on the real axis and become slightly faster as percentage wing loss increases. This supports the behaviour depicted in Figures 5.51 and 5.52 due to the similar response observed. Lastly, the Bode plot reveals a minimum phase margin of $90°$ and an infinite gain margin as the phase never crosses $-180°$. The response itself only varies with $0.5dB$ in magnitude and $0.3°$ in phase over all wing loss cases. This thus indicates a very robust inner loop for axial acceleration.

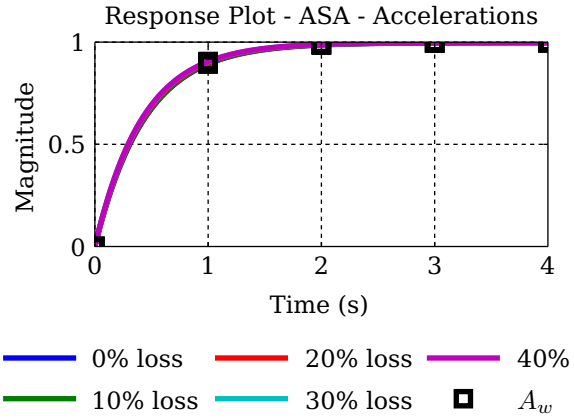

Figure 5.51 – ABC - Response - ASA - Acceleration

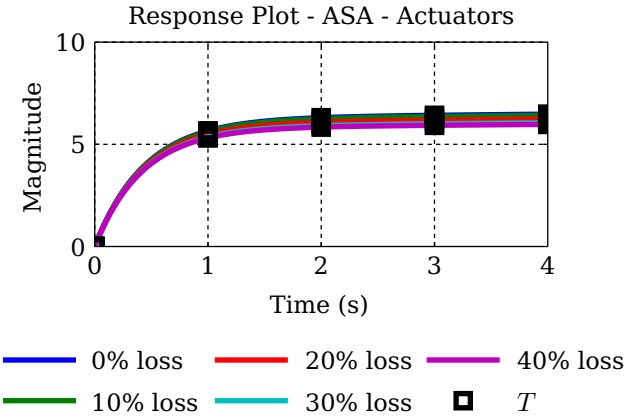

Figure 5.52 – ABC - Response - ASA - Actuator

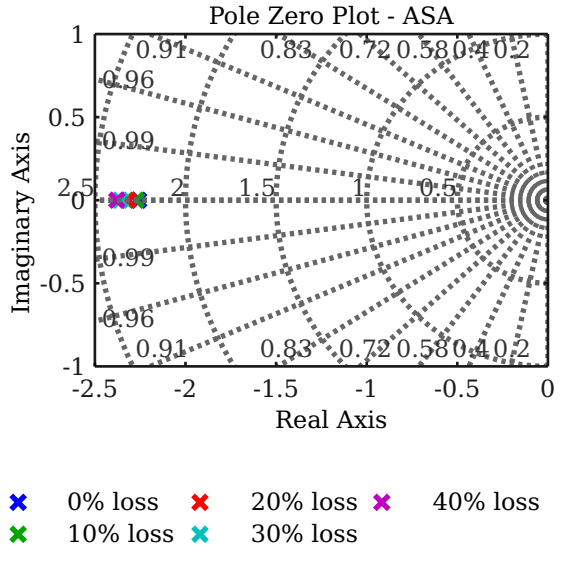

Figure 5.53 – ABC - Poles - ASA

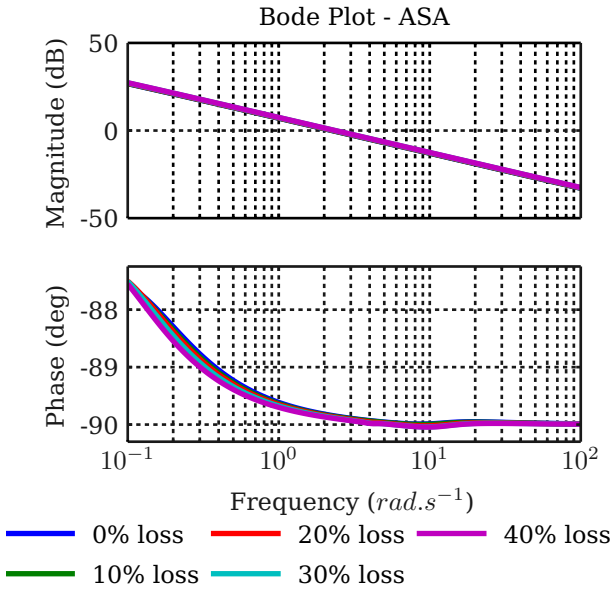

Figure 5.54 – ABC - Bode - ASA

5.2.4.2 Normal Specific Acceleration Controller (NSA)

The results acquired from the NSA can be found in Figures 5.55 to 5.58. The closed-loop step response of the NSA controller for different wing loss percentages is shown in Figures 5.55 and 5.56. The closed-loop pole plot of the NSA controller as a function of percentage wing loss is shown in Figure 5.57. The Bode plot of the open-loop transfer function of the NSA controller for different wing loss percentages is shown in Figure 5.58.

The response is again as designed for, with a slightly bigger variation than the ASA. It is also clear that more elevator is required to attain the same normal acceleration as the percentage of wing loss increases. This is to be expected as wing loss will have a larger effect on normal acceleration than on axial. As the NSA relies on the ASA, the difference in actuator command for the NSA is affected by the time it takes the ASA to adjust. Observing the poles in Figure 5.57, it is clear that they vary more than the ASA's. The frequency changes from $11.3 rad.s^{-1}$ to $11.7 rad.s^{-1}$, while the damping ration reduces from 0.945 to 0.852. As the response is critically damped, this is not a big issue and still delivers an over-damped system. Lastly, when examining the Bode plot in Figure 5.58, a magnitude margin of 15.9dB is observed, along with a phase margin of $68.6°$. The largest magnitude deviation between plants is 1.2dB and the largest phase deviation is $5°$. The uncompensated plant had magnitude deviations of 5dB and phase deviations of $10°$. These values are not big but have been halved by the compensation and also result in a more linear magnitude response. These results thus prove that this controller is very robust against wing loss.

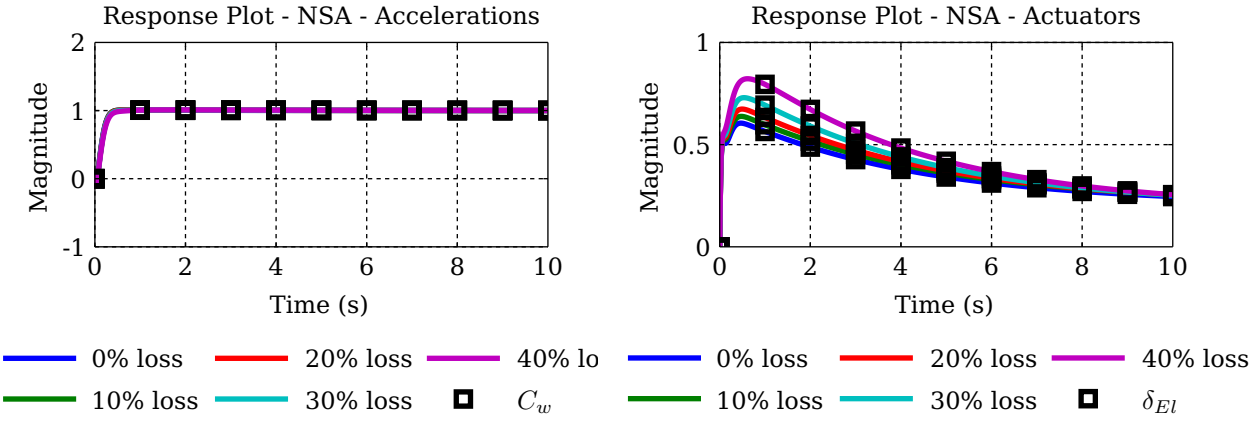

Figure 5.55 – ABC - Response - NSA - Acceleration

Figure 5.56 – ABC - Response - NSA - Actuator

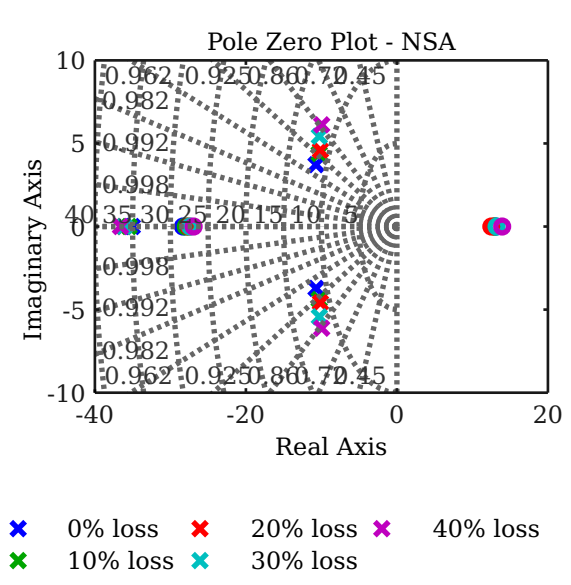

Figure 5.57 – ABC - Poles - NSA

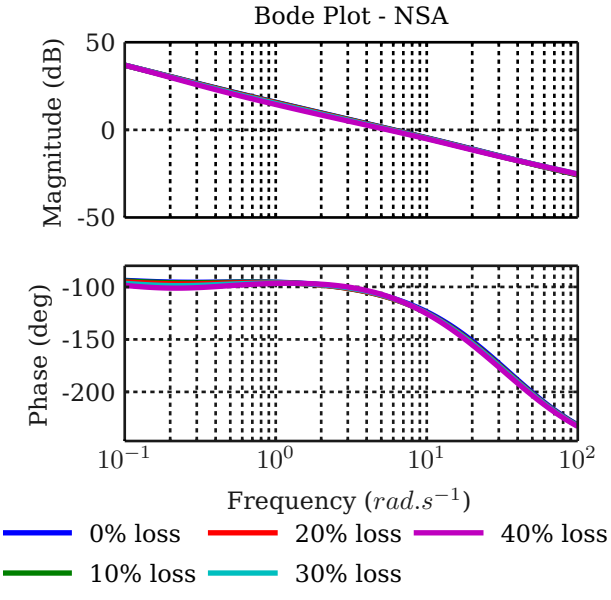

Figure 5.58 – ABC - Bode - NSA

5.2.4.3 Lateral Specific Acceleration Controller (LSA)

The results of the LSA compensated system can be found in Figures 5.59 to 5.61. The closed-loop step response of the LSA controller for different wing loss percentages is shown in Figures 5.59 and 5.60. The closed-loop pole plot of the LSA controller as a function of percentage wing loss is shown in Figures 5.61. The Bode plot of the open-loop transfer function of the LSA controller for different wing loss percentages is shown in Figure 5.67.

When examining the response, it is clear that this regulation controller does not fare very well. It has been designed with a damping ratio of 0.707 but depicts a ratio of far below 0.6. Observing the pole plot in Figure 5.61, it can be seen that the poles do exist in the frequency range they were designed for but with less than half the damping. This is due to the added integrator dynamics. As [1] stated, the rudder is a highly ineffective surface to use, especially on this UAV. In order to find a better solution, the regulation part of the LSA was removed, thus only keeping the stabilisation part. This is done by removing the integrator and not commanding the lateral acceleration but only the output as feedback. Eigenvalue excitation can then be used to acquire comparable responses. This is done by initialising a plant with a set of eigenvalues that dominantly excite a desired output. Figures 5.63 to 5.66 depict these stabilisation results. The first set includes the regulation compensator, while the second does not. It is clear from the response that the stabiliser on its own fares quite well but the regulator causes some trouble in the plant. This is also supported by the comparison of the poles between the two implementations. As stated in the LSA design section, it is far better to use the LSA purely for stabilisation instead of regulation and thus it will be implemented as such.

It is clear from Figure 5.68, that the plant is very stable, suppressing most of the low frequency range and stabilising on the higher frequency range. This is good, as the compensator will only remove those frequencies known to cause excitation of the poles. The response itself also varies with only 0.7dB in magnitude and 1° in phase and this proves that the plant is stable.

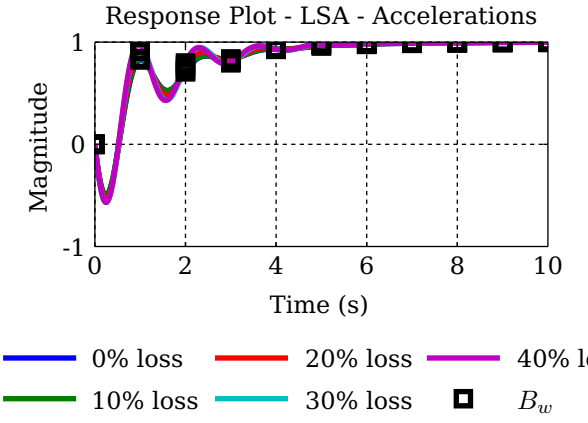

Figure 5.59 – ABC - Response - LSA - Acceleration

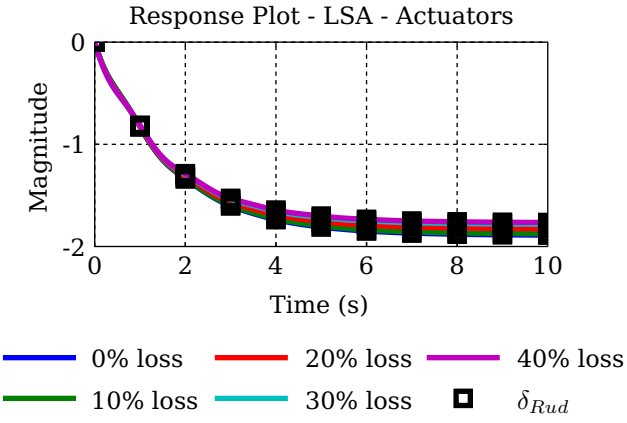

Figure 5.60 – ABC - Response - LSA - Actuator

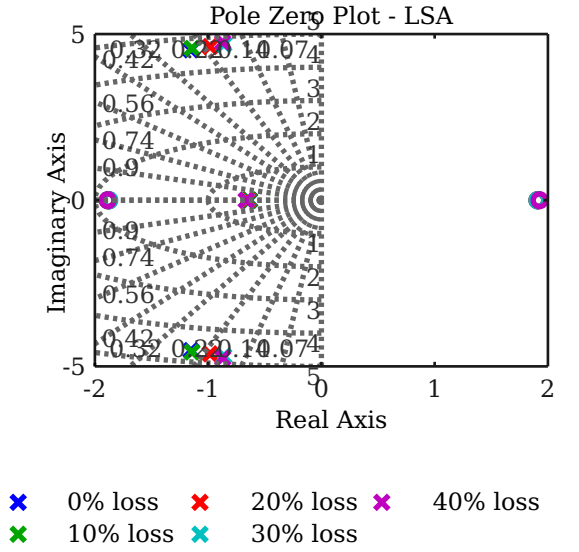

Figure 5.61 – ABC - Poles - LSA - Full Regulation

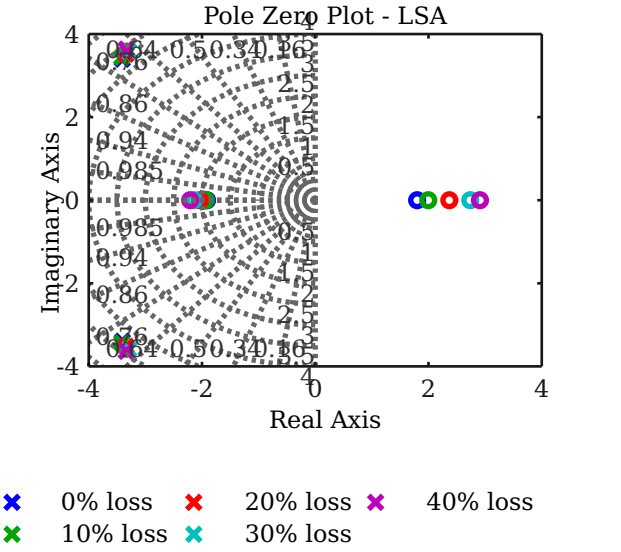

Figure 5.62 – ABC - Poles - LSA - Stabilisation

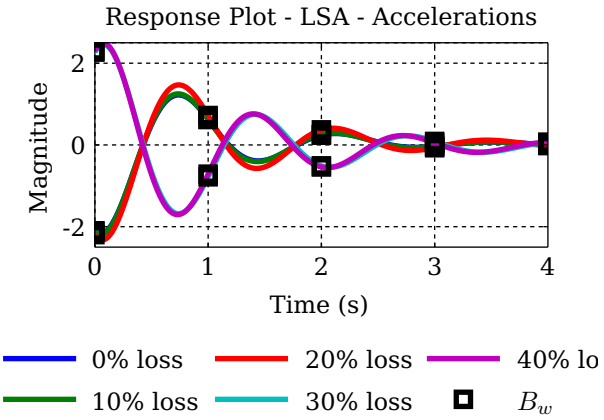

Figure 5.63 – ABC - Response - LSA - Acceleration - Eigenvalue Excitation

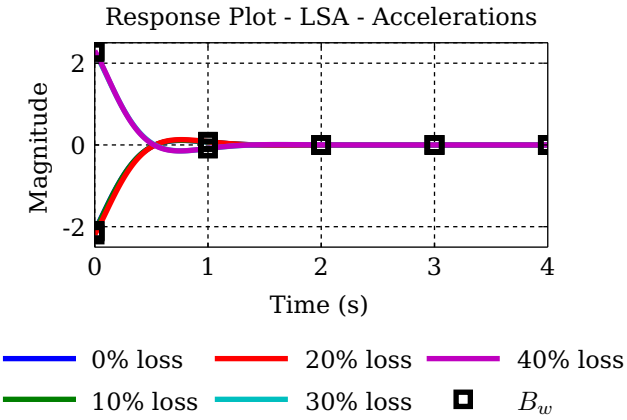

Figure 5.64 – ABC - Response - LSA - Actuator - Eigenvalue Excitation

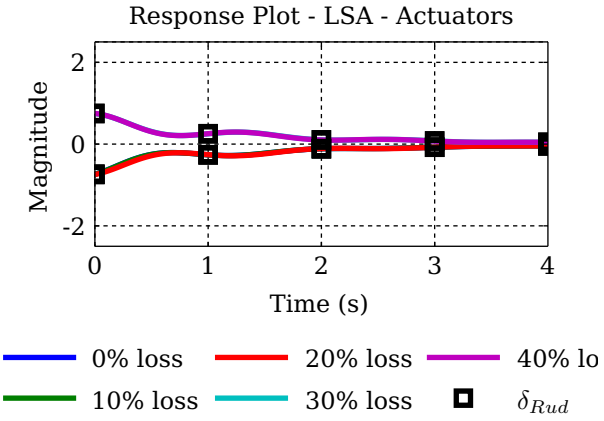

Figure 5.65 – ABC - Response - LSA - Full Regulation - Actuators - Eigenvalue Excitation

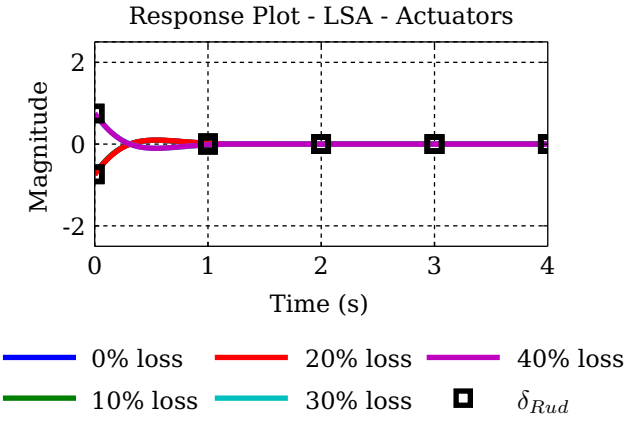

Figure 5.66 – ABC - Response - LSA - Stabilisation - Actuators - Eigenvalue Excitation

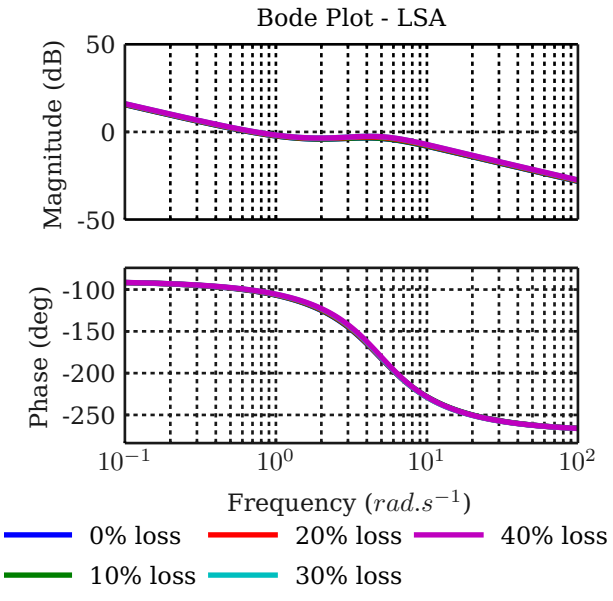

Figure 5.67 – ABC - Bode - LSA - Full Regulation

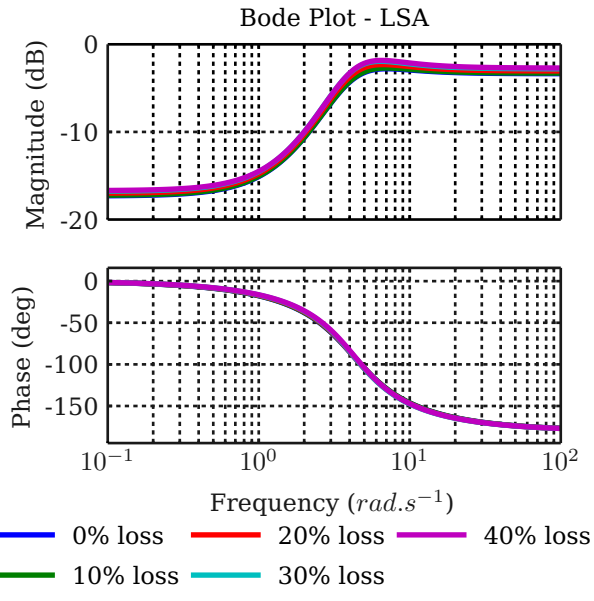

Figure 5.68 – ABC - Bode - LSA - Stabilisation

5.2.4.4 Roll Rate Controller (RRC)

The results of the RRC system can be found in Figures 5.69 to 5.72. The closed-loop step response of the RRC controller for different wing loss percentages is shown in Figures 5.69 and 5.70. The closed-loop pole plot of the RRC controller as a function of percentage wing loss is shown in Figures 5.71. The Bode plot of the open-loop transfer function of the RRC controller for different wing loss percentages is shown in Figure 5.72.

When examining the response, it can be seen that the RRC acts extremely fast just as designed. It shows little deviation in responses over the range of percentage wing loss but requires almost double the amount of initial actuator deflection at 40% wing loss. This might be a bit excessive in some cases and causes the response to run out of control authority. The response itself does however fare well between the different cases. When observing the poles in Figure 5.71, the response observed becomes clear as some of the pole-zero cancellation pairs start to diverge from each other. These pairs thus start to influence the response. Lastly, the Bode response in Figure 5.72 shows a fairly linear response over the frequency range with a minimum phase margin of $75°$. Infinite gain margin is observed due to no $-180°$ line crossing. The response hardly differs for most of the frequency range but starts to diverge by 4dB at the end. The same can be said for the phase, which differs $25°$ at the end. This is by far the most varying controller but still behaves in a stable manner.

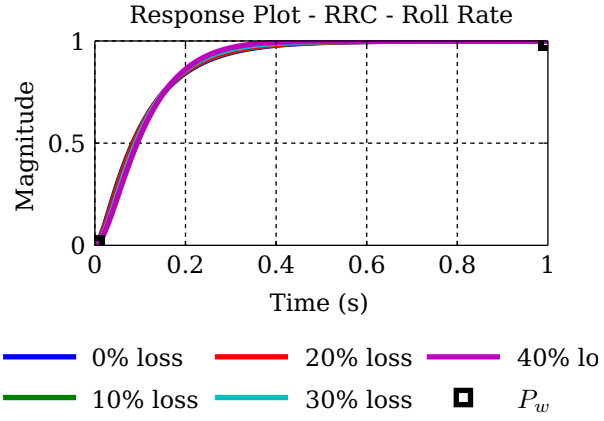

Figure 5.69 – ABC - Response - RRC - Rate

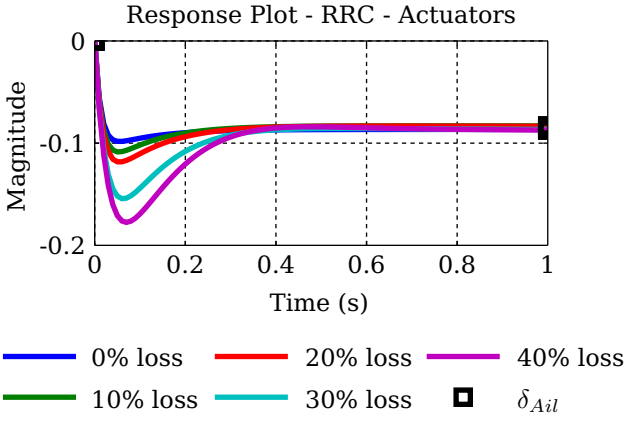

Figure 5.70 – ABC - Response - RRC - Actuator

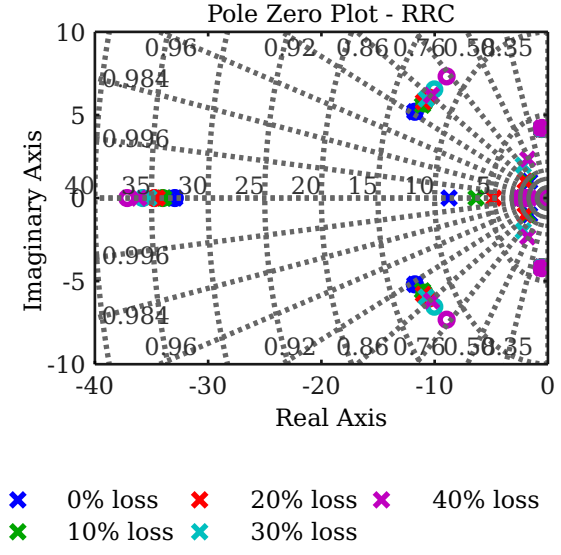

Figure 5.71 – ABC - Poles - RRC

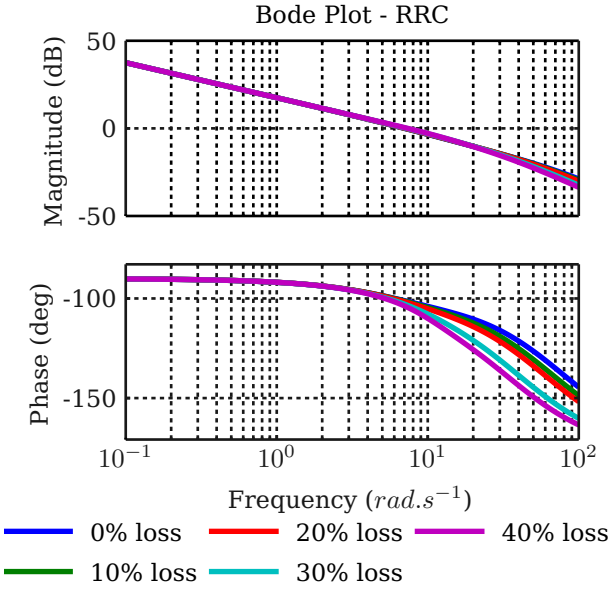

Figure 5.72 – ABC - Bode - RRC

5.2.4.5 Velocity and Position

As stated in the velocity and position controller design section, these controllers are abstracted from the UAV's dynamics. Between them, the outer-loop controllers, and the ABC, the inner-loop controllers, two non-linear transformations occur. This makes normal stability analysis inaccurate as the non-linearities bring in undefined dynamics. [1] stated that if a TSS can be enforced between the inner- and outer-loops, the inner-loop dynamics should not affect these controllers and they should be stable and robust in response.

The responses acquired from the axial velocity and altitude position controllers can be observed in Figures 5.73 to 5.76. It is clear from these responses that the abstraction assumption is valid and that there are nearly identical responses on both axial velocity and altitude steps over time.

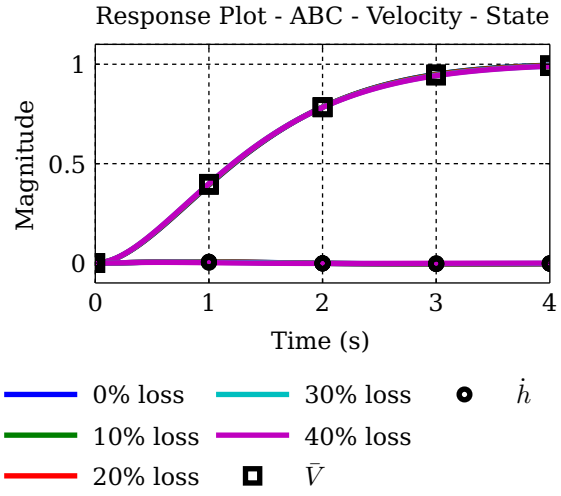

Figure 5.73 – ABC - Response - Velocity - Axial

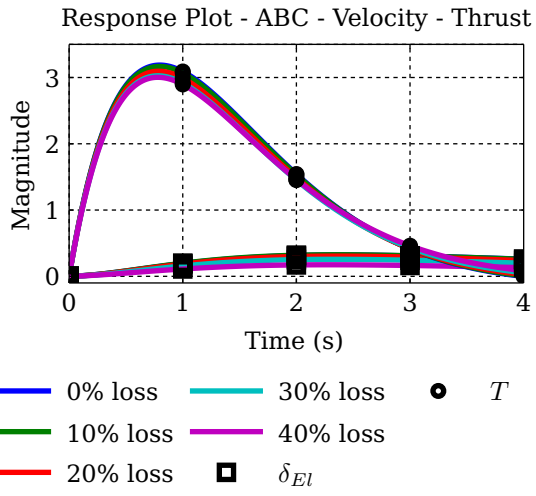

Figure 5.74 – ABC - Response - Velocity - Actuator

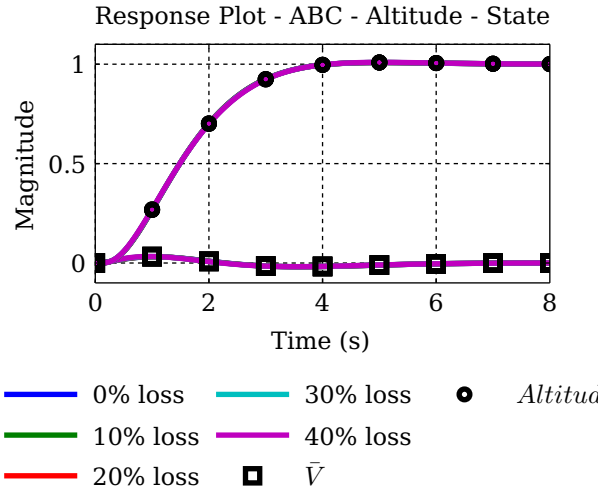

Figure 5.75 – ABC - Response - Position - Altitude

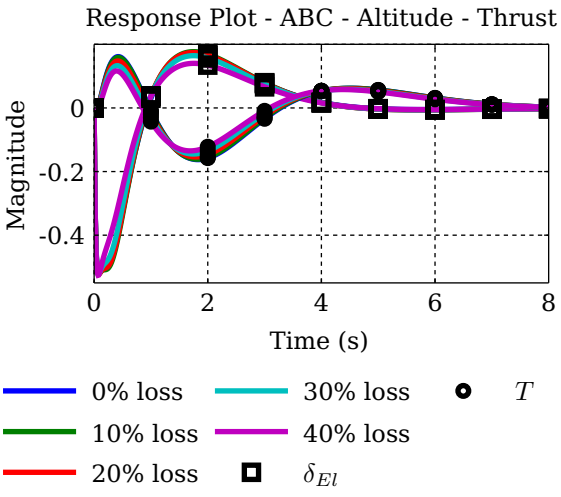

Figure 5.76 – ABC - Response - Position - Actuators

5.2.5 Possible Cross-Coupling Issues

As mentioned in Section 5.1.5, after compensation has been done on the plant, some input-output pairs need to be taken into consideration. Again, only the three dominant pairs as listed in Section 5.1.5 will be displayed here.

Figure 5.77 shows the influence of the ailerons on airspeed. As in Section 5.1.5 this input to output

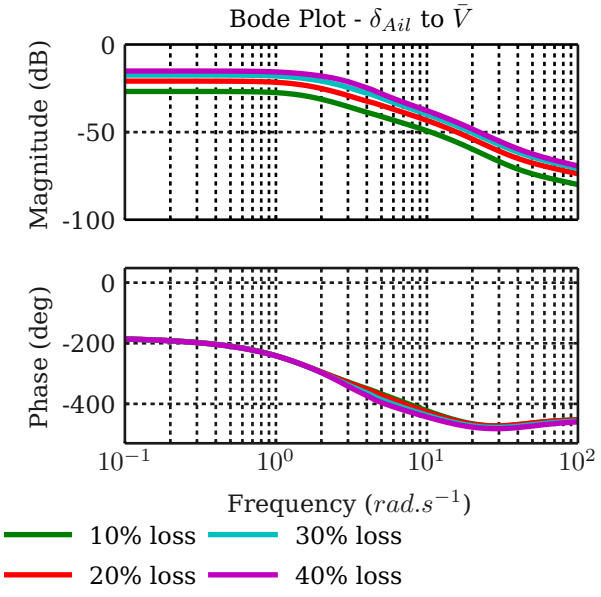

Figure 5.77 – ABC - Bode - δ_{Ail} to $\bar{V}$

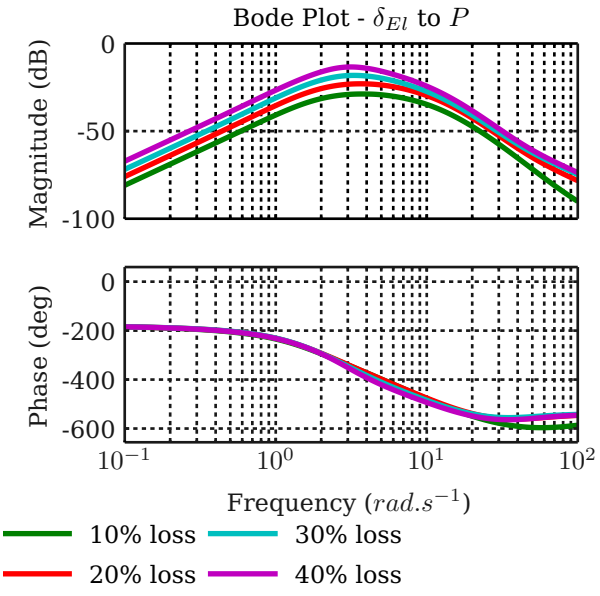

Figure 5.78 – ABC - Bode - δ_{El} to P

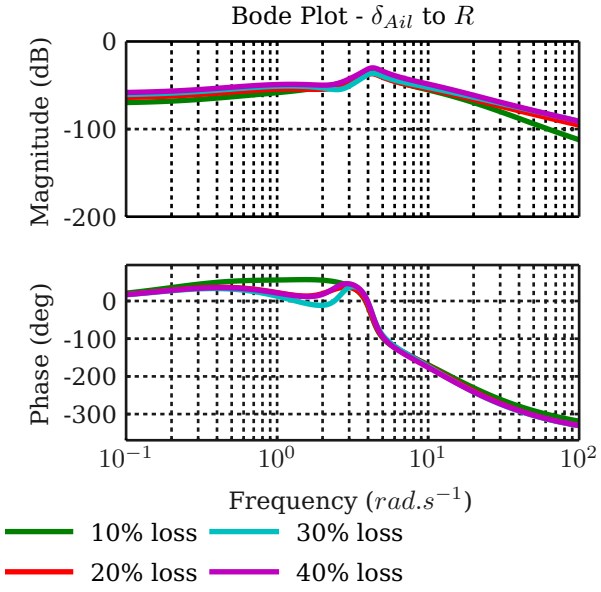

Figure 5.79 – ABC - Bode - δ_{El} to R

pair is suppressed, with a maximum gain of -15.1dB and a gain variation of 12.4dB.

Figure 5.78 shows the influence of the elevator on roll rate. This response has a peak gain of -13dB, with a gain variation of 14.6dB. This equals a 33.1dB suppression from the uncompensated open-loop dynamics and can be assumed uncoupled.

Figure 5.79 shows the influence of the elevator on yaw rate. The response peaks at a gain of -30.4dB, with a gain variation of 10dB. Again, this is a large suppression from input to output, should not cause any disturbances and can be assumed uncoupled.

5.2.6 Conclusion

In this section an acceleration based design was followed. This design implements integrators at the lowest levels to reject disturbances and capture model uncertainties. Axial and normal accelerations are regulated extremely well but only stabilisation proves to be a viable option on lateral acceleration. The roll rate and angle controller also fare quite well. The Bode plots show that the controllers have large gain

and phase margins relative to the expected plant gain and phase variations over the range of percentage wing loss. Abstracting the velocity and position controllers on top of these inner-loop controllers, results in almost identical responses over the various cases of partial wing loss. It is thus believed that these controllers will be robust against partial wing loss, with their capability to encapsulate any model uncertainty at low level.

5.3 Practical Architecture

As concluded in the previous two sections, both control sets yield stable results over the partial wing loss cases of interest. This leads to the conclusion that explicit robust design methods are not needed for this particular UAV or scalable model thereof. The practical system can thus be implemented with either of the two control architectures or a combination thereof.

The analysis in this chapter can be used as a baseline in this decision. Both control architectures delivered acceptable results. The classic architecture used root locus shaping to acquire the best performance possible, while the acceleration based architecture used knowledge of the plant poles to determine acceptable pole locations.

The airspeed controller in the classical architecture is favourable above the ASA due to having the same underlying architecture and not requiring an additional airspeed controller. Looking at the cross-coupling to airspeed in Sections 5.1.5 and 5.2.5, the classical airspeed better suppresses external disturbances.

When examining the NSA with climb rate controller vs PRD with climb rate controller, it is found that the NSA is favourable. It provides a lower level of disturbance rejection due to its integrator which will remove any steady state errors. The PRD with climb rate controller can also remove any steady state errors but its integrator is situated one level higher. Choosing the NSA and climb rate controller also allows ABC's normal specific acceleration vector direction changing algorithm (NSAVDC) to easily implement bank to turn commands.

When examining the DRD vs LSA, there is really no determining factor. As the DRD has been successfully implemented on the aircraft in the past, it was decided to stick to a working product.

When examining the classical roll angle controller vs the ABC roll rate angle controller, it is clear that the ABC version is favourable. This controller explicitly takes the roll rate dynamics in account when designing the roll angle controller. The controller is presented in a much more elegantly way than the classic one.

Concluding the choices for the inner loop controllers, higher level guidance controllers are necessary for practical flight testing. The ABC's position controllers require a predefined path to follow and command accelerations based on the aircraft's divergence from this path. This requires direct access to command accelerations, which the current hybrid architecture does not support. A second option is a normal cross-track error algorithm. This algorithm receives two waypoints and navigates a straight line, with a circle turn once it reaches the second waypoint, and is fairly simple. A third option is the non-linear guidance controller designed by Sanghyuk Park. It is a fairly simple algorithm that follows a point in front of the aircraft and is said to reduce cross-track errors better than the plain cross-track algorithm. Upon reviewing these options, the Sanghyuk non-linear controller seemed the best.

The list below provides a condensed version of the practical control architecture that will be implemented on the UAV:

- An airspeed controller will be implemented like the one described in Section 5.1.2.2
- A NSA controller as described in Section 5.2.1.2 will be implemented to regulate normal specific accelerations
- A climb-rate and altitude controller as described in Section 5.1.2.2 & 5.1.2.3
- A DRD as designed in Section 5.1.3.1
- A roll rate and angle as described in Section 5.2.1.4

- A simplified version of the SAT and NSAVDC as will be described in Section 5.3.2
- Sanghyuk's non-linear guidance controller as will be described in Section 5.3.3
- Lastly, a waypoint system will be included to allow full circuit navigation. This is implemented in parallel to the above mentioned guidance controller

5.3.1 Robustness of Controllers to Partial Wing Loss

Figure 5.80 depicts the practical control setup. All the controllers were implemented with the design specifications as done in Sections 5.1 and 5.2. This figure is divided into three categories: one, the inner-loop controllers which already have been analysed and can be found in Sections 5.1 and 5.2. This can be observed in the blue block. Two, the change made due to the hybrid NSA, climb rate and altitude controller combination. The robustness of the climb rate and altitude controllers will be discussed. This can be observed in the grey block. Three, the guidance section, which only serves as a testing platform, can be observed in the yellow block.

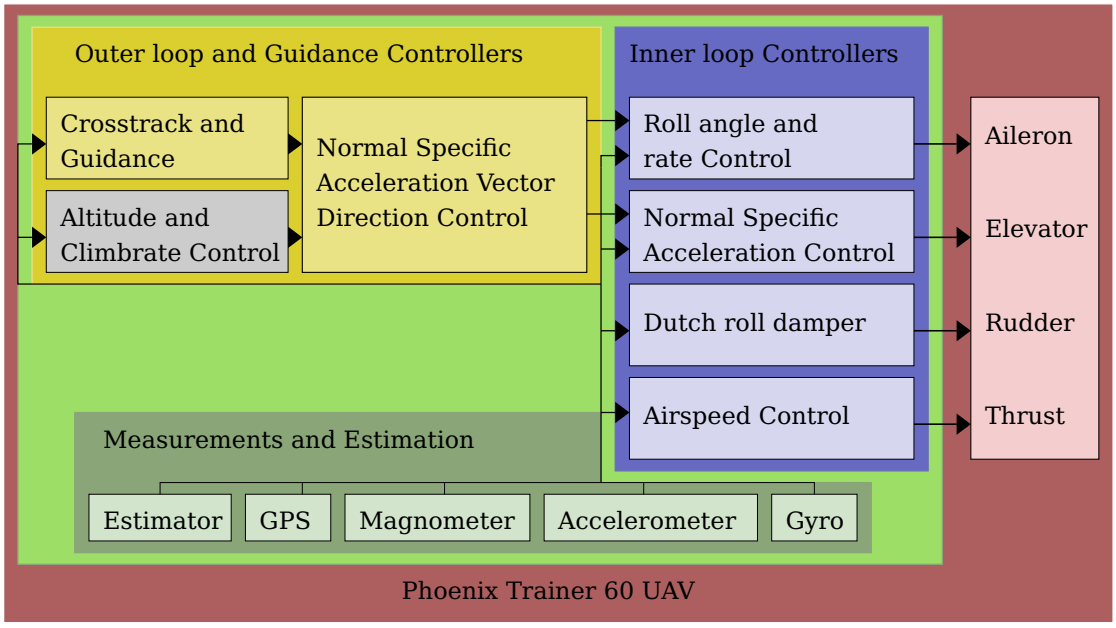

Figure 5.80 – Practical Control Architecture

5.3.1.1 Climb Rate Controller

Figure 5.81 shows the climb rate controller's bode response when implemented on a NSA controller. It is clear that in this case the climb rate controller does not cross -180° multiple times as it did in the classical control case depicted in Figure 5.22. It has a gain margin of 14.8dB, with phase margin of 61.2°. The largest variation in gain over all the cases of partial wing loss is 2.8dB while the largest variation in phase is 12°. This is a little lower than the classical case's climb rate controller's stability margins, but not by much. It should be stated that this bode analysis was done on the complete plant and not only the decoupled longitudinal one as in the case of the classical controller's case. There will thus be more variation due to some of the lateral dynamics influencing it.

5.3.1.2 Altitude Controller

Figure 5.82 shows the altitude controller's bode response when implemented on a NSA and climb rate controller. It has a gain margin of 15.4dB, with a phase margin of 46.8°. The largest variation in gain over all the cases of partial wing loss is 2.6dB while the largest variation in phase is 11°. Again, the classical case may have better margins, but not by much. This controller should however be sufficiently robust to handle partial wing loss.

Although the NSA, climb rate and altitude combination may seem a bit less robust than the classical

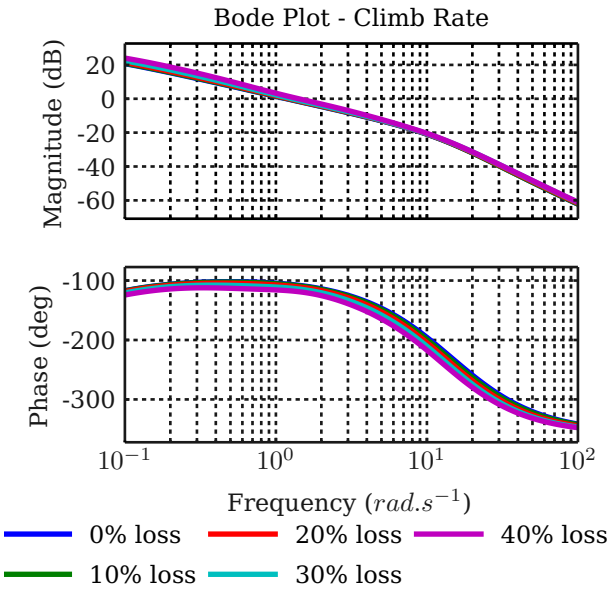

Figure 5.81

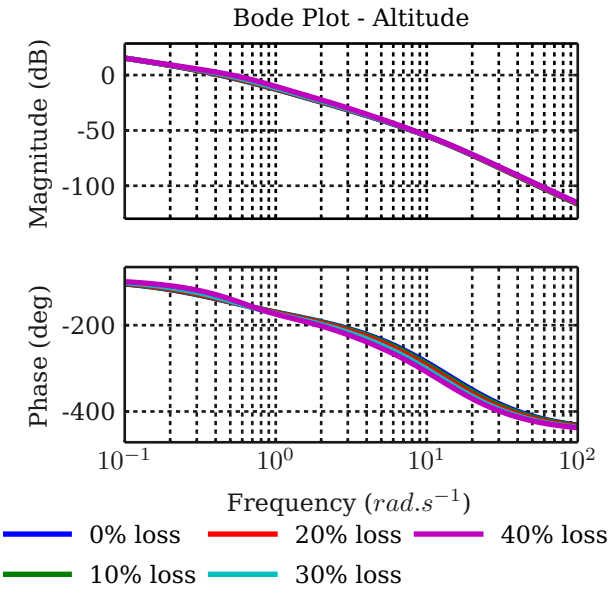

Figure 5.82

approach, they capture the model uncertainty at a lower level. As stated in Chapter 4, the result of partial wing loss revolves more around finding the new trim than compensating for large dynamic changes. As this structure captures the uncertainty faster than the normal climb rate and altitude structure does, it should find the new trim on the elevator faster.

5.3.2 SAT and NSAVDC

When examining the NSAVDC as described in [1], one requires DCM vectors, a jerk vector, which is the derivative of the commanded accelerations, the commanded acceleration vector and a reference commanded C_W unit vector. The implementation as described above allows acrobatic manoeuvres to be performed, such as inverted flight etc. This is highly unlikely and thus unnecessary for the problem defined in this thesis. A simplified version of the NSAVDC will be implemented as specified by the equations provided below.

The NSAVDC originally accepts an acceleration vector, which it then converts into axial and normal accelerations and a roll angle. Due to no ASA being implemented, the controller no longer needs to accept or produce an axial acceleration. It will thus combine the lateral and normal accelerations into only a normal acceleration, accompanied by the angle between them. The total normal acceleration can be calculated as follows:

$$C_R = \sqrt{B_W^2 + C_W^2} \tag{5.3.1}$$

The angle between the lateral and normal accelerations can be calculated by,

$$\phi = sin(B_W / C_R) \tag{5.3.2}$$

Although all the mathematical corrections necessary for inverted flight are not taken into account during this method, it proves to work just as well as long as the UAV does not roll over $\pm 90°$.

5.3.3 Non-linear Guidance Controller

The non-linear guidance controller for cross-track errors was invented by Sanghyuk Park [23] as an alternative to the normal linear cross-track error implementation. The basic principle of this controller is to follow a point x metres in front of the UAV on a given track. The lateral acceleration it should apply to remove the cross-track error is given by the angle between three vectors. These vectors are: the track, the “stick” and the UAV’s airspeed direction. Using the angles obtained between the track and the stick

and the stick and the airspeed along with a sine function, generates the necessary lateral acceleration to minimise the cross-track error. This relationship can also be written in vector calculus as follows:

$$B_{cmd} = \frac{2}{|L|^2}\left(\bar{V} \times L\right) \times \bar{V} \tag{5.3.3}$$

By using this equation to remove the cross-track error from the path to follow between two points, guidance of the UAV can be achieved. This allows the implementation of full circuit navigation by defining consecutive waypoints. The non-linear cross-track error can then be used to guide the UAV onto the new waypoint leg once it is in the proximity of the end waypoint on its current leg. The problem with this transition between two waypoint legs is the instantaneous cross-track error it creates at the switch. This error can be removed by rather using the point of the stick as contact point to the track instead of the vehicle's current location.

As this is not an ideal way of navigation, further investigation into [23]'s algorithm was used to reveal how to implement circular turning. This required the "stick" to follow the circumference of a circle instead of just tracking the transition between two waypoint legs. In using a circle for the transition, the instantaneous cross-track error is removed when switching waypoint legs and this allows a planned path to be executed. The following changes are made to the angle calculated in equation 5.3.3 for circle navigation:

$$B_{cmd} = \frac{2\bar{V}^2}{L}\left(\eta_1 Cos(\eta_3) + \eta_2 Cos(\eta_3) + sin(\eta_3)\right) \tag{5.3.4}$$

$$\eta_1 = \frac{d}{L} Cos(\eta_3) \tag{5.3.5}$$

$$\eta_2 = \frac{\dot{d}}{\bar{V}} \tag{5.3.6}$$

$$\eta_3 = -\frac{1}{2} aCos\left(\frac{L^2 - R^2 - (R+d)^2}{2(R)(R+d)}\right) \tag{5.3.7}$$

In the equations above, d is the cross-track error from the UAV's current position to the circle's circumference if a line is drawn through the circle's centre, $\dot{d}$ is the rate of change of d and R is the circle's radius.

5.4 Chapter Summary and Conclusion

In this chapter, two methods of UAV control system design were followed in an attempt to gain enough knowledge about the standard methods' robustness against wing loss. It was concluded that both the classical and in-house acceleration based control provided sufficient robustness against wing loss to exclude the necessity for full on robust design methods.

A control architecture which is a hybrid between the two methods, was implemented. This was done due to previous knowledge of similar controllers implemented on the UAV in the past and also the ease of implementation. As all of the above point to a stable and fairly robust system, the transients between the nominal and wing loss cases can now be investigated in both software in the loop (SIL) and hardware in the loop (HIL) simulations, after which enough confidence in the system should exist to allow practical vehicle flight tests.

Chapter 6

Non-Linear Simulation

In this chapter non-linear simulations are performed to verify the robustness and performance of the flight control system in preparation for actual flight testing. The two main methods used for this are software-in-the-loop (SIL) and hardware-in-the-loop (HIL) simulations. The chapter will be divided as follows: First a short description of how SIL and HIL are conducted will be given. After this the SIL simulation will be conducted, followed by HIL simulations. To conclude there will be an evaluation of the results.

6.1 Description of SIL and HIL Environments

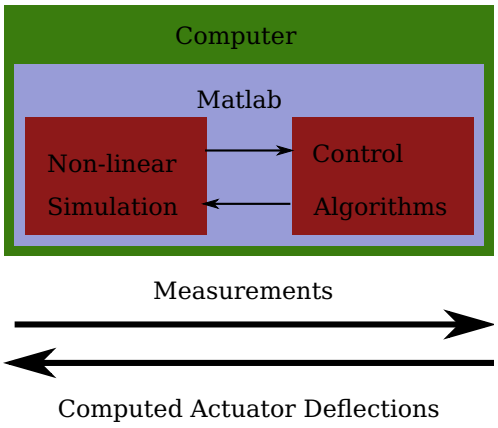

Figure 6.1 – Hardware in the Loop Simulation Setup

SIL is a complete software simulation. A full non-linear simulation model of the UAV flight dynamics, both symmetric and asymmetric, was created as a Matlab Simulink block diagram. A simulation of the flight control system was then added. At first the control architecture was built with Simulink blocks and later it was coded into the format as required by the OBC software. The coded version was also simulated in the Simulink environment. After successfully verifying the flight control system in software, the coded version was ported to the UAV's OBC in order to also verify it in HIL simulations.

HIL simulations involve connecting the UAV's OBC to Matlab with a HIL-board. The HIL board is connected to either a COM- or USB-port on the computer and allows communication with Matlab. On the other end of the HIL board a connection to the OBC is made. This connection allows all sensor data to be "faked" onto the CAN-bus and UART and thus allowed real-time simulation and verification before taking the complete UAV out for practical flight tests. In the following section, the practical system's capability to perform circuit navigation will be shown and also the transients associated with wing loss will be discussed.

6.2 Simulation Results

In this section the results obtained from both SIL and HIL simulation will be presented. It should be noted that the SIL simulation was conducted without any noise added to the sensor measurements and without

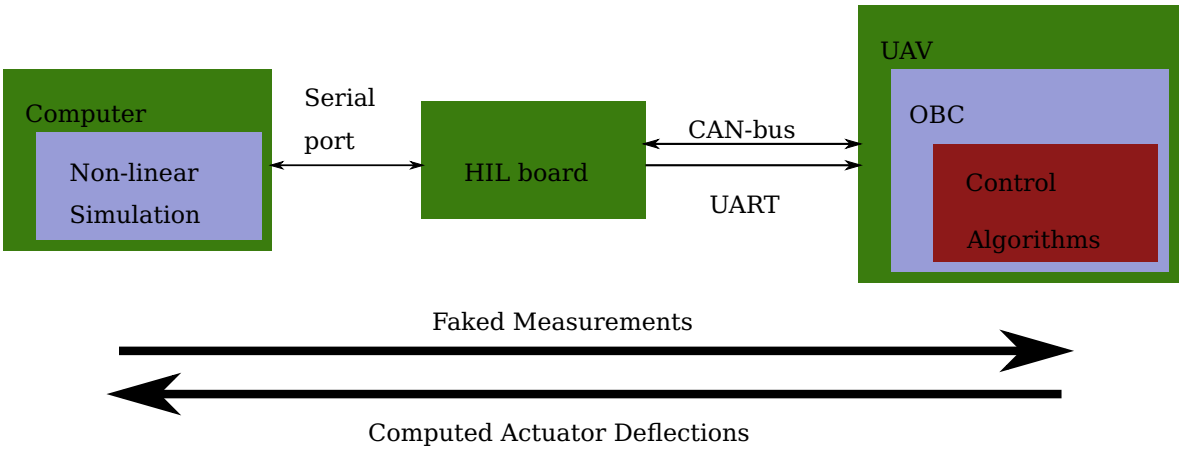

Figure 6.2 – Hardware in the Loop Simulation Setup

simulated wind disturbances. This was done to provide a clear benchmark of the designed controller architecture's performance. However, the HIL simulation included both measurement noise and simulated wind gusts.

These simulations are conducted for a few reasons. One, they should verify that the control algorithm has been correctly implemented. Two, they should provide insight into how the UAV will react to instantaneous partial wing loss, particularly in terms of the transients experienced due to the change in model from symmetric to asymmetric. It is expected that the UAV will swerve to the left and recover to its original path. It should also experience a loss in altitude and recover. Three, the control architecture should find the new trim. This should be visible as a bias on the ailerons and a slight bias change in thrust and elevator. Having verified this, the necessary confidence will be gained to proceed with practical flight tests.

6.2.1 Software in the Loop Simulation (SIL)

In real life damage can occur at any time and this could include take-off, landing, straight flight, turning etc. As this thesis is mainly concerned with the robustness of the UAV's control system, only straight flight and turning will be simulated.

In this simulation the UAV will fly a 600m x 150m circuit in a counter-clockwise manor. Figure 6.3 is an illustration of the actual flight path where loss is instigated 35 seconds into the flight. This point in time and space is represented by the little black circle on the circuit. The UAV cannot fly with more than 30% loss without the control system becoming unstable. This is because even though the UAV is trimmable up to 40% partial wing loss, the ailerons run out of control authority in one direction, as shown in Section 3. As the controller does not know about this limit, its compensation will prematurely saturate and leave it incapable of loss recovery.

Close-ups of the loss instance can be found in Figures 6.4 to 6.9. It is clear that the cross-track error is corrected within 15 second of loss. This result is quite pleasing as the UAV stays within 1.5 metres of its original path. The UAV only drops 0.15 metres in total. The transient itself shows signs of an underdamped response but stabilises as soon as the ailerons have picked up the lift imbalance.

With regard to the actuators, the trim prediction correlates closely to what is observed in the responses. Most of the disturbance is rejected by the ailerons. This is as expected due to the lift imbalance which they need to cancel out. The thrust decreases as the elevator increases. This is also as expected. The elevator deflection increases the angle of attack, thus producing more lift, at which stage the UAV will start to climb if the thrust is not decreased. Lastly, the rudder rejects and damps unwanted yaw. As no regulation is implemented, it settles back to zero.

As explained at the beginning of this section, both straight flight and turning will be simulated. Considering that the UAV is flying a circuit, this has already been performed to some extent in the above simulation.

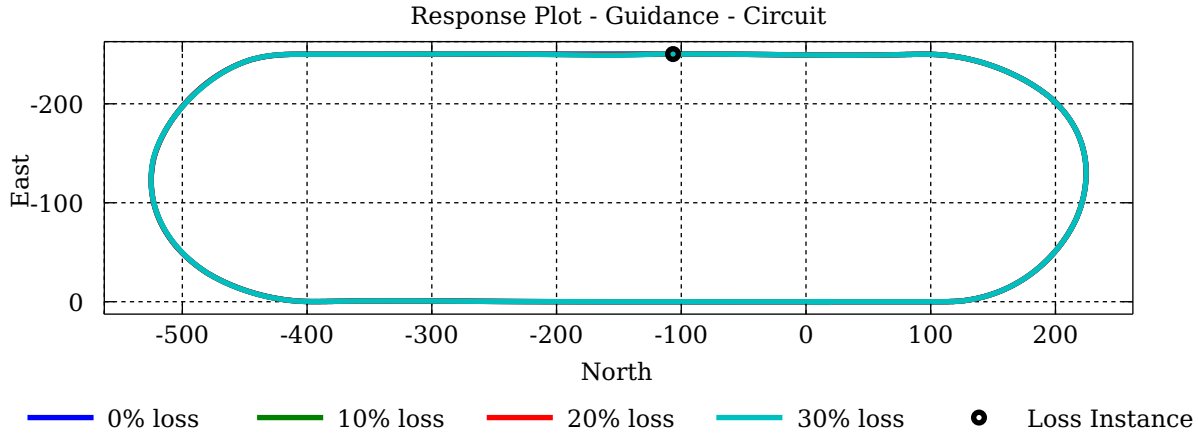

Figure 6.3 – SIL - Navigation with loss recovery

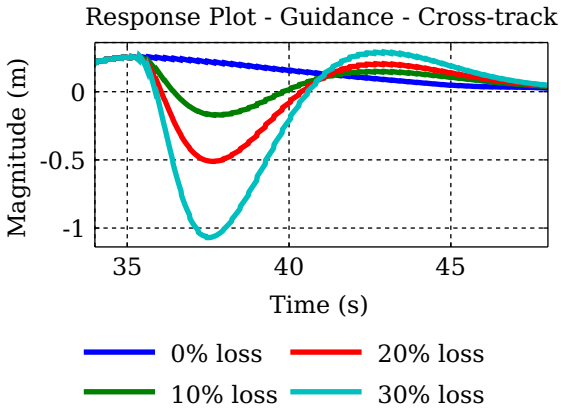

Figure 6.4 – SIL - Loss recovery - Cross-track

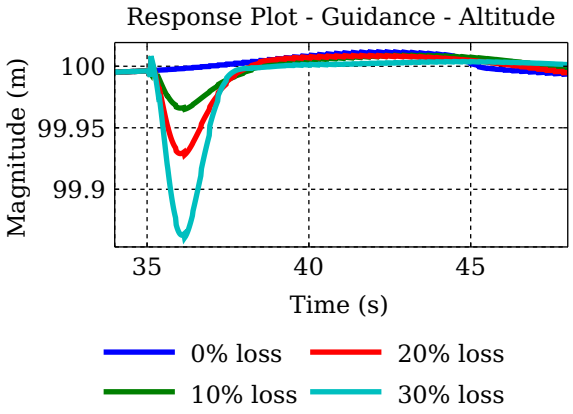

Figure 6.5 – SIL - Loss recovery - Altitude

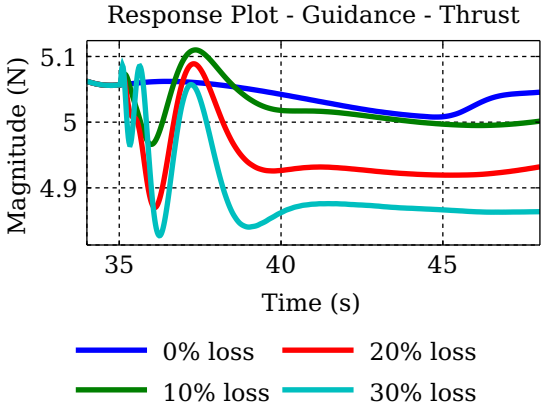

Figure 6.6 – SIL - Loss recovery - Thrust

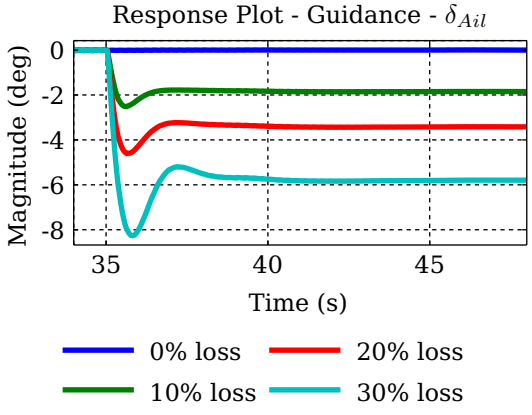

Figure 6.7 – SIL - Loss recovery - δ_{Ail}

It proved that turning posed no problem to the control system if loss occurred during straight line flight. Taking this a step further, the response of the control system will be tested with in-turn loss. Figure 6.10 shows the flown circuit, with loss in a turn. A slight deviation becomes visible just after the loss event but the control system still remains capable of keeping the UAV in the air. The cross-track error, depicted in Figure 6.11, is larger than in the straight line case. This is expected as the UAV is already manoeuvring around a turn and thus its attitude is biased on roll angle. This is expected as the control system does not know that there is a roll bias on the partially lost wing's side. The commands issued for positive and negative roll are the same but will induce different responses due to the partial wing generating less lift. The cross track error is however reduced over time and stays well within acceptable limits.

Figure 6.12 shows the altitude and it is clear that a larger drop occurs after loss than shown in Figure 6.5.

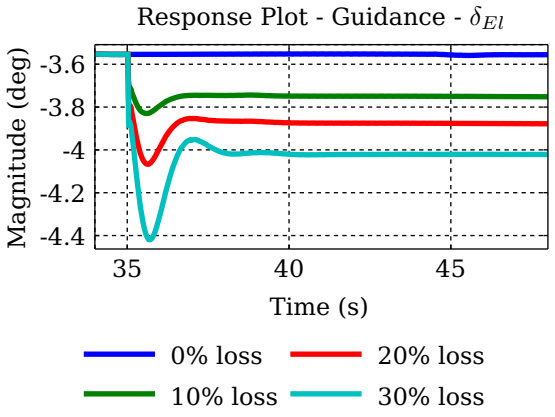

Figure 6.8 – SIL - Loss recovery - δ_{El}

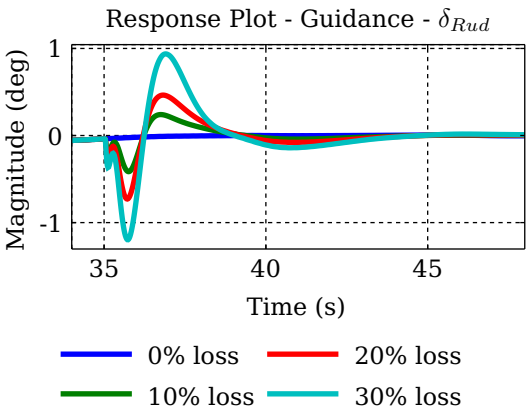

Figure 6.9 – SIL - Loss recovery - δ_{Rud}

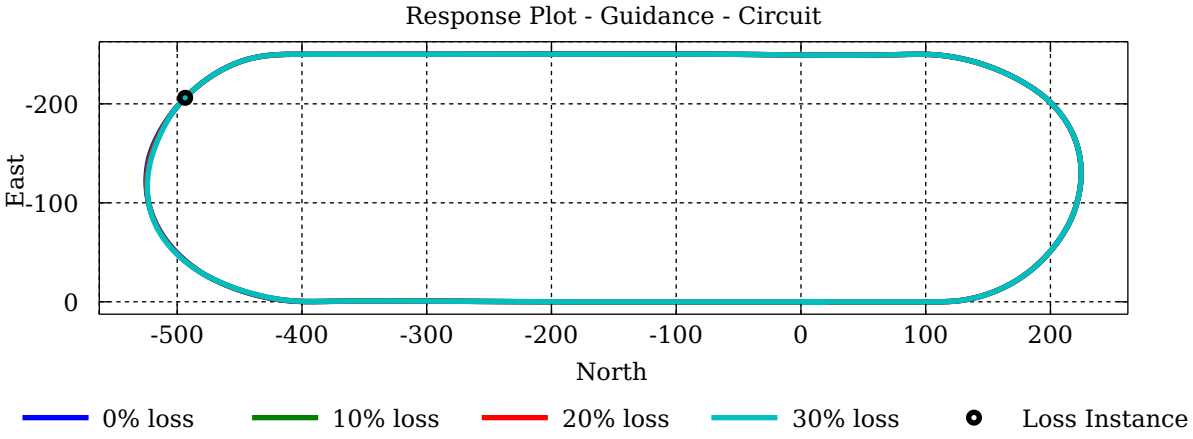

Figure 6.10 – SIL - Navigation with in-turn loss recovery

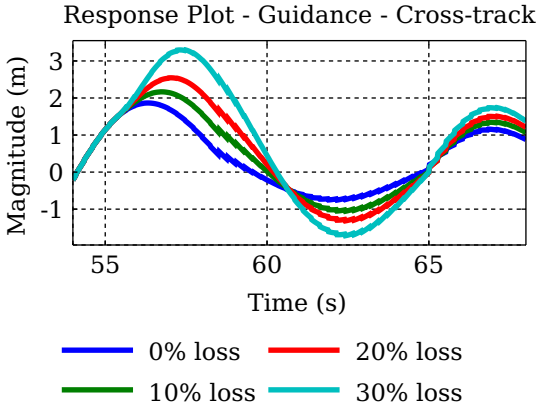

Figure 6.11 – SIL - Loss recovery - Cross-track

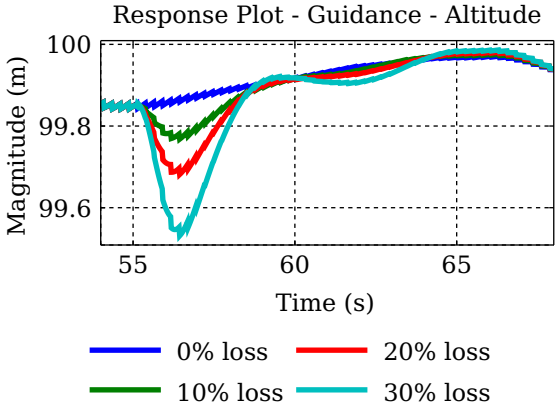

Figure 6.12 – SIL - Loss recovery - Altitude

Although the drop is larger, it is still relatively small and can easily be explained. As the ailerons are used to negate the difference in lift, it takes a second or two for the controller's integrator to zero out the steady state error. Due to the UAV being in a turn, the effect of an increase roll angle decreases the ability of the NSAVDC to provide the correct command to the NSA controller. As soon as the RRC has found this new steady state, the NSAVDC can now predict the a more correct NSA and the NSA controller can begin to restore the difference in altitude.

Figures 6.13 to 6.16 depict the actuator responses. It is clear that the actuators are commanded far more often than in the straight line case. As all of the controllers' integrators have not yet zeroed out all of the steady state errors introduced by the loss, different transients are observed due to reinitialisation on the last part of the turn at roughly $65s$. This reinitialisation is due to the guidance controller switching

between waypoint legs, and initialises a new guidance trajectory axis. Although the commanding vector's magnitude stays fixed, the orientation changes a little, which causes a slightly bigger cross-track error.

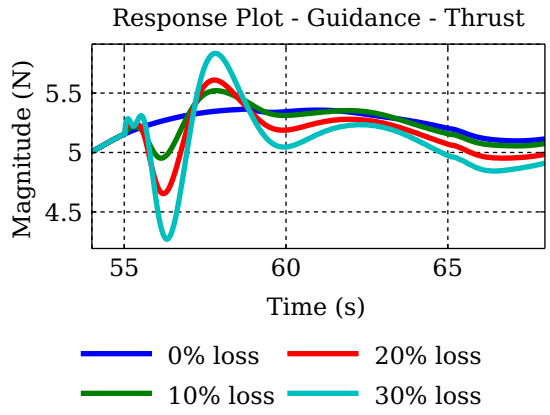

Figure 6.13 – SIL - Loss recovery - Thrust

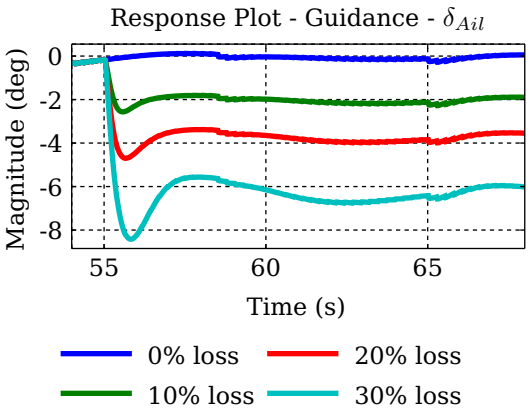

Figure 6.14 – SIL - Loss recovery - δ_{Ail}

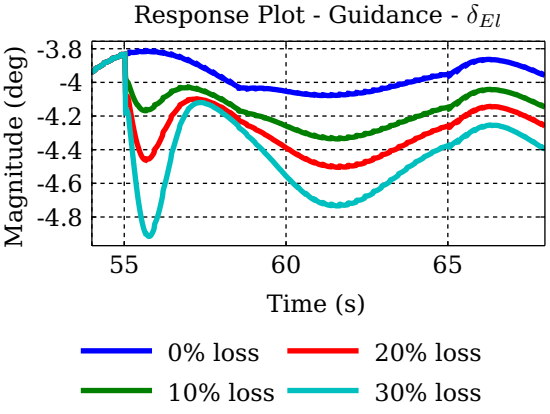

Figure 6.15 – SIL - Loss recovery - δ_{El}

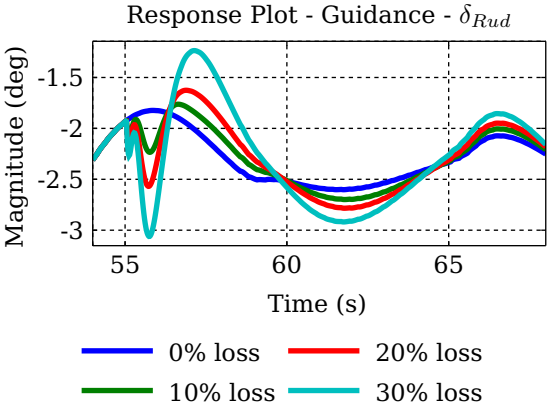

Figure 6.16 – SIL - Loss recovery - δ_{Rud}

Taking both the straight line loss and turn loss into account, it is clear that the control architecture is capable of handling instantaneous wing loss under circuit navigation. It is also capable of handling both the transients introduced by the instantaneous loss of part of the wing, zeroing out the steady state errors and thus finding the new trim location. Upon the successful executing of these simulations, the control code can now be transferred to the OBC for HIL simulation.

6.2.2 Hardware in the Loop Simulation (HIL)

As it was verified in the previous section that the system is capable of handling in-flight wing loss, the hardware in the loop simulation of the actual flight tests will be described in this section. External disturbances such as measurement noise and wind will be introduced. The simulation will only be conducted for the 20% loss case on a straight leg. 20% wing loss provides a safe environment for the safety pilot to do manual upset recovery should something go wrong during testing.

The HIL simulation structure allows testing the UAV's physical hardware before taking the UAV out for a practical flight. In the HIL simulation, the UAV's OBC does all the computations from virtual sensor measurements and also deflects the hardware servos accordingly. This enables verification of the virtual flight behaviour with physical deflections of the UAV's control surfaces.

The following set of figures depicts the responses obtained during wing loss. Figure 6.17 shows the circuit flown and closely resembles the SIL simulation's circuit. Figures 6.18 & 6.19 display the cross

track error and altitude. It is clear in these figures that disturbances are present and prevent a clear view of the impact of wing loss. It can however be observed that a slight degradation in both cross-track error and altitude take place. This result is in some ways similar to that depicted in Figures 6.4 & 6.5. It should be noted that the jaggedness observed in altitude and cross-track error is mostly due to the slow GPS updates, and influences the estimates made by the estimator. The estimator propagates using accelerometers, gyroscopes and velocity measurements inbetween every GPS update. These measurements are less trusted than the GPS and thus the estimator corrects its estimate with every GPS measurement received.

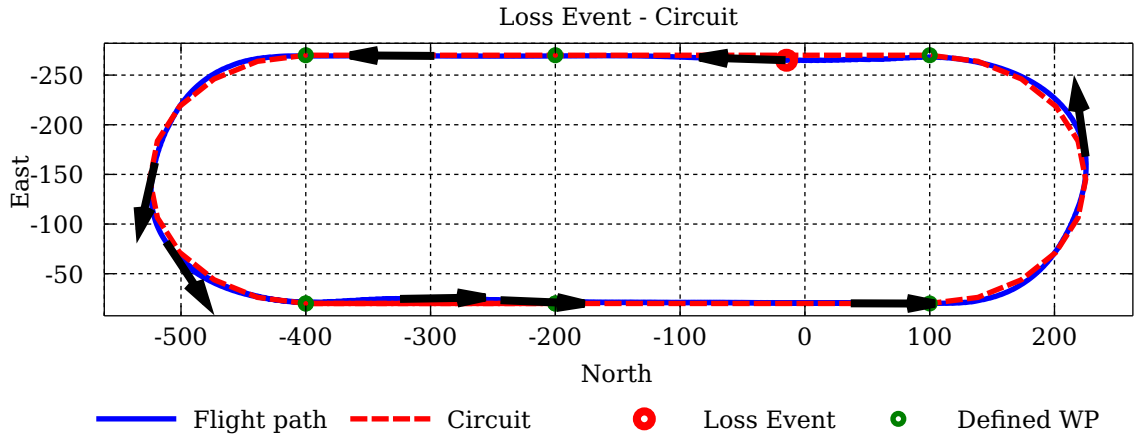

Figure 6.17 – HIL - Navigation with loss recovery

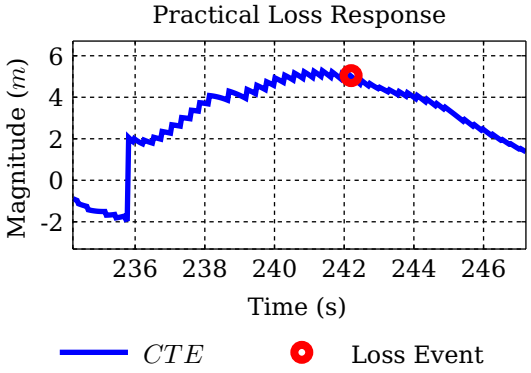

Figure 6.18 – HIL - Loss recovery - Cross-track

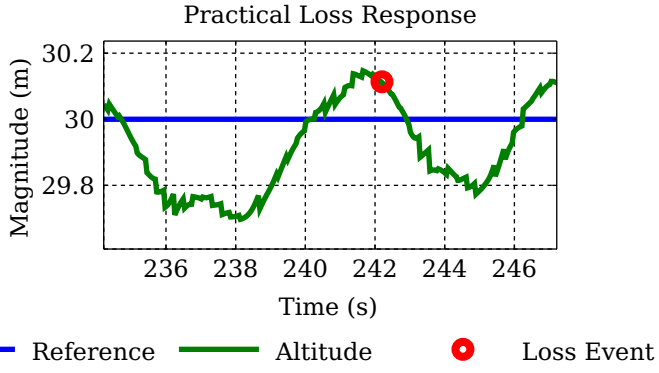

Figure 6.19 – HIL - Loss recovery - Altitude

Figures 6.20 to 6.23 depict the actuator responses. The thrust is too noisy to allow us to observe any valuable information in the data. The noise makes it seem very aggressive. A clear bias is visible on the ailerons. This bias also closely resembles that of the 20% case in Figure 6.7. The elevator's response seems a bit off but it is clear that it's actively rejecting external disturbances. A change in actuator can however be observed and correlates to the response as seen in Figure 6.8. The rudder also behaves as expected.

It is thus clear from the above results that the system can handle a noisy environment. The hardware used in the UAV is also able to compute the control laws and issue the necessary actuator command needed to regulate the UAV's behaviour and reject disturbances.

6.3 Evaluation

In this section various cases of wing loss have been simulated. These cases were conducted with both in-turn and straight flight loss instances. The control architecture was successful over all cases tested. This success provided confidence in the ability of the control architecture to handle the transients between the nominal full wing case and the off-nominal wing loss cases. The simulations also depicted that if the

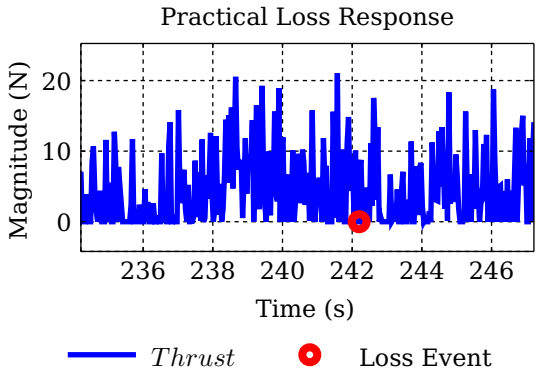

Figure 6.20 – HIL - Loss recovery - Thrust

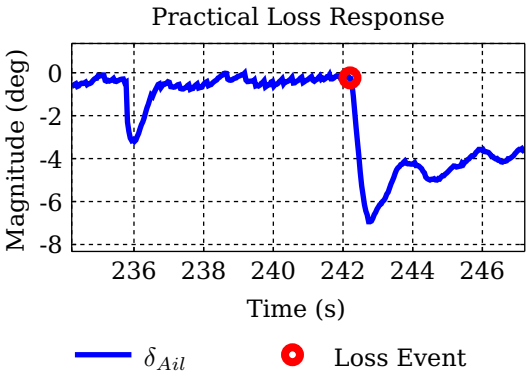

Figure 6.21 – HIL - Loss recovery - δ_{Ail}

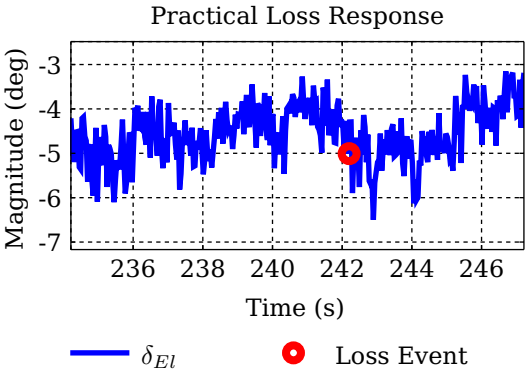

Figure 6.22 – HIL - Loss recovery - δ_{El}

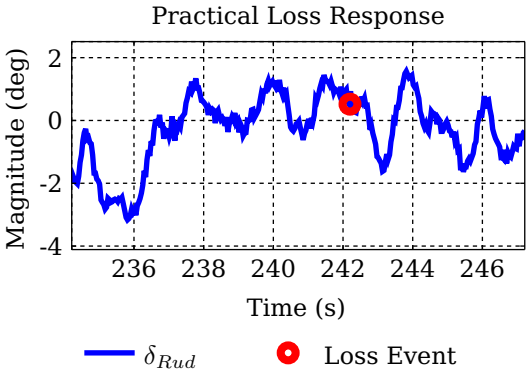

Figure 6.23 – HIL - Loss recovery - δ_{Rud}

difference in lift has not yet been negated by the ailerons, wing loss in a turn will cause a larger drop in altitude than it would in straight flight. The drop itself is however relatively small and easily recoverable.

Chapter 7

Hardware, Firmware and Software of the Demonstration Vehicle

In this chapter the modifications done on the UAV acquired for this research will be described. As this UAV has been in the ESL for quite some time, a basic description of the existing system will be provided before stating the modifications. The main physical change to the UAV, namely to its wing, will be discussed. The changes to the firmware on various of the avionics components will be stated and also the changes to ground station software.

7.1 UAV Background

The ESL provides various vehicles for the testing of projects. One of these vehicles is a Trainer 60 aircraft names Phoenix, see Figure 7.1.

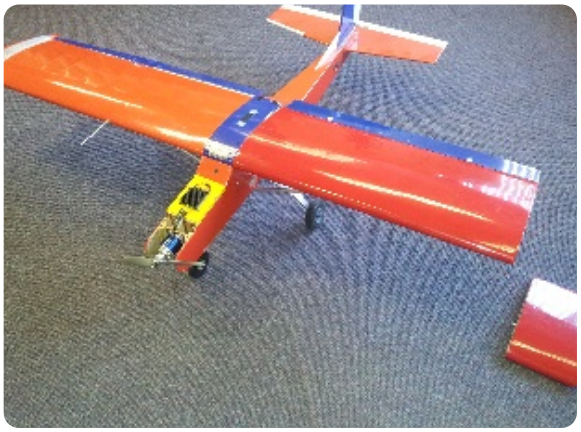

Figure 7.1 – Phoenix, the Trainer 60 UAV

The picture in Figure 7.1 shows the modification already done to its wing for the purpose of this project. It is a small model RC aircraft with a wingspan of roughly 2 metres. For the purpose of conducting real-world tests, the aircraft has been modified as depicted in Figure 7.2. The UAV's motion can be controlled with its electric motor and speed controller, ailerons, elevator and rudder. It is equipped with a GPS, IMU and pressure board, which provide measurements of inertial position, linear and angular body accelerations, airspeed and altitude. Lastly it can be commanded by either the safety pilot or the ground station, which are connected via two separate RF-links.

The safety pilot is equipped with a standard RC remote and has the ability to take control of the UAV at any time during a test. The ground station allows project specific control over the UAV. It provides all the measurements taken by the UAV to the ground station operator, while allowing controllers to be armed and disarmed and project specific test commands to be issued.

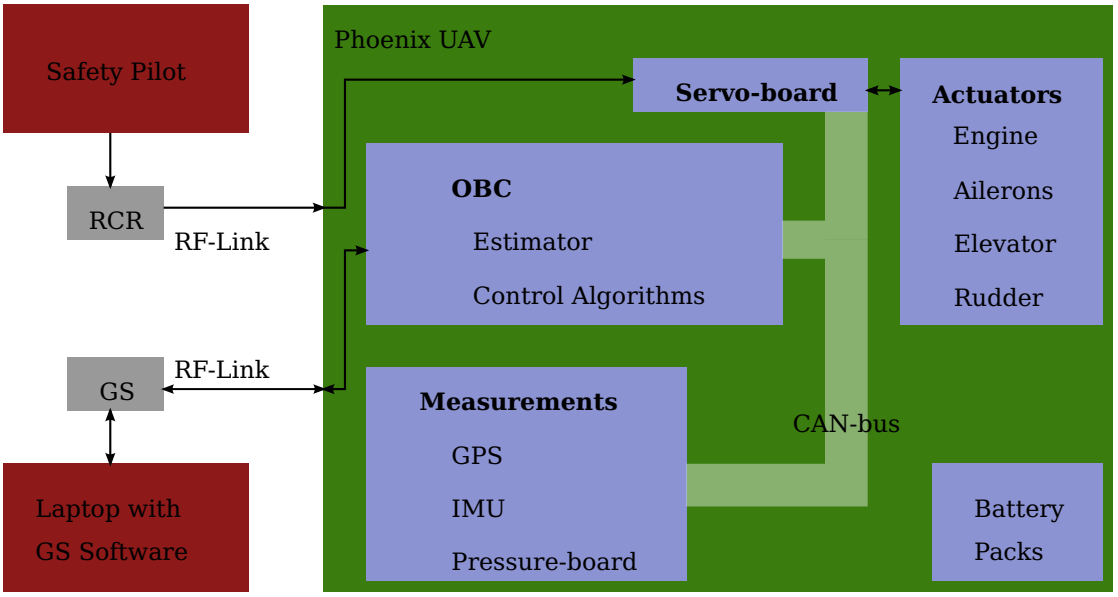

Figure 7.2 – Physical System Overview

More detailed information on the aircraft and its components can be found in Appendix F.

7.2 Hardware Changes

Since the topic of this thesis revolves around an asymmetric UAV with partial wing loss, a practical method of testing and validating the designed system had to be implemented. To accomplish this, the main wing of the UAV had to be modified to provide a reproducible, reusable testing environment for system performance data acquisition under wing loss situations.

Initial thoughts on how to implement this ranged from flying through a suspended hot metal wire all the way to remote controlled explosives. As the method had to be reproducible, the suspended hot metal wire approach would introduce a fair amount of uncertainty in the test conditions. This is due to the fact that the system used does not have the precision and accuracy to fly within centimetres of the wire to produce a predefined percentage sectioned cut repeatedly. This method thus did not fit the criteria and was rejected.

As for the case of remote controlled explosives, this method could repeatedly produce a predefined percentage sectioned cut but would still require the reproduction of the wing after every test. It was also deemed fairly unsafe and would require the use of trained professionals in the field of explosives at every test. Although this method would be spectacular to observe, it would be rather cost inefficient, and was rejected.

A drastic rethink on how to remove part of the wing, with reduced theatrical execution, was necessary. It was at this stage that the notion was introduced to detach a section of the wing mechanically. Two methods stood out. The first would use linear servos to retract part of the ribbed wing's cover. The second would use a catch mechanism in the wing to detach part of the wing instantaneously. Both methods come with significant advantages and disadvantages which will be explained next.

When using linear servos, the loss induced can be undone at any time. This is a major advantage as the UAV could be restored to its original form. The disadvantages of this method are the following:

- Slow linear servos would have to be used to prevent damage to the covered ribbed wing while retracting or expanding. This would not produce an instantaneous change as modelled in this thesis

- Fast linear servos would require more precision and stronger materials to ensure that the wing is strong enough for repeated retractions. This would adhere to the instantaneous change model but at an increased cost
- More than one servo or an advanced gearing system would be required to retract the wing. This is due to undesirable drag effects caused by a rod or guide sticking out of the wing after retraction
- The linear servo could get stuck on a part of the retracting wing. This is only a minor disadvantage as the maximum linear range would be predefined and not exceed the modelled range

As the disadvantages are mostly design issues, the advantage of restoring the wing still weighs in quite strongly in the decision between methods.

When using the catch mechanism, the loss would be instantaneous. The mechanism itself is also quite easily manufactured. The disadvantages of this method are:

- Once loss has been induced, the effect is permanent for the remainder of the flight. This requires the safety pilot to be able to safely land the aircraft with partial wing loss
- There is always a risk of the catch not releasing properly and keeping the “loss” piece attached to the UAV in an unnatural way

When examining the methods above, it is clear that both have distinct advantages and disadvantages. These advantages and disadvantages can mainly be categorised into modelled behaviour, recoverability and manufacturability. Regarding modelled behaviour, both the fast linear servos and catch mechanism fall favourably within this category. Regarding recoverability, the linear servos are favourable. Keeping in mind that a human safety pilot will be monitoring every test with the ability to take over full control at anytime, the catch mechanism should also be fairly recoverable, given that it is within the pilot’s ability to recover. Lastly the manufacturability comes into play and favours both the slow linear servos and the catch mechanism.

Taking all of the above into consideration a decision was made to use the catch mechanism. The likelihood that something would go wrong with a simple mechanism is considerably less than with a more complex one. The ability of the safety pilot is also considered to be quite high as he has been flying RC aeroplanes for more than a decade. The following subsections will explain the hardware changes needed to implement this method of loss on the UAV.

7.2.1 Wing Modifications and Loss Mechanism

In order to implement the catch mechanism, the current wing had to be disassembled or a new one had to be built. The decision to build a new wing was made so that both the original wings would still be available to other projects that also use the UAV. The current wing is made with a balsa ribbed structure, covered with plastic. These wings are freely available in the RC aeroplane kits but require a lot of man hours to modify into the configuration used on this UAV. This is due to the kit wing being a full wing, while the configuration on the UAV requires a split wing.

An alternative to ribbed wings are Styrofoam wings. The wing consists of a Styrofoam core, covered with balsa sheeting and shrink wrapped with plastic. This method of wing manufacturing is fairly fast and easy to modify. The only problem with using a Styrofoam wing would be balance and weight. As the ribbed- and Styrofoam wings would have different densities, both would have to be matched in weight distribution to keep the UAV as close to a nominally symmetric one as possible. This is a fairly easy practise as the completed wings can just be attached to the UAV and balanced by distributing weights over the length of the lighter wing.

The original wing was sectioned so that 20% of its span could be jettisoned. A simple catch and bolt system was designed, with the help of Wessel Croukamp and Wynand van Eeden, to release the wingtip. The catch was inserted inside a Teflon block and spring loaded to stay closed. The back of this catch protrudes from the Teflon block and was attached to a servo, which in turn could open and close it. This part of the mechanism was implemented in the section of the wing which will stay attached to the UAV at all times. In the wingtip, a bolt with a cavity was inserted into the leading edge and a simple pin was

attached on the tail end. Both the wing and wingtip were strengthened where the mechanism had been inserted. The whole mechanism can be seen in Figure 7.3 and a photo of the implemented mechanism in the finished wing in Figure 7.4.

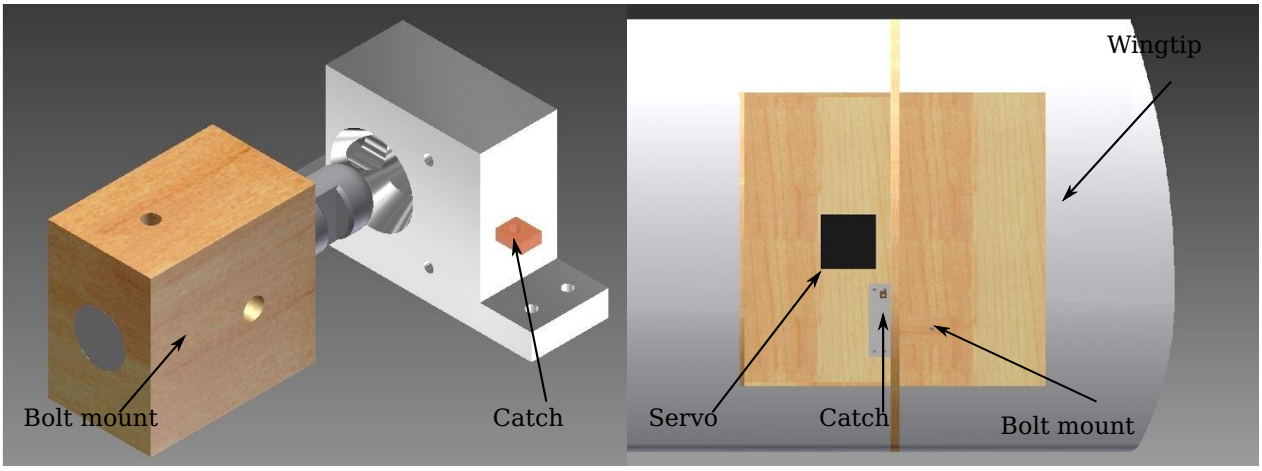

Figure 7.3 – Wing loss Mechanism

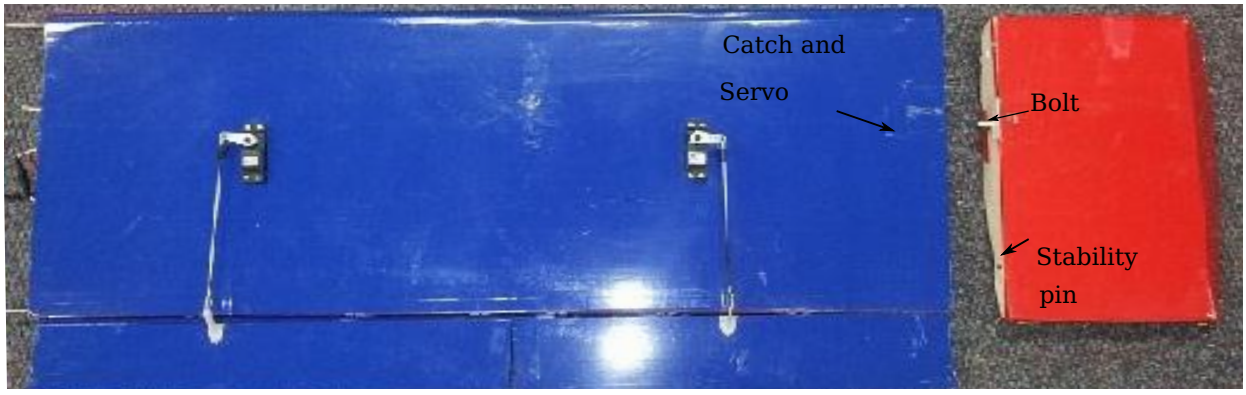

Figure 7.4 – Implemented Wing loss Mechanism

7.3 Firmware Changes

The changes made to the firmware on the UAV were fairly basic. The servo board was programmed to allow the use of an extra servo on one of its channels. As the servo board developed in the ESL has the capability to command sixteen different servos, of which only eight were used on the existing UAV, this was a fairly easy process.

As the servo board was developed in the ESL, it came with a script to automate the assignment of commands on a servo board. The script requires the following information before it can calculate the necessary mixing matrices for the commands:

- The input channel: This will be the channel on which it will receive commands from the RX transmitter, which is the pilot remote
- The output channel: This will be the channel on which the command is outputted to the servo
- The upper and lower limits: These limits specify the minimum and maximum servo actuation
- The servo offset: This bias will be used to accurately zero the position of the servo
- The servo gain: The mechanical gain which will allow zero (0.0) to 100 percent (1.0) of the full range of actuating of the servo

Once all of the above have been specified, the script is run to produce .c and .h files with are included in the servo board MPLab project provided. This project is then compiled and programmed to the servo board.

7.4 Software Changes

Some minor software changes were done on the ground station to arm or disarm the ability to detach the wing. The main idea behind this is that the safety pilot should have full control of the UAV while expected to operate it and only limited control when the control system is active.

The wing loss mechanism thus had to be armed during a test before it was possible to detach the wingtip. This prevents premature or accidental detachment of the tip while a test is being conducted.

Chapter 8

Flight Test Results

In this chapter the flight tests that were performed to practically verify the flight control system, are described. The flight test plan will be presented as an incremental build-up of flight tests leading to an actual in-flight partial wing loss event while the flight control system is active. The chronological execution of the flight tests will be described, and the flight test results will be presented and discussed. The chapter will then be concluded with the final full navigation test, practical results and in-flight wing loss event.

8.1 Flight Test Plan

Testing a new control architecture is not a simple task. In general, assembled systems are tested in incremental stages to ensure the proper response at each stage, before continuing. Although all components of the designed architecture have been tested in a simulation environment, real-world conditions may differ and there may still be implementation errors that were not revealed by the simulation testing. To minimise risk, a careful incremental approach to flight testing will therefore be followed.

First, the safety pilot will verify his ability to control the aircraft under damaged asymmetric conditions. If the pilot is confident he can recover and land the aircraft in this asymmetric state, the wing loss mechanism can be tested in flight. Assuming the mechanism works, control system testing on the symmetric, undamaged aircraft will commence. If all the controllers work on the symmetric aircraft, an asymmetric test will be conducted to ensure that the control system can indeed control and stabilise the asymmetric aircraft. After successful asymmetric flight, the final in-flight symmetric to asymmetric transient handling capability of the controllers will be tested with partial loss of the one wing.

During the controller testing phase, the controllers will be armed and tested as follow:

1. The DRD will be armed to improve the yaw damping of the aircraft and the airspeed controller to regulate the desired airspeed
2. The NSA and climb rate and altitude controllers will be armed sequentially. As the airspeed controller has already been tested, it should regulate the airspeed with regard to the commanded climb rate and allow thorough testing of the NSA and climb rate, and altitude
3. The roll angle controller will be armed next as the airspeed and altitude controllers should regulate these two states, allowing coordinated turning
4. The guidance controllers can be armed to allow waypoint tracking and thus autonomously navigate a circuit

In the next section more detail on the tests conducted and the results obtained will be provided.

8.2 Description of Flight Tests

8.2.1 Flight Tests: Day 1

The purpose of the first flight tests was to establish that the new wing with detachable wingtip operated correctly. A secondary objective was to allow the safety pilot to familiarise himself with the behaviour of

the asymmetric aircraft, and to establish that he would be able and comfortable to take off, fly and land the aircraft in the asymmetric configuration. The UAV was operated in radio-control mode only, and the autopilot was not used. In fact, due to the risk of flying the aircraft in the asymmetric configuration for the first time, most of the expensive avionics pack was replaced with dummy mass. Only the servo board was used, since it is required for detaching the wingtip via remote control. The test day was divided into three parts: first the symmetric, undamaged, UAV was flown. Then the asymmetric, 20% partial wing loss case was flown and lastly the transition between the symmetric and asymmetric cases was tested.

In the first test the safety pilot confirmed that the adapted UAV was as close to its symmetric model with the new wing as it was with its original wing. The second test was conducted for the safety pilot's sake. This provided knowledge of the UAV's behaviour with part of the wing missing and thus gave the safety pilot the chance to experience the change in the response of the UAV. The third test tested the wing loss mechanism itself. It also gave the safety pilot experience in recovering the UAV during a loss event. These steps were crucial for gaining enough confidence that the safety pilot would be able to successfully recover the UAV should anything go wrong during subsequent flight tests.

All the tests above were conducted with relative ease and success.

8.2.2 Flight Tests: Day 2

On the second flight test day, the natural modes of the longitudinal and lateral dynamics were experimentally measured for both the symmetric and asymmetric cases. These system identification tests were performed to verify that the actual dynamics are close enough to the modelled dynamics on which the flight control design is based. After this, the DRD and airspeed controllers were armed and tested on the symmetric case only. When conducting the asymmetric cases, the safety pilot took off with the wingtip already detached.

The symmetric cases provided usable data of the Dutch roll mode, and the short period mode but unfortunately the asymmetric cases did not. This was mainly due to the safety pilot's interference to prevent the UAV from entering an unrecoverable state. The phugoid mode is very slow and could hardly be observed, but the spiral mode was clearly visible. However, again the data was unusable due to safety pilot's control actions.

When testing the two controllers specified, the airspeed controller work as designed. The DRD did not behave as expected. It proved to decrease the damping of the Dutch roll mode instead of increasing it. After thorough data examination and comparison with previous projects done on Phoenix, it was concluded that the Dutch roll mode poles are a bit more damped than the AVL coefficients predicted. Alterations were accordingly made to the DRD.

8.2.3 Flight Tests: Day 3

On the third flight test day the DRD, climb-rate and altitude controllers were tested. This was only done on the symmetric case. The wind began to pick up halfway through the altitude tests and testing had to be halted for the day.

The DRD worked perfectly as designed this time, providing noticeably improved handling for the safety pilot. This visual observation is also supported by the measured data. The climb-rate controller proved to be a bit noisy but also fared well. Its performance was close enough to the designed case to not require any tuning.

The altitude controller was very slow and control was not as tight as designed for. This mainly occurred when the safety pilot commanded turns. Due to the NSA, the change in normal vector did not yet compensate for turning and the increase necessary to keep the UAV at the same altitude. Although this was expected, the resulting altitude drops were larger than anticipated.

After conducting this test and going through the data, it was decided that the altitude controller would be tested again on the next flight test day, after enabling the RAC. This would remove the safety pilot's disturbances and should give a clearer picture on whether the altitude controller works as expected or needs some additional tuning.

During this test day, the cable tie fastening the two wings also broke, which caused the wings to slowly separate from the fuselage. Fortunately, this happened near the end of a flight and did not cause the UAV to come apart in-flight. Up to this point, only one cable tie had ever been used on tests flights with Phoenix and another comparable UAV in the ESL. It was decided to use two cable ties for all future tests.

8.2.4 Flight Tests: Day 4

On the fourth flight test day the roll angle controller, altitude controller and navigation controller were tested. Again, these tests were only done in the symmetric configuration.

The RAC worked better than designed for and tracked 0° and 15° roll angle references extremely quickly. This controller was a bit aggressive but due to its fast response did not raise any alert at that stage. The altitude controller was tested again and performed better than the previous flight test. It did however perform a bit slowly and after comparing this data with data obtained during other projects where phoenix was used, it was tuned to be tested again during the next set of flight tests.

The navigation algorithm did not perform as expected. During debugging of the controller architecture on the OBC, some safety measures were removed and not replace afterwards. This led to the UAV banking at almost 80° in the turns, which led to excessive speed and altitude changes. The UAV also went in an unsuspected direction. At this stage the tests were halted for the day, pending future investigation before testing could continue.

When examining the data, it became apparent that the estimator lagged the actual response. This caused the RAC to “overactuate” the ailerons, inducing a longer roll rate and angle command than necessary. This was not picked up during HIL testing as the RAC responded more slowly and the estimator lag did not come into play. The unsuspected behaviour came from the difference between magnetic and true north. The original set of waypoints regarded the runway to be aligned 0° North, where in actual fact the runway at HRF was aligned $\pm 20^\circ$ North. The RAC’s aggressiveness was reduced by slowing down the controller’s response, while the navigation algorithm was adapted to allow easy transformation of a set of waypoint through x°. This allows the waypoint set to align with the runway.

8.2.5 Flight Tests: Day 5

On the fifth test day, the RAC and navigation controller were tested for the symmetric configuration, the asymmetric configuration and the transition from symmetric to asymmetric due to in-flight partial wing loss. Based on the results of the previous flight test day, the RAC controller’s gain was tuned to make the response less aggressive. The limits were also reinstated on the roll angle at $\pm 30^\circ$ and the navigation circuit was changed to align with the orientation of the runway instead of with magnetic north.

Due to the 80° bank angle behaviour observed on the previous flight test day, the test procedure for the RAC was adapted. The testing began with 0° and 15° references but then the actual bank angle limiter was tested. This was done by loading a 30° bank angle step and initialising the controller whilst the UAV was in a banked turn. The test was a success and the bank angle was limited at 30°.

When testing the navigation, the circuit now ran parallel with the runway and full autonomous flight could be achieved. Some strange behaviour was observed during this test. On making a circuit turn, the UAV only proceeded halfway through the turn and then changed direction. The navigation algorithm is however equipped with the ability to recalculate its circuit if it detects that it has gone too far off course. Upon closer inspection of the data it was noted that the turn was too sharp for the bank angle limited controller to be able to reject wind gusts. This led to the UAV slowly drifting off course until the navigation stick lost contact. At this stage it started turning in the opposite direction until it was parallel to the next waypoint leg and created a new waypoint. This new waypoint was at its current location and it then navigated a straight line towards the end of the original circuit leg. Although this response was not what was intended, it did provide the UAV with the ability to recover once it lost contact with the track.

Although the algorithm did not work as desired, it was still stable and able to safely navigate the circuit. Anton Runhaar, one of the flight test support engineers on site, suggested that the length of the short legs of the circuit be increased and that the circle navigation be removed to enable continuing with the

flight tests. If the circle navigation was removed, the algorithm should then in theory perform as described below:

- Upon reaching the end of a leg, it will bank as hard as it can
- It should then lose contact with the track but keep turning in until it is parallel with the short leg and it should then insert a new waypoint
- It should then follow a straight line to the end of that short leg and follow the same procedure for the long leg

This solution was accepted by all the members of the flight test crew and was subsequently tested. It worked as described above and allowed continuation of the day's testing. At this stage it should be noted that the guidance controller was only a means to an end. The actual project required testing of the underlying control architecture, not the design of a guidance controller. If the guidance controller could provide a track for testing, it was deemed as an acceptable compromise.

Upon successful symmetric circuit navigation, the asymmetric case was tested. This also worked as expected and allowed the testing of a partial wing loss event in practice.

When testing the partial wing loss event, the UAV was piloted off the runway in its symmetric case. Once the UAV was safely in the air, circuit navigation was enabled and one complete circuit was flown. The partial wing loss event was initiated and the UAV left to recover. Upon successful recovery another circuit was flown before the safety pilot took control to commence landing. This test was successful and it was concluded that the control system was capable of handling partial wing loss.

8.3 Flight Test Results

The results acquired from the flight tests will be represented in three categories. The first set of results will show the performance of the flight control system when controlling the symmetric UAV with no wing loss. The second set of results will show the performance of the flight control system when controlling the asymmetric UAV with 20% partial wing loss. The third set of results will show the performance of the flight control system during a partial wing loss event, including how well it handles the transient from the symmetric to the asymmetric dynamics.

It should be noted that the data depicted in the figures below were taken directly from the logged flight data over several flights. Every step was commanded after a circuit turn had been completed. It will be apparent from the following figures that in some cases the transients due to turning are still present when the step command was given.

When examining the data, it also became apparent that the UAV flew at a slight banked angle. This is possible due to an offset on the IMU or magnetometer which was not calibrated accurately enough. As a result of this, the measurements depict a slight offset on the ailerons to counter this offset while trying to fly "straight and level". As the ailerons cause a slight roll angle, the aircraft flew straight but not wings level.

8.3.1 Symmetric UAV Behaviour

The part of the circuit on which all of the step commands were issued is shown in Figure 8.1. As stated in Section 8.2.5, changes to the waypoint sequence had to be made on the flight day to allow further testing. In doing this, the condition validating circle navigation could be removed. This allowed the circuit to be flown in only one direction, as the airfield's rules require, and delivered an acceptable flight path. As the waypoints now represented a rectangular circuit, the UAV would be forced to do bank limit turns on the short legs. On every turn the UAV's guidance controller would lose contact and keep on turning until it was parallel to the leg it was trying to follow. At this stage it would generate a temporary waypoint, thus creating a new leg to follow to the next waypoint. These waypoints will be depicted as undefined waypoints in the following circuit plots. Figure 8.1 represents the circuit flown for the symmetric tests.

The response to a $2m.s^{-1}$ airspeed step is displayed in Figure 8.2. The response required 3.23s to achieve the reference. This is 0.4s slower than the designed response but was deemed acceptable due to the

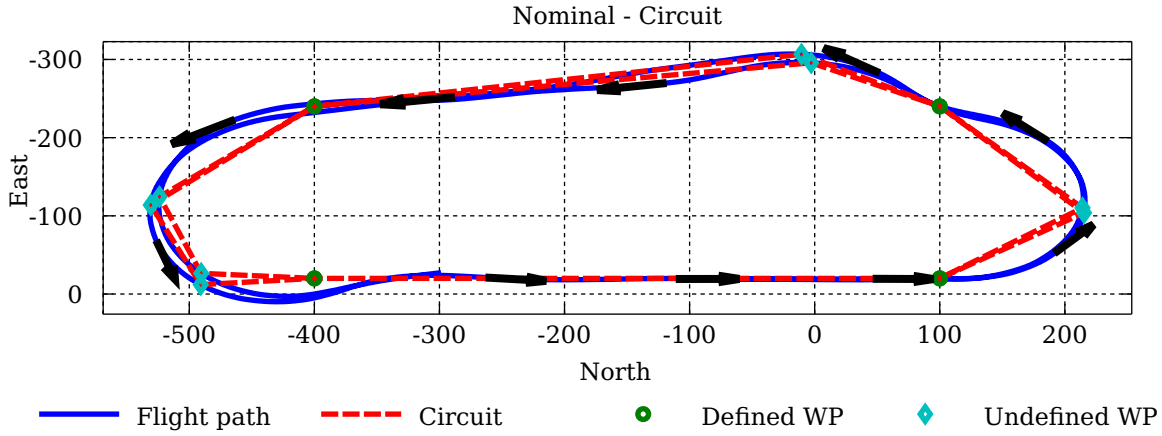

Figure 8.1 – Practical Response - Nominal Flight - Circuit

external disturbances clearly visible in the figure.

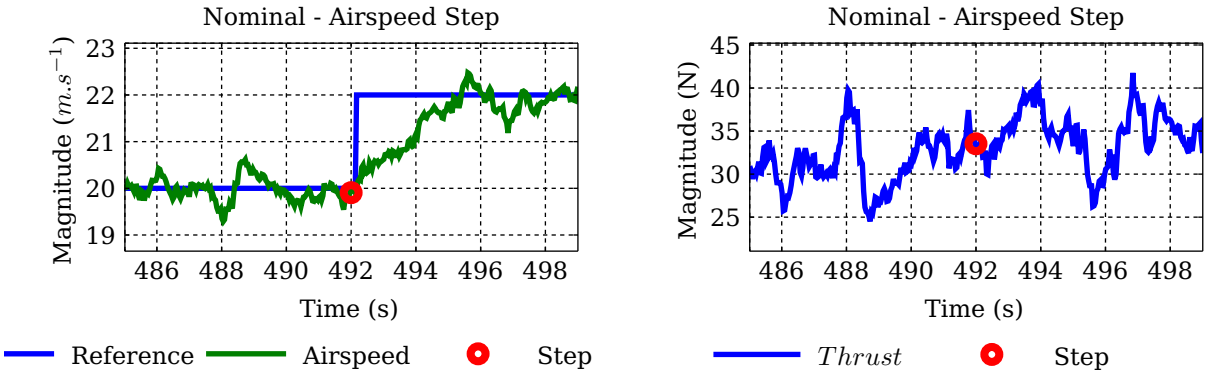

Figure 8.2 – Practical Response - Nominal Flight - $2m.s^{-1}$ Airspeed Step

Figure 8.3 displays the result of a full limited roll angle command. It took 1.2s to settle from the start of the response until it reached it reference. This result is 0.3s faster than the designed response of 1.5s. The reason for this could be due to the external disturbances visible on the response or a slight error in the UAV's inertia parameters.

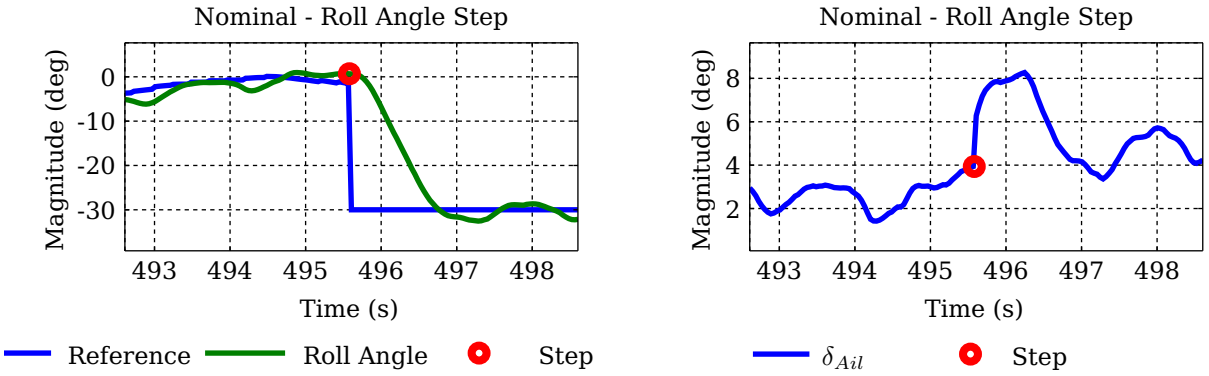

Figure 8.3 – Practical Response - Nominal Flight - Roll Anlge Step to Limit

Figure 8.4 displays the result of a 5m altitude step. The response took 9.4s to settle, which is 0.6s faster than the designed response of 10s. The fast rise and slow regulation to its final value is also clear in the

controller's behaviour as depicted in Figure 5.26 of the control design section. The altitude drift at the beginning of this response may raise some concern at first but can be explained by the flight conditions. There was a slight cross-wind blowing during this test and the step was commanded very close to the completion of a circuit turn. In the modelling section it was made clear that AVL cannot accurately model an aircraft's fuselage. As the fuselage can roughly be described as a bulky wing, it will generate lift when turned into the wind. As the UAV turns in the cross-wind, some attitudes produce more lift than others.

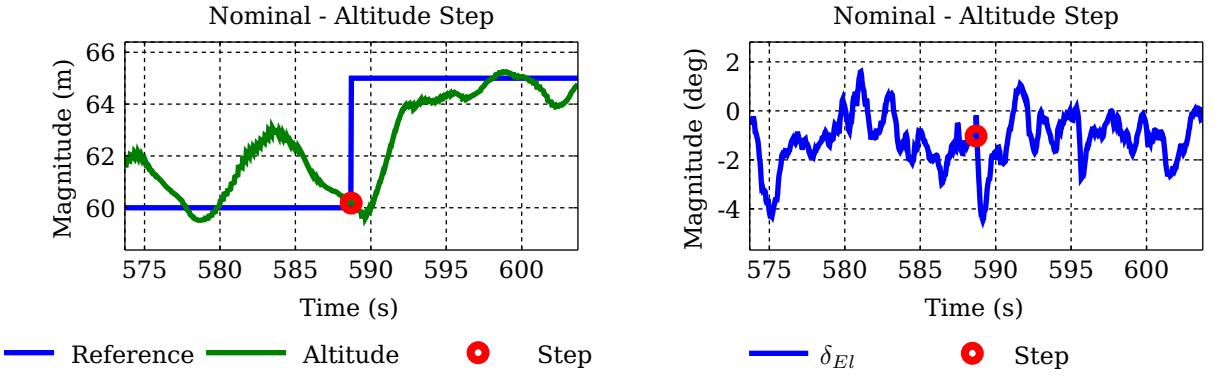

Figure 8.4 – Practical Response - Nominal Flight - 5m Altitude Step

Figure 8.5 represents a lateral step and demonstrates the ability of the navigation controller to keep the UAV on its referenced ground track. For the sake of simplicity, the results of only the cross-track error (CTE) and roll angle are shown. At zero CTE, the UAV is perfectly on track. It is clear that the controller can correct this offset to within 2m in 10s. Due to the non-linear nature of the control law, the command to reduce the CTE becomes significantly smaller if the CTE is small. This makes it harder for the controller to perfectly follow the track when external disturbances are present. When examining the roll angle and comparing it to the reference, it becomes clear that some disturbances are present. Taking into account that the UAV's estimator calculated that it flew with a slight bank angle, this would generate a constant disturbance and due to no integrator in the navigation controller, the controller does not have the ability to remove this disturbance.

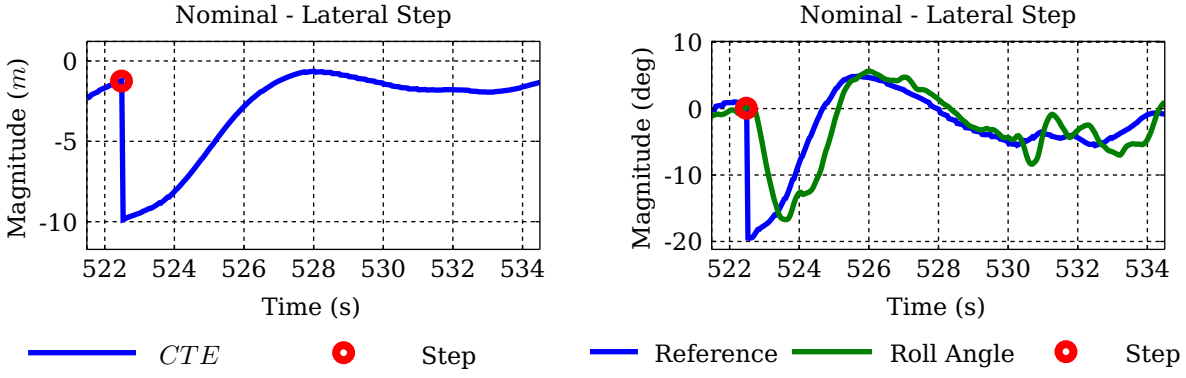

Figure 8.5 – Practical Response - Nominal Flight - 10m Lateral Step

8.3.2 Asymmetric UAV Behaviour with Partial Wing Loss

When looking at the asymmetric behaviour, the same sequence as followed for the symmetric will be followed when describing the responses. Figure 8.6 shows the circuit on which the step commands were issued. Note the difference in flight path due to different undefined waypoints inserted by the navigation controller to guide the UAV back on track.

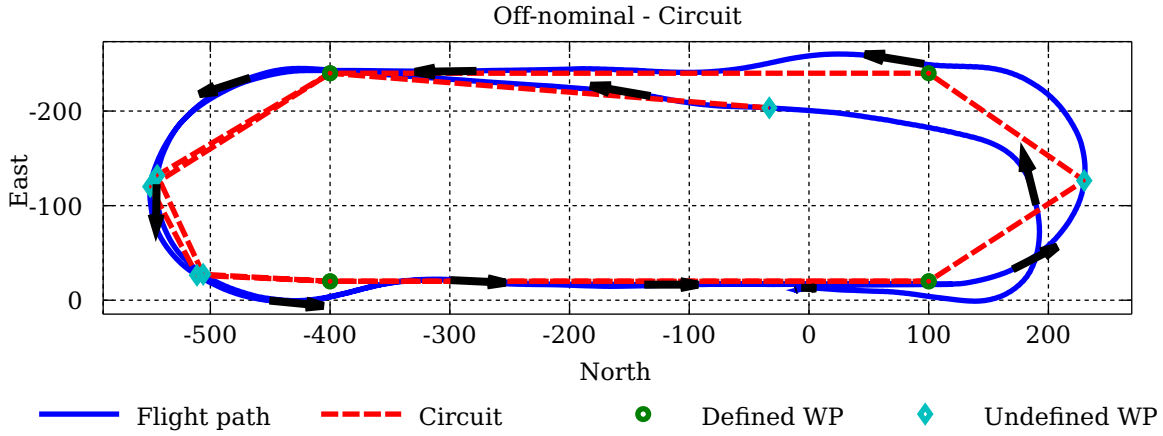

Figure 8.6 – Practical Response - Off Nominal Flight - Circuit

Figure 8.7 displays the response to an airspeed step. In this asymmetric case the response took 3.13s to reach the first step input. This is basically in the same region as that of the symmetric case and correlates well with the theoretical difference prediction between the two cases. When examining the throttle response, it is clear that for a step more throttle was needed overall. This result, at first, seems contradictory to the results in the theoretical test but in fact it is not. Although the trim section predicts a slightly lower thrust, the control design section depicted an increase in throttle to perform a desired step when wing loss occurred. Taking this into consideration it is clear that the increased throttle is due to constant disturbance rejection and thus validates the response.

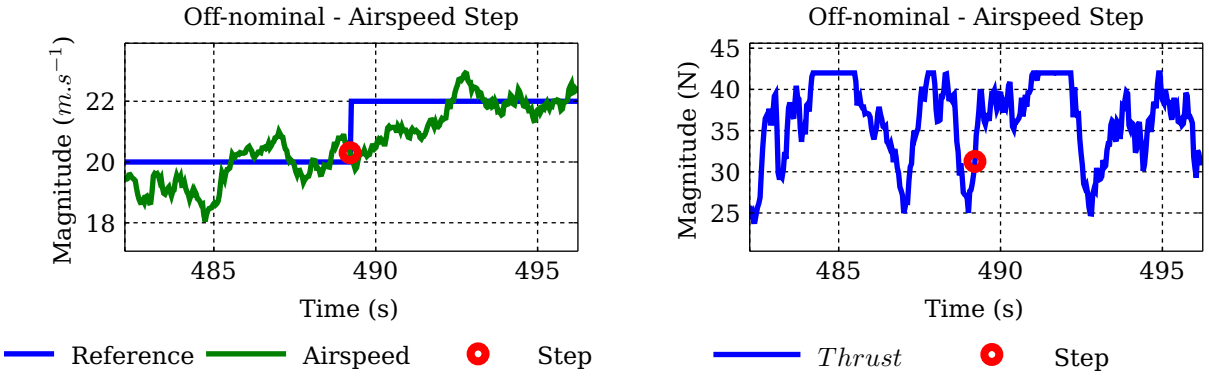

Figure 8.7 – Practical Response - Off Nominal Flight - $2m.s^{-1}$ Airspeed Step

Figure 8.8 displays the response of the UAV to a roll angle limit step. The response took 1.06s from start to the first reference touch, which is faster than in the symmetric case. This effect can be explained by the fact that the circuit turn was in the negative y-axis direction of the body, which is the side where wing loss occurred. There would thus be more lift on the positive y-axis side and less on negative, thus inflicting a larger rolling moment and decreasing the response time. It is also clear that the response is slower when commanded in the opposite direction. When looking at the ailerons, it is clear that the trim has shifted to around $-2°$. Taking into account that there was a bias on the roll angle, which resulted in a bias on the ailerons in the symmetric case, the difference in trim between the symmetric- and asymmetric cases is $4°$s. This difference is fairly close to the $4.2°$s predicted by the trim algorithm.

Figure 8.9 displays a 5m altitude step response. The response was a lot quicker to cross the reference value, taking only 2.84s, but only came close to the reference again at 11.7 seconds. The behaviour of the symmetric and asymmetric cases depicts the same notion in response, being a quick initial rise and a slow convergence on the reference value. The figure does however display a slight altitude offset, which is consistent throughout the flight. Upon closer inspection of all the data for the different flights, this same offset is clearly visible. It can most likely be ascribed to a slight calibration error in the fine altitude sensor, used to correct the estimator's prediction.

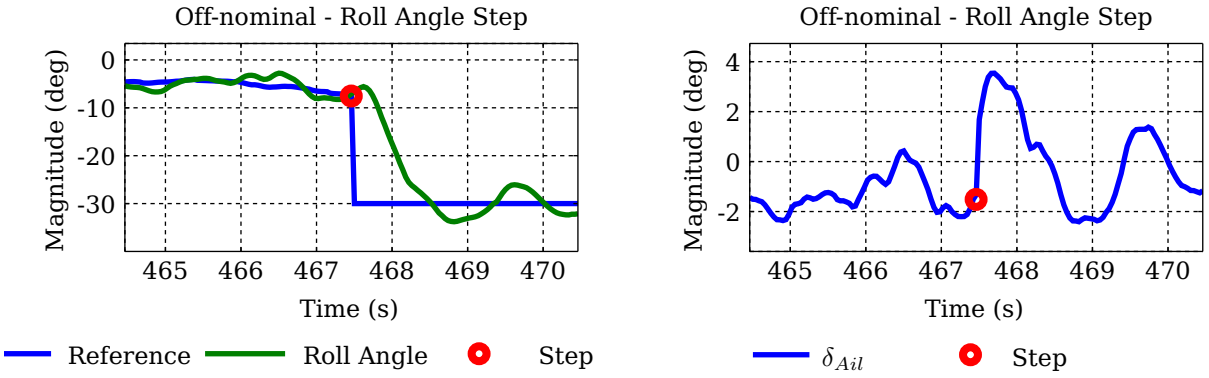

Figure 8.8 – Practical Response - Off Nominal Flight - Roll Anlge Step to Limit

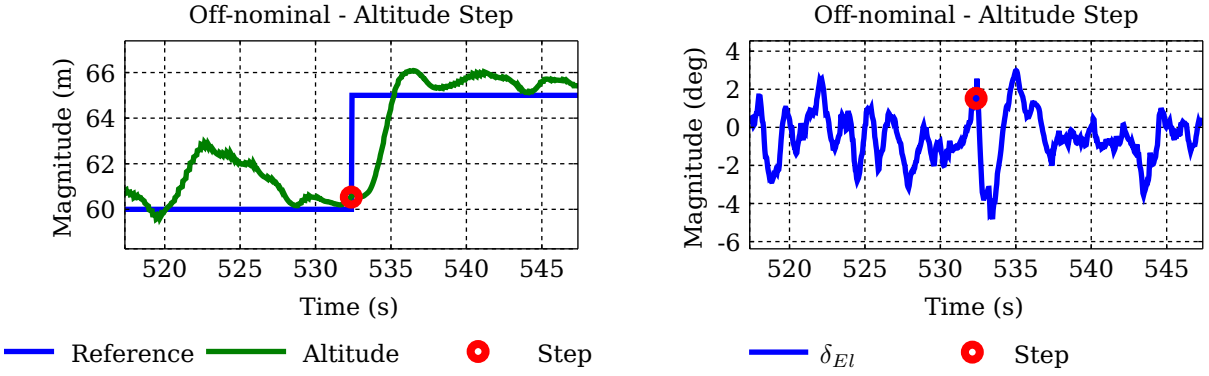

Figure 8.9 – Practical Response - Off Nominal Flight - 5m Altitude Step

Figure 8.10 shows a 10m lateral step. It is clear from the figure that the controller was still converging to a zero cross track error when the step command was issued. When looking at the angle command being issued, it is clear that it was a lot more responsive to disturbances than in the case of the symmetric UAV. Due to greater disturbances acting in on the UAV, the controller could not command the angle as accurately as the symmetric UAV case. The difference in behaviour in the case of a positive and negative angle also deteriorated the response. Furthermore, it seems that the cross track error settles at roughly 5m. Upon further examining the cross track, this steady state error is visible every time the UAV passes this leg of the circuit. The error on the other leg is a lot smaller. This led to the conclusion that the direction of the wind had a far greater influence on the UAV in its asymmetric state than previously believed. Taking all of this into account, the response obtained does however look good, even though it had a steady state error.

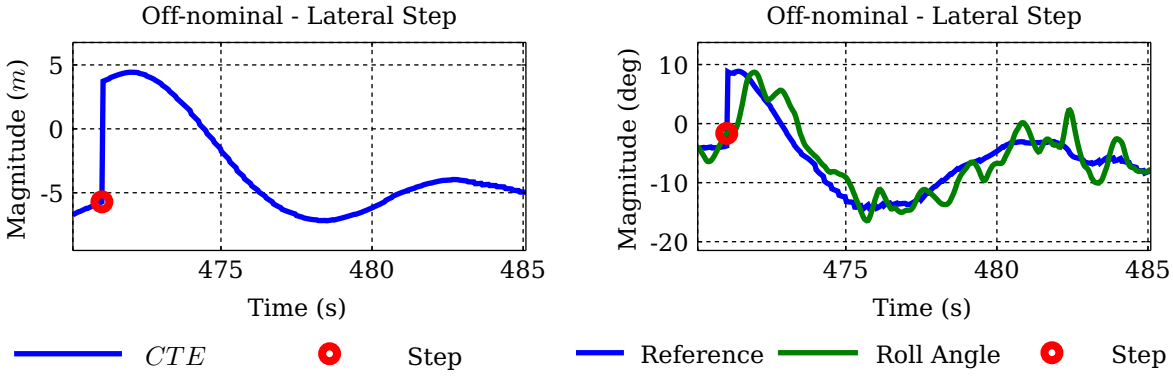

Figure 8.10 – Practical Response - Off Nominal Flight - 10m Lateral Step

8.3.3 Symmetric to Asymmetric Transients due to Partial Wing Loss

At this stage it is known that the UAV's control system can handle both the symmetric and asymmetric cases. For it to be robust against partial wing loss it needs to be able to handle the transient between the two cases. Figure 8.11 depicts the circuit flown for this test. It is again a bit skew due to the UAV flying too far off circuit and the navigation algorithm inserting additional waypoints to guide it back.

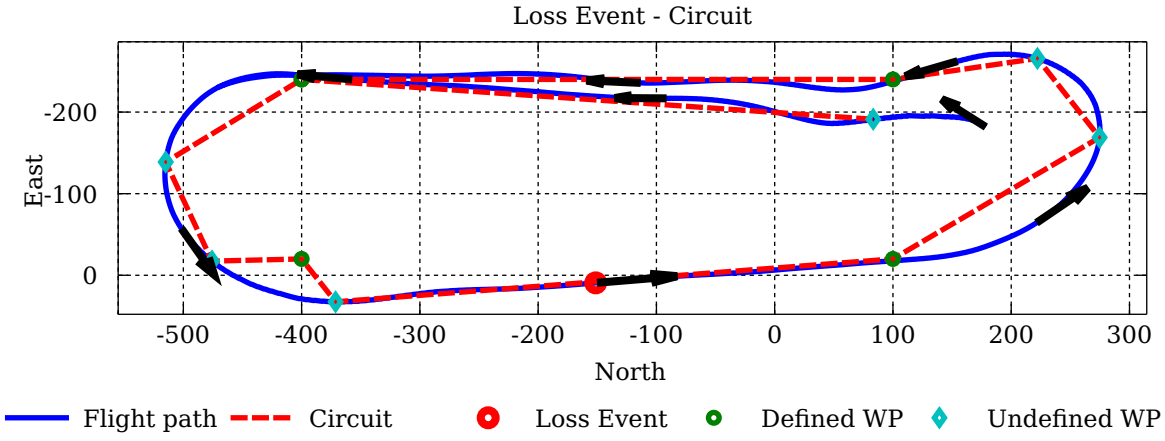

Figure 8.11 – Practical Response - Nominal to Off-symmetric Transients - Circuit

Figures 8.12 to 8.14 below display the data measured during this flight test.

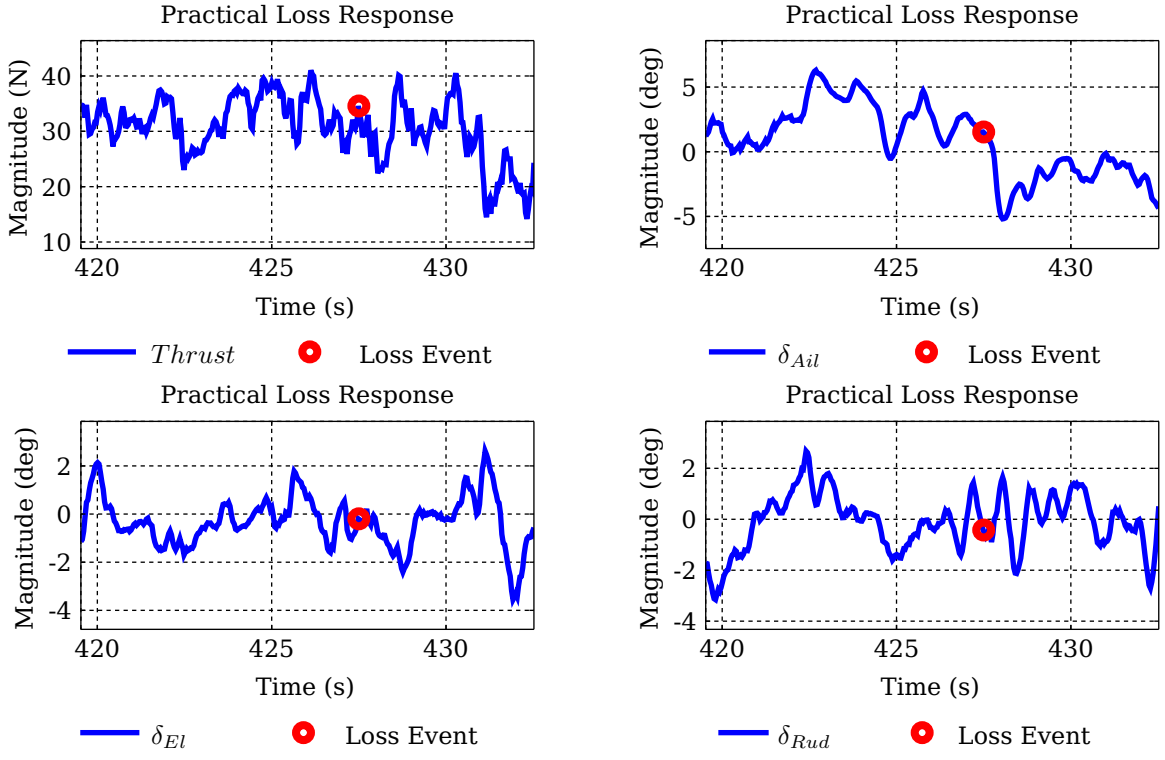

Figure 8.12 – Practical Response - Nominal to Off-symmetric Transients - Actuators

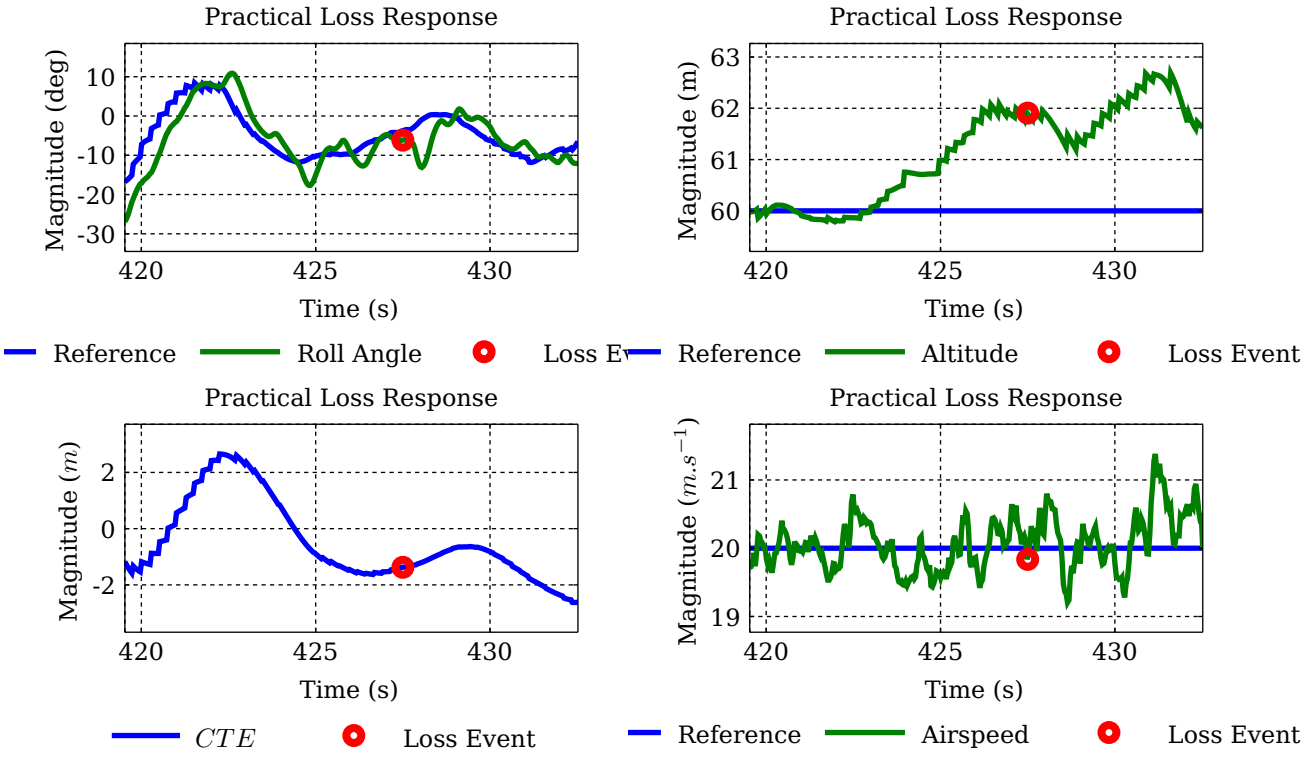

Figure 8.13 – Practical Response - Nominal to Off-symmetric Transients - States

When examining Figures 8.11 to 8.13, it is clear that the control architecture managed to recover after the partial wing loss incident. It handled the transient between the symmetric and asymmetric state as the simulations in Chapter 6 stated it would and this can clearly be observed by the behaviour of the ailerons and rudder. The ailerons mainly counteracted the rolling moment and correcting the lift imbalance, while the rudder counteracted the sudden yawing moment experienced by the UAV. The moments they counteracted can be observed on the x- and z-gyroscopes in Figure 8.14. A slight change in thrust and elevator occurs but can hardly be seen in the figures due to the active disturbance rejection done by the controllers.

Referring back to Chapter 3 and 6, the new trim location should represent the following on the actuators:

- 0.2 N decrease in thrust
- $3.8°$ increase in ailerons, defined in the negative direction
- $0.3°$ increase in elevator, defined in the negative direction
- $1.0°$ increase in angle of attack
- $0.0°$ increase in sides slip

The ailerons clearly found this trim, increasing about $4°$ in the negative direction. This is very close to the pre-calculated and non-linear simulation trims. Due to the large amount of disturbance rejection done by the elevator and throttle, their small increase and decrease cannot be observed in the data. As the UAV is not equipped with an angle of attack and side-slip sensor, these trim values cannot be compared.

Figure 8.13 shows the states that are most influenced. A sudden decrease in roll angle is clearly visible and quickly corrected. When examining both the airspeed and altitude, it becomes apparent why the expected change in thrust and elevator is not seen clearly. Due to the altitude, which is already above the reference, the elevator change would not be clearly seen due to the two events cancelling each other out. The same can be said for the airspeed.

Lastly, the cross track error also depicts this cancelling behaviour. Thus the swerve from the path is delayed and only later corrected.

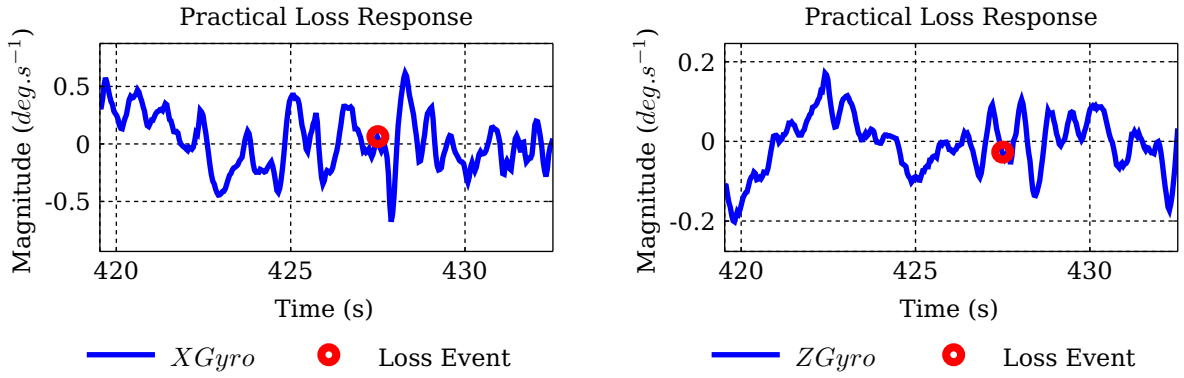

Figure 8.14 – Practical Response - Nominal to Off-symmetric Transients - Sensors

8.3.4 HIL Square Waypoint Circuit

As explained earlier, changes to the planned waypoint sequence were made to allow testing. As a result a sub optimal circuit was flown. This sequence of waypoints was entered into a HIL simulation to verify that the navigation algorithm did function as planned. Figure 8.15 shows this simulation.

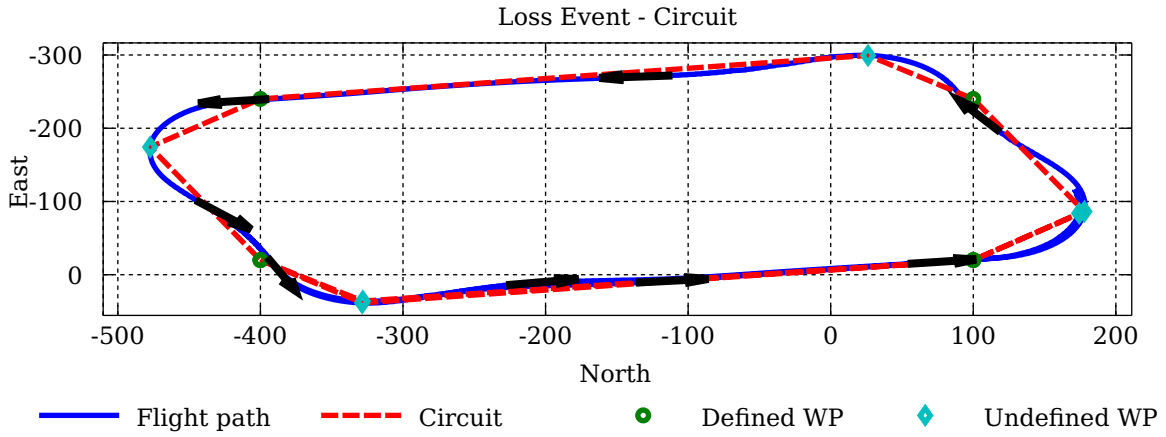

Figure 8.15 – HIL simulation - Square Waypoint Circuit

It is clear that this circuit has a lot in common with the three circuits observed in the various flight tests. Figure 8.1's top overshoot is clearly visible here, with parallel waypoints inserted every time the UAV is on an East leg. It does however not depict the same behaviour as the test flights do on the bottom North leg. This is mostly due to the simulation which does not accurately simulate wind disturbances and also AVL's inability to accurately describe the aerodynamic behaviour of the fuselage.

8.4 Evaluation

Looking at the practical data as a whole, the control architecture successfully flew the UAV in both its symmetric and asymmetric states. It also handled the transient from symmetric to asymmetric configuration quite well during the event of partial wing loss. The new trim was also clearly visible on the ailerons and rudder, supporting the simulated results of Chapter 6. Overall the same behaviour could be observed on the practical data set as predicted by the simulation and trim chapters.

Some discrepancies did however occur. The navigation controller's waypoints needed to be modified at the airfield. As this controller was not the main focus of this project but only a means to an end, its sub-optimal performance did not affect the outcomes of the project. Correcting this controller would require more time but only deliver marginally better results. As the focus of this project was to obtain a robust control system to partial wing loss, it did achieve its goal and can support this statement with the practical data obtained.

Chapter 9

Summary and Recommendations

In this chapter a summary of the research performed is provided, followed by the main conclusions reached, and finally the recommendations for future work.

9.1 Summary

In this thesis the successful design and implementation of a UAV flight control system which is robust to partial wing loss is presented. The control system was verified with practical flights and it successfully tolerated an in-flight partial wing loss of 20% of the left wing of the aircraft. The tests showed that the problem of handling a partial wing loss event is largely solved by finding a new trim condition for the aircraft.

In Chapter 2 the general conventions used for this thesis were defined. A model which could accurately simulate partial wing loss was implemented. This included an asymmetric equations of motion model, an aerodynamic coefficients model and the necessary physical quantities for describing the change in inertia and the object's CG location. AVL was used to model the aerodynamic coefficients and described most of them accurately. It did however lack accuracy on the side force coefficients due to AVL's shortcoming when modelling a fuselage. The model showed that the main effect of partial wing loss is the lift imbalance.

In Chapter 3 an analysis was conducted to find possible trim points for the asymmetrically damaged UAV. Both an analytical approach and a numerical approach were taken to calculate the trim. The numerical approach proved to be more accurate due to approximations made by the analytical approach. It was concluded that to fly the UAV with as little side-slip as possible would result in the most stable trim. It was also found that for this configuration of UAV, up to 40% wing loss is trimmable. After this stage, the aileron control surfaces saturate and the UAV quickly goes into a downwards spiral.

In Chapter 4 the stability of the open-loop system was analysed. This required linearising the full non-linear asymmetric equations of motion. In linearising these equations it became apparent that some terms necessary to describe the asymmetric nature of the UAV did not play a vital role and these were removed. The linearisation showed that the longitudinal dynamics are quite decoupled from the lateral dynamics but that the lateral dynamics are coupled to the longitudinal dynamics once the UAV enters an asymmetrically damaged state. This indicated that some of the coupling terms could be problematic and would need to be examined after applying control to see whether they would significantly disturb the system.

In Chapter 5 two different flight control systems were designed, the first using a classical architecture, and the second using an acceleration-based control architecture, as proposed by Peddle [1]. The robustness of both flight control architectures to partial wing loss was analysed, and both were found to be sufficiently robust. A hybrid of the two architectures was then selected for implementation on the research aircraft and verification through practical flight testing.

In Chapter 6 the performance and robustness of the flight control system were verified using non-linear simulations. Initial simulations were pure software simulations and were fully conducted on a desktop computer. These were followed by hardware in the loop simulations where the flight control software was executed on the actual aircraft avionics while the non-linear simulation of the flight dynamics was executed on a desktop computer. Simulated sensor measurements were passed to the avionics and the control deflections calculated by the flight control software were fed back to the non-linear flight dynamics

simulation. Various scenarios were tested and provided sufficient confidence that the flight control architecture is robust to partial wing loss and was ready for practical flight tests.

Chapter 7 described the modifications that were made to the hardware, firmware and software of the UAV to enable practical flight test verification of the flight control system's ability to accommodate partial wing loss. This included building a wing that consists of two sections and implementing a latch system which enables 20% partial wing loss on the left wing by detaching the wingtip section.

In Chapter 8 the flight test results obtained from practical tests were presented. Tests were conducted incrementally, ensuring that each controller worked properly before enabling the next controller. The controllers were then tested on the asymmetric UAV with 20% partial wing loss and proved capable of navigating the asymmetrically damaged UAV through a set of waypoints. Finally, the wing tip was jettisoned in-flight and it was demonstrated that the flight control system was capable of transitioning from the undamaged case to the asymmetrically damaged case with acceptable transients.

9.2 Recommendations

The following recommendations are made for future work that continues this research:

- AVL could not accurately describe the aerodynamic coefficients related to side force. This is due to it being unable to model the fuselage properly. An alternative program should be found and the results analysed to find accurate side force coefficients
- Partial wing loss did not cause a large variation in the UAV's dynamics. An event of vertical, horizontal or combination tailplane loss should cause a large variation in the UAV's dynamics. The control architecture implemented in this thesis should be analysed for tailplane loss and possibly be redesigned with robust methods
- In the case of light wind at the airfield, the safety pilot had to concentrate considerably harder to safely land the UAV. It is suggested that a safety pilot assist control configuration be implemented to ease the effort of landing the UAV under partial wing loss conditions. An automated landing control architecture can also be analysed to determine its capabilities with respect to the UAV under partial wing loss
- While finding a new trim, the control architecture used the ailerons to correct the lift imbalance caused by partial wing loss. Implementing a flaps controller to balance lift instead of the ailerons, should improve handling and also allow more partial wing loss before the UAV's control surface deflections saturate
- It was noted in the trim chapter that at higher speeds, the aircraft could lose more of its wing. This theoretical result should be tested in practice but will require the UAV to be fitted with a more powerful engine
- The UAV's avionics can be upgraded to provide faster estimation. This should allow the initial fast roll rate and angle controller to be implemented and tested

Appendix A

Aerodynamic Coefficients

A.1 Aerodynamic Coefficient Dimensionilisation

The following dimensional terms were acquired from [13]. These terms will be used to acquire the dimensional forms of the aerodynamic coefficients needed in Section 2.4.

Dimensionless Term	Multiplier
C_{y_P}	$\frac{1}{2}\rho V_0 Sb$
C_{y_R}	$\frac{1}{2}\rho V_0 Sb$
$C_{y_{\Delta Rud}}$	$\frac{1}{2}\rho V_0^2 S$
C_{l_β}	$\frac{1}{2}\rho V_0^2 S$
C_{l_P}	$\frac{1}{2}\rho V_0 Sb^2$
C_{l_R}	$\frac{1}{2}\rho V_0^2 Sb^2$
$C_{l_{\Delta Ail}}$	$\frac{1}{2}\rho V_0^2 Sb$
$C_{l_{\Delta Rud}}$	$\frac{1}{2}\rho V_0^2 Sb$
C_{m_α}	$\frac{1}{2}\rho V_0^2 S$
C_{m_Q}	$\frac{1}{2}\rho V_0 S\bar{\bar{c}}$
$C_{m_{\Delta El}}$	$\frac{1}{2}\rho V_0 S\bar{\bar{c}}$
C_{n_β}	$\frac{1}{2}\rho V_0 Sb$
C_{n_P}	$\frac{1}{2}\rho V_0 Sb^2$
C_{n_R}	$\frac{1}{2}\rho V_0 Sb^2$
$C_{n_{\Delta Ail}}$	$\frac{1}{2}\rho V_0^2 Sb$
$C_{n_{\Delta Rud}}$	$\frac{1}{2}\rho V_0^2 Sb$

Table A.1 – Coefficient Dimensionilisation Terms

A.2 Math vs AVL non-dimensional coefficient plots

In this section the non-dimensional coefficient plots, as described in Section 2.4 are displayed.

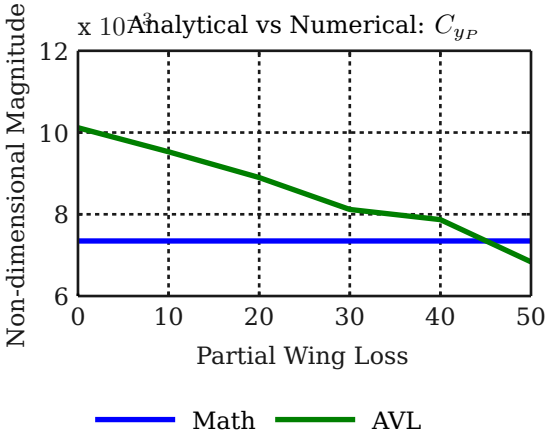

Figure A.1 – Analytic vs. AVL: C_{y_P}

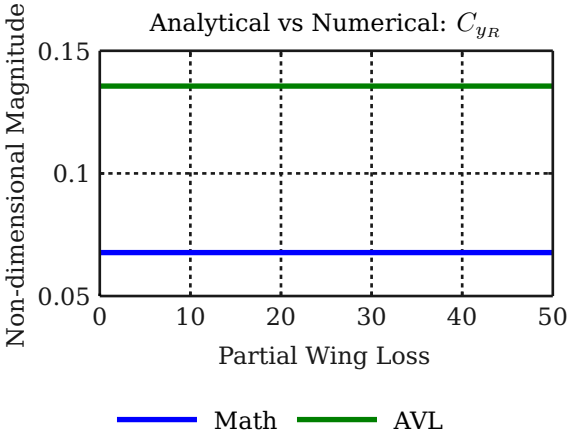

Figure A.2 – Analytic vs. AVL: C_{y_R}

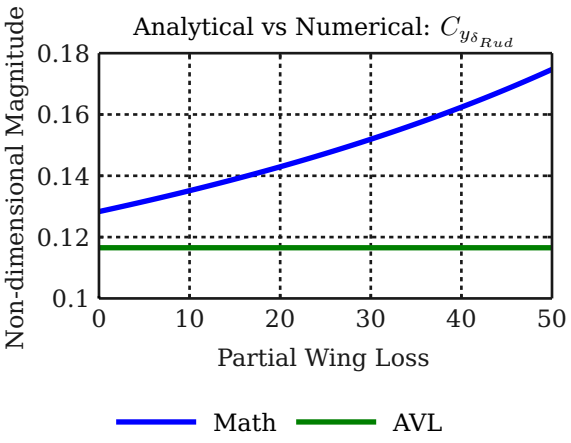

Figure A.3 – Analytic vs. AVL: $C_{y_{\delta_{Rud}}}$

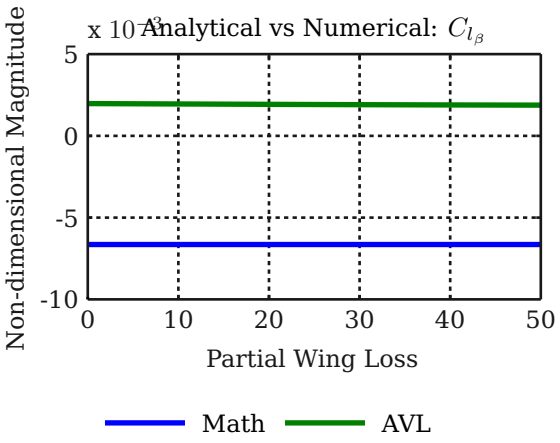

Figure A.4 – Analytic vs. AVL: C_{l_β}

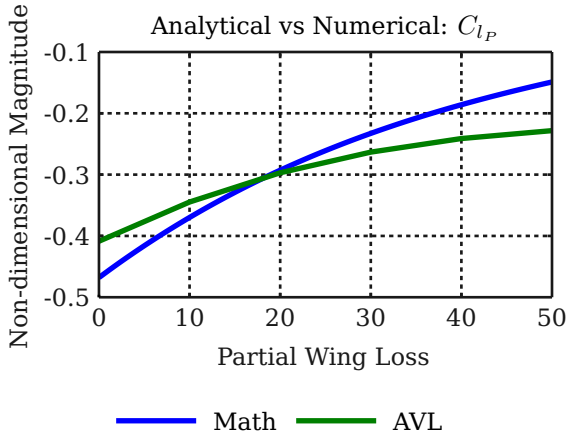

Figure A.5 – Analytic vs. AVL: C_{l_P}

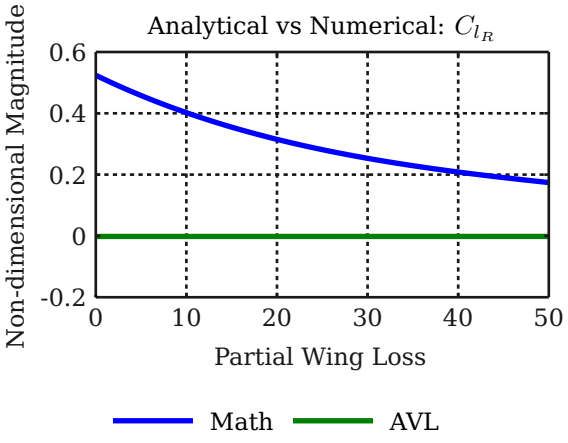

Figure A.6 – Analytic vs. AVL: C_{l_R}

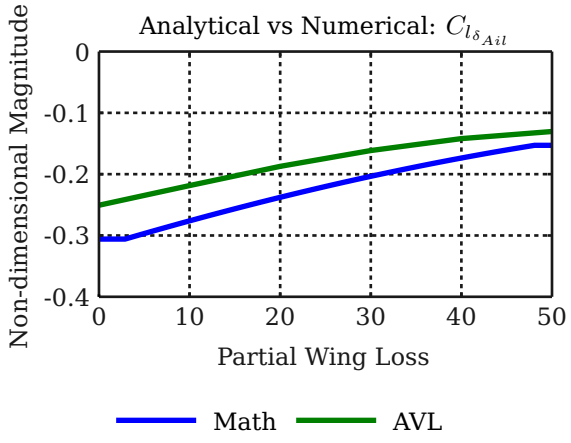

Figure A.7 – Analytic vs. AVL: $C_{l_{\delta_{Ail}}}$

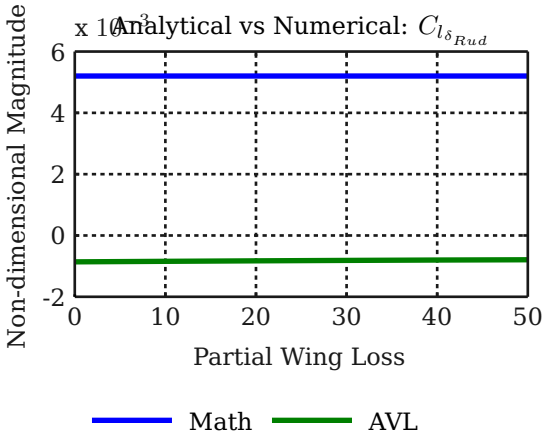

Figure A.8 – Analytic vs. AVL: $C_{l_{\delta_{Rud}}}$

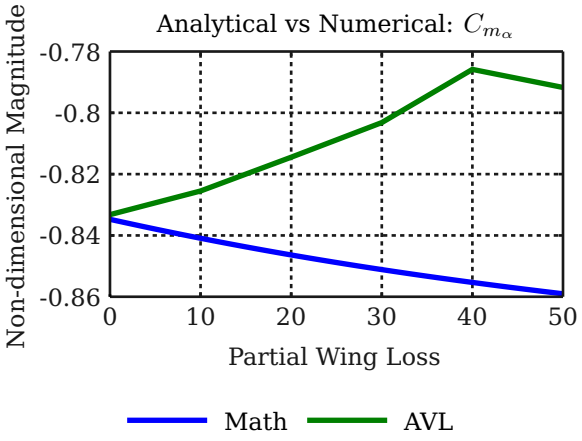

Figure A.9 – Analytic vs. AVL: C_{m_α}

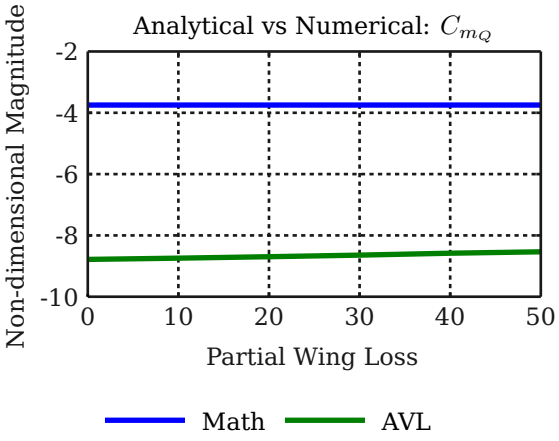

Figure A.10 – Analytic vs. AVL: C_{m_Q}

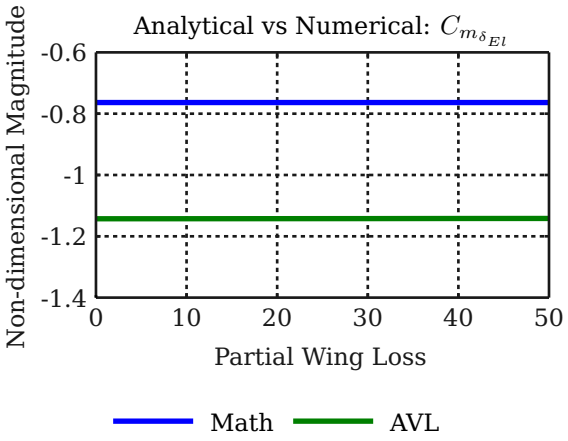

Figure A.11 – Analytic vs. AVL: $C_{m_{\delta_{El}}}$

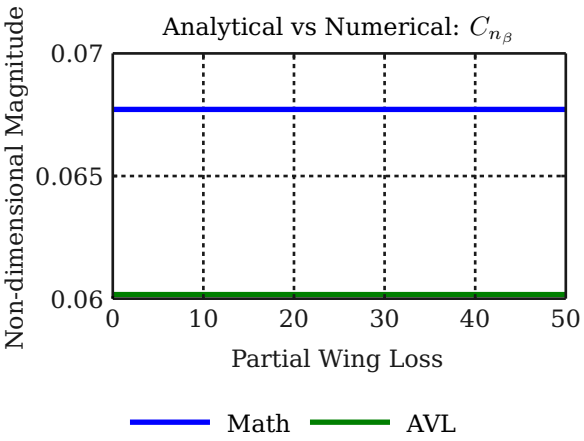

Figure A.12 – Analytic vs. AVL: C_{n_β}

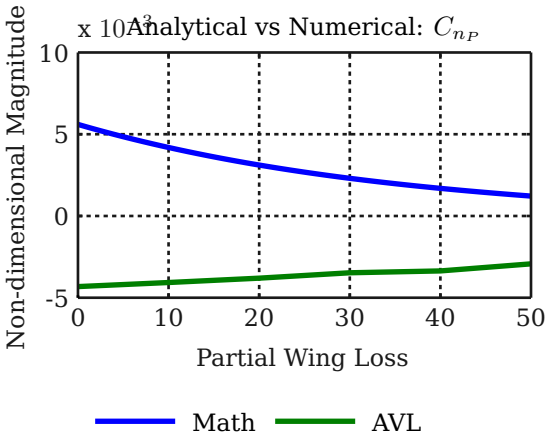

Figure A.13 – Analytic vs. AVL: C_{n_P}

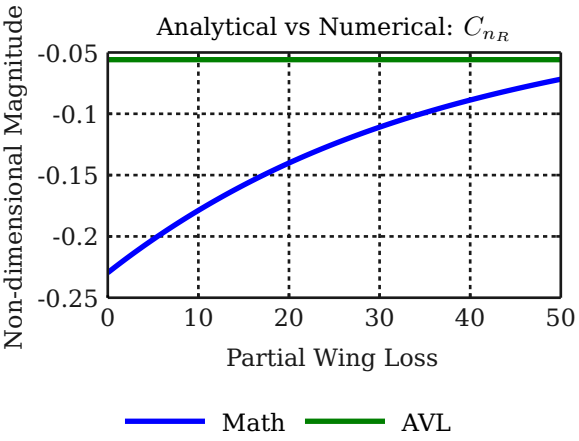

Figure A.14 – Analytic vs. AVL: C_{n_R}

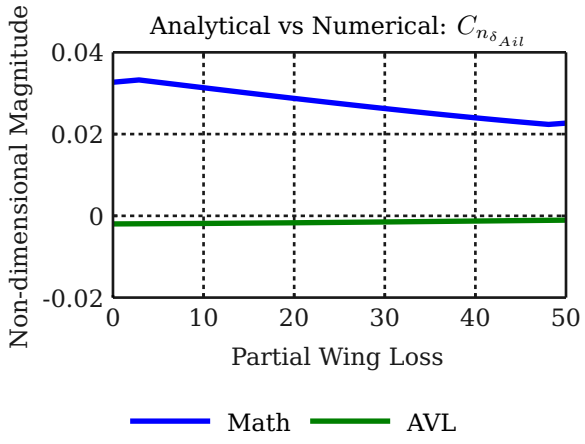

Figure A.15 – Analytic vs. AVL: $C_{n_{\delta_{Ail}}}$

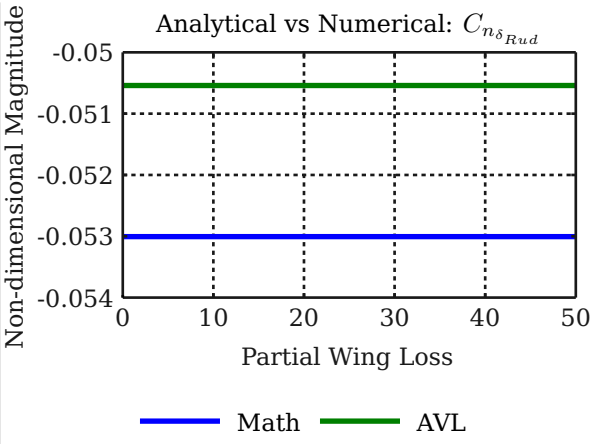

Figure A.16 – Analytic vs. AVL: $C_{n_{\delta_{Rud}}}$

A.3 Pure AVL non-dimensional coefficient plots

In this section all of the acquired AVL non-dimensional coefficients are displayed. Please note the magnitude of most of the coefficients that depict weird behaviour. In most cases, the change in coefficient is more likely to be due to numerical inaccuracies in AVL than actually wing loss generated effects.

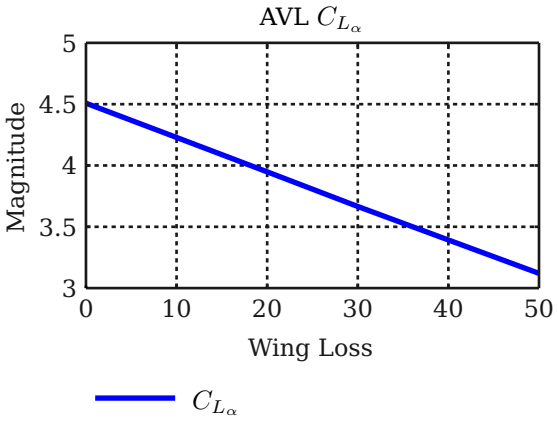

Figure A.17 – AVL non-dimensional CL_α

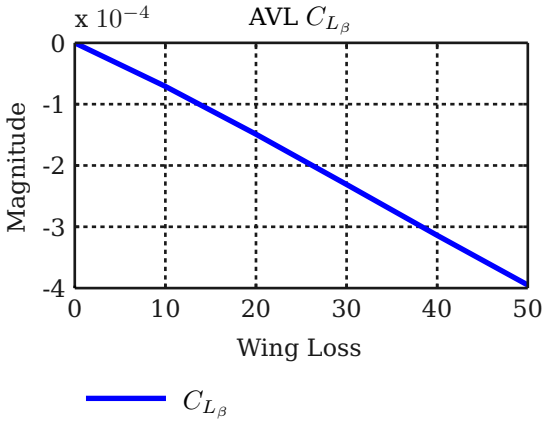

Figure A.18 – AVL non-dimensional CL_β

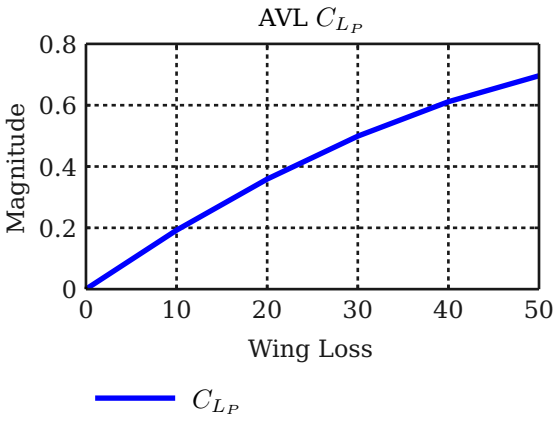

Figure A.19 – AVL non-dimensional CL_P

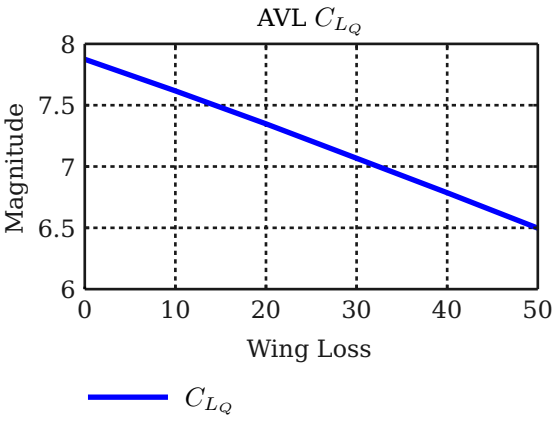

Figure A.20 – AVL non-dimensional CL_Q

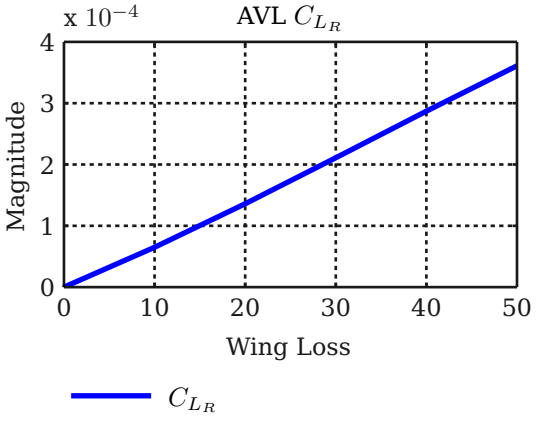

Figure A.21 – AVL non-dimensional CL_R

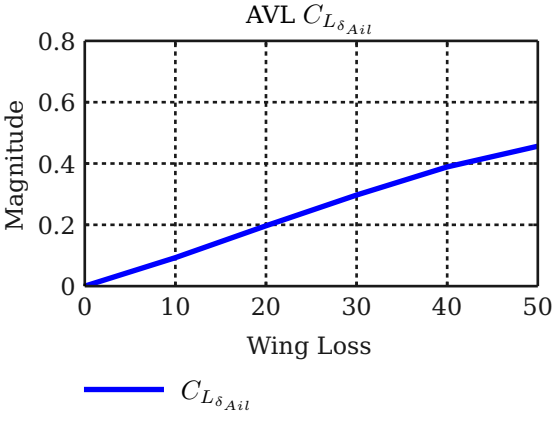

Figure A.22 – AVL non-dimensional $CL_{\delta_{Ail}}$

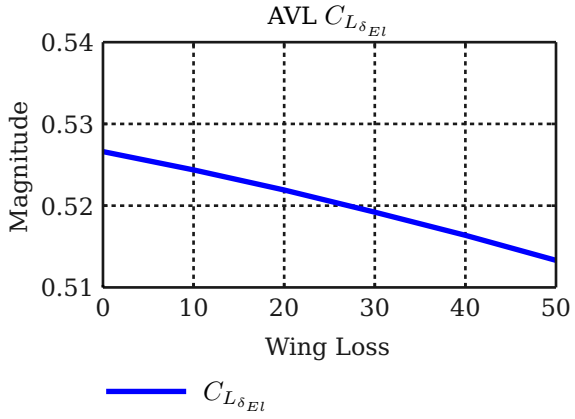

Figure A.23 – AVL non-dimensional $CL_{\delta_{El}}$

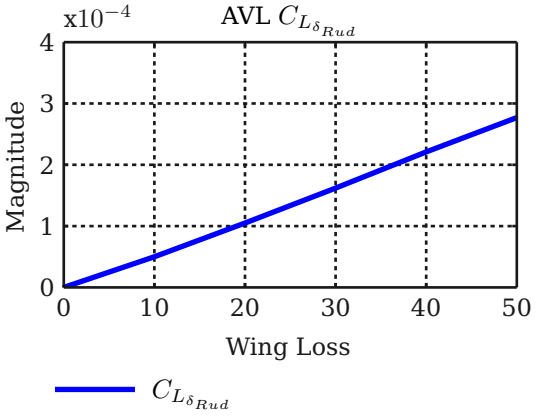

Figure A.24 – AVL non-dimensional $CL_{\delta_{Rud}}$

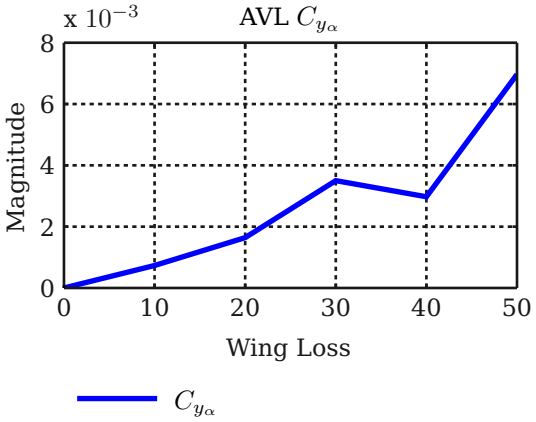

Figure A.25 – AVL non-dimensional $Cy - \alpha$

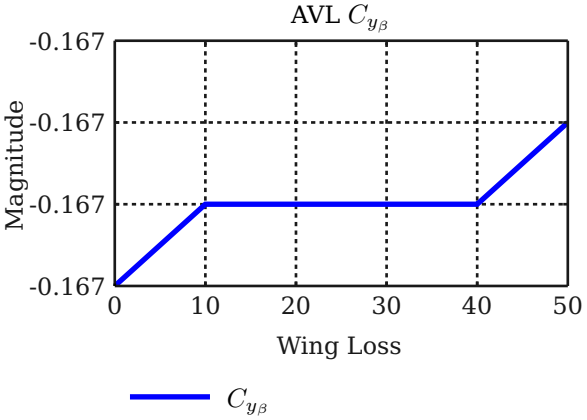

Figure A.26 – AVL non-dimensional Cy_β

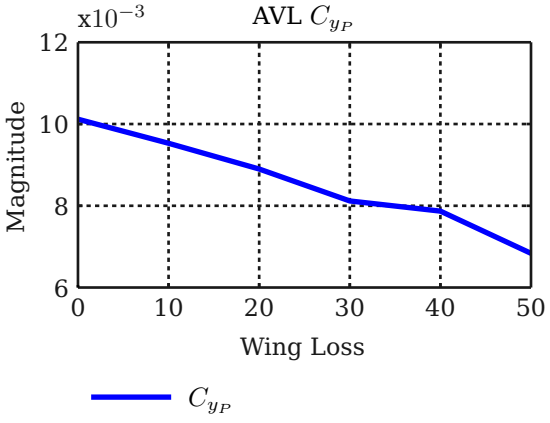

Figure A.27 – AVL non-dimensional Cy_P

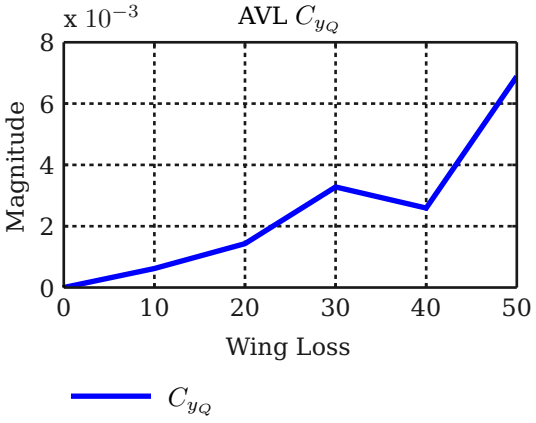

Figure A.28 – AVL non-dimensional Cy_Q

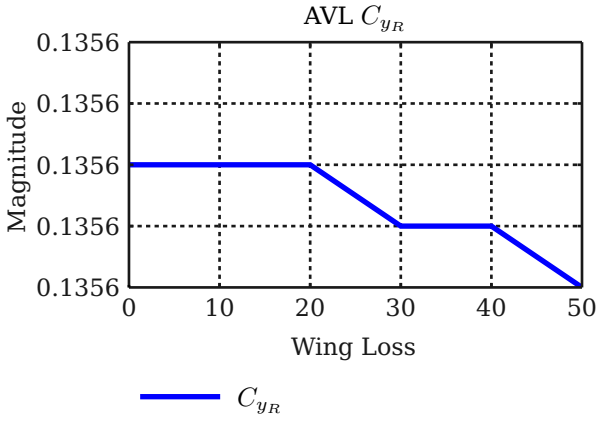

Figure A.29 – AVL non-dimensional Cy_R

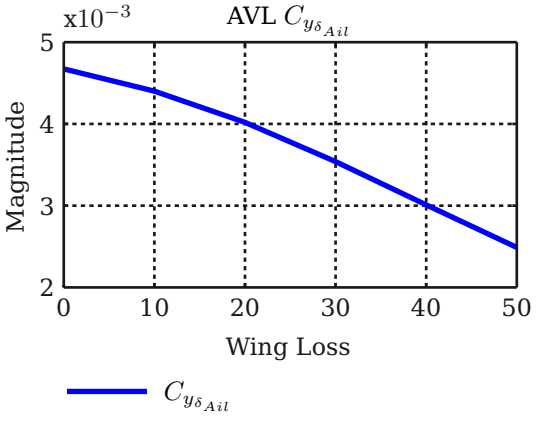

Figure A.30 – AVL non-dimensional $Cy_{\delta_{Ail}}$

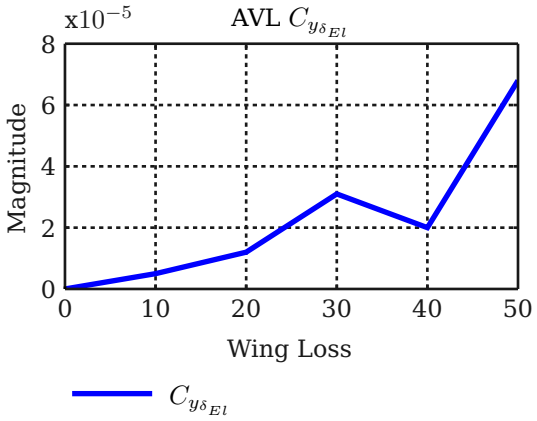

Figure A.31 – AVL non-dimensional $Cy_{\delta_{El}}$

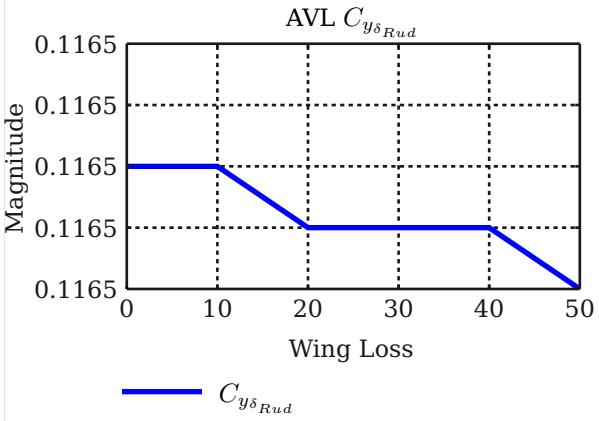

Figure A.32 – AVL non-dimensional $Cy_{\delta_{Rud}}$

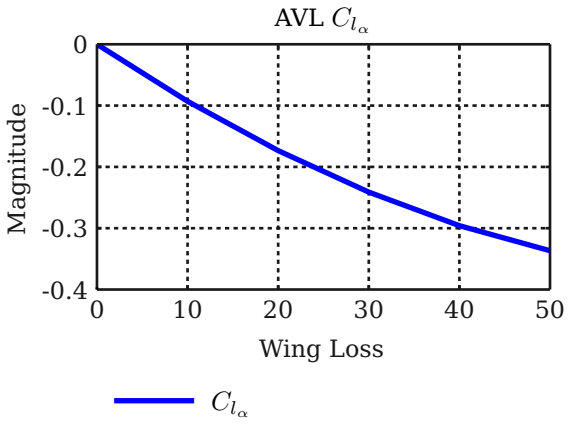

Figure A.33 – AVL non-dimensional Cl_α

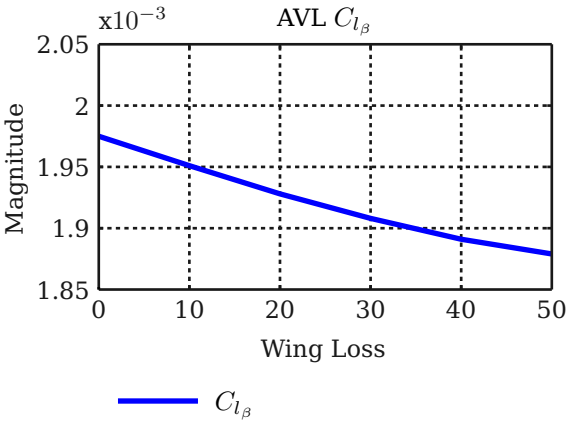

Figure A.34 – AVL non-dimensional Cl_β

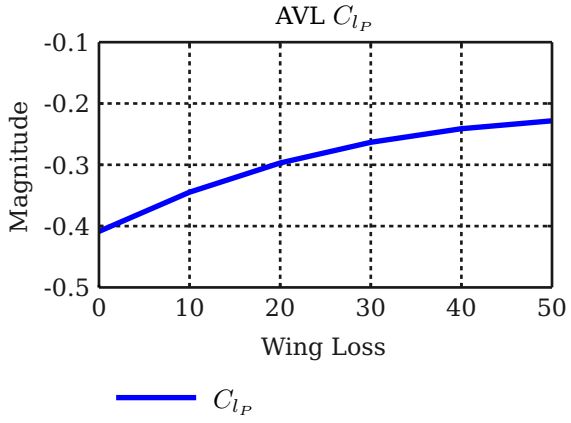

Figure A.35 – AVL non-dimensional Cl_P

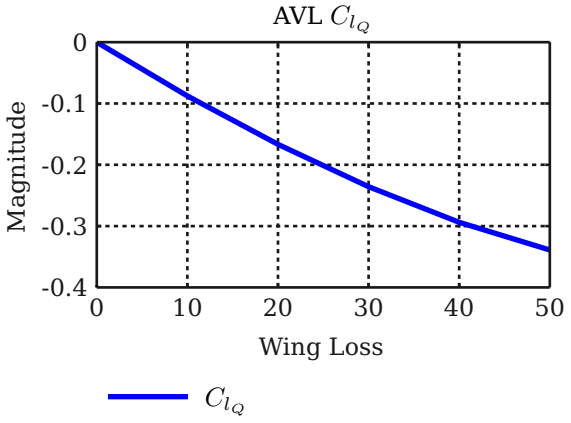

Figure A.36 – AVL non-dimensional Cl_Q

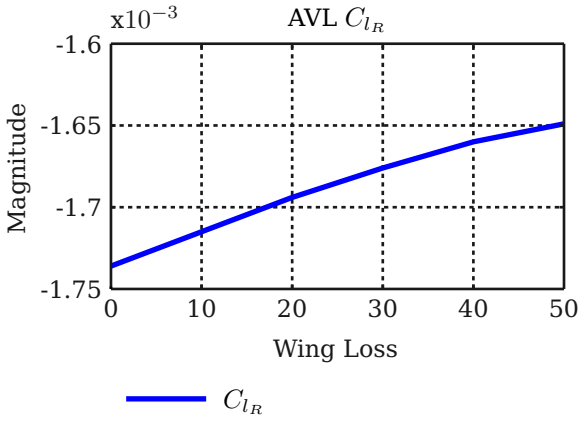

Figure A.37 – AVL non-dimensional Cl_R

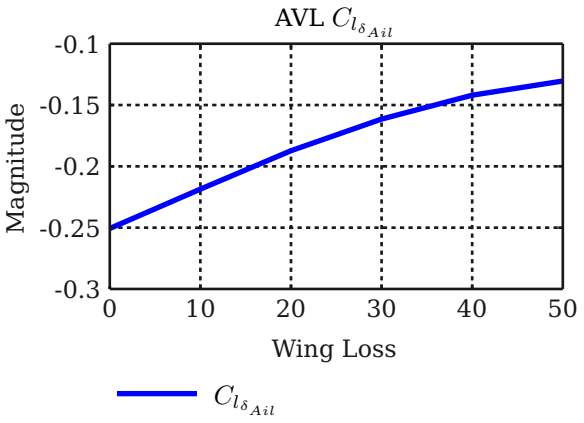

Figure A.38 – AVL non-dimensional $Cl_{\delta_{Ail}}$

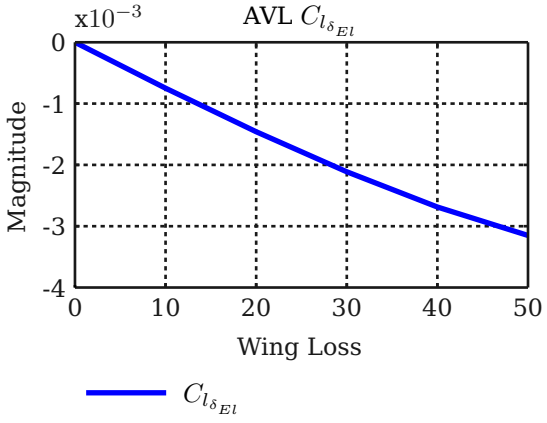

Figure A.39 – AVL non-dimensional $Cl_{\delta_{El}}$

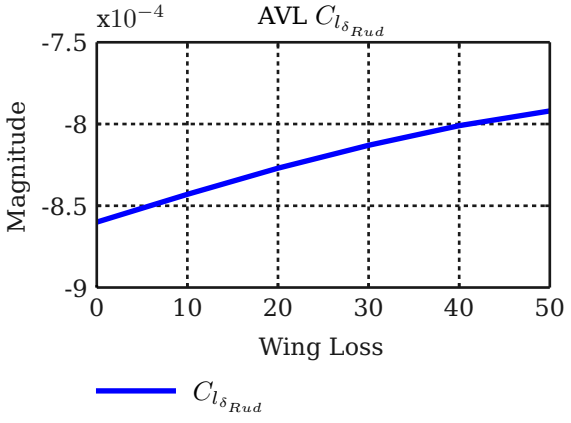

Figure A.40 – AVL non-dimensional $Cl_{\delta_{Rud}}$

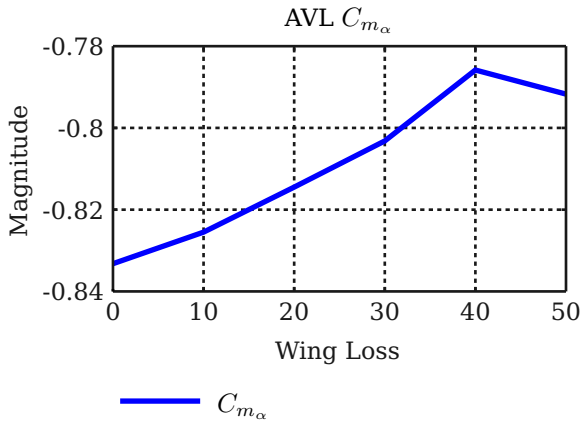

Figure A.41 – AVL non-dimensional Cm_α

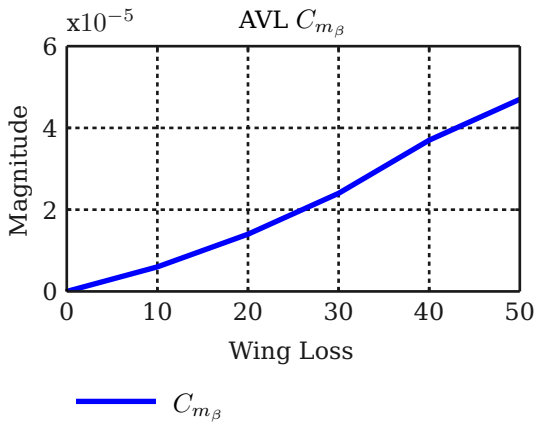

Figure A.42 – AVL non-dimensional Cm_β

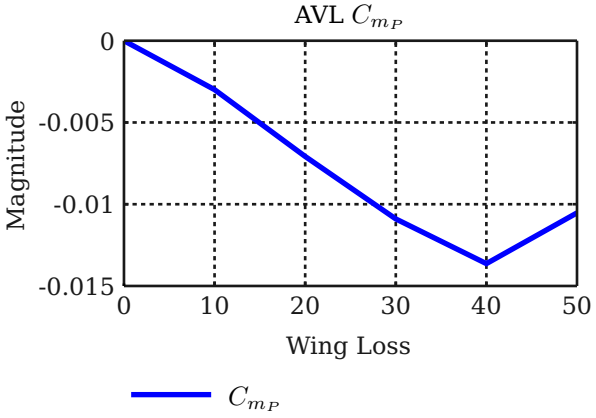

Figure A.43 – AVL non-dimensional Cm_P

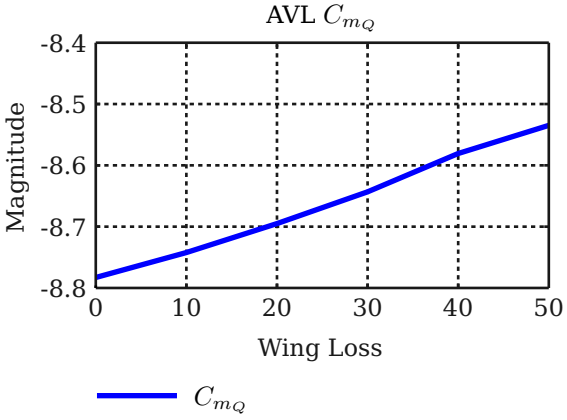

Figure A.44 – AVL non-dimensional Cm_Q

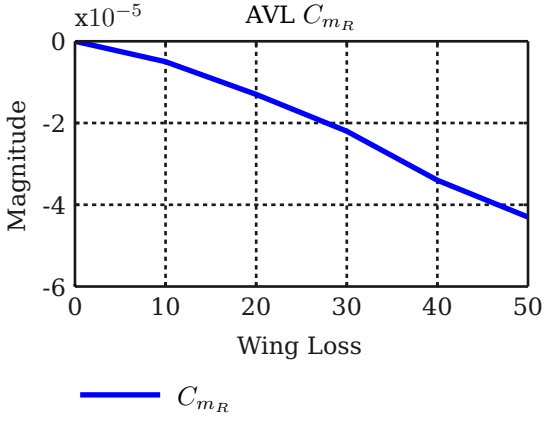

Figure A.45 – AVL non-dimensional Cm_R

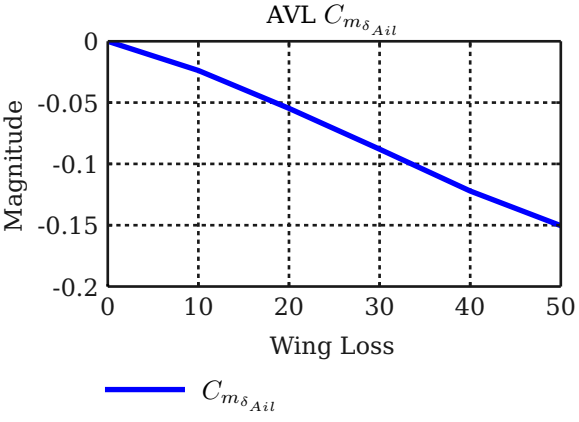

Figure A.46 – AVL non-dimensional $Cm_{\delta_{Ail}}$

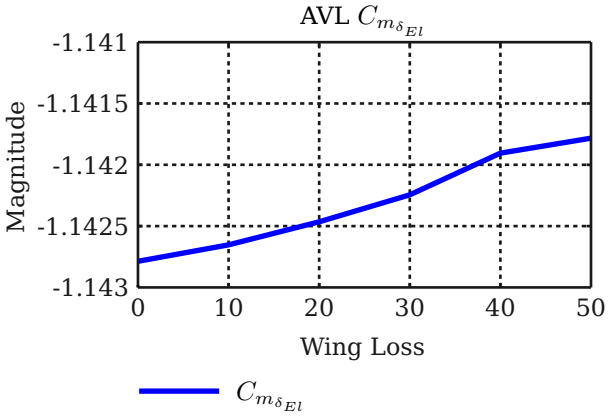

Figure A.47 – AVL non-dimensional $Cm_{\delta_{El}}$

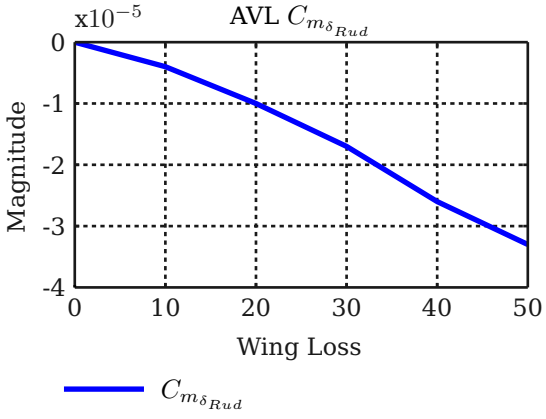

Figure A.48 – AVL non-dimensional $Cm_{\delta_{Rud}}$

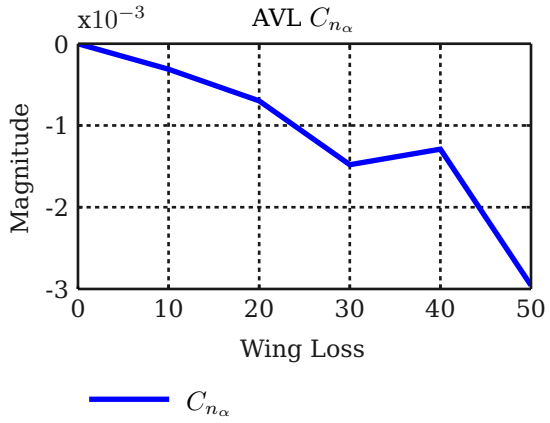

Figure A.49 – AVL non-dimensional Cn_α

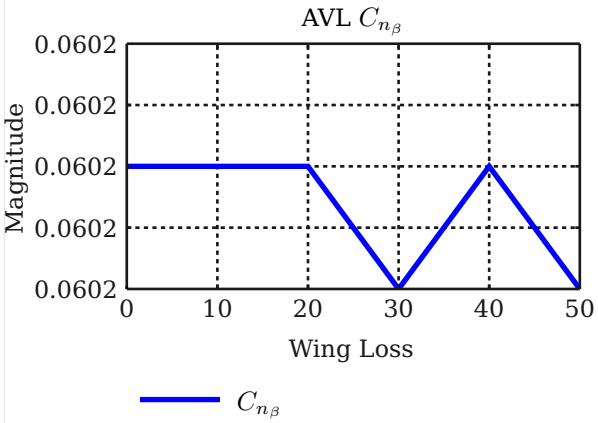

Figure A.50 – AVL non-dimensional Cn_β

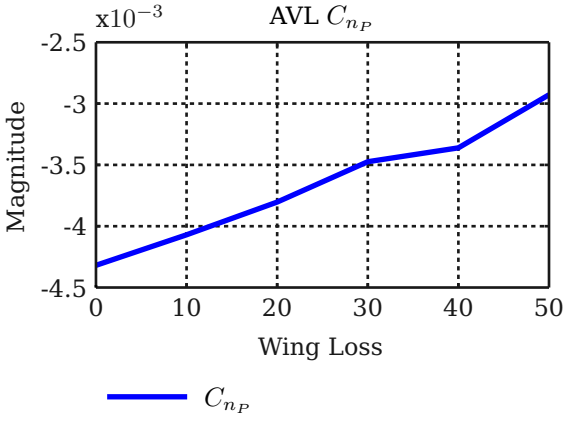

Figure A.51 – AVL non-dimensional Cn_P

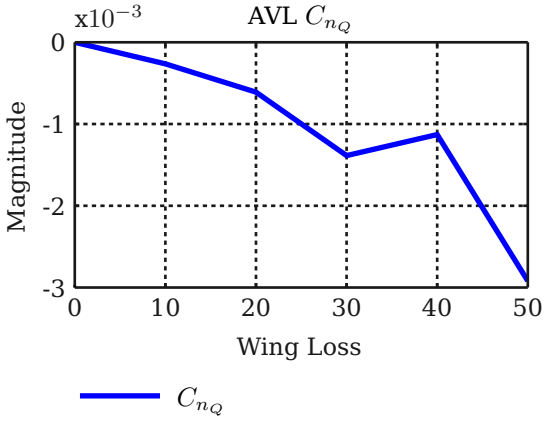

Figure A.52 – AVL non-dimensional n_QC

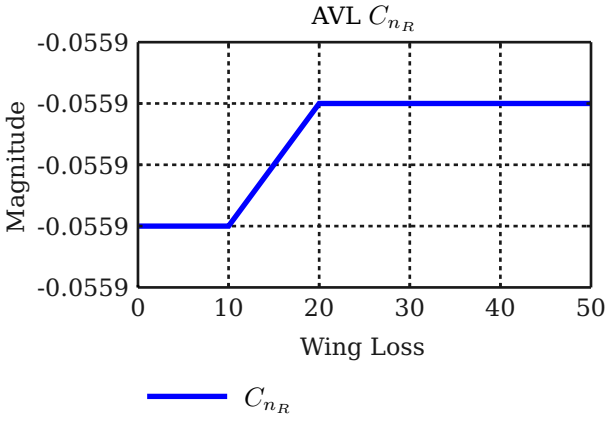

Figure A.53 – AVL non-dimensional Cn_R

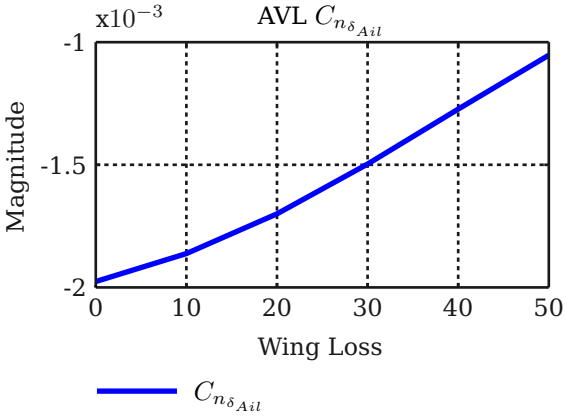

Figure A.54 – AVL non-dimensional $Cn_{\delta_{Ail}}$

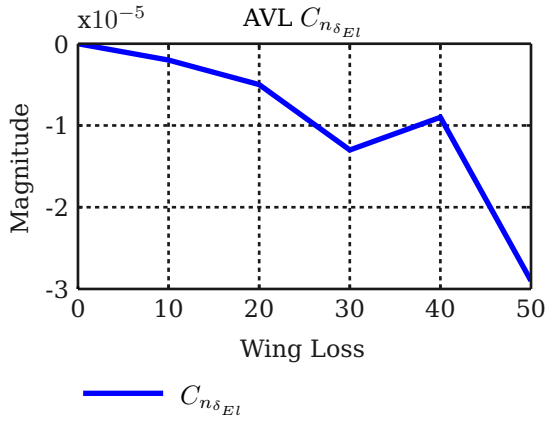

Figure A.55 – AVL non-dimensional $Cn_{\delta_{El}}$

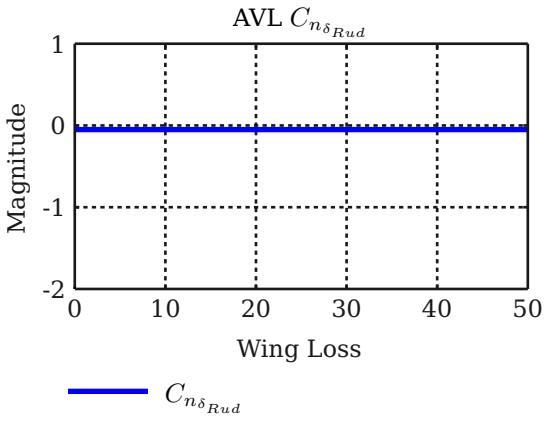

Figure A.56 – AVL non-dimensional $Cn_{\delta_{Rud}}$

Appendix B

SQP Trim Results

I this appendix the results of various cost function configurations acquired during the search for the best trim possible are presented. The section heading describes the cost used to acquire the trim displayed. Please note the magnitude of the north-south, down-up axis plots as they are relatively small in comparison to the north-south, east-west plots right next to them.

B.1 Equal Trim

In this trim solution, all the variables in the design vector have been given an equal weight. It might not look the case at first glance but it should be remembered from the analysis in the Section 3.4 that some of these variables are better suited than others to correct the effects of wing loss.

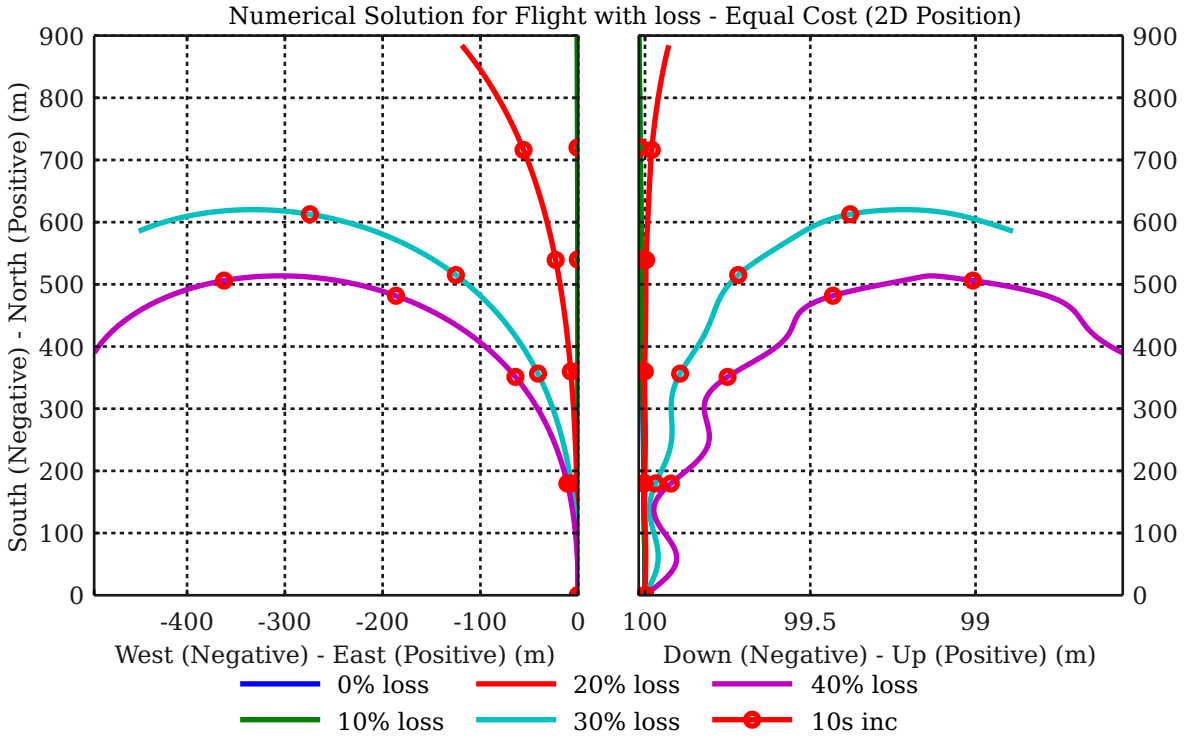

Figure B.1 – SQP Trim Flight with Wing loss - Equal Trim

	Thrust	α	β	ϕ	δ_{Ail}	δ_{El}	δ_{Rud}
0%	4.73463	6.05468	0.00000	0.00000	0.00000	-4.41453	0.00000
10%	4.70676	6.48422	-0.05587	-0.00735	-2.29597	-4.66377	0.01806
20%	4.60456	6.94370	-1.01153	-0.14472	-4.24582	-4.82138	-1.06233
30%	4.46883	7.66007	-4.72024	-0.68781	-7.13597	-4.96959	-5.41845
40%	4.37518	9.07542	-7.44675	-1.09087	-13.22541	-4.99634	-8.55522

Table B.1 – SQP - Deflections - Equal Cost trim

	F_X	F_Y	F_Z	L	M	N
0%	-3.97e-012	0.00e+000	-4.05e-013	0.00e+000	2.12e-015	0.00e+000
10%	4.43e-013	4.86e-017	3.55e-014	-4.72e-015	-1.13e-015	-3.55e-015
20%	-4.52e-004	-7.16e-006	-7.94e-005	-3.97e-005	2.14e-006	1.77e-005
30%	-4.24e-003	-3.06e-004	-7.82e-004	-5.96e-004	2.90e-005	2.76e-004
40%	-8.28e-003	-8.72e-004	-1.66e-003	-1.18e-003	3.15e-005	5.78e-004

Table B.2 – SQP - Forces and Moments - Equal Cost trim

B.2 Side-slip Trim

In this trim the side-slip angle is optimised. It is clear from Table B.3 that this is case as the UAV starts off with basically zero side-slip. Due to the zero side-slip,a lot less rudder deflection is required to keep the aircraft in its desired attitude.

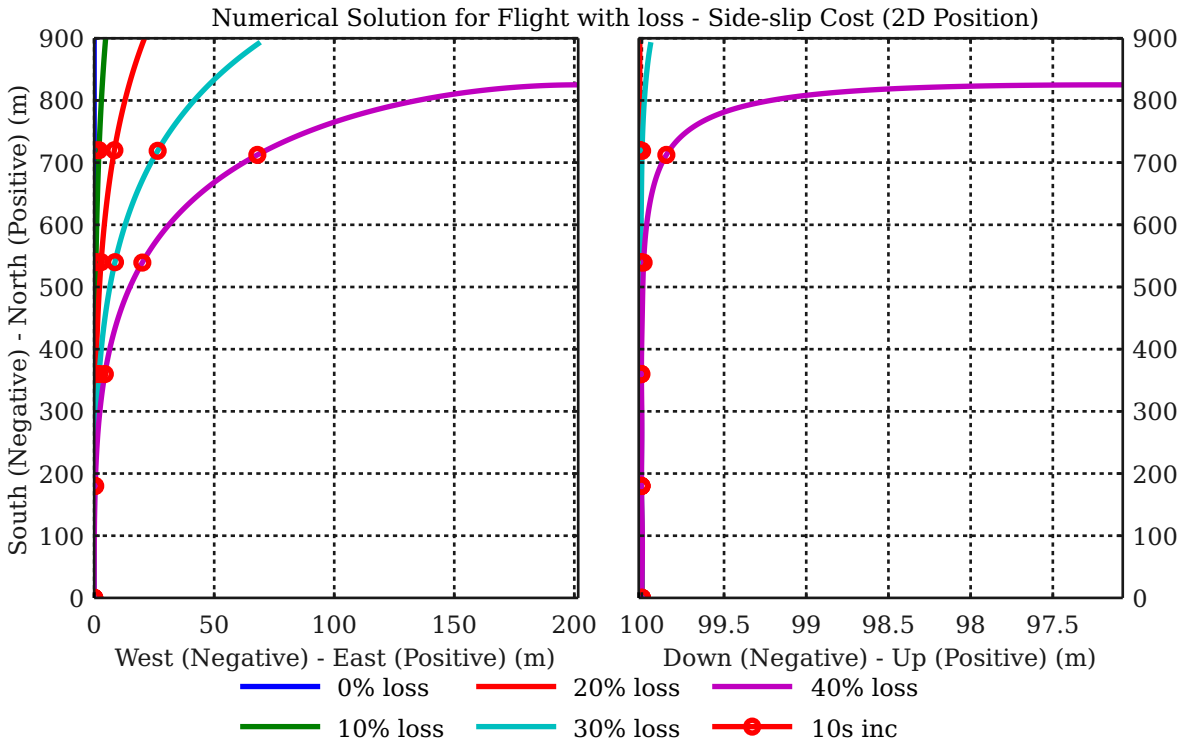

Figure B.2 – SQP Trim Flight with Wing Loss - Side-slip Trim

	Thrust	α	β	ϕ	δ_{Ail}	δ_{El}	δ_{Rud}
0%	4.73463	6.05468	0.00000	0.00000	0.00000	-4.41453	0.00000
10%	4.70676	6.48423	-0.00000	0.00057	-2.29587	-4.66386	0.08458
20%	4.60693	6.94481	-0.00000	0.00100	-4.25040	-4.82817	0.14297
30%	4.51467	7.67429	-0.00000	0.00154	-7.22435	-5.02199	0.21400
40%	4.48637	9.11827	-0.00000	0.00250	-13.49015	-5.08720	0.33983

Table B.3 – SQP - Deflections - Side-slip Cost trim

	F_X	F_Y	F_Z	L	M	N
0%	-3.92e-012	0.00e+000	-4.19e-013	0.00e+000	7.08e-016	0.00e+000
10%	-1.89e-013	1.73e-018	-1.42e-014	1.11e-016	1.73e-017	1.46e-015
20%	-2.97e-010	-6.51e-019	-3.62e-011	-1.14e-012	-5.55e-013	9.39e-012
30%	6.18e-012	1.08e-018	8.24e-013	4.53e-014	1.93e-014	-3.37e-013
40%	-1.75e-012	-1.60e-017	-2.84e-013	-1.69e-014	-6.05e-015	1.10e-013

Table B.4 – SQP - Forces and Moments - Side-slip Cost trim

B.3 Banked Trim

In this trim solution, the bank angle was optimised. It is clear from Table B.6 that this solution is quite good but as far as deflections and angles acquired are concerned it may not be such an optimal solution. Due to quite a large side-slip angle, the rudder control surface is basically maxed. It does however require less aileron deflection but in comparison to the previous trim, the bank angle itself is actually larger. This led to the conclusion that bank angle optimisation is definitely not an optimal solution.

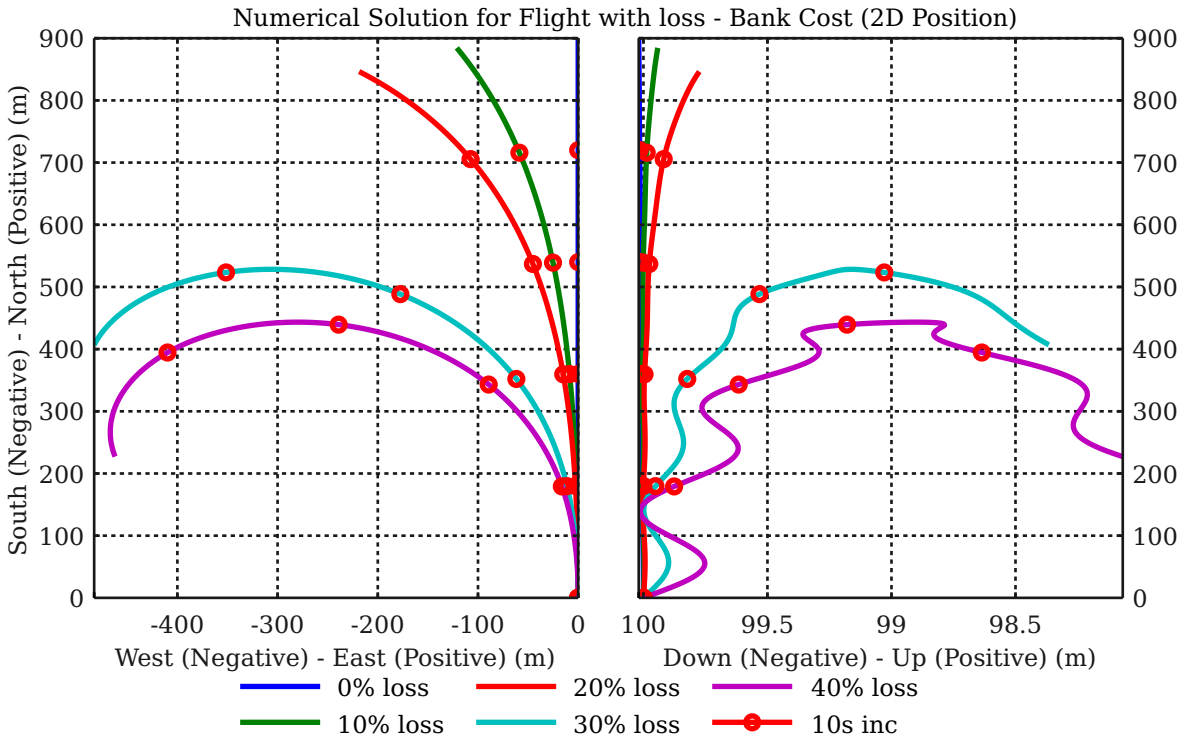

Figure B.3 – SQP Trim Flight with Wing Loss - Bank Angle Trim

	Thrust	α	β	ϕ	δ_{Ail}	δ_{El}	δ_{Rud}
0%	4.73463	6.05468	0.00000	0.00000	0.00000	-4.41453	0.00000
10%	4.70362	6.48403	-1.28618	-0.18184	-2.29820	-4.66173	-1.44684
20%	4.59960	6.94267	-1.98150	-0.28441	-4.24217	-4.81482	-2.21789
30%	4.39947	7.65206	-7.87269	-1.14404	-7.09692	-4.93350	-9.17680
40%	4.19703	9.05483	-12.52018	-1.81798	-13.12162	-4.93040	-14.60722

Table B.5 – SQP - Deflections - Bank Cost trim

	F_X	F_Y	F_Z	L	M	N
0%	-3.92e-012	0.00e+000	-4.19e-013	0.00e+000	7.08e-016	0.00e+000
10%	6.84e-006	-4.32e-008	6.32e-007	-5.07e-008	5.79e-009	-4.63e-008
20%	5.75e-005	-1.71e-007	6.62e-006	-3.72e-007	1.27e-007	-1.77e-006
30%	3.12e-004	-3.69e-006	3.98e-005	-3.09e-006	1.25e-006	-1.66e-005
40%	1.94e-004	-3.49e-006	2.98e-005	-2.09e-006	9.16e-007	-1.21e-005

Table B.6 – SQP - Forces and Moments - Bank Cost trim

B.4 Angle of Attack Trim

In this trim, the angle of attack is optimised. As depicted in Figure B.4, the response itself closely resembles that of the previous trim. When examining the design vector variables and the resulting forces and moments, it can be seen that the acquired values are basically identical. In optimising the angle of attack, the UAV will generate less lift at the current airspeed. As an explicit amount is necessary to keep the UAV in the air, this reduction needs to be compensated for in some of other variables.

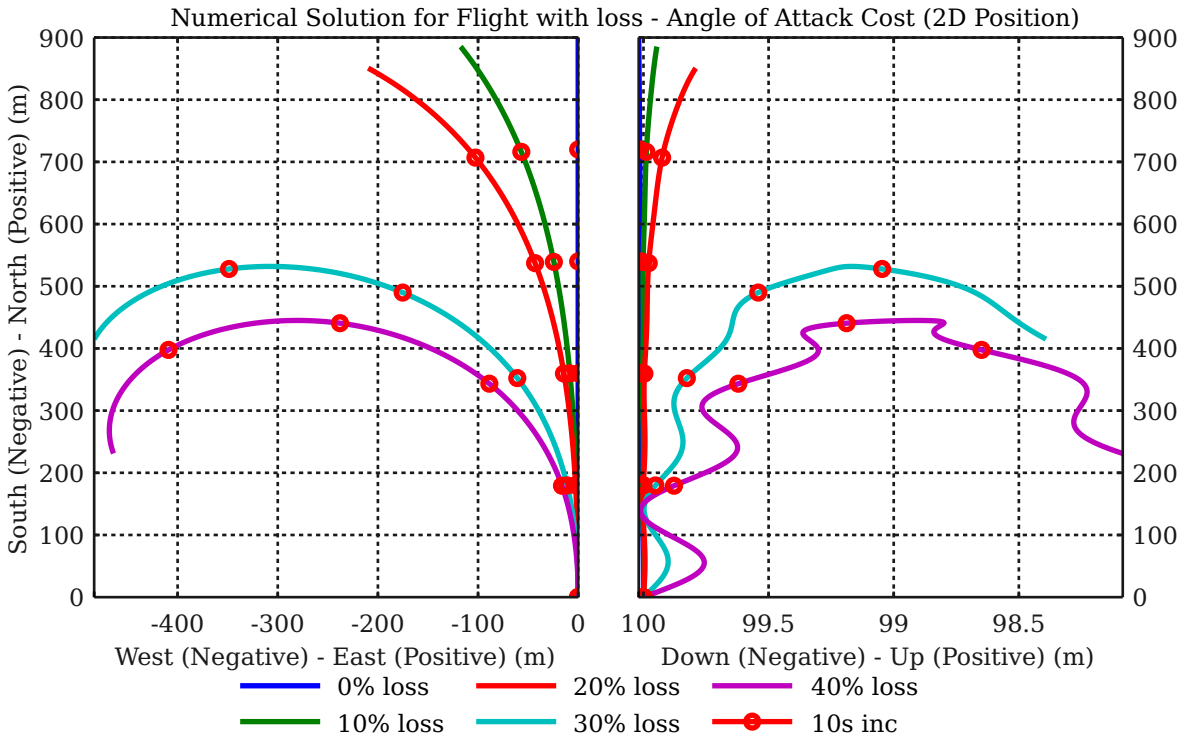

Figure B.4 – SQP Trim Flight with Wing Loss - Angle of Attack Trim

	Thrust	α	β	ϕ	δ_{Ail}	δ_{El}	δ_{Rud}
0%	4.73463	6.05468	0.00000	0.00000	0.00000	-4.41453	0.00000
10%	4.70382	6.48403	-1.24444	-0.17592	-2.29812	-4.66180	-1.39714
20%	4.60022	6.94277	-1.88963	-0.27119	-4.24250	-4.81544	-2.10844
30%	4.40282	7.65236	-7.74708	-1.12595	-7.09823	-4.93495	-9.02706
40%	4.20230	9.05523	-12.40131	-1.80119	-13.12340	-4.93197	-14.46541

Table B.7 – SQP - Deflections - Angle of Attack Cost trim

	F_X	F_Y	F_Z	L	M	N
0%	-3.89e-012	0.00e+000	-3.27e-013	0.00e+000	4.96e-015	0.00e+000
10%	6.16e-007	-6.99e-010	6.76e-008	-4.15e-010	3.10e-010	-4.53e-009
20%	8.19e-006	-7.17e-010	9.96e-007	2.97e-008	1.54e-008	-2.59e-007
30%	1.56e-005	-1.55e-008	2.09e-006	9.07e-008	5.10e-008	-8.51e-007
40%	3.11e-005	-1.86e-007	4.89e-006	8.36e-008	1.22e-007	-1.95e-006

Table B.8 – SQP - Forces and Moments - Angle of Attack Cost trim

B.5 Actuator Trim

In this trim solution, only the actuators have been give equal weights for optimisation. This trim roughly relates to the side-slip trim, with small side-slip and bank angles. The ailerons and rudder use less deflection than most other trims but the elevator is increased. This is mainly due to the larger angle of attack.

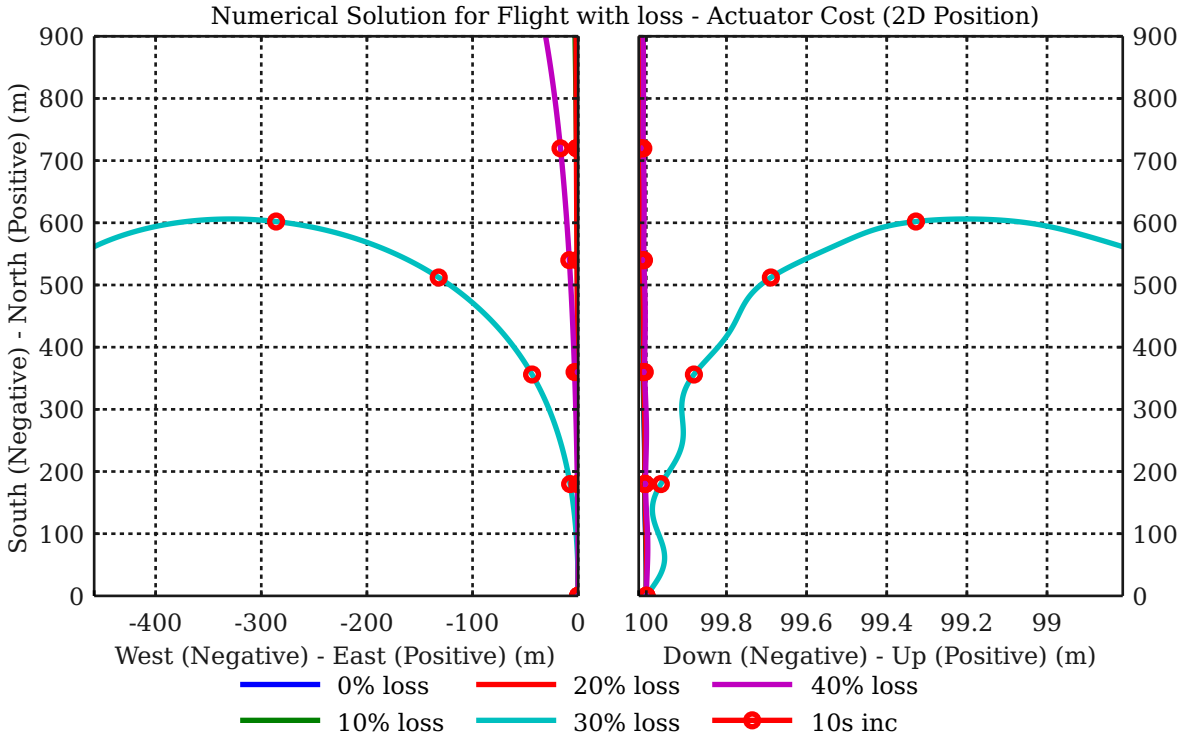

Figure B.5 – SQP Trim Flight with Wing Loss - Equal Actuators Trim

	Thrust	α	β	ϕ	δ_{Ail}	δ_{El}	δ_{Rud}
0%	4.73463	6.05468	0.00000	0.00000	0.00000	-4.41453	0.00000
10%	4.70675	6.48422	-0.07367	-0.00988	-2.29600	-4.66374	-0.00314
20%	4.60689	6.94463	-0.15707	-0.02163	-4.24964	-4.82711	-0.04418
30%	4.46209	7.65914	-5.07003	-0.73862	-7.13090	-4.96565	-5.83572
40%	4.48537	9.11342	-0.72889	-0.10509	-13.45882	-5.07861	-0.53069

Table B.9 – SQP - Deflections - Actuator Cost trim

	F_X	F_Y	F_Z	L	M	N
0%	-3.91e-012	0.00e+000	-4.76e-013	0.00e+000	7.08e-016	0.00e+000
10%	6.01e-013	-3.64e-017	7.11e-014	2.94e-015	3.64e-016	-4.41e-015
20%	-3.55e-010	-2.01e-016	-4.32e-011	-1.37e-012	-6.58e-013	1.12e-011
30%	-4.59e-003	-2.78e-004	-8.16e-004	-5.39e-004	5.07e-005	2.96e-004
40%	-4.52e-013	1.25e-016	-2.13e-014	2.22e-015	-4.27e-015	3.16e-014

Table B.10 – SQP - Forces and Moments - Actuator Cost trim

B.6 Aileron Trim

In this trim solution, the ailerons are optimised. The results are comparable with those of the angle of attack trim. As the ailerons are the main deflection surface used to correct the lift imbalance, is it expected that they will cause a sub-optimal trim. This again comes back to lift generation. Reducing the optimal surfaces deflections to correct this imbalance will require a lot more deflection on sub-optimal surfaces.

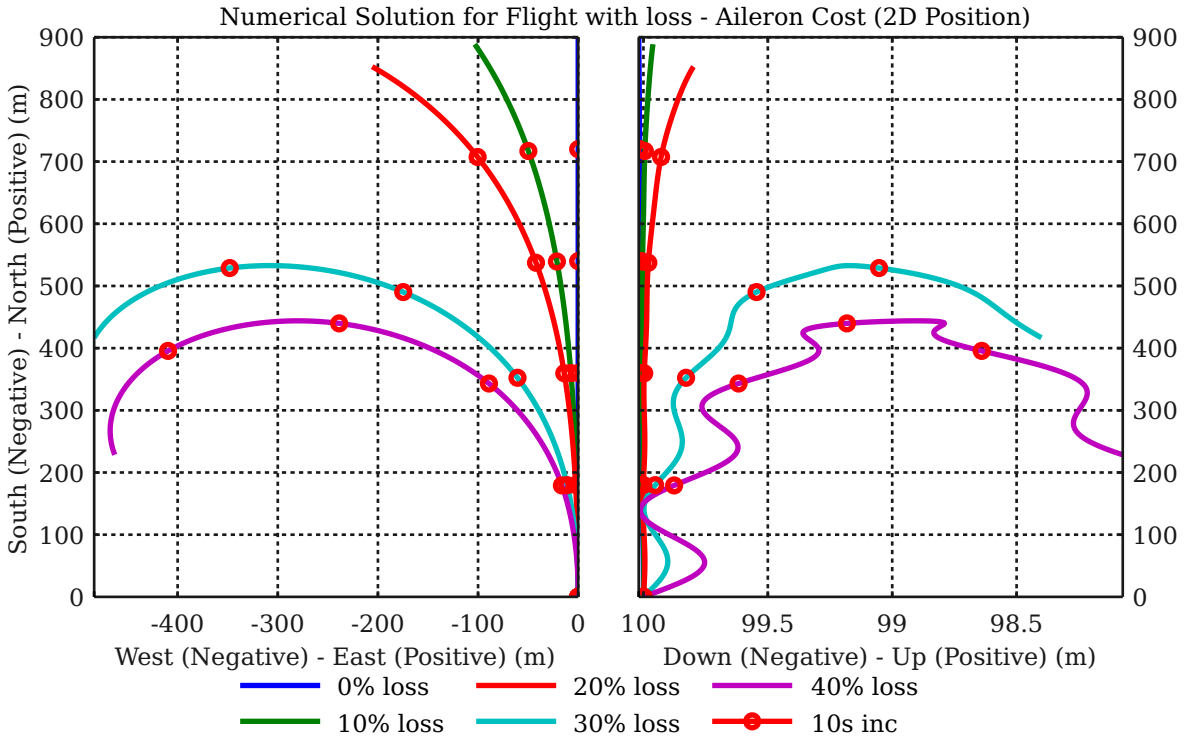

Figure B.6 – SQP Trim Flight with Wing Loss - Aileron Trim

	Thrust	α	β	ϕ	δ_{Ail}	δ_{El}	δ_{Rud}
0%	4.73463	6.05468	0.00000	0.00000	0.00000	-4.41453	0.00000
10%	4.70451	6.48406	-1.08923	-0.15391	-2.29783	-4.66206	-1.21234
20%	4.60051	6.94281	-1.84891	-0.26533	-4.24264	-4.81572	-2.05992
30%	4.40382	7.65243	-7.71611	-1.12150	-7.09854	-4.93531	-8.99009
40%	4.19879	9.05496	-12.48061	-1.81239	-13.12221	-4.93093	-14.56001

Table B.11 – SQP - Deflections - Aileron Cost trim

	F_X	F_Y	F_Z	L	M	N
0%	-3.92e-012	0.00e+000	-4.19e-013	0.00e+000	7.08e-016	0.00e+000
10%	-1.61e-007	-6.33e-010	-2.08e-008	-1.14e-009	-1.75e-011	1.29e-009
20%	1.50e-005	-6.52e-009	1.81e-006	3.60e-008	2.88e-008	-4.73e-007
30%	1.25e-004	-3.61e-007	1.65e-005	4.17e-007	4.22e-007	-6.75e-006
40%	1.39e-004	-2.33e-006	2.15e-005	-1.34e-006	6.41e-007	-8.69e-006

Table B.12 – SQP - Forces and Moments - Aileron Cost trim

B.7 Elevator Trim

In this trim solution the elevator was optimised. As observed in Figure B.7, the response is basically the same as that of the ailerons and Tables B.13 and B.14 confirm this with nearly identical values. In essence, it comes down to the same conclusion as stated for the ailerons.

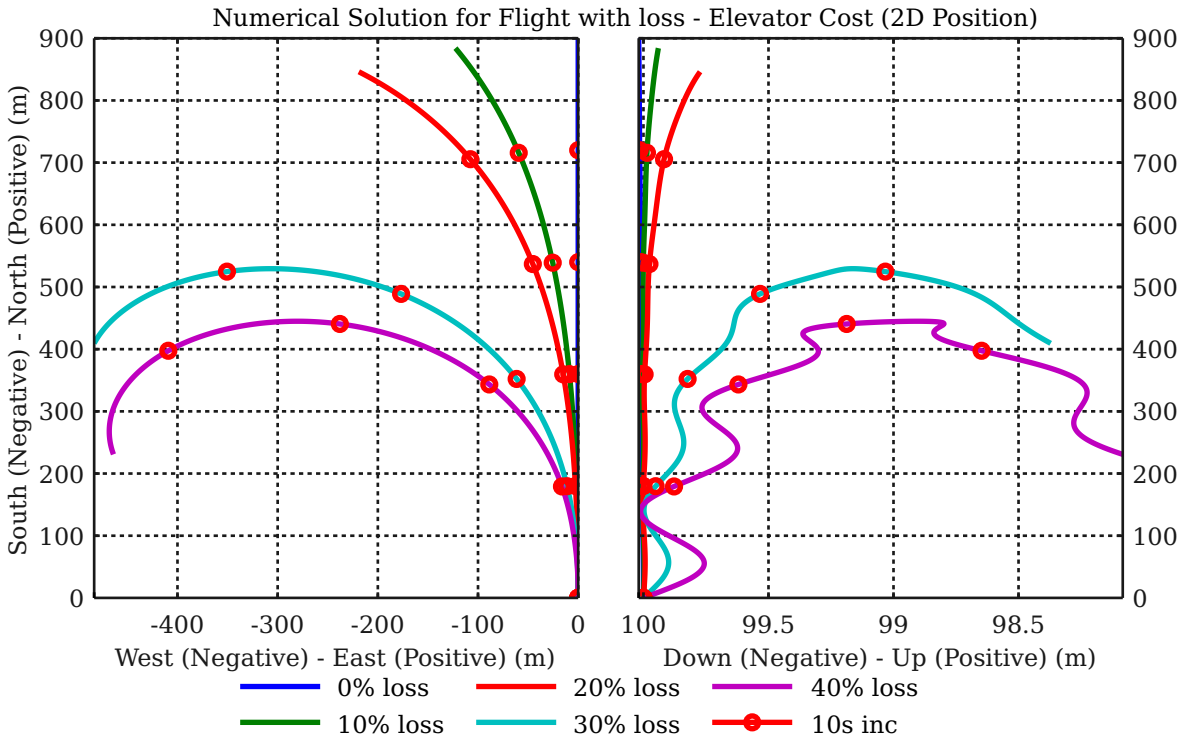

Figure B.7 – SQP Trim Flight with Wing Loss - Elevator Trim

	Thrust	α	β	ϕ	δ_{Ail}	δ_{El}	δ_{Rud}
0%	4.73463	6.05468	0.00000	0.00000	0.00000	-4.41453	0.00000
10%	4.70354	6.48403	-1.30148	-0.18401	-2.29823	-4.66171	-1.46506
20%	4.59954	6.94266	-1.98628	-0.28510	-4.24216	-4.81479	-2.22359
30%	4.40029	7.65215	-7.83665	-1.13884	-7.09730	-4.93392	-9.13387
40%	4.20194	9.05521	-12.40882	-1.80225	-13.12329	-4.93187	-14.47438

Table B.13 – SQP - Deflections - Elevator Cost trim

	F_X	F_Y	F_Z	L	M	N
0%	-3.90e-012	0.00e+000	-6.04e-013	0.00e+000	-3.54e-015	0.00e+000
10%	1.80e-006	-2.18e-009	1.98e-007	-1.20e-009	9.09e-010	-1.33e-008
20%	4.02e-005	-8.10e-008	4.72e-006	-1.21e-007	8.43e-008	-1.25e-006
30%	7.98e-005	-8.21e-008	1.07e-005	4.86e-007	2.60e-007	-4.34e-006
40%	8.75e-006	-3.36e-007	1.29e-006	-3.52e-007	4.56e-008	-5.44e-007

Table B.14 – SQP - Forces and Moments - Elevator Cost trim

B.8 Rudder Trim

In this trim solution the rudder is optimised. The response is one of the best acquired graphically, even though the forces and moments are a bit bigger than those of some of the other trims. This is due to the UAV staying in close to this configuration a lot longer before it started to diverge from the calculated design vector values. Although the rudder is optimised, its value is quite large in comparison to the side-slip optimised trim, with only a slight improvement in response. Taking everything into account, this trim may be a good choice but it is still trumped by the side-slip optimised trim.

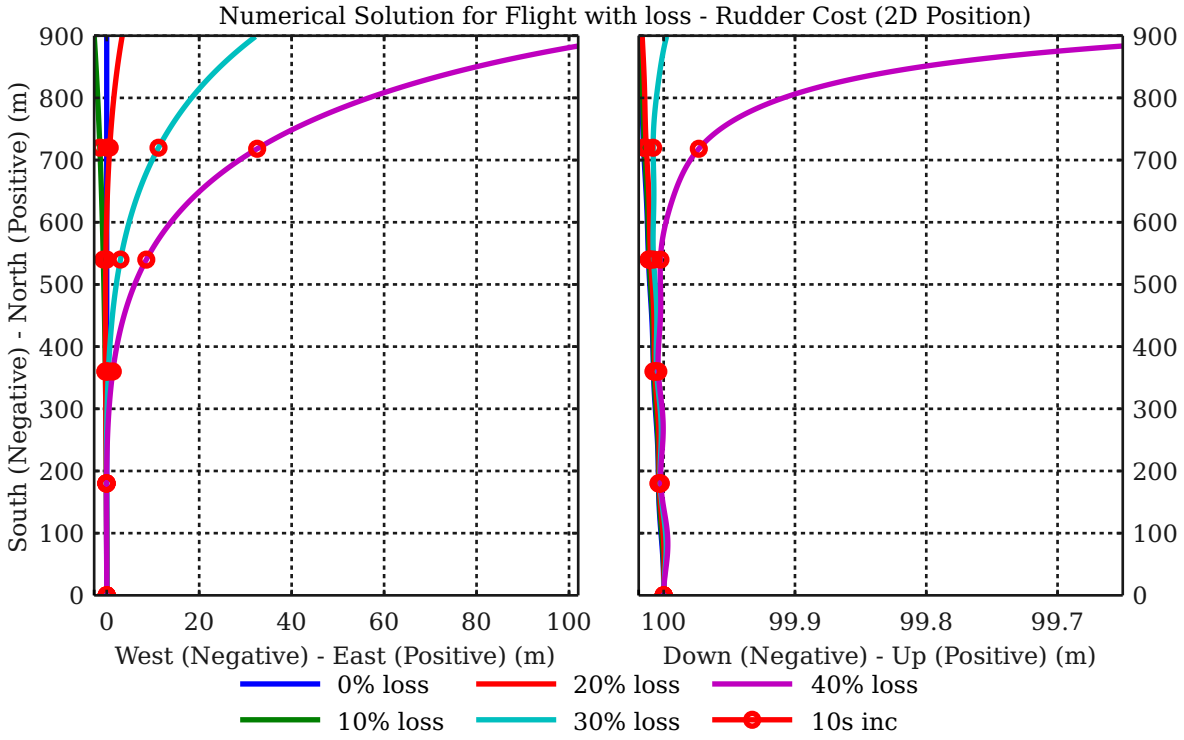

Figure B.8 – SQP Trim Flight with Wing Loss - Rudder Trim

	Thrust	α	β	ϕ	δ_{Ail}	δ_{El}	δ_{Rud}
0%	4.73463	6.05468	0.00000	0.00000	0.00000	-4.41453	0.00000
10%	4.70676	6.48422	-0.05587	-0.00735	-2.29597	-4.66377	0.01806
20%	4.60456	6.94370	-1.01153	-0.14472	-4.24582	-4.82138	-1.06233
30%	4.46883	7.66007	-4.72024	-0.68781	-7.13597	-4.96959	-5.41845
40%	4.37518	9.07542	-7.44675	-1.09087	-13.22541	-4.99634	-8.55522

Table B.15 – SQP - Deflections - Rudder Cost trim

	F_X	F_Y	F_Z	L	M	N
0%	-3.97e-012	0.00e+000	-4.05e-013	0.00e+000	2.12e-015	0.00e+000
10%	4.43e-013	4.86e-017	3.55e-014	-4.72e-015	-1.13e-015	-3.55e-015
20%	-4.52e-004	-7.16e-006	-7.94e-005	-3.97e-005	2.14e-006	1.77e-005
30%	-4.24e-003	-3.06e-004	-7.82e-004	-5.96e-004	2.90e-005	2.76e-004
40%	-8.28e-003	-8.72e-004	-1.66e-003	-1.18e-003	3.15e-005	5.78e-004

Table B.16 – SQP - Forces and Moments - Rudder Cost trim

Appendix C

Linearisation Script for EoM

In this appendix the Matlab linearistaion script used to acquire the linear model of the AEoM is presented.

```
,%%%%%%%%%%%%%%%%%%%%%%%%%%%%%%%%%%%%%%%%%%%%%%%%%%%%%%%%%%%%%%%%%%%%%%%%%%%%%%%%
% Linearisation of EoM for asymmetric aircraft                                   %
%%%%%%%%%%%%%%%%%%%%%%%%%%%%%%%%%%%%%%%%%%%%%%%%%%%%%%%%%%%%%%%%%%%%%%%%%%%%%%%%
% Equations implemented from:
% % Bacon, Barton J; Gregory, Irene M — General Equations of Motion for a Damaged Asymmetric
    Aircraft
% % Peddle, I.K — Advanced Automation 833 — introductory course to aircraft dynamics
% % Hough, Willem — ESL calAeroModel.c file
clc
clear all

%% EoM
%Variables
syms ('Vt','alpha','beta','real');
syms ('U','V','W','P','Q','R','real');
syms ('Ixx','Ixy','Ixz','Iyy','Izz','Iyz','real');
syms ('cgX','cgY','cgZ','m','real');

% Matrix and Vector Composition
v_A_omega = [U V W P Q R]';
I = [Ixx -Ixy -Ixz; -Ixy Iyy -Iyz;-Ixz -Iyz Izz];
dCG = [0 -cgZ cgY;cgZ 0 -cgX;-cgY cgX 0];
Dx = m*dCG;

Omega_x = [0 -R Q; R 0 -P; -Q P 0];

V_x = [0 -W V; W 0 -U; -V U 0];


%% Aerodynamic Forces and Moments
% Variables
syms ('da','de','dr','real');
syms ('daT','deT','drT','real');
syms ('CL_alpha','CL_beta','CL_p','CL_q','CL_r','CL_da','CL_de','CL_dr','real');
syms ('CY_alpha','CY_beta','CY_p','CY_q','CY_r','CY_da','CY_de','CY_dr','real');
syms ('Cl_alpha','Cl_beta','Cl_p','Cl_q','Cl_r','Cl_da','Cl_de','Cl_dr','real');
syms ('Cm_alpha','Cm_beta','Cm_p','Cm_q','Cm_r','Cm_da','Cm_de','Cm_dr','real');
syms ('Cn_alpha','Cn_beta','Cn_p','Cn_q','Cn_r','Cn_da','Cn_de','Cn_dr','real');
syms ('AR','e','b','c','rho','Sref','real');
syms ('theta','thetaT','phi','phiT','psi','psiT','G','real');
syms ('alphaT','betaT','ARpie','CLt','S','real');

CL_0 = 0;
CD_0 = 0;

% Coefficient of lift
CL = CL_0 + CL_alpha*alpha + CL_de*de + CL_da*da;
% Coefficient of drag
CD = CD_0 + (CL*CL)/(ARpie);

% X-force coefficient in wind (stability) axis
CXs = -CD;
% Y-force coefficient in wind (stability) axis
```

```
CYs = CY_alpha*alpha+ CY_beta*beta + (b/(2*Vt))*(CY_p*P + CY_r*R) + CY_da*da + CY_dr*dr;
% Z-force coefficient in wind (stability) axis
CZs = -CL +(b/(2*Vt))*(CL_p*P) +(c/(2*Vt))*(CL_q*Q);
% Roll moment coefficient in wind (stability) axis
Cls = Cl_alpha*alpha + Cl_beta*beta + (b/(2*Vt))*(Cl_p*P + Cl_r*R) +(c/(2*Vt))*(Cl_q*Q) + Cl_da*da +
    Cl_de*de + Cl_dr*dr;
% Pitch moment coefficient in wind (stability) axis
Cms = Cm_alpha*alpha + (b/(2*Vt))*(Cm_p*P) + (c/(2*Vt))*(Cm_q*Q) + Cm_da*da + Cm_de*de;
% Yaw moment coefficient in wind (stability) axis
Cns = Cn_alpha*alpha + Cn_beta*beta + (b/(2*Vt))*(Cn_p*P + Cn_r*R) + Cn_da*da + Cn_dr*dr;

% X-force coefficient in body axis
CX = CXs*cos(alpha)*cos(beta) - CYs*cos(alpha)*sin(beta) - CZs*sin(alpha);
% Y-force coefficient in body axis
CY = CXs*sin(beta) + CYs*cos(beta);
% Z-force coefficient in body axis
CZ = CXs*sin(alpha)*cos(beta) - CYs*sin(alpha)*sin(beta) + CZs*cos(alpha);
% Roll moment coefficient in body axis
Cl = Cls*cos(alpha)*cos(beta) - Cms*cos(alpha)*sin(beta) - Cns*sin(alpha);
% Pitch moment coefficient in body axis
Cm = Cls*sin(beta) + Cms*cos(beta);
% Yaw moment coefficient in body axis
Cn = Cls*sin(alpha)*cos(beta) - Cms*sin(alpha)*sin(beta) + Cns*cos(alpha);

% X-force in body axis
Xa = 0.5*rho*Vt*Vt*Sref*CX;
% Y-force in body axis
Ya = 0.5*rho*Vt*Vt*Sref*CY;
% Z-force in body axis
Za = 0.5*rho*Vt*Vt*Sref*CZ;
% Roll moment in body axis
La = 0.5*rho*Vt*Vt*Sref*b*Cl;
% Pitch moment in body axis
Ma = 0.5*rho*Vt*Vt*Sref*c*Cm;
% Yaw moment in body axis
Na = 0.5*rho*Vt*Vt*Sref*b*Cn;

%% Gravity
% Forces and moments due to gravity and a CG shift - Small angle
% approximation inserted
Xg = -sin(theta)*G;
Yg = sin(phi)*cos(theta)*G;
Zg = cos(phi)*cos(theta)*G;
MomG = dCG*[Xg;Yg;Zg];
Lg = MomG(1);
Mg = MomG(2);
Ng = MomG(3);


%% Thrust
% Forces and moments due to engin thrust
syms ('Xt','real');
Yt = 0;
Zt = 0;
Lt = 0;
Mt = 0;
Nt = 0;

%% Total Forces and Moments

sFx = Xa + Xg + Xt;
sFy = Ya + Yg + Yt;
sFz = Za + Zg + Zt;
sMx = La + Lg + Lt;
sMy = Ma + Mg + Mt;
sMz = Na + Ng + Nt;

sF = [sFx sFy sFz]';
sM = [sMx sMy sMz]';

%% Symbolic Solution Finder
% % Full Asym EoM describing equations
% v_dot_A_omega = inv([m*eye(3),-Dx;Dx,I])*([sF;sM]-[m*Omega_x,-Omega_x*Dx;Omega_x*Dx,(Omega_x*I-V_x
    *Dx)]*v_A_omega);
```

```
% % Comment code above and uncomment code below to replace inverse matrix with constant terms
for i=1:6
    for j = 1:6
        name = sprintf('a%d%d',i,j);
        syms(name);
    end
end
% % % Asym EoM with inverse matrix defined by term placement.
% adjInv =  [a11,a12,a13,a14,a15,a16;...
%            a12,a22,a23,a24,a25,a26;...
%            a13,a23,a33,a34,a35,a36;...
%            a14,a24,a34,a44,a45,a46;...
%            a15,a25,a35,a45,a55,a56;...
%            a16,a26,a36,a46,a56,a66];

% % Simplification due to off diagonal terms being factor 10 smaller than
% % diagonal terms
adjInv =  [a11,0,0,0,0,a16;...
           0,a22,0,0,0,0;...
           0,0,a33,a34,0,0;...
           0,0,a34,a44,0,0;...
           0,0,0,0,a55,0;...
           a16,0,0,0,0,a66];

v_dot_A_omega = adjInv*([sF;sM]-[m*Omega_x,-Omega_x*Dx;Omega_x*Dx,(Omega_x*I-V_x*Dx)]*v_A_omega);

% Addition of theta_dot and phi_dot
v_dot_A_omega = [v_dot_A_omega;...
                 (Q*cos(phi)-R*sin(phi));...
                 (P+Q*sin(phi)*sin(theta)/cos(theta)+R*cos(phi)*sin(theta)/cos(theta))];


% Partial differentiation - equations require manual simplification after
%                           differentiation.

temp = subs(v_dot_A_omega,Vt,U);
ddU = subs(diff(temp,U),U,Vt);


temp = subs(v_dot_A_omega,beta,V/Vt);
ddV = subs(diff(temp,V),V/Vt,beta);

temp = subs(v_dot_A_omega,alpha,W/Vt);
ddW = subs(diff(temp,W),W/Vt,alpha);

ddP = diff(v_dot_A_omega,P);
ddQ = diff(v_dot_A_omega,Q);
ddR = diff(v_dot_A_omega,R);
ddTheta = diff(v_dot_A_omega,theta);
ddPhi = diff(v_dot_A_omega,phi);
ddDa = diff(v_dot_A_omega,da);
ddDe = diff(v_dot_A_omega,de);
ddDr = diff(v_dot_A_omega,dr);
ddXt = diff(v_dot_A_omega,Xt);

% Simplicifation
ddMat = [ddU;ddV;ddW;ddP;ddQ;ddR;ddTheta;ddPhi;ddDa;ddDe;ddDr;ddXt];
ddMat = subs(ddMat,U,Vt);
ddMat = subs(ddMat,P,0);
ddMat = subs(ddMat,Q,0);
ddMat = subs(ddMat,R,0);
ddMat = subs(ddMat,CL_da*da + CL_de*de + (CL_alpha*W)/Vt,CLt);
ddMat = subs(ddMat,V,0);
ddMat = subs(ddMat,W,0);
ddMat = subs(ddMat,CL_alpha*alpha + CL_da*da + CL_de*de,CLt);
ddMat = subs(ddMat,cos(theta),1);
ddMat = subs(ddMat,cos(phi),1);
ddMat = subs(ddMat,sin(theta),alphaT);
ddMat = subs(ddMat,sin(phi),phiT);
ddMat = subs(ddMat,cos(alpha),1);
ddMat = subs(ddMat,cos(beta),1);
ddMat = subs(ddMat,sin(alpha),alpha);
ddMat = subs(ddMat,sin(beta),0);
```

```
ddMat = subs(ddMat,da,0);
ddMat = subs(ddMat,de,0);
ddMat = subs(ddMat,dr,0);
ddMat = subs(ddMat,Sref,S);
ddMat = subs(ddMat,alpha,alphaT);
ddMat = subs(ddMat,beta,0);

[ddMat,how] = simple(expand(ddMat));

start = 1;
finish = 8;
ddU = ddMat(start:finish)
start = start + 8;
finish = finish + 8;
ddV = ddMat(start:finish)
start = start + 8;
finish = finish + 8;
ddW = ddMat(start:finish)
start = start + 8;
finish = finish + 8;
ddP = ddMat(start:finish)
start = start + 8;
finish = finish + 8;
ddQ = ddMat(start:finish)
start = start + 8;
finish = finish + 8;
ddR = ddMat(start:finish)
start = start + 8;
finish = finish + 8;
ddTheta = ddMat(start:finish)
start = start + 8;
finish = finish + 8;
ddPhi = ddMat(start:finish)
start = start + 8;
finish = finish + 8;
ddDa = ddMat(start:finish)
start = start + 8;
finish = finish + 8;
ddDe = ddMat(start:finish)
start = start + 8;
finish = finish + 8;
ddDr = ddMat(start:finish)
start = start + 8;
finish = finish + 8;
ddT = ddMat(start:finish)
```

Appendix D

0% to 40% Wing Loss Linearised State Equation Values

D.1 0% Wing loss

$$\begin{bmatrix}\dot{\bar{V}}\\ \dot{\alpha}\\ \dot{Q}\\ \dot{\theta}\\ \dot{\beta}\\ \dot{P}\\ \dot{R}\\ \dot{\phi}\end{bmatrix} = \begin{bmatrix}-0.03340 & 14.18119 & -0.18679 & -9.81000 & 0.00000 & -0.00000 & -0.00000 & -0.00000\\ -0.06026 & -5.58806 & 1.09820 & -0.05759 & 0.00000 & 0.00000 & -0.00000 & -0.00000\\ 0.00000 & -82.54108 & -8.74654 & -0.00000 & 0.00000 & 0.00000 & 0.00000 & -0.00000\\ 0.00000 & 0.00000 & 1.00000 & 0.00000 & 0.00000 & 0.00000 & -0.00000 & 0.00000\\ 0.00000 & 0.00000 & 0.00000 & -0.00000 & -0.22379 & 0.00067 & -0.99107 & 0.54500\\ -0.00000 & -0.00000 & 0.00000 & -0.00000 & 0.73655 & -8.09377 & -0.03439 & -0.00000\\ 0.00000 & 0.00000 & -0.00000 & -0.00000 & 17.51553 & -0.06678 & -0.86382 & -0.00000\\ 0.00000 & 0.00000 & 0.00000 & 0.00000 & 0.00000 & 1.00000 & 0.10567 & 0.00000\end{bmatrix}\begin{bmatrix}\bar{V}\\ \alpha\\ Q\\ \theta\\ \beta\\ P\\ R\\ \phi\end{bmatrix} + \begin{bmatrix}0.00000 & 0.51619 & -0.00000 & 0.15873\\ -0.00000 & -0.65752 & -0.00000 & 0.00000\\ 0.00000 & -113.20805 & 0.00000 & 0.00000\\ 0.00000 & 0.00000 & 0.00000 & 0.00000\\ 0.00580 & 0.00000 & 0.14455 & 0.00000\\ -93.48236 & -0.00000 & -0.32072 & 0.00000\\ -0.57524 & 0.00000 & -14.71326 & 0.00000\\ 0.00000 & 0.00000 & 0.00000 & 0.00000\end{bmatrix}\begin{bmatrix}\delta_{Ail}\\ \delta_{El}\\ \delta_{Rud}\\ T\end{bmatrix} \tag{D.1.1}$$

D.2 10% Wing loss

$$\begin{bmatrix}\dot{\bar{V}}\\ \dot{\alpha}\\ \dot{Q}\\ \dot{\theta}\\ \dot{\beta}\\ \dot{P}\\ \dot{R}\\ \dot{\phi}\end{bmatrix} = \begin{bmatrix}-0.03311 & 14.70386 & -0.19531 & -9.81003 & 0.13797 & -0.02652 & -0.00719 & 0.00021\\ -0.06027 & -5.26601 & 1.09593 & -0.06168 & -0.00032 & 0.01581 & -0.00002 & 0.00001\\ 0.00000 & -81.88076 & -8.80523 & -0.05094 & 0.00000 & -0.01577 & 0.00000 & 0.00000\\ 0.00000 & 0.00000 & 1.00000 & 0.00000 & 0.00000 & 0.00000 & -0.00001 & 0.00000\\ 0.00000 & 0.00092 & 0.00000 & -0.00000 & -0.22527 & 0.00063 & -0.99100 & 0.54500\\ 0.54057 & -30.43518 & -0.46993 & -0.00002 & 0.77640 & -7.30107 & 0.04231 & -0.04281\\ 0.00355 & 0.11388 & -0.04095 & 0.00018 & 18.42484 & -0.06758 & -0.96015 & 0.02806\\ 0.00000 & 0.00000 & 0.00000 & 0.00000 & 0.00000 & 1.00000 & 0.11317 & 0.00000\end{bmatrix}\begin{bmatrix}\bar{V}\\ \alpha\\ Q\\ \theta\\ \beta\\ P\\ R\\ \phi\end{bmatrix} + \begin{bmatrix}0.04755 & 0.61264 & -0.11590 & 0.16004\\ -0.08079 & -0.66034 & 0.00014 & 0.00000\\ -2.36339 & -113.33936 & 0.00000 & 0.00000\\ 0.00000 & 0.00000 & 0.00000 & 0.00000\\ 0.00550 & 0.00000 & 0.14568 & 0.00000\\ -86.84517 & 0.52495 & -0.33547 & 0.00000\\ -0.57702 & 0.00669 & -15.47709 & 0.00853\\ 0.00000 & 0.00000 & 0.00000 & 0.00000\end{bmatrix}\begin{bmatrix}\delta_{Ail}\\ \delta_{El}\\ \delta_{Rud}\\ T\end{bmatrix} \tag{D.2.1}$$

D.3 20% Wing loss

$$\begin{bmatrix}\dot{\bar{V}}\\ \dot{\alpha}\\ \dot{Q}\\ \dot{\theta}\\ \dot{\beta}\\ \dot{P}\\ \dot{R}\\ \dot{\phi}\end{bmatrix} = \begin{bmatrix}-0.03266 & 15.62679 & -0.21270 & -9.81035 & 0.65295 & -0.05653 & -0.03724 & 0.00275\\ -0.06143 & -5.00303 & 1.09847 & -0.06606 & -0.00181 & 0.03981 & -0.00068 & 0.00041\\ 0.00000 & -80.97873 & -8.93449 & -0.21742 & 0.00000 & -0.03738 & 0.00000 & 0.00000\\ 0.00000 & 0.00000 & 1.00000 & 0.00000 & 0.00000 & 0.00000 & -0.00002 & 0.00000\\ 0.00000 & 0.00213 & 0.00000 & -0.00000 & -0.23258 & 0.00061 & -0.99072 & 0.54503\\ 1.65169 & -57.14095 & -1.53730 & -0.00020 & 1.02187 & -8.52884 & 0.38469 & -0.23565\\ 0.02101 & 0.81990 & -0.12005 & 0.00374 & 20.51552 & -0.08199 & -1.17013 & 0.08632\\ 0.00000 & 0.00000 & 0.00000 & 0.00000 & 0.00000 & 1.00000 & 0.12121 & 0.00000\end{bmatrix}\begin{bmatrix}\bar{V}\\ \alpha\\ Q\\ \theta\\ \beta\\ P\\ R\\ \phi\end{bmatrix} +$$

$$\begin{bmatrix} 0.02071 & 0.75489 & -0.54849 & 0.16713\\ -0.08441 & -0.68816 & 0.00078 & 0.00000\\ -5.43897 & -113.58812 & 0.00000 & 0.00000\\ 0.00000 & 0.00000 & 0.00000 & 0.00000\\ 0.00521 & 0.00000 & 0.15103 & 0.00000\\ -97.49427 & 3.86984 & -0.43832 & 0.00000\\ -0.64618 & 0.12241 & -17.23328 & 0.04035\\ 0.00000 & 0.00000 & 0.00000 & 0.00000\end{bmatrix}\begin{bmatrix}\delta_{Ail}\\ \delta_{El}\\ \delta_{Rud}\\ T\end{bmatrix} \tag{D.3.1}$$

D.4 30% Wing loss

$$\begin{bmatrix}\dot{\bar{V}}\\ \dot{\alpha}\\ \dot{Q}\\ \dot{\theta}\\ \dot{\beta}\\ \dot{P}\\ \dot{R}\\ \dot{\phi}\end{bmatrix} = \begin{bmatrix}-0.03353 & 17.58097 & -0.25026 & -9.81082 & 1.29766 & -0.09479 & -0.08744 & 0.01277\\ -0.06531 & -4.83689 & 1.10596 & -0.07300 & -0.00319 & 0.06142 & -0.00220 & 0.00127\\ 0.00000 & -80.27511 & -9.25800 & -0.36326 & 0.00000 & -0.05785 & 0.00000 & 0.00001\\ 0.00000 & 0.00000 & 1.00000 & 0.00000 & 0.00000 & 0.00000 & -0.00003 & 0.00000\\ 0.00000 & 0.00485 & 0.00000 & -0.00000 & -0.24764 & 0.00060 & -0.99024 & 0.54512\\ 2.60924 & -69.72613 & -2.35188 & -0.00119 & 1.00645 & -7.79357 & 0.69568 & -0.40473\\ 0.04537 & 1.66856 & -0.22749 & 0.01202 & 22.77443 & -0.10989 & -1.53455 & 0.22420\\ 0.00000 & 0.00000 & 0.00000 & 0.00000 & 0.00000 & 1.00000 & 0.13394 & 0.00000\end{bmatrix}\begin{bmatrix}\bar{V}\\ \alpha\\ Q\\ \theta\\ \beta\\ P\\ R\\ \phi\end{bmatrix} +$$

$$\begin{bmatrix} 0.07979 & 1.00466 & -1.09007 & 0.18184\\ -0.15985 & -0.74738 & 0.00136 & 0.00000\\ -8.79486 & -114.16293 & 0.00000 & 0.00000\\ 0.00000 & 0.00000 & 0.00000 & 0.00000\\ 0.00490 & 0.00000 & 0.16144 & 0.00000\\ -80.45460 & 7.12127 & -0.42885 & 0.00000\\ -0.76053 & 0.33866 & -19.13111 & 0.08019\\ 0.00000 & 0.00000 & 0.00000 & 0.00000\end{bmatrix}\begin{bmatrix}\delta_{Ail}\\ \delta_{El}\\ \delta_{Rud}\\ T\end{bmatrix} \tag{D.4.1}$$

D.5 40% Wing loss

$$\begin{bmatrix}\dot{\bar{V}}\\ \dot{\alpha}\\ \dot{Q}\\ \dot{\theta}\\ \dot{\beta}\\ \dot{P}\\ \dot{R}\\ \dot{\phi}\end{bmatrix} = \begin{bmatrix}-0.03595 & 21.11783 & -0.31928 & -9.81113 & 1.70690 & -0.15069 & -0.12741 & 0.02356\\ -0.07145 & -4.69643 & 1.11519 & -0.08674 & -0.00425 & 0.08040 & -0.00354 & 0.00201\\ 0.00000 & -78.88803 & -9.46759 & -0.41054 & 0.00000 & -0.07269 & 0.00000 & 0.00002\\ 0.00000 & 0.00000 & 1.00000 & 0.00000 & 0.00000 & 0.00000 & -0.00004 & 0.00000\\ 0.00000 & 0.00448 & 0.00000 & -0.00000 & -0.26899 & 0.00063 & -0.98954 & 0.54522\\ 3.93744 & -97.69371 & -3.09595 & -0.00286 & 1.07990 & -8.00031 & 0.89923 & -0.51752\\ 0.07752 & 2.60977 & -0.34961 & 0.01657 & 24.13150 & -0.14827 & -1.80126 & 0.33309\\ 0.00000 & 0.00000 & 0.00001 & 0.00000 & 0.00000 & 1.00000 & 0.15914 & 0.00000\end{bmatrix}\begin{bmatrix}\bar{V}\\ \alpha\\ Q\\ \theta\\ \beta\\ P\\ R\\ \phi\end{bmatrix} +$$

$$\begin{bmatrix} 0.44171 & 1.47346 & -1.43382 & 0.20033\\ -0.30526 & -0.82265 & 0.00180 & 0.00000\\ -12.25862 & -114.63302 & 0.00000 & 0.00000\\ 0.00000 & 0.00000 & 0.00000 & 0.00000\\ 0.00454 & 0.00000 & 0.17567 & 0.00000\\ -72.78748 & 9.48184 & -0.45743 & 0.00000\\ -0.83979 & 0.61068 & -20.27075 & 0.10548\\ 0.00000 & 0.00000 & 0.00000 & 0.00000\end{bmatrix}\begin{bmatrix}\delta_{Ail}\\ \delta_{El}\\ \delta_{Rud}\\ T\end{bmatrix} \tag{D.5.1}$$

Appendix E

Open loop Input to Output Bode plots

In this appendix all of the bode plots left out in Section 4's analysis are presented.

E.1 Longitudinal input to Lateral state Output

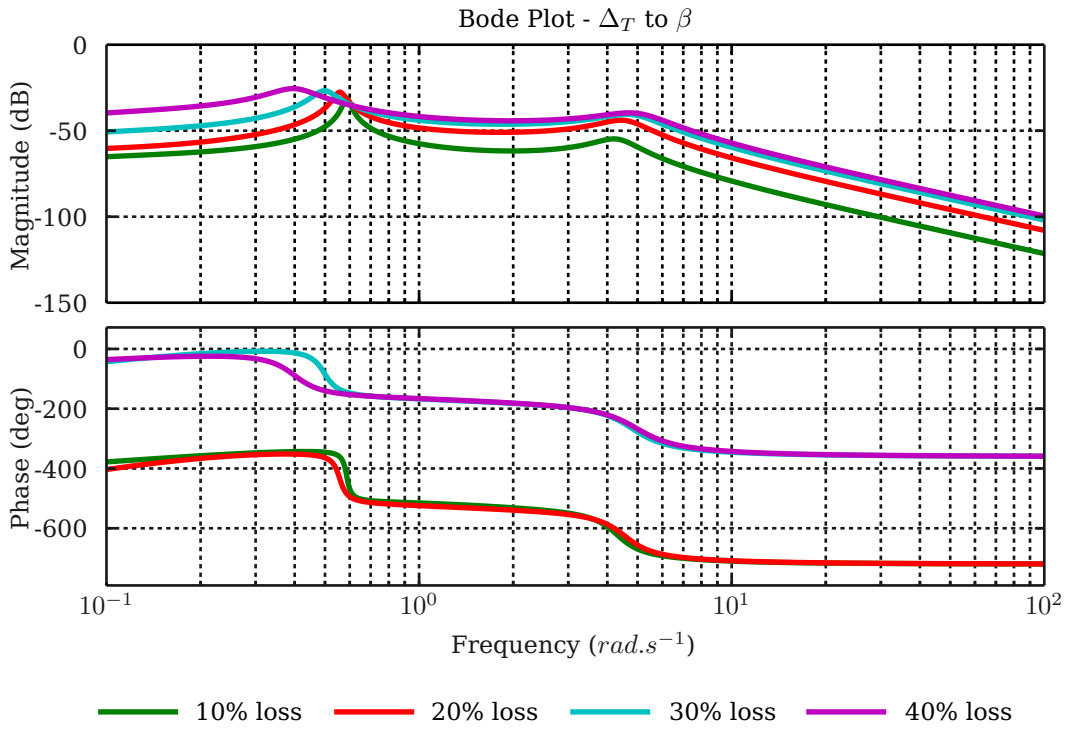

Figure E.1 – Thrust to Side-slip

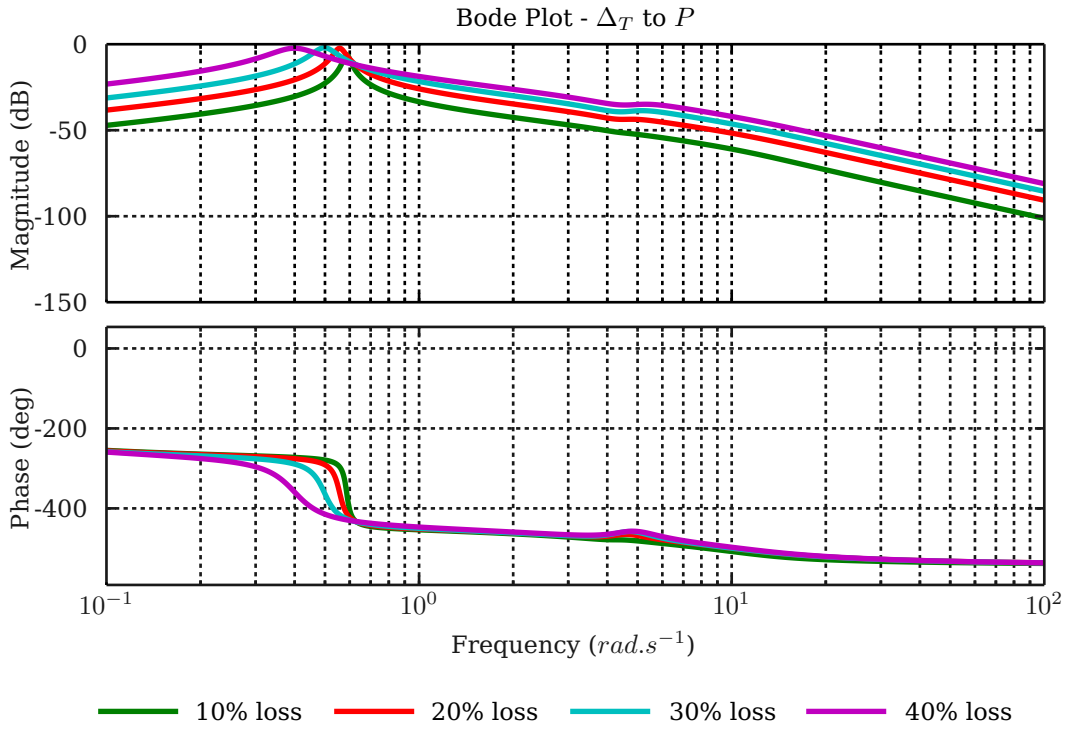

Figure E.2 – Thrust to Roll

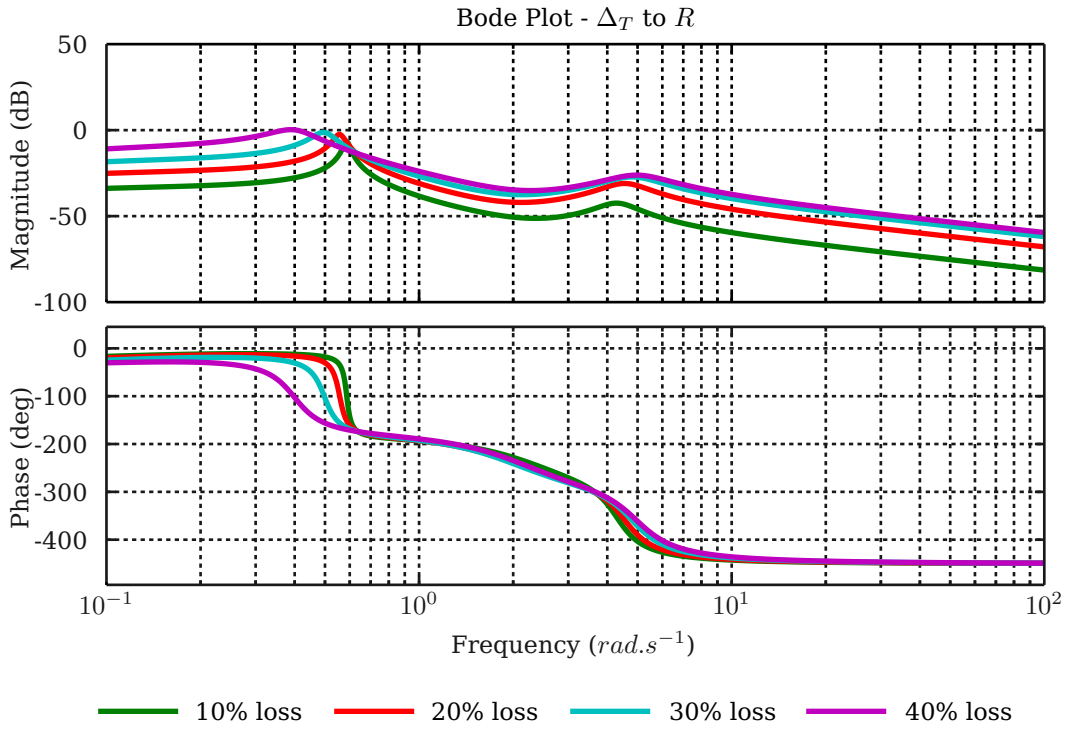

Figure E.3 – Thrust to Yaw

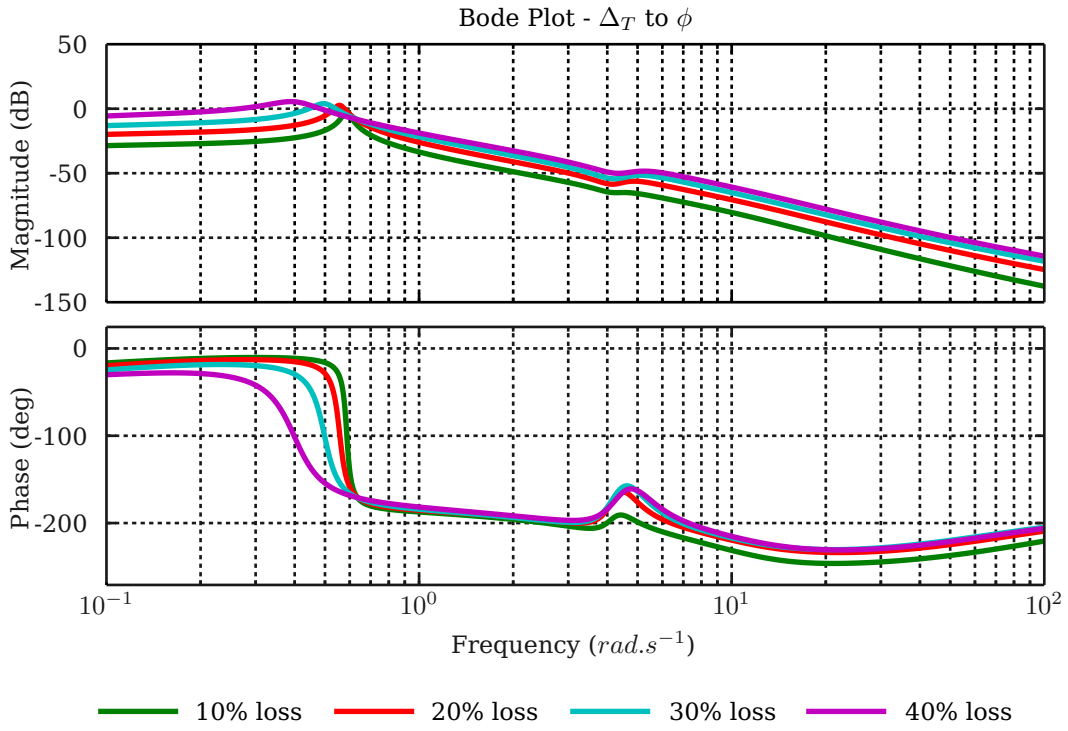

Figure E.4 – Thrust to Bank Angle

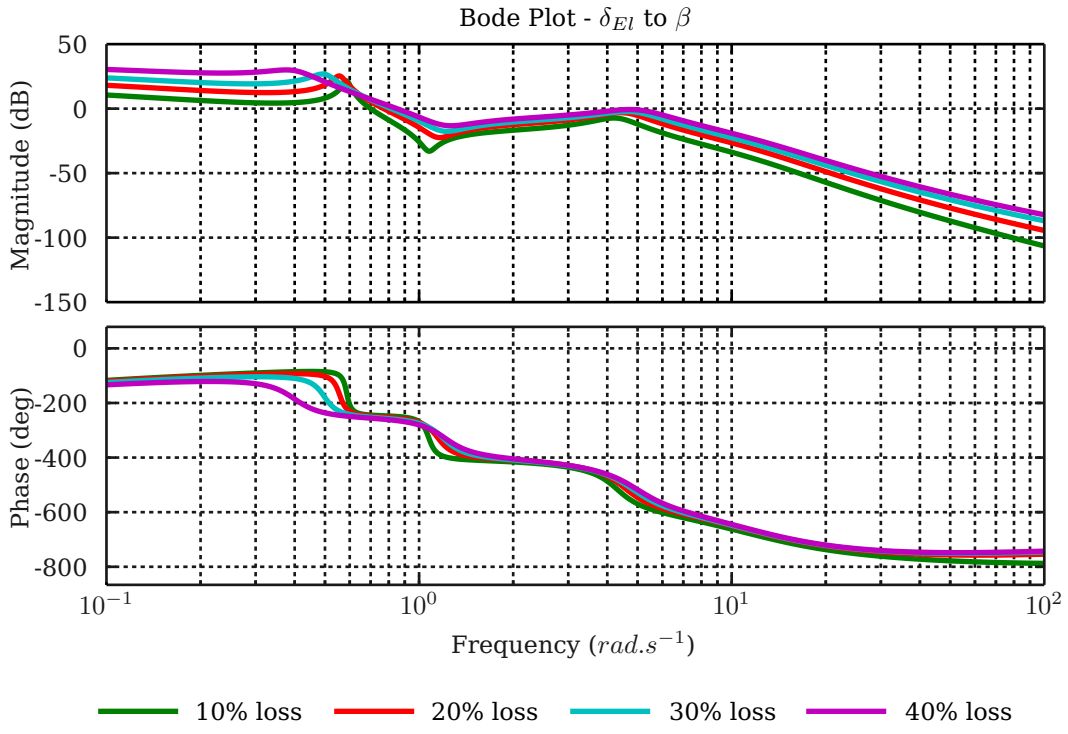

Figure E.5 – Elevator to Side-slip

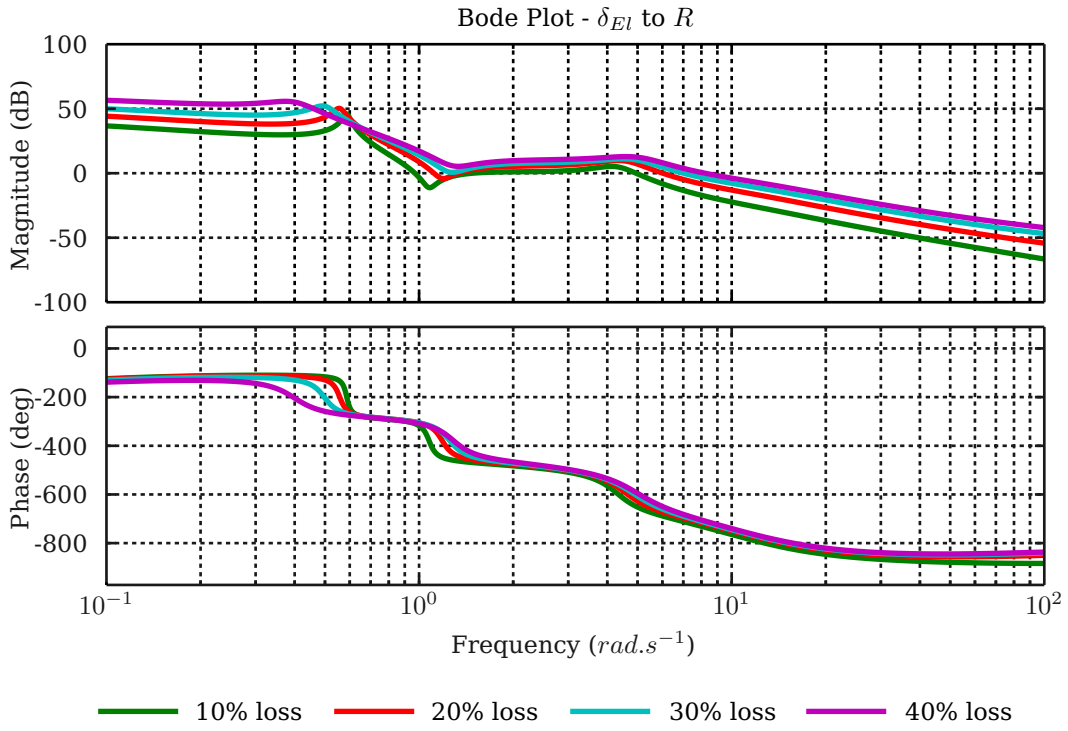

Figure E.6 – Elevator to Yaw

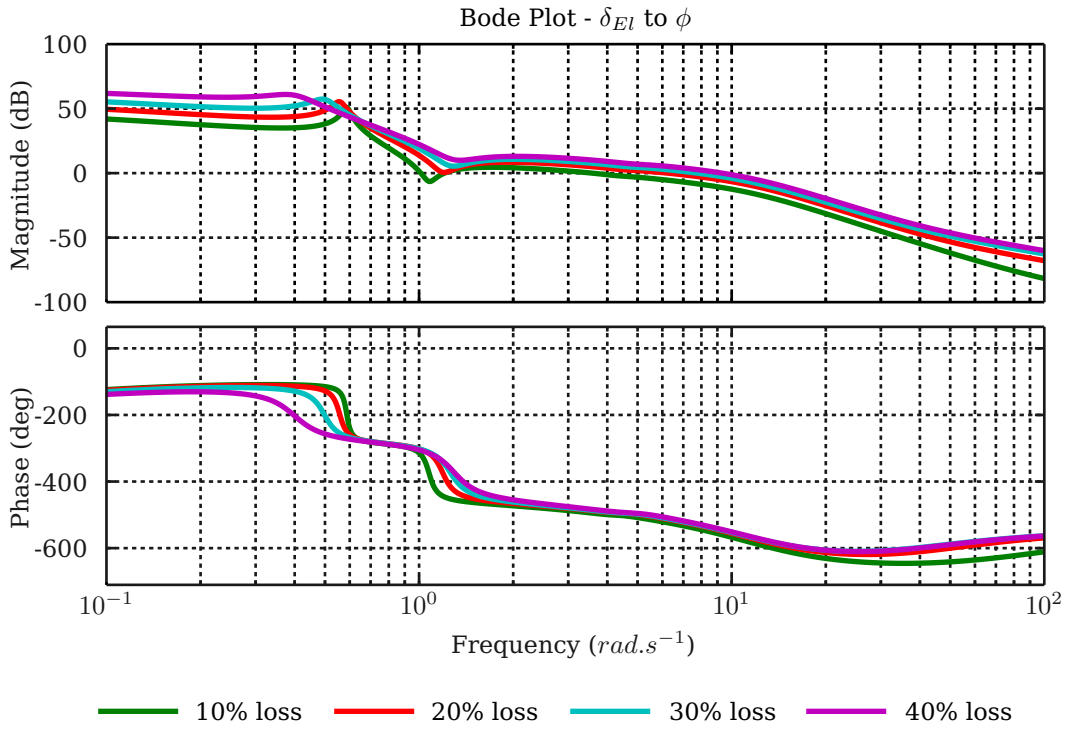

Figure E.7 – Elevator to Bank Angle

E.2 Lateral input to Longitudinal state Output

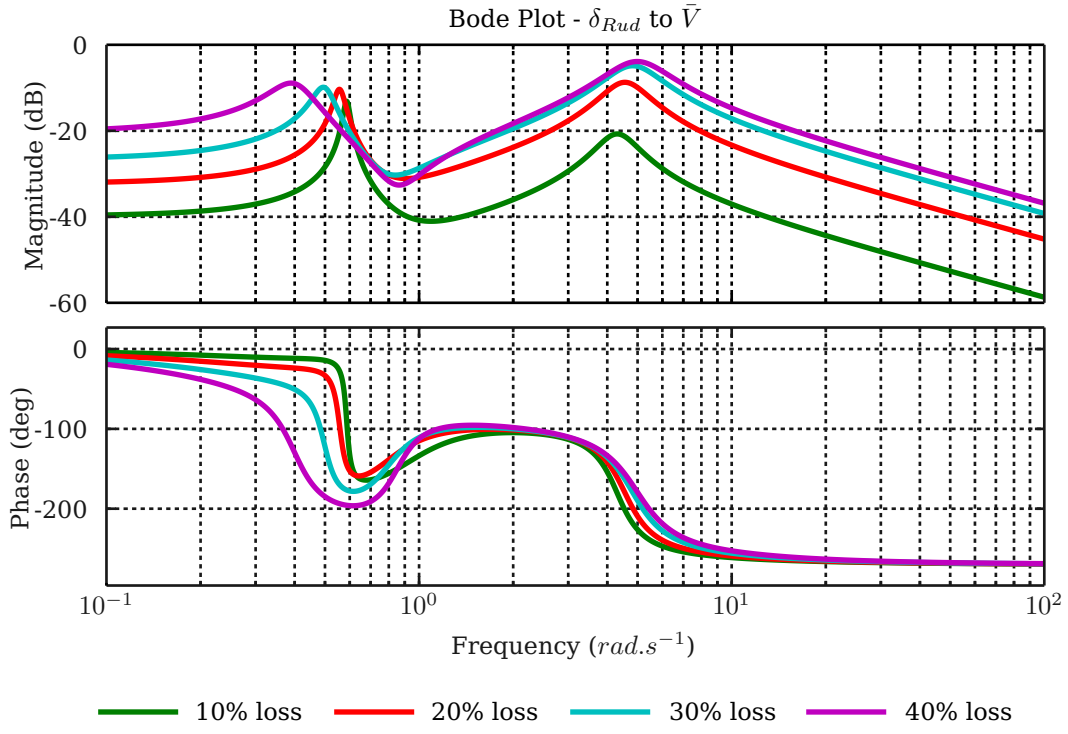

Figure E.8 – Rudder to Airspeed

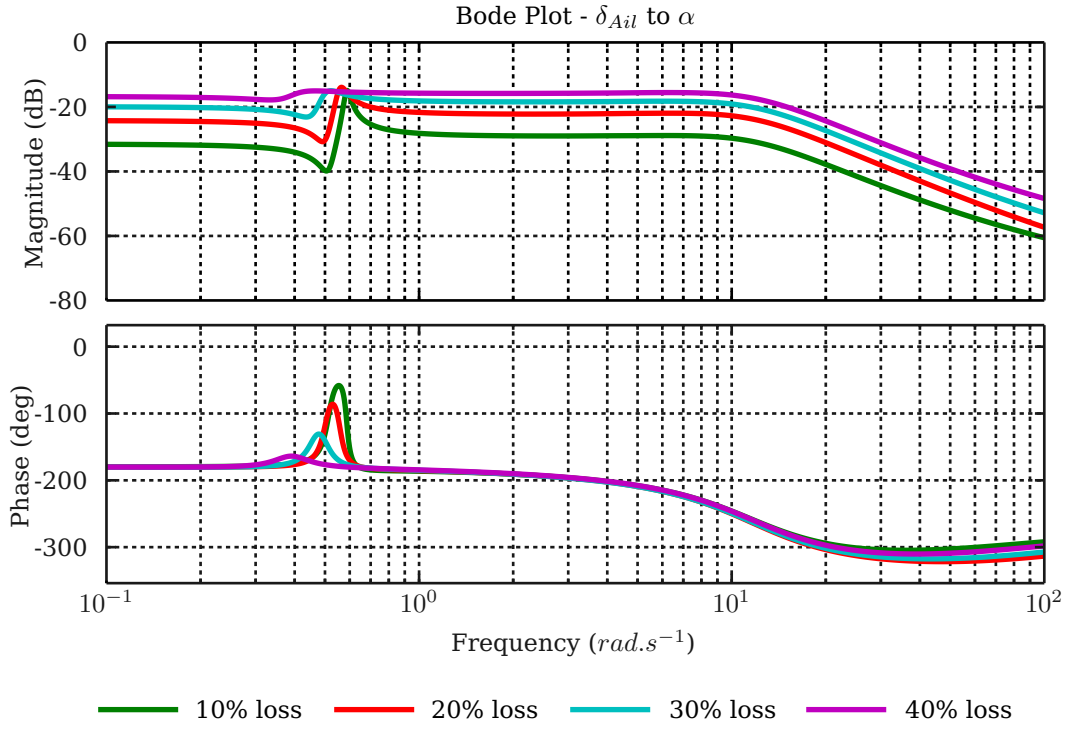

Figure E.9 – Ailerons to Angle of Attack

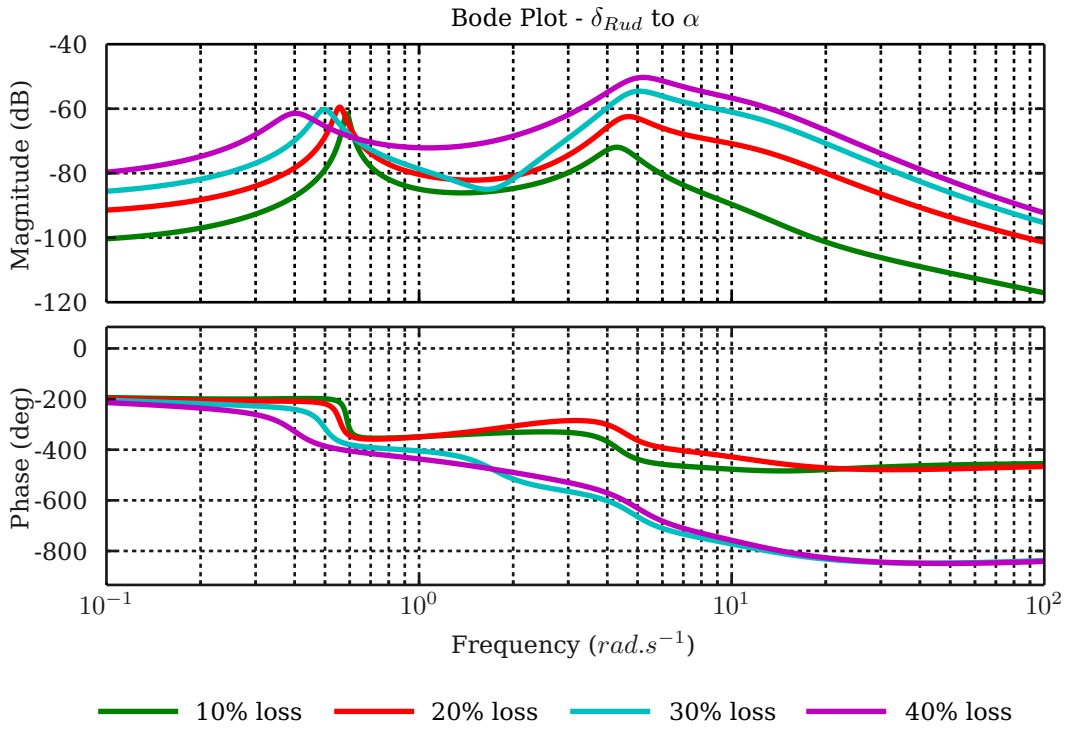

Figure E.10 – Rudder to Angle of Attack

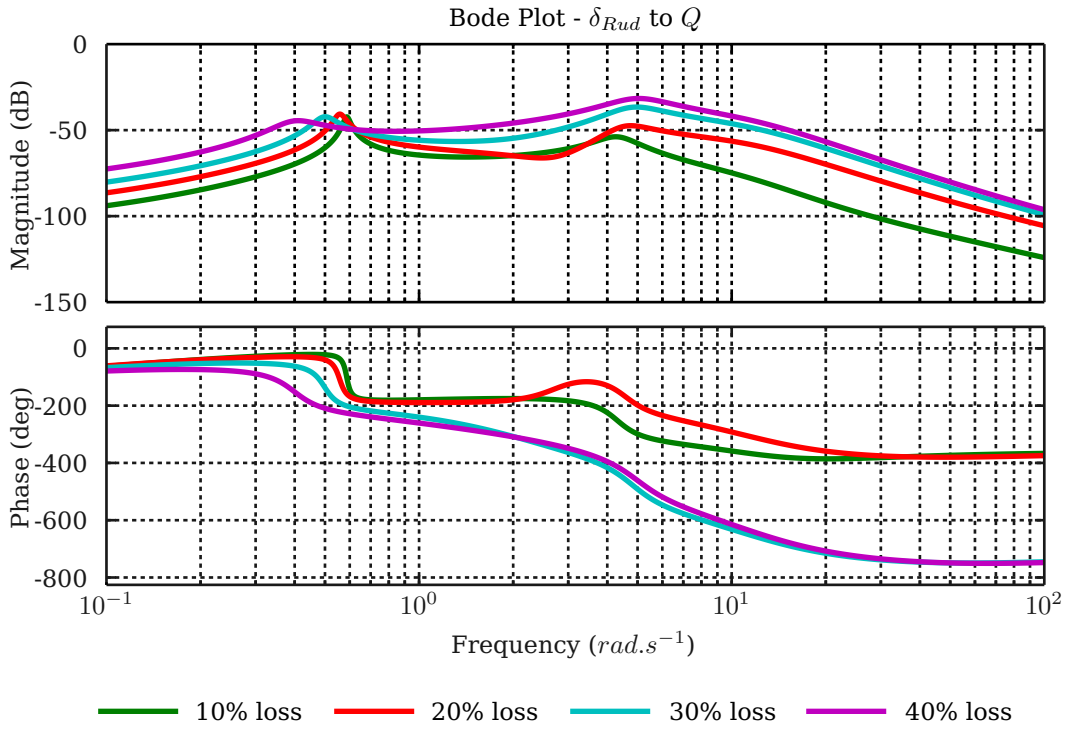

Figure E.11 – Rudder to Pitch

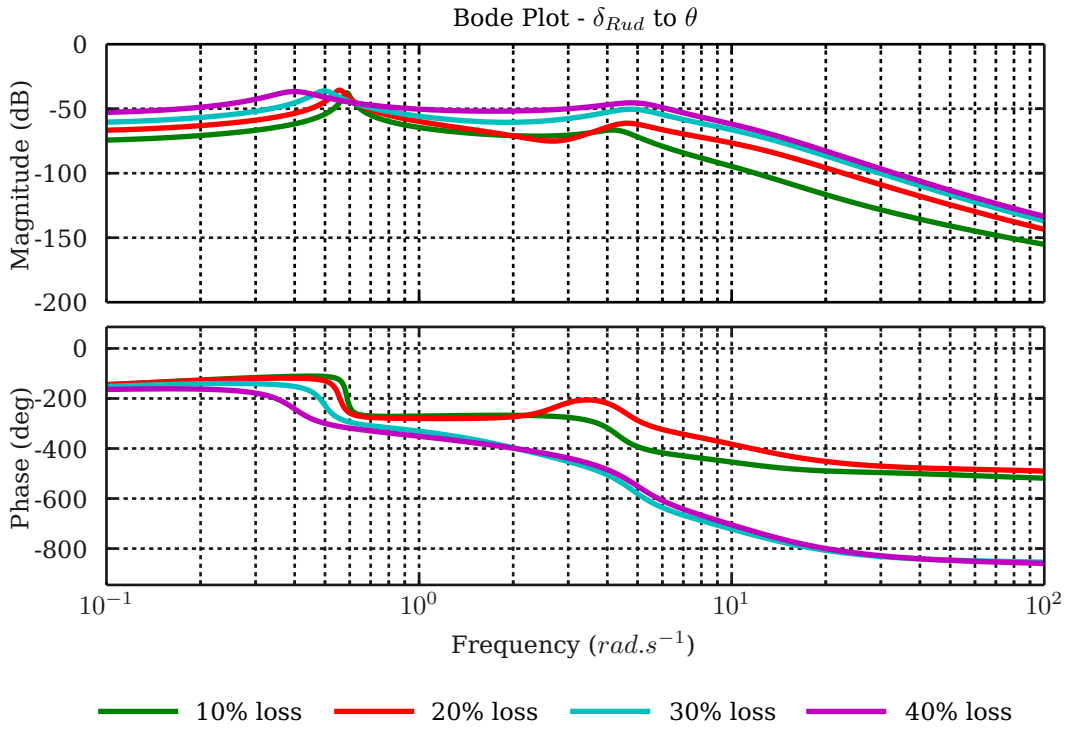

Figure E.12 – Rudder to Theta

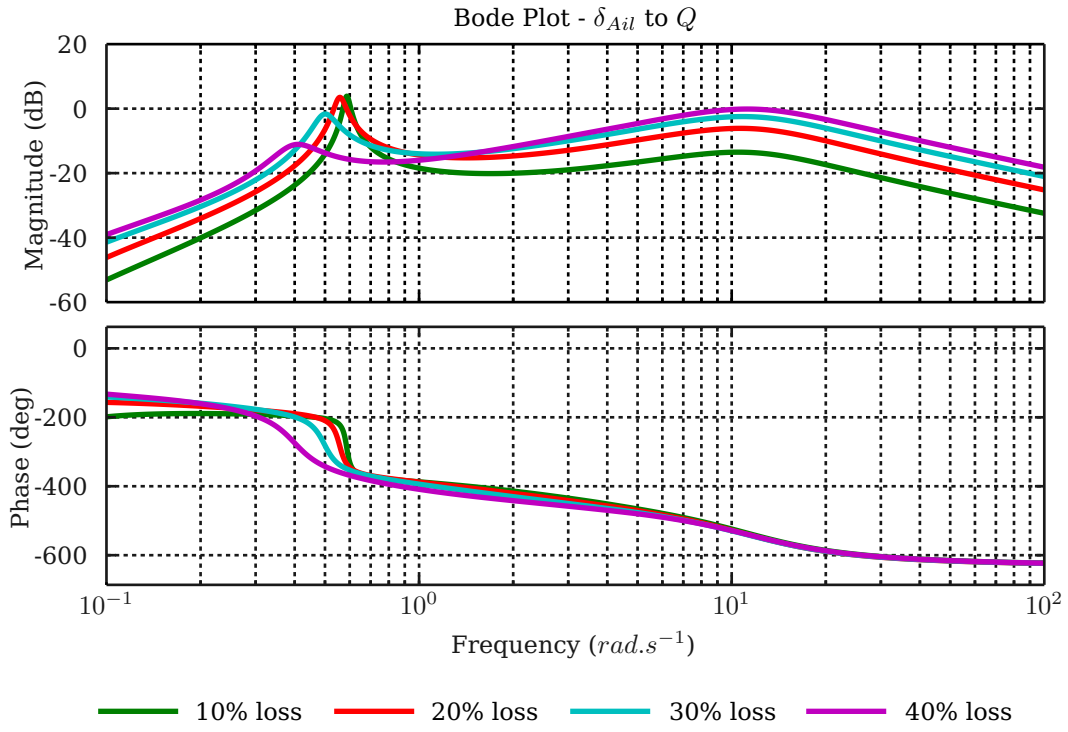

Figure E.13 – Ailerons to Pitch

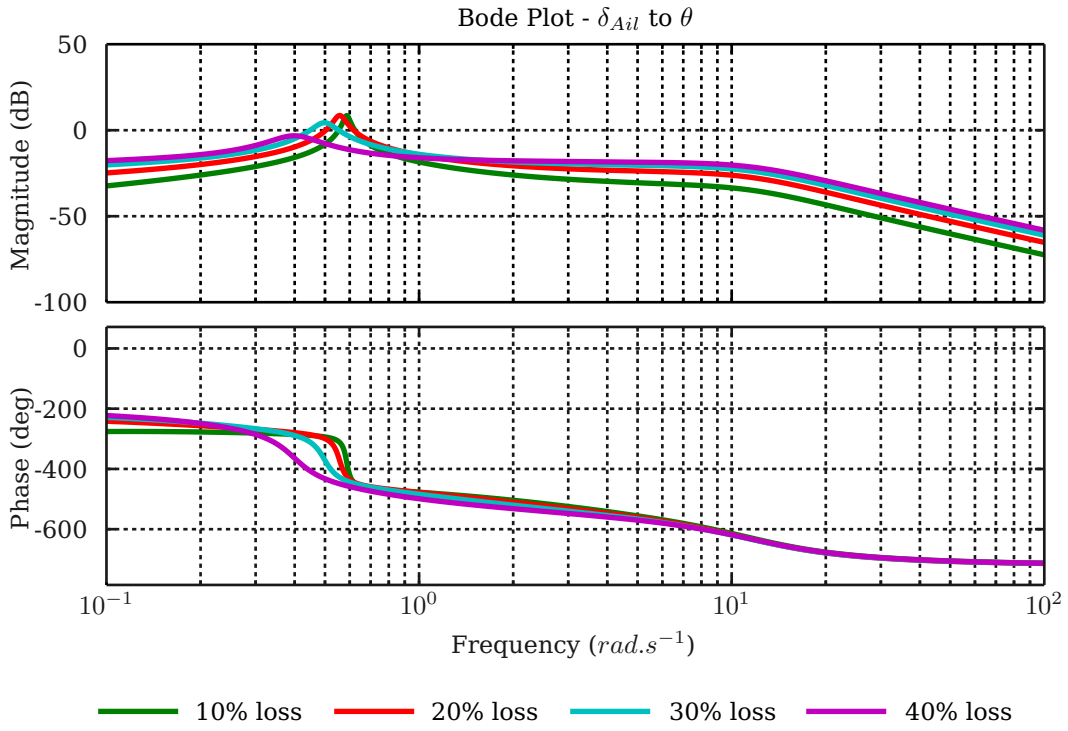

Figure E.14 – Ailerons to Theta

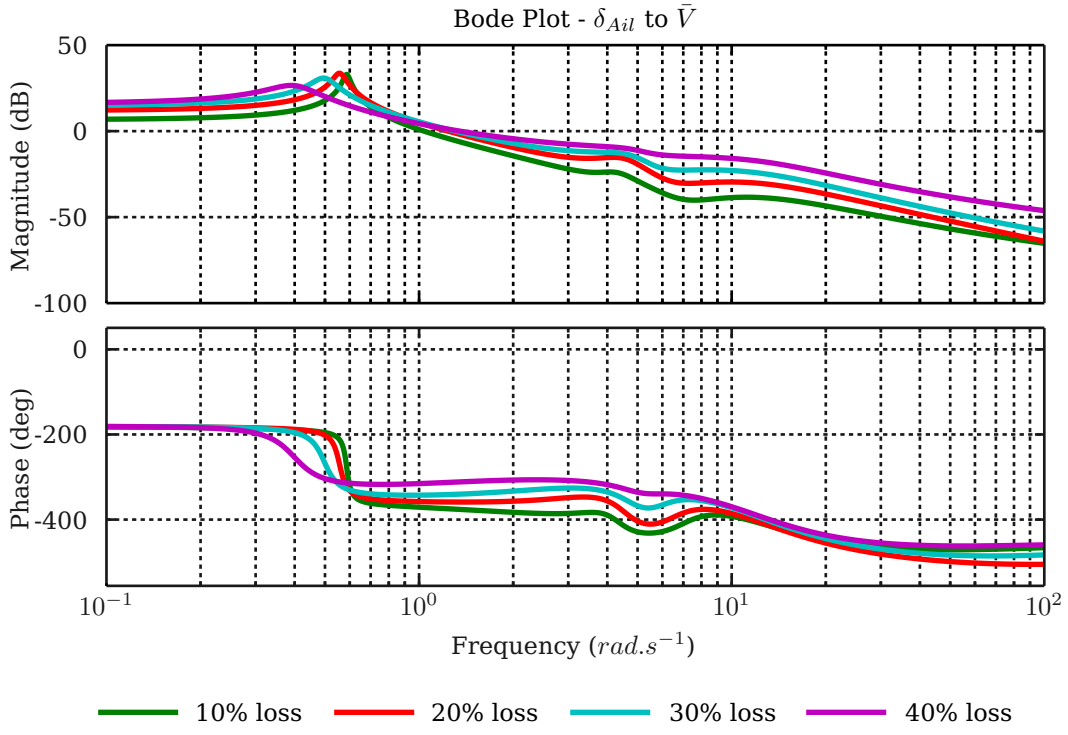

Figure E.15 – Ailerons to Airspeed

Appendix F

Hardware, Software and Physical values

F.1 Ground Station

The ground station consists of three parts: the laptop, the ground station software (GSS) and the ground station transmitter and receiver (GS_TXRX). For most projects the laptop and GS_TXRX stay the same and customisation is done on the GSS to enable testing of the specific needs of the current project.

The GS_TXRX consists of a MaxStream RF chip, connected to the laptop via USB. The GSS consists of a Qt GUI which enables real-time telemetry data tracking of the UAV during flight. This data includes estimator values such as position, velocity and attitude angles. It also allows direct sensor measurement data of the pressure-board, IMU, magnetometer and GPS to be displayed. The GSS also enables data to be sent up to the UAV such as instructions needed for setting up the estimator, zeroing the IMU, zeroing the pressure-board, enabling controllers and setting specific reference values for each controller.

F.2 System Identification

In this section of the appendix, all the system variables will be stated for clarification.

F.2.1 Mass and Moment of Inertia

The mass of Phoenix has been measured at 6.3kg for symmetric undamaged case. The moment of inertia values obtained measured $I_{xx} = 0.7212$, $I_{yy} = 0.5139$ and $I_{zz} = 0.9239$ for symmetric undamaged case.

The Inventor acquired values can be found in Table F.1. These values are necessary for modelling wing loss as described in Chapter 2.

Wing loss	Tip mass	$I_x x$	I_{xy}	I_{xz}	I_{yy}	I_{yz}	I_{zz}	$tip_{x_{CG}}$	$tip_{y_{CG}}$	$tip_{z_{CG}}$
0%	0	0	0	0	0	0	0	0	0	0
10%	0.0490	0.0000	0.0000	0.0003	0.0000	-0.0000	0.0004	-0.0513	-0.9556	-0.0602
20%	0.2210	0.0397	0.0004	0.0007	0.0000	0.0024	-0.0387	-0.0314	-0.8698	-0.0552
30%	0.3880	-0.0765	0.0020	0.0016	0.0001	0.0048	-0.0745	-0.0419	-0.8308	-0.0542
40%	0.4560	-0.0750	0.0025	0.0025	0.0002	0.0048	-0.0720	-0.0499	-0.8069	-0.0545

Table F.1 – Inventor acquired mass, inertia and CG values for wing loss

F.2.2 Engine Thrust

Originally Phoenix had a Hyperion ZS4025-10 brush-less motor running on a 5 cell, 18.5V, 5000mAh LiPo battery pack and fitted with a 14x7 E prop. This configuration generated a maximum of 33N thrust. It was decided to increase Phoenix's thrust by changing the prop to a 15x8 E prop. This proved a cost effective method to increase thrust and led to the generation of 43N thrust. By increasing the thrust, easier upset recovery can be done by the safety pilot due to the increase in maximum airspeed Phoenix can now achieve.

F.2.3 Aerodynamic Coefficients and dimensionalising variables

The nominal case's aerodynamic coefficient values will be displayed in Table F.2. The values used to dimensionalise these coefficients can be found in Table F.3.

	α	β	P	Q	R	δ_{Ail}	δ_{El}	δRud
C_L	4.5079	0	0	7.8746	0	0	0.5266	0
C_y	0	-0.1669	0.0101	0	0.1356	0.0047	0	0.1165
C_l	0	0.0020	-0.4086	0	-0.0017	-0.2507	0	-0.0009
C_m	-0.8332	0	0	-8.7829	0	0	-1.1428	0
C_n	0	0.0602	-0.0043	0	-0.0559	-0.0020	0	-0.0505

Table F.2 – Nominal Case Aerodynamic Coefficients

V	A	b	c	e	S
20	5.28	1.912	0.3628	0.85	0.6919

Table F.3 – Dimensionalisation Values

In Table F.3 $\bar{V}$ is the trim airspeed, A is the aspect ratio, b is wing span, c is the aerodynamic cord length, e is the Oswald number and S is the wing surface area.

F.3 Hardware

As stated at the beginning of the thesis, Phoenix was equipped with a custom ESL avionics pack. This section will provide a bit more detail on the sensors and hardware used to implement this avionics pack.

F.3.1 Servo-board

The servo-board generates all the servo commands sent out to the actuators. In general it receives actuator commands from either the RCR or the OBC, depending on if the autopilot is armed or not. It is connected to the OBC by the CAN-bus. The servo-board has the capability to receive and command 16 individual actuators. It can also combine and mix 8 inputs to the 16 actuator outputs through a mixing matrix. This matrix is computed with the specific actuator setup required and implemented during the programming of the servo-board.

F.3.2 OBC

The OBC itself consists of two Mircochip dsPIC30F6014A MCUs and a MAXStream 2.4Ghz Communication module. The two MCUs perform all the computation during Phoenix's flights. They process the measurement data obtained from the various sensors, calculate output values according to the specific control laws, output actuator commands to the servo-board, estimate inertial position and velocity and enable communication with the GS_TXRX. The GPS and IMU modules are mounted on the OBC's PCB. Most of the computation currently occurs on only one MCU but the OBC also supports integration with a NovAtel DGPS, which requires extra processing power. This is mainly done on the second MCU. Currently the OBC runs at a 20ms cycle for control purposes. The MCUs' data sheet can be found in [24].

F.3.3 GPS

The GPS used in Phoenix is a uBlox RCB-4H GPS module. This module provides global positioning data at a rate of 4Hz with a circular error probability of 2m at 50% of the position fixed acquired. Its data sheet can be found in [25].

F.3.4 IMU

The IMU used in Phoenix is a ADIS16350. This is a high precision tri-axis inertial sensor. It consists of a triple axis gyroscope and triple axis accelerometer. Its data sheet can be found in [26].

F.3.5 Pressure-board

The pressure-board consists of a static- and differential pressure sensor connected to a Pitot-tube. This board is situated in Phoenix's right wing. The data sheets for these chips can be found at [27] and [28]. The measured values get sent to the OBC via a CAN-bus.

F.3.6 Battery Packs

As stated Phoenix's OBC runs on more than one battery pack. The OBC and engine both have their own battery pack, as the engine's pack depletes quite fast and could cause a loss of control of Phoenix during a flight test.

The OBC shares a battery pack with the servo-board. This main avionics battery pack consists of a 3 cell, 11.1V, 1800mAh LiPo battery. In addition to the main battery pack, the OBC also has a backup battery pack consisting of a 4.8V, 1500mAh, Nickel Metal Hydride battery. This backup battery pack provides power to the servo-board and RF-link, enabling communication between Phoenix and the RCR if the OBC should malfunction.

Bibliography

[1] Peddle, I.: *Acceleration Based Manoeuvre Flight Control System for Unmanned Aerial Vehicles*. Ph.D. thesis, University of Stellenbosch, 2008.
Available at: http://scholar.sun.ac.za/handle/10019.1/1172

[2] Pietersen, W.: *System Identification for Fault Tolerant Control of Unmanned Aerial Vehicles*. Master's thesis, University of Stellenbosch, 2010.
Available at: http://scholar.sun.ac.za/handle/10019.1/4164

[3] Basson, W.: *Fault Tolerant Adaptive Control of an Unmanned Aerial Vehicle*. Master's thesis, Stellenbosch University, 2011.
Available at: http://ir1.sun.ac.za/handle/10019.1/17898

[4] Basson, L.: *Control allocation as part of a fault-tolerant control architecture for UAVs*. Master's thesis, Stellenbosch University, 2011.
Available at: http://ir1.sun.ac.za/handle/10019.1/6722

[5] Odendaal, H.: *An analysis and comparison of two methods for UAV actuator fault detection and isolation*. Master's thesis, University of Stellenbosch, 2012.
Available at: http://scholar.sun.ac.za/handle/10019.1/71780

[6] Bacon, B. and Gregory, I.: General equations of motion for a damaged asymmetric aircraft.
Available at: http://ntrs.nasa.gov/archive/nasa/casi.ntrs.nasa.gov/20070030307_2007030398.pdf

[7] Shah, G.: Aerodynamic effects and modeling of damage to transport aircraft. 2008.
Available at: http://ntrs.nasa.gov/archive/nasa/casi.ntrs.nasa.gov/20080034656_2008034489.pdf

[8] de Marco, A., Claudio, V. and Duke, E.: A general solution to the aircraft trim problem. *AIAA Modeling and Simulation Technologies Conference and Exhibit*, 2007.

[9] Nguyen, N., Krishnakumar, K., Kaneshige, J. and Nespeca, P.: Dynamics and adaptive control for stability recovery of damaged asymmetric aircraft. 2007.

[10] Arruda, M.: *Dynamic Inverse Resiliant Control For Damaged Asymmetric Aircraft: Modeling And Simulation*. Master's thesis, Wichita State University, 2009.

[11] AlSwailem, S.: *Application of Robust Control in Unmanned Vehicle Flight Control System Design*. Ph.D. thesis, Cranfield University, 2004.

[12] Peddle, I.: Introductory course to aircraft dynamics. 2011.

[13] Cook, M.: *Flight Dynamics Principles*. 2nd edn. Butterworth-Heinemann, 2007. ISBN 978-0-7506-6927-6.

[14] Shevell, R.: *Fundamentals of Flight*. Prentice-Hall.

[15] Anderson, J.: *Fundamentals of Aerodynamics*. Mc Graw Hill, 2007. ISBN 007-125408-0.

[16] Kuethe, A., Schetzer, J. and Chow, C.: *Foundations of Aerodynamics: Bases of Aerodynamic Design*. 3rd edn. John Wiley & Sons Inc, 1976. ISBN 978-0471509530.

[17] Jaquet, C.: *Control Surfaces in Confined Spaces: The optimisation of trailing edge tabs to reduce control surface hinge moments*. Master's thesis, Stellenbosch University, 2010.
Available at: http://scholar.sun.ac.za/handle/10019.1/4327

[18] Drela, M. and Youngren, H.: *AVL 3.22 User Primer*, 2011.
Available at: http://web.mit.edu/drela/Public/web/avl/

[19] Arora, J.: *Introduction to Optimum Design*. 2nd edn. Elsevier Academic Press, 2004. ISBN 0-12-064155-0.

[20] *Control Systems - Principles and Design*. 2nd edn. Mc Graw Hill, 2003. ISBN 0-07-048289-6.

[21] de Hart, R.: *Advanced Take-off and Flight Control Algorithms for Fixed Wing Unmanned Aerial Vehicles*. Master's thesis, Stellenbosch University, 2010.
Available at: http://scholar.sun.ac.za/handle/10019.1/4179

[22] Hahn, J., Edison, T. and Edgar, T.: A note on stability analysis using bode plots. 2001.

[23] Park, S., Deyst, J. and How, J.: A new nonlinear guidance logic for trajectory tracking.

[24] dspic30f6011a/6012a/6013a/6014a data sheet.
Available at: http://ww1.microchip.com/downloads/en/DeviceDoc/70143E.pdf

[25] Rcb-4h antaris 4 programmable gps.
Available at: http://ec-mobile.ru/user_files/File/u-blox/RCB-4H_Data_Sheet.pdf

[26] Adis16350: High precision tri-axis inertial sensor.
Available at: http://www.analog.com/static/imported-files/data_sheets_obsolete/OBSOLETE%20WATERMARK/ADIS16350_16355.pdf

[27] Integrated silicon pressure sensor for manifold absolute pressure, altimeter or barometer applications on-chip signal conditioned, temperature compensated and calibrated. .
Available at: http://www.promelec.ru/pdf/mpx4115A.pdf

[28] Integrated silicon pressure sensor on-chip signal conditioned, temperature compensated and calibrated. .
Available at: http://doc.chipfind.ru/image/freescale/mpxv5004g.gif